High-Voltage ESD Structures and ESD Protection Concepts in Smart Power Technologies

Bei der Fakultät für Elektrotechnik und Informationstechnik der
Technischen Universität Dortmund eingereichte

Dissertation

zur Erlangung des akademischen Grades

Doktor der Ingenieurwissenschaften
(Dr.-Ing.)

von

Dipl.-Ing. Yiqun Cao

Dortmund, 2019

Hauptreferent:	Prof. Dr.-Ing. Stephan Frei
Korreferent:	Prof. Dr.-Ing. Bernd Deutschmann
Tag der mündlichen Prüfung:	8. Oktober 2019

Danksagung

Diese Arbeit entstand während meiner Tätigkeit als Infineon Technologies AG Mitarbeiter in Zusammenarbeit mit dem Arbeitsgebiet Bordsysteme der Technischen Universität Dortmund.
Besonders danken möchte ich Prof. Dr.-Ing. Stephan Frei, Leiter des Arbeitsgebiets Bordsysteme der Technischen Universität Dortmund, der mir die Möglichkeit gegeben hat, diese Arbeit unter seiner kompetenten Betreuung durchzuführen. Prof. Dr.-Ing. Bernd Deutschmann, Leiter des Instituts für Elektronik der Technischen Universität Graz danke ich sehr für die freundliche Übernahme des Zweitberichters und die wertvollen Vorschläge zu dieser Dissertation.
Mein besonderer Dank gilt auch meinem technischen Betreuer von Infineon Dr. Matthias Stecher, der mich in den vergangenen Jahren immer wieder motiviert hat.
Weiterhin danke ich allen derzeitigen und ehemaligen Arbeitskollegen bei Infineon, Dr. Ulrich Glaser, Michael Mayerhofer, Dr. Friedrich zur Nieden, David Johnsson, Dr. Werner Simbürger und Dr. Joost Willemen für die technischen Diskussionen und Unterstützungen.
Ein ganz lieber Dank an meiner Frau Ye Shang, die mir jederzeit unterstützend zur Seite stand, und meinen Söhne Felix und Lennox, die immer für abwechslungsreiche Auszeit sorgten.

Vaterstetten, 2019

Overview

Electro-static discharge (ESD) event can cause upset or permanent damage of integrated circuits (IC) and electrical systems. The risk of ESD fails needs to be mitigated or prevented. ESD robustness of IC products and electrical systems is specified, verified and qualified according to respective ESD standards. For high-voltage IC products based on smart power semiconductor technologies for industrial, power and automotive applications, design of effective and cost-efficient ESD protection is a big challenge, demanding wide and deep technical knowledge throughout high-frequency and high-power characterization techniques, semiconductor device physic, circuit design as well as modeling and simulation.

The required measurement setups and tester components are developed and introduced. The characterization of ESD protection devices, IC and off-chip circuit elements is enabled and improved. The rise-time filters are important for the study of rise-time dependent ESD robustness. The human metal model (HMM) tester as an alternative to IEC ESD generators provides voltage waveform measurement with good quality in addition to current waveform measurement. It can be used for wafer-level or package-level device characterization. The measurement results of HMM tester and IEC ESD generator are compared.

The on-chip ESD protection design relies on proper choice of different types of ESD protection devices and structures, depending on ESD specifications and IC applications. Typical on-chip ESD protection, whether snapback or non-snapback, single device or ESD circuit is introduced. The failure levels studies give a systematic benchmark of the ESD protection devices and structures, concerning device area, clamping voltage and other relevant parameters. The trade-off between those parameters and limitation of different ESD protection is discussed. Moreover, understanding of ESD failure modes is the key to implement effective ESD design. A unique ESD failure mode of smart power semiconductor device is discovered and investigated in detail. In the scope of finding ESD solutions, new active ESD clamps have been further developed in this work.

The study of ESD protection is extended to the system-level involving on- and off-chip ESD protection elements. The characteristics of typical off-chip elements as well as the interaction between IC and off-chip protection elements plays essential role on the system robustness. A system-level ESD simulation incorporating IC and off-chip protection elements is desired for system efficient ESD design (SEED). A behavioral ESD model is developed which reproduces pulse-energy-dependent failure levels and self-heating effects. This modeling methodology can be used for assessment of system robustness even beyond ESD time-domain. The validation of the models is given by representative application examples.

Several main challenges of high-voltage ESD design in smart power technologies have been addressed in this work, which can serve as guidance for ESD development and product support in future power semiconductor technologies.

Table of Contents

Danksagung II

Overview IV

Table of Contents 1

Chapter 1 3

Chapter 2 7

2.1 Rise-Time Filters of a TLP System 7

2.1.1 Rise-Time Filters Design 8

2.1.2 Filter Implementation and Measurement Results 10

2.1.3 Summary 13

2.2 TLP Based Human Metal Model Tester 15

2.2.1 Measurement Setup of TLP based HMM 16

2.2.2 HMM vs. IEC: Transient Waveforms 21

2.2.3 HMM vs. IEC: Failure levels 26

2.2.4 Discussion and Summary 29

2.3 Conclusion 32

Chapter 3 33

3.1 Failure Levels Studies of On-Chip ESD Protections 34

3.1.1 npn-BJT 35

3.1.2 pn-Diode 38

3.1.3 Simple Active Clamps 43

3.1.4 Comparison of the ESD Devices 51

3.1.5 Summary 56

3.2 Case Studies for Failure Modes of ESD Protections 57

3.2.1 Case Studies and TLP Results 58

3.2.2 Study on the Dynamic Issues 62

3.2.3 Failure Analysis and HBM Results 72

3.2.4 Improvement Proposals 74

3.2.5 Summary 77

3.3 Novel On-Chip Statically Triggered Active Clamps 77

3.3.1 Studied Active ESD Clamps 78

3.3.2 Measurement and Simulation 84

3.3.3 Discussion 89

3.3.4 Summary 97

3.4 Conclusion 97

Chapter 4 99

4.1 Characterization and Systematic Evaluation of External ESD Protection Elements....................99

4.1.1 High-Current TLP Characterizations....................100

4.1.2 IEC 61000-4-2 Generator Characterizations 108

4.1.3 Characterizations using Network-Analyzer....................108

4.1.4 Summary....................109

4.2 ESD Simulation with a Wunsch-Bell based Behavior Modeling Methodology....................110

4.2.1 Modeling Methodology 111

4.2.2 Models of ESD Structures 114

4.2.3 Application of the Behavior Models....................122

4.2.4 Summary....................126

4.3 Conclusion 127

Chapter 5 128

List of Abbreviations 130

Bibliography 132

List of Own Publications 140

Chapter 1

Introduction

Modern automotive technologies require high complexities of electrical systems to fulfill increasing demands of driver assistance system, automated driving, safety, comfort functions and advanced security and energy efficient applications [1]. Semiconductor technologies like smart power technologies enable the development of large assortment of products of integrated circuits (IC) which cover a wide spectrum of product portfolio such as supply chips, system basis chips, engine management ICs, driver ICs, DC/DC converters, low-side and high-side switches, LED drivers, sensor chips etc.

Smart power technologies [2] enable the integration of power modules, digital processors, analog circuits and memories in one technology platform introducing numerous challenges and opportunities in the technology development as well as in the product development. Figure 1.1 illustrates the block diagram of a typical microcontroller IC with integrated LIN transceiver and MOSFET driver for automotive applications. Besides the high integration, high quality and robustness is a critical prerequisite for competitive automotive IC products, especially as functional safety (ISO 26262) [3] has gained nowadays crucial importance in the automotive industry.

In light of robust design of automotive IC products, the protection of ICs from damages or functional upset caused by electrostatic discharge (ESD) or other electrical fast transients (EFT) [4] has become one of the important and challenging tasks during the IC and system development. ESD is the transient discharge of static charge, which can arise from human handling or contact with machines. The high voltages result in large electric fields and high current densities in the small devices, which can lead to breakdown of insulators and thermal damage in the IC [52].

The ESD challenges have become more apparent by the high complexity of the IC product features and the used smart power technologies. The increasingly higher complexity of integrated function blocks on IC products is driven by the required feature set and cost position demanded by automotive suppliers and car manufactures.

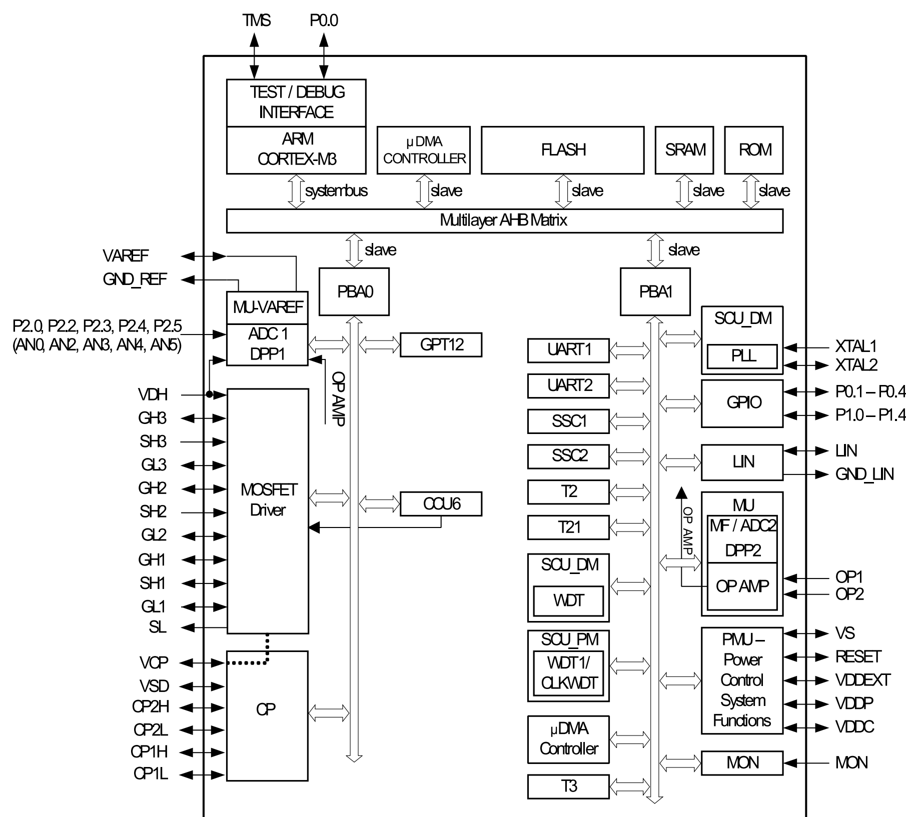

Figure 1.1: Block diagram of a typical Microcontroller IC with LIN and MOSFET driver for automotive applications.

In fact, the development of on-chip ESD protection belongs to one of the technology fundamentals that have to be considered and addressed throughout the entire technology development. As part of IC product design on the other hand, on-chip ESD protection implemented on IC products ensures safe frontend and backend fabrication and assembly within IC manufacturing. The so-called component-level ESD protection to fulfill the ESD requirements for IC fabrication and assembly is addressed by the standards such as human body model (HBM) [85] and charged device model (CDM) [5] with dedicated discharge current waveforms. For automotive IC products the qualification is performed according to AEC-Q100 [6] [7].

Towards system-level protection, as it is especially relevant for the automotive applications, ESD and EFT robustness in electrical systems became essential because the severity of the stress induced failures can be high as they can be related to safety function applications. The IC failures are possible causes for overall electrical system malfunctions and failures, which signify high cost of repair or replacement. The ESD test methods on system level are described in the standards IEC 61000-4-2 [29] or ISO 10605 [113] which are much different from the component-level ESD e.g. HBM and CDM concerning the discharge current waveforms. Depending on the applications, the discharge current finally diverted in the ICs can be strongly distorted by the on-board elements and traces and is difficult to predict. This makes an effective and cost efficient ESD protection on system-level very challenging where component-level ESD robustness cannot be simply translated to system-level ESD robustness [117]. As one of the results of those investigations in this area during the past years [8] [9], co-design

of on-chip and off-chip ESD protection published as “system-efficient ESD design” (SEED) approach [10] provides a concept to enable system optimized ESD solution. An effective and efficient ESD protection solution on system-level therefore requires deep understanding of on-chip and off-chip ESD protection elements in terms of their behaviors under various ESD stress conditions. Moreover, it requires strong technical knowledge about the interaction between on-chip and off-chip protection elements.

Traditional on-chip ESD protection for IC focuses more on ESD device concept and device parameter engineering for component-level ESD protection [50]. However, a comprehensive ESD development approach with an overview of broad technical relevance, not only for component-level but also for system-level protection has still not been systematically studied and evaluated for automotive power technologies. The scope of this work is hence to provide the insight of several key components of ESD development with respect to high-voltage domains in smart power technologies. The high-voltage applications in the context of this work aim at voltage classes typically ranging from 10 V to 100 V whereas the advanced CMOS technologies focusing on computing applications with 3.3 V as already an ultra-high voltage. On the other hand, 250 V for power discrete technologies can be considered as a low voltage for example MOSFETs for the power supply switching applications.

Development of high-voltage ESD protection elements to fulfill both component-level and system-level ESD encounters several major challenges. It is well known that the IC hardware failures and their failure mechanisms caused by ESD or EFT events strongly depend on the electrical signature of inrush pulses. The miscorrelation of system-level and component-level ESD robustness has much to do with the different parameters like rise-time, pulse duration, peak voltage and current, power and energy etc. [11]. In order to uncover device characteristics and the influences of different stress conditions on the devices under test, advanced measurement techniques are prerequisites that must be well reproducible and precisely capture the devices’ behaviors. Commonly used transmission line pulse [18] system requires an upgrade to provide definable rise-times, source impedance and dedicated pulse shapes to enable advanced device characterizations especially on wafer-level measurements. The developed test methods in this work can find their applications at each ESD development stage.

The state-of-the-art high-voltage on-chip and off-chip device portfolios need to be evaluated and benchmarked from many relevant aspects such as ESD performance and footprint area associated with chip cost, responding time and triggering mechanisms associated with protection effectiveness as well as application ranges concerning pulse durations. Only if the advantages and disadvantages of each type of ESD protection elements are well understood, a good trade-off can be made for optimized protection scheme consisting co-design of on-chip and off-chip ESD protections that fulfills the requirements. Beyond the ESD requirements, ESD protection must be successfully implemented without affecting circuit functions is usually a challenging task. On the contrary, functional devices such as DMOS transistors for driver applications can inherently conduct ESD current that provides new opportunities for ESD device development [55]. Hence new protection device concepts are often necessary to ensure overall a good ESD design kit. In this work, design details of novel high-voltage on-chip ESD protection elements are introduced and discussed.

Although the IC hard failures are mainly dielectric rupture or thermal runaway of semiconductor as results, the fail mechanisms are rather manifold. Overvoltage and overcurrent across and through the devices and structures depending on their amplitude

and duration can result in physical damage in different severity [12]. The damage can occur in any devices and structures exposed directly or indirectly to the disturbances. Dielectric breakdown mainly gate-oxide breakdown during ESD regarding time-dependent dielectric breakdown (TDDB) has been extensively revealed in publications e.g. [13]. On the other hand junction burnout including uniformed and non-uniformed overheating of semiconductor devices under high current injection are investigated e.g. in [14]. However for automotive power technologies, the failures modes which involve interaction of protection and protected devices beyond the classical failure mechanisms were not yet intensively investigated. Undiscovered failure modes should be anticipated and considered during the ESD development and design. This work shows a detailed investigation on a unique failure mode of ESD protection concept and respective solutions.

As IC behaviors under system-level ESD stress conditions are essential, sophisticated IC models that are useful for system-level ESD simulation and verification are generally desired by system engineers [15]. The advanced modeling methodology enables precise simulation that gives guidance of choosing adequate ESD solutions for system applications. Compact modeling is often used for chip-level ESD simulation and design [16]. In recent years, several compact modeling and mixed-mode simulation approaches were introduced also for system-level ESD design [17]. As the failure levels as well as the I-V characteristics of on-chip ESD protection elements can differ significantly depending on the stress condition at IC pins on system level, it is believed the behavior modeling approach introduced in this work offers easy-to-implement simulation models which can precisely predict overall ESD robustness of a system for a fairly wide application range of ESD and EFT stresses.

This work is structured as follows: Chapter 2 describes the used ESD testing techniques: the rise-time filters designed for a TLP measurement system provide the possibility to study in detail the turn-on time of different ESD protection elements. The so-called human metal model (HMM) measurement system emulates ESD pulse of an IEC 61000-4-2 ESD generator that is used for device characterization both on wafer and package-level. In Chapter 3, different on-chip ESD protection elements are studied in terms of their protection levels and failure mechanisms. The high-voltage active clamps were further optimized with advanced circuit design techniques achieving good balance between size, ESD performance and effects on functional circuitry. The characterization of ESD elements is then extended to off-chip elements discussed in Chapter 4. The combined effectiveness of on-chip and off-chip elements is investigated and understood by the advanced ESD modeling methodology which reproduces ESD devices behavior depending on the energy level and time duration of in-rush pulses.

Chapter 2

ESD Testing Techniques

Well-developed testing techniques are essential for ESD investigations. Precise and reliable test equipment can be used to verify ESD performance of studied structures, diagnose ESD related problems and characterize devices features. Transmission line pulse (TLP) systems count as one of the most powerful test equipment, which is necessary for ESD problem shooting, verification and characterization of ESD concepts and devices throughout the work. A fully functional TLP system provides electrical pulses with definable rise-time and pulse duration. The pulse duration can be simply adjusted with the length of the charge cable. The setup of the rise-time requires the filtering techniques in high voltage and high current environment. This chapter provides the design and the implementation of a set of rise-time filters, which belong to the major hardware components in TLP system. Further, by modifying the hardware of the TLP system, a so-called human metal model (HMM) tester both for wafer- and package level measurements is developed enabling a new characterization method. It delivers system-level ESD (also called IEC) like pulses into device under test (DUT). The HMM tester enables easy and reliable characterization of ESD protection devices and circuits compared to the traditional system-level ESD tests using a system-level ESD generator according to ISO 10605. The results from the HMM tests and the system-level ESD tests are comparable. The HMM tests provide much better measurement quality of the transient voltage waveforms.

2.1 Rise-Time Filters of a TLP System

The integrated circuit (IC) industry has been using TLP testing equipment based on the theory introduced by Maloney and Khurana [18] to characterize on-chip and off-chip ESD protection structures and ESD protected circuits since 1985.

The most common ESD failures in ICs such as thermal runaway of metal interconnections, junction burnout, dielectric ruptures in the ESD protection devices and protected circuits depend heavily on the pulse energy. Thus their robustness and especially the robustness of those thermally limited devices and circuits can be characterized by setting the TLP pulse width and TLP current according to the Wunsch Bell theory [19]. However, as many ESD failures are not induced by pulse energy but

rather by a high electric field such as voltage overshoots when ESD protections cannot react sufficiently fast to the transient pulses, various TLP rise-times become very important for the characterization and verification of the ESD hardness of DUTs. Therefore, it is desired to design a set of rise-time filters [20] for the high power and high frequency applications to achieve well-established TLP characterization in the measurement setup.

Time domain systems often contain significant energy beyond the relation of the bandwidth to the rise-time: $t_r = 0.35/f_{BW}$ [21]. f_{BW} denotes the bandwidth. Pulse shaping by dimensioning the rise-time and bandwidth can be accomplished by simply low pass filtering the output signal. Classical frequency domain filters such as Butterworth and Chebyshev filters have inherently poor group delay characteristics that cause jitter in the time domain by delaying parts of the high frequency data with respect to low frequency.. Furthermore, a mismatched filter can result in multiple reflections in the TLP system that can also deteriorate the pulse shape to unacceptable form. For the purpose of building a qualified TLP system, the rise-time filters should have near Gaussian roll-off characteristics, which is absorptive as wideband as possible both in the pass- and stopband to meet the requirements. Since high voltage or current may damage the components in the filters during the TLP testing, robust components should be selected in the filter design.

A theoretical derivation and a simplified approach of such filters were published in [22] and [23], respectively. The rise-time filters described in this section have the same topology as in [23] but are based on completely different power levels. The rise-time filters consist of the passive components RLC in an appropriate order to fulfill the special demand of very fast TLP (vf-TLP) applications. In addition, a more precise approximation of derivation and a more practical design flow using the lumped-element approach and the microstrip approach are shown.

2.1.1 Rise-Time Filters Design

From the numerical derivations [22], the lossy transmission line represents a broadband (all-pass) attenuator, with a frequency-invariant attenuation. Hence, based on the model of a lossy transmission line, lumped-element ladder-network can be considered as the fundamental structure of the rise-time filters. As approximation of the incomplete Gaussian transmission line, the topology of lumped-element filters is used for the rise-time filter design. Symmetrically, the filter shows absorption rather than reflection at both ports and in both pass- and stopband.

Figure 2.1 shows the topology of a 9th-order rise-time filter. The inductance values are identical as $L1 = L2 = L3 = L4 = 2 \cdot L$. Due to superposition of parallel capacitance

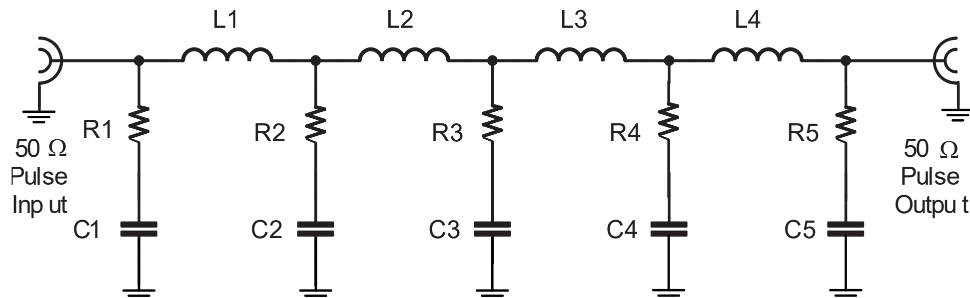

Figure 2.1: Topology of a 9th-order rise-time filter.

and resistance with the half-cells, $C2 = C3 = C4 = 2 \cdot C$ and $C1 = C5 = C$. $R1 = R5 = R$ must be equal to the given characteristic impedance $Z_c = 50\ \Omega$ in this design. R2 to R4 yield principally a value of $R/2$ but empirically a value between $R/3$ and $R/2$ for better performance.

According to the mathematical deviations [22], following equations can be used to determine the unique values of R, L and C for a given Z_c and the quantity of inductors N (e.g. $N = 4$ in Figure 2.1). $\omega_0 = 2\pi \cdot f_{BW}$ is given as the cut-off frequency.

$$L = Z_c^2 \cdot C = R^2 \cdot C \tag{2.1}$$

$$C = \frac{1}{\omega_0 \cdot Z_c \cdot \sqrt{\frac{2N}{ln2} - \frac{5}{8}}} \approx \frac{1}{1.71 \cdot \omega_0 \cdot Z_c \cdot \sqrt{N}}. \tag{2.2}$$

It has been found that the approximation in $\approx \frac{1}{1.71 \cdot \omega_0 \cdot Z_c \cdot \sqrt{N}}$. is very reliable if $N \geq 4$. The order of filter is simply $2N + 1$ that equals the quantity of used reactive devices. For the application of TLP and vf-TLP systems, the requirements of rise-time filter design can be roughly concluded in the following points:

- Transmission line in TLP testing with impedance matching.
- Maximally flat group delay and minimal reflections to avoid pulse distortion.
- Robust components for high voltages and high currents.
- Mechanical robustness.
- A set of filter for 300 ps, 500 ps, 1 ns, 2 ns, 5 ns, 10 ns, 20 ns and 50 ns rise-time required.

The design of the filter set is implemented with two approaches: the microstrip filters and the lumped-element filters. The microstrip filters need to be made for rise-time smaller than 500 ps due to their relative higher cut-off frequency and consequently smaller values of L and C. Extremely small lumped devices can have unacceptable tolerance in L and C values, and are thus not used. Parasitic effects can also easily harm the performance. Hence, the SMD lumped-element filters are more appropriate for rise-times larger as 1 ns, having minimal size and low influence of parasitic effects due to the smaller bandwidth. The mutual coupling effects of the coil inductors are considered negligible according to the FastHenry [24] simulation. Furthermore, the physical size of the small scaled inductance or capacitance in the microstrip implementation is comparable with those of larger lumped-elements, so that all filters can be intentionally designed for an identical mechanical dimension and placed into the same metal enclosure with size of $37.2\ mm \times 67.2\ mm \times 16\ mm$.

The Advanced Design System (ADS) from Agilent [25] is applied as the simulation tool. In both implementation approaches, the filter simulation is carried out including microstrip components like microstrip lines, stubs and curve bends. However, the capacitive coupling between these components are not well considered, which indeed causes a certain level of mismatches between simulation and measurement results especially for filters with smaller rise-times.

All printed circuit board (PCB) layouts are designed using PADS Designer by Mentor Graphics [26]. A 50 ns lumped-element filter and a 500 ps microstrip filter from the series of the designed TLP rise-time filters are concretely described as examples.

2.1.2 Filter Implementation and Measurement Results

Rather than each specified rise-time of the filters, the main difference of the filter design comes from two types of the implementation concepts: the lumped-element filters and the microstrip filters. Thus for each type of the filters, one example is elaborately introduced to present the design procedures and the evaluation of the measured results. The optimized parameter settings of the other filters are also summarized.

2.1.2.1 50 ns Lumped-Element Filter

In general, using a high-order near-Gaussian low pass filter can improve the performance by lowering the reflection in the stopband. Limited by the physical size of the filters, a 9th order ($N = 4$) structure drawn in Figure 2.1is a good compromise to fulfill the design requirements. Starting from $t_r = 50\ ns$, ω_0 is simply 7 MHz. With the given characteristic impedance Z_c=50 Ω, the total values of the RLC can be readily calculated using 2.1 and 2.2 as 50 Ω, 334 nH and 134 pF, respectively.

The coil inductor produced by Coilcraft [27] 132_20SM has the inductance of 538 nH that is comparable with 2·L in this filter design. Rather than 25 Ω, R2 to R4 is designed between 18 Ω and 22 Ω to achieve better group delay performance. In addition, the S-parameter models of the inductors are used in parameter sweep simulations in order to determine the value of R and C for the optimal performance.

A prototype of the filter is developed on the PCB material ROGERS 4003C. The substrate has a relative permittivity ε_r of 3.38 and a thickness of 1.524 mm. The microstrip interconnections are included in the filter simulation as well. High Q and high voltage multilayer capacitors are chosen in order to ensure the ruggedness of components during TLP testing. The ATC [28] capacitor 100C131JW2500X 130 pF is used as C1, C5. 100C271JW2500X with the value of 270 pF is applied as C2, C3 and C4. All of the capacitors can work perfectly up to 2500 V DC that is sufficiently robust for the filter stressed by high voltage pulses with very short pulse width. Instead of high power resistors, high frequency specified metal layer resistors with small parasitic inductance are desired for the filter design. SMD resistors, type Yageo RC1206 with 51 Ω, 0.25 W are used for R1 and R5. Also, R2, R3 and R4 are implemented with 20 Ω.

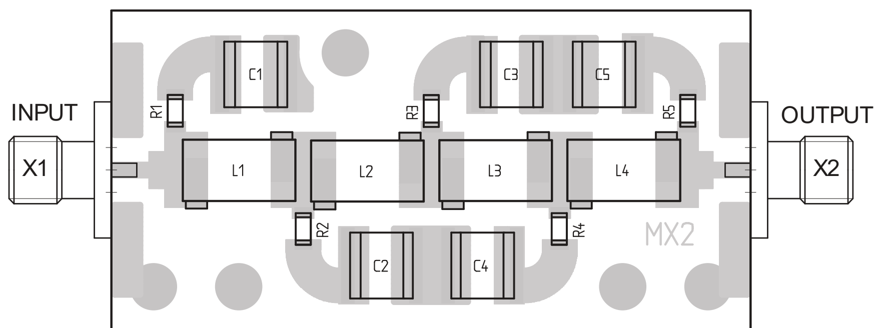

Figure 2.2: Layout of the 50 ns lumped-element rise-time filter.

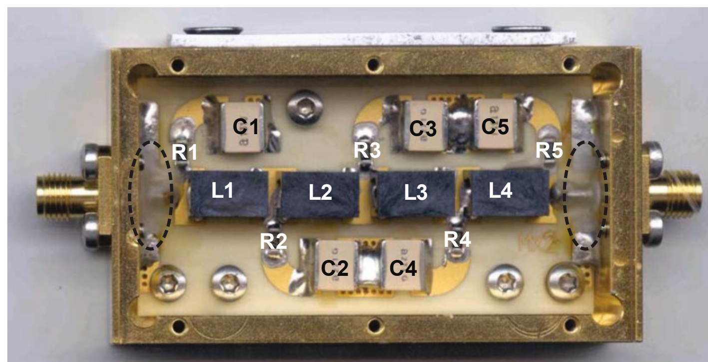

Figure 2.3: Photograph of the 50 ns lumped-element rise-time filter.

Figure 2.2 and Figure 2.3 show the layout of the 50 ns rise-time filter and a photograph of the fabricated filter. Indicated with dashed ovals in Figure 2.3, extra paraffin wax is used at the input and output interface to avoid occasionally air breakdown under high voltage. Figure 2.4 displays the measured magnitude of the reflection |S11| and transmission |S21| coefficient compared to the results of ADS simulation. As expected for the filter with relatively slower rise and fall slopes (>5 ns), very good agreement between the theoretical and experimental results can be obtained. Parasitic effects are rather negligible compared to the designed RLC values, thus do not have much negative impact on the circuit. Note that since the filter design is very symmetrical, |S12| and |S22| are not explicitly shown.

2.1.2.2 500 ps Microstrip Filter

According to 2.1.2.1 the inductance and capacitance should be implemented using microstrip technique in this design to eliminate parasitic effects of lumped elements. The highest order of the filter depends on the geometrical size limit of the filter metal enclosure which is already defined by the lumped-element filters. Within the given PCB with the size of 30 $mm \times 60$ mm, an 11th-order low pass filter is implemented for a 500 ps rise-time. Figure 2.5 shows the schematic diagram of the filter. Several $\lambda/4$

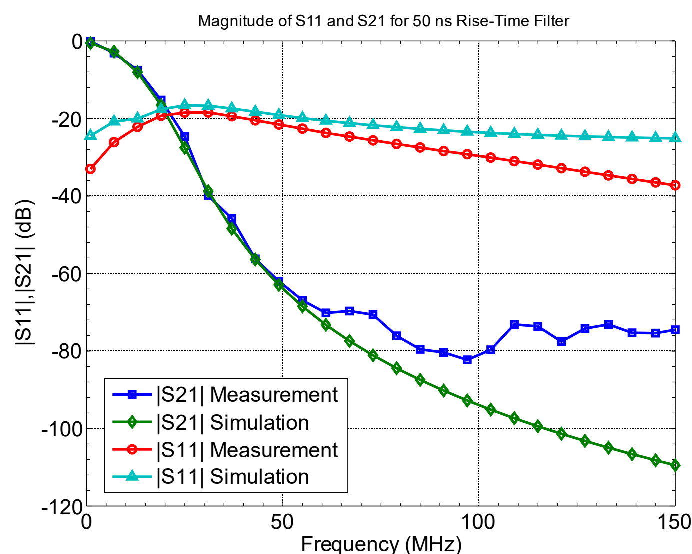

Figure 2.4: |S11| and |S21| of the 50 ns filter.

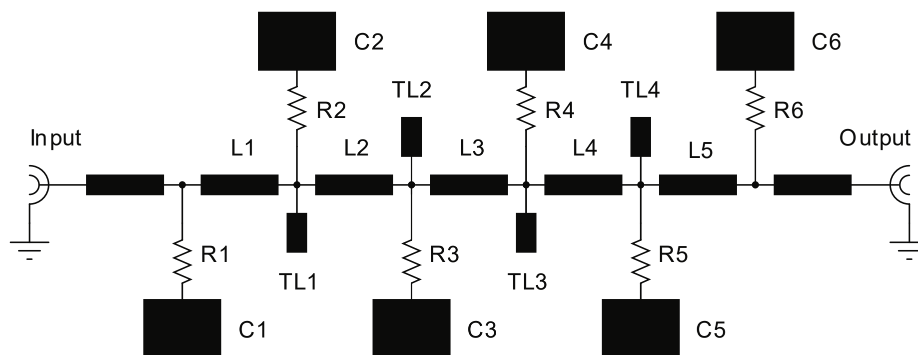

Figure 2.5: Schematic diagram of the 500 ps microstrip rise-time filter.

microwave stubs TL1 to TL4 were also designed to suppress |S21| in the high frequency stopband and to smooth the output.

Again, for $Z_c = 50\,\Omega, N = 5$ and a cut-off frequency of 700 MHz, the parameter-settings of L and C are derived as 3.0 nH and 1.2 pF. It is found in the design procedure that the capacitance has usually more influence on the circuit performance. Therefore, the capacitors made as microstrip elements must be carefully dimensioned. Using the same PCB material ROGERS 4003C as for the lumped-element filters, the inductors are differently implemented with narrow microstrips with trace width 0.8 mm and length 10 mm. The microstrip capacitances have the dimensions of $5\,mm \times 9.8\,mm$, and $10\,mm \times 10.8\,mm$ depending on their positions. The only used SMD components in the microstrip filters are 1206 resistors which are the same resistors used in the lumped-element filters. The parasitic capacitive coupling becomes the main challenging task in the design of the microstrip filters. Figure 2.6 shows the picture of the fabricated prototype.

Base on the simulation, R1 and R6 are implemented with 51 Ω while the other resistors have the value of 18 Ω. Because the small rise-time filter is relatively sensitive to the coupling capacitances, Figure 2.7 exhibits a certain level of mismatch between simulation and measurement results. The rise-time has been expanded to about 590 ps that is larger than the expected value of 500 ps. Nevertheless, the low reflection requirement is also important and can be fulfilled for the TLP testing applications.

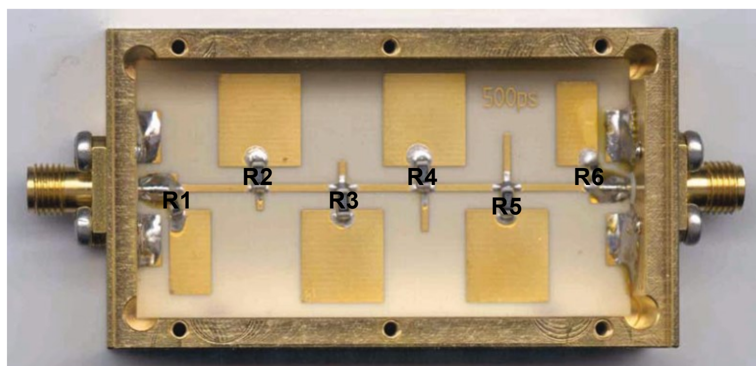

Figure 2.6: Photograph of the 500 ps micro-strip rise-time filter.

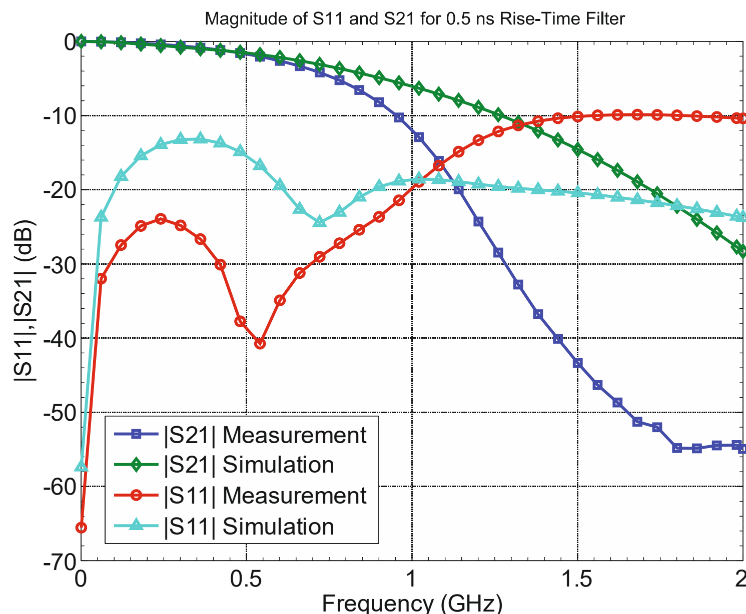

Figure 2.7: |S11| and |S21| of the 500 ps filter.

2.1.3 Summary

The absorptive low pass filters with different rise-times are designed and fabricated. The dynamic responses of all the filters are measured by using a TLP system, which can originally provide very precise rectangular pulses with an initial rise-time of about 100 ps as the reference pulse without filter. The pulse duration is less relevant for the testing of the rise-time filters, thus is set to 100 ns in the TLP measurements. In order to test the robustness of the rise-time filters under high voltage and high current condition, the discharge voltage of the transmission line is set to 800 V resulting in a pulse with the peak power of 12.8 kW at 50 Ω load. All pulses are recorded using

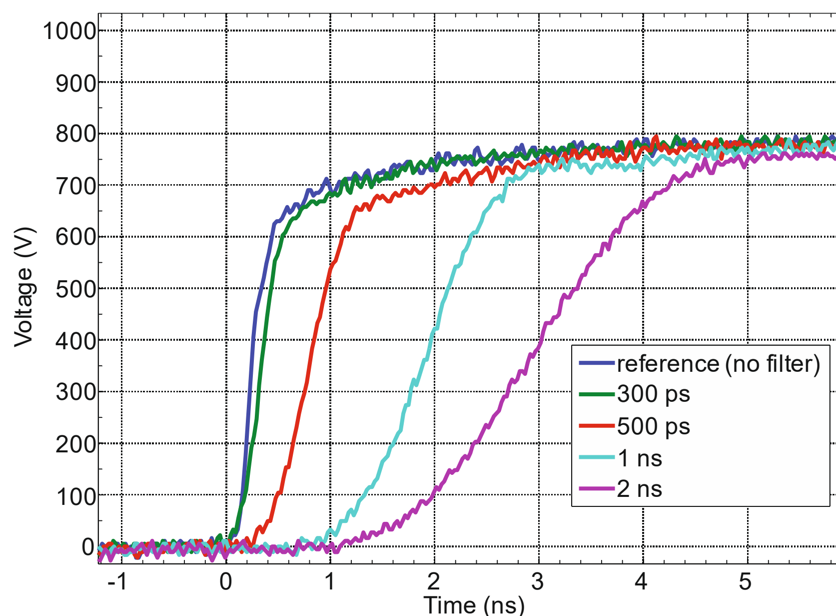

Figure 2.8: Measured reference pulse and pulse response of rise-time filters up to 2 ns.

Tektronix TDS6124C, a 40 GS/s oscilloscope with the input limit of 5 V. Therefore, in series connected attenuators with $3dB + 3dB + 3dB + 3dB + 10dB + 10dB + 20dB = 52dB$ attenuation (factor 398.1 in voltage) are added between the output of the filters and the oscilloscope. The first five high power attenuators are chosen to withstand the high voltage signal. Due to the sufficient bandwidth of the oscilloscope, pulses with smaller rise-times up to 2 ns including the reference pulse are precisely measured, and depicted zoomed-in in Figure 2.8. The overview of all the pulse responses with various rise-times from 300 ps to 50 ns is then illustrated in Figure 2.9. The reference pulse, which can be considered as the input signal of rise-time filter, is not displayed in this plot.

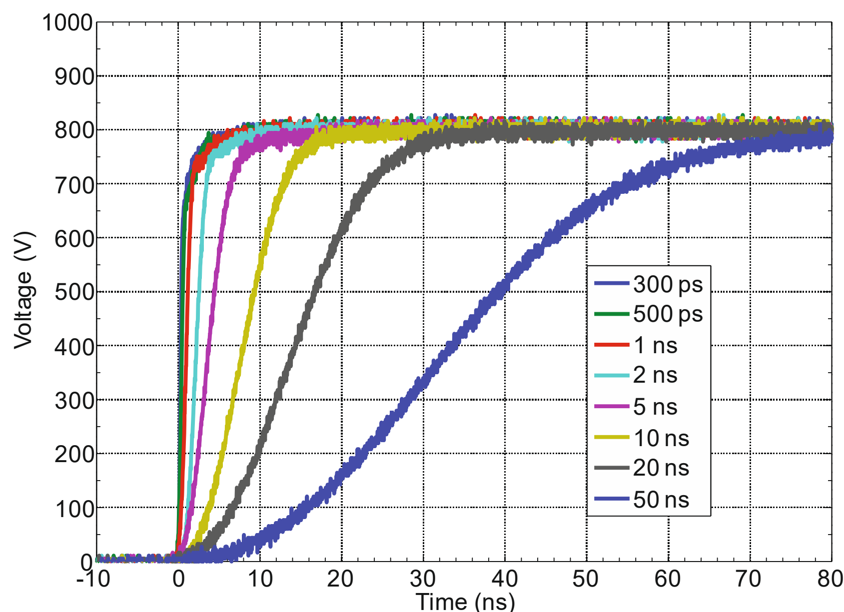

Figure 2.9: Measured pulse response of all realized rise-time filters.

The lumped-element rise-time filters are implemented based on the 9th-order low pass filter topology and already described in Figure 2.1. Table 2.1 shows the parameter settings and the used components in detail for all designed lumped-element filters. Table 2.2 summarizes the experimental results of all the measured rise-times t_r (10%-90%) based on S-parameter measurements. Mismatch is noticeable for the microstrip filters since the parasitic components especially capacitances have large impact on the frequency response of the filters. A more complex 2-D or 3--D electromagnetic simulator could be applied for further improvements on more precise designs. On the other hand, the microstrip filters require only resistors as the lumped components. The filters can be implemented easily with lower cost. The parameter settings of resistors are not summarized explicitly. The 300 ps filter is similarly developed by applying the same resistors as in the 500 ps filter. Although it is designed with a higher filter order (17th) in order to utilize the given size of PCB frame.

Table 2.1: Parameter settings and used components of the lumped-element rise-time filters.

t_r (ns)	R1,R5(Ω) (Size)	R2~R4(Ω) (Size)	L1~L4(nH) (Product Code)	C1,C5(pF) (Product Code)	C2~C4(pF) (Product Code)
1	51 (1206)	20 (1206)	17.5 (B06T)	2.4 (100B2R4BW500X)	5.1 (100B5R1CW500X)
2	51 (1206)	20 (1206)	27 (1812SMS27N)	5.6 (100B110KW500X)	11 (100B110KW500X)
5	51 (1206)	20 (1206)	56 (1812SMS56N)	15 (100B150KW500X)	30 (100B300KW500X)
10	51 (1206)	20 (1206)	130 (132_11SM)	30 (100B300KW500X)	62 (100B620KW500X)
20	51 (1206)	20 (1206)	246 (132_15SM)	62 (100B620KW500X)	110 (100C111JW2500X)
50	51 (1206)	20 (1206)	538 (132_20SM)	130 (100C131JW2500X)	270 (100C271JW2500X)

Table 2.2: Simulation vs. measurement for the rise-time filters.

Simulation (ns)	0.3	0.5	1	2	5	10	20	50
Measurement (ns)	0.29	0.6	1.1	2.1	4.8	10	19	45

2.2 TLP Based Human Metal Model Tester

As discussed, TLP systems are widely used in the field of ESD testing and characterization for devices and components. System-level ESD tests are also often required as one of the specifications on the product data sheets. Over the last few years, system-level ESD tests according to IEC 61000-4-2 [29] (often referred as "IEC" or "GUN") have been applied directly on standalone ICs or on external ESD protection elements on PCB or on combination of both. Those tests are done with a short discharge connection between the ESD generator tip and the devices or networks under tests [30]. The motivations to test directly IC pins according the IEC standard are manifold. One of them is that there is a tendency to avoid discrete ESD protection devices on PCB to minimize the product cost on the production of electronic systems. Another one is that in the area of electric vehicle networks the ICs have to become more and more robust since the number of electrical overstress (EOS) [11] events such as switching of inductive load has significantly increased. This is especially requested for pins, which are for example attached directly to the connector of an electronic control unit (ECU). A further reason for improved system-level ESD robustness of such pins e.g. of controller area network (CAN) and local interconnect network (LIN) communication ICs within a car is the need to avoid signal distortion caused by additional external protection devices. However, up to now the ESD generators for system-level ESD testing do not show experimental results with very high quality: Traditional system-level ESD tests often suffer from poor reproducibility, poor measurement precision, elaborate setup etc. [31]. These can yield ambiguous results from vendors and customers on verification of ESD requirements.

In order to improve this unsatisfied situation the so-called human metal model (HMM) evaluation method has been discussed intensively in the standardization committee SP5.6, ESDA [32]. HMM is a testing method which by definition is directly applied to IC components. The current stress waveform of HMM is similar to the IEC 61000-4-2 one. Recent publications [33] [34] [35] reported that there is an alternative way to generate IEC-like pulses by employing coaxial transmission lines, passive networks and a proper rise-time filter. A wafer-level HMM tester with a non-coaxial approach is also presented in [36] [37] to compare the impact of HMM and HBM stresses on on-chip devices.

With all these considerations, a new HMM tester constructed based on TLP with the coaxial transmission line approach is presented in this work with an accurate measurement technique for recording voltage and current waveforms both on board- and on wafer-level [38]. Several measurement setups for measuring transient waveforms are introduced. Not only to describe the HMM tester, the goal is also to validate this ESD testing technique for the application of high-voltage ESD development. In the following sections, various DUTs are stressed both with the IEC ESD generator and the HMM tester in order to compare the waveforms. Failure levels regarding thermal and electrical damages of IC pins are determined in the experiments by IEC and HMM for the comparison. Further, conditions of the usage of the HMM tester for ESD tests are discussed. The attempt of applying the TLP based HMM measurement technique on real system-level is also experimentally shown. The advantages and limitations of the HMM method comparing to the IEC test on components are given as well.

2.2.1 Measurement Setup of TLP based HMM

2.2.1.1 Pulse Generation of HMM Tester

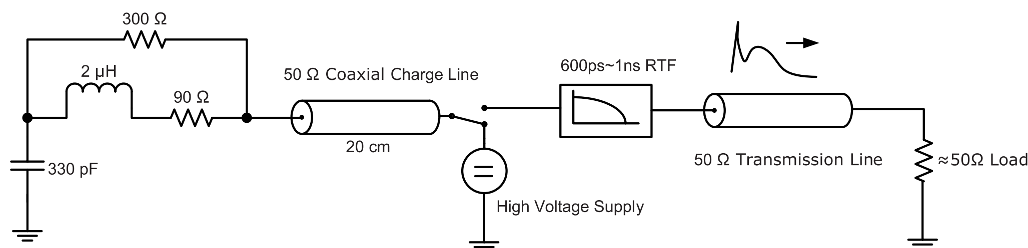

Figure 2.10: Simplified schematic diagram of a TLP based HMM pulse generation.

Different to firstly introduced by Grund Technical Solutions [34], another approach of the coaxial HMM tester with schematic diagram shown in Figure 2.10 was basically outlined in [39]. This work further improves the design. The short charge line with about 20 cm length is responsible for the generation of the first peak current. The RLC network is used to generate the broad peak (also called second peak) current. The values can be easily determined using circuit simulation using simulators such as SPICE. Note that the transmission cable length between the rise-time filter (RTF) and the system load is normally several meters, which means when the system load differs much from 50 Ω, a reflected signal will distort the IEC-like waveform after several tens of

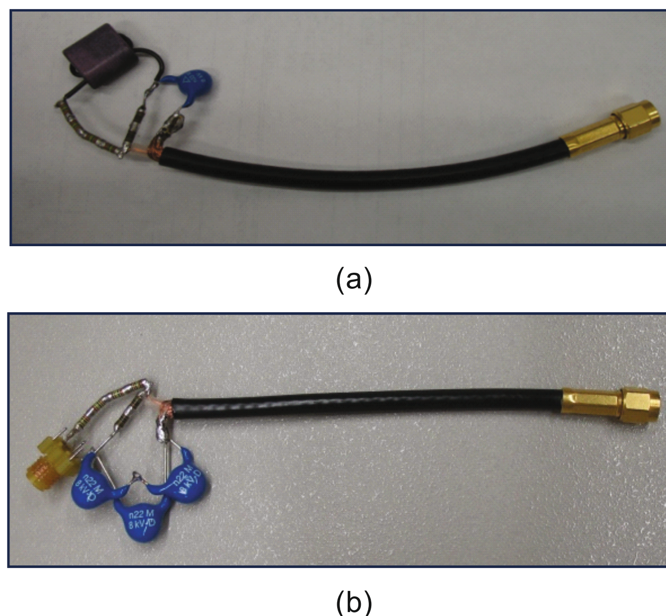

Figure 2.11: Prototypes of pulse shaping circuits using (a) ferrite inductor and (b) air coil inductor. The equivalent capacitances are the same although in (a) one capacitor and in (b) three capacitors are used.

nanoseconds. Thus, to avoid the reflection and deliver an acceptable current waveform to the DUT, nearly 50 Ω system load must be insured during HMM tests. The maximal voltage on the 20 cm charge line is limited by the used TLP at 4 kV. This results in a maximal peak current of $4\ kV/2/50\ \Omega\ =\ 40\ A$ corresponding to a discharge voltage level of about 10 kV IEC pulse (peak current 37.5 A). High power attenuators usually employed for the TLP pulse generation are completely removed in the HMM measurement system to obtain highest possible stress levels.

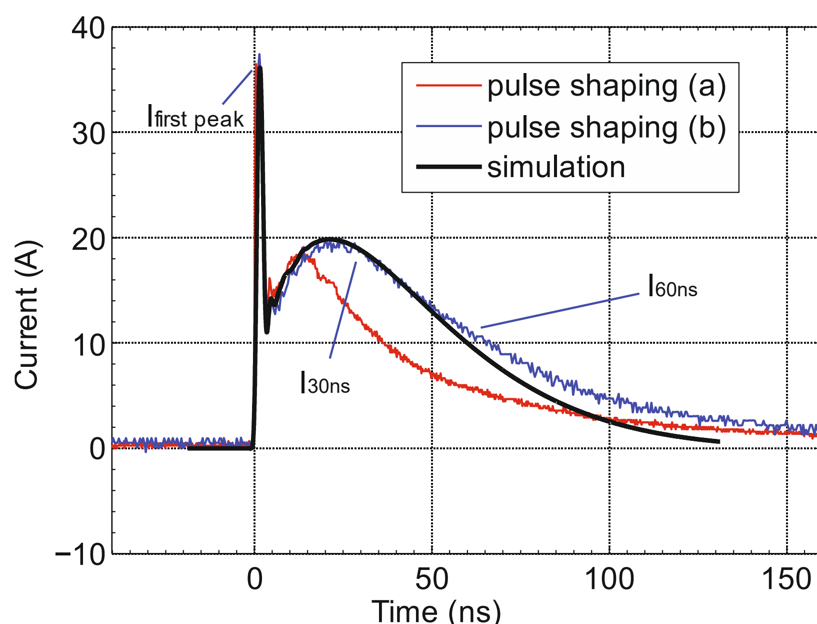

Figure 2.12: Measured current waveforms at 10 kV IEC level using different pulse shaping circuits (a) and (b) according to Figure 2.11. SPICE Simulation result referring to the schematic in Figure 2.10 is also shown for comparison.

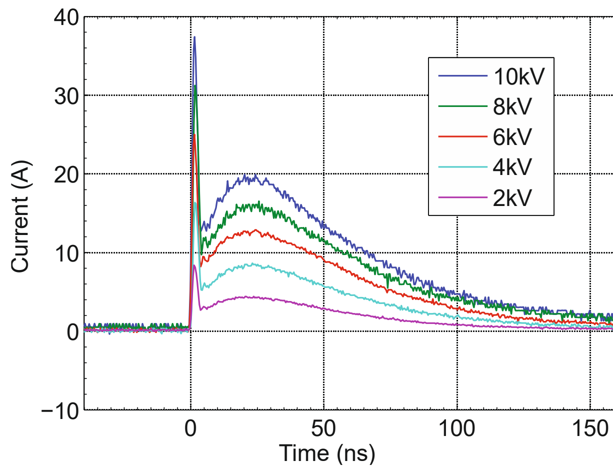

Figure 2.13: Measured HMM current waveforms at different IEC levels.

Table 2.3: Deviations of the current values referring to the standard.

V (kV)	$\Delta I_{first\ peak}$ (%)	ΔI_{30ns} (%)	ΔI_{60ns} (%)
2	2%	8%	0%
4	6%	6%	10%
6	5%	6%	10%
8	4%	8%	9%
10	4%	3%	11%

The main challenge of the implementation of HMM pulse shaping is in the RLC network. Only by carefully choosing the passive elements, the current waveforms delivered by the HMM tester can fit in with the IEC pulses. Figure 2.11 shows two different implementations of the pulse shaping circuits. Main differences are the types of inductors: one is ferrite the other is air coil inductor. Figure 2.12 gives the comparison of the current pulses at 10 kV IEC level delivered using both pulse shaping circuits. All current waveforms are recorded by a 10 GS/s oscilloscope. The ferrite inductor experiences saturation effect when the current density is too high. It results in the distortions in the waveforms, as the pulse shaping circuit cannot give the current waveforms defined in IEC 61000-4-2 especially at higher current level. The air coil inductor does not have such problem and the generated HMM pulses are very similar to the IEC standard. The deviation from measured and simulated results at the end of the pulse can be caused by the coupling of the parasitic capacitances and inductances. Figure 2.13 shows the measured current waveforms corresponding to different IEC levels where the deviations to the IEC standard values are given in Table 2.3. Within the allowed range of deviations (+/-20%) according to the standard, the pulse shaping circuits based on the air coil inductor is used in the HMM tester.

2.2.1.2 Measurement Setups for PCB-Level Tests

One of the main drawbacks of the system-level ESD tests using an IEC generator is that it is very difficult to measure the voltage transient waveforms. Therefore the measurement setups in the TLP based HMM tester aim for a high quality of measuring transient signals especially the voltage signals by applying adequate methods. The ESD protection devices are supposed to be turned on and behave lowresistive to divert main ESD current during ESD event. At least two test setups on the PCB test boards are possible for achieving a nearly 50 Ω load for the HMM tester output (Figure 2.10) without strong pulse reflections and distortions. After the 50 Ω transmission-line cable as depicted in Figure 2.14, the HMM pulses see approximately 50 Ω into the test boards:

On the test board 1 (TB1), the system load consists of a robust 47 Ω resistor and a serial connected low-resistive ESD or ESD protected device as DUT. The voltage and current at DUT are easily obtained as described in:

$$V_{DUT,TB1} = V_2,\ I_{DUT,TB1} = \frac{V_2 - V_1}{47\ \Omega} \qquad 2.3$$

The configuration of the test board 2 (TB2) is similar to the approach proposed in [34]. The current at DUT is measured with the 50 Ω attenuators and the 50 Ω oscilloscope input:

$$V_{DUT,TB2} = V_2 - V_1,\ I_{DUT,TB2} = \frac{V_2}{50\ \Omega} \qquad 2.4$$

Note that no current probe is involved in either of the measurement setups above. Practically, a proper current probe instead of the voltage probe measuring V_1 can be applied for the current measurements as well. The voltage measurements require a voltage probe with large measurement bandwidth and high input impedance to avoid significant current flow into the voltage probe. Figure 2.15 gives an implementation example of such voltage probe with a measurement bandwidth of above 2 GHz. The method to obtain a large bandwidth is the compensation of the parasitic capacitance of the probe resistor. Theoretically the relation of V_o/V_i is simply calculated as the voltage divider:

$$\frac{V_o}{V_i} = \frac{50\ \Omega}{50\ \Omega + 4.7\ k\Omega} \qquad 2.5$$

However, the parasitic capacitance of the resistor bypasses the signal at higher frequency, making the simple voltage divider calculation invalid. To solve the problem, an extra compensation capacitor is added at output side to ensure the relation as:

$$\frac{C_{parasitic}}{C_{compensation}} = \frac{Z_{attenurator}}{R_{series}} = \frac{50\ \Omega}{4.7\ k\Omega} \qquad 2.6$$

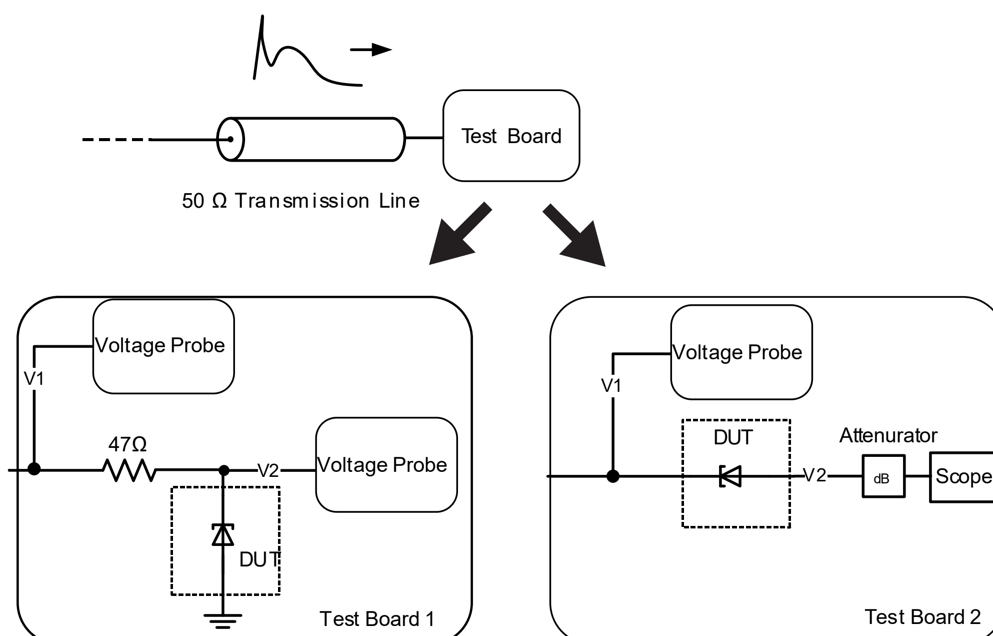

Figure 2.14: Concepts of two HMM test setups for PCB with nearly 50 Ω from the input of test boards to ground.

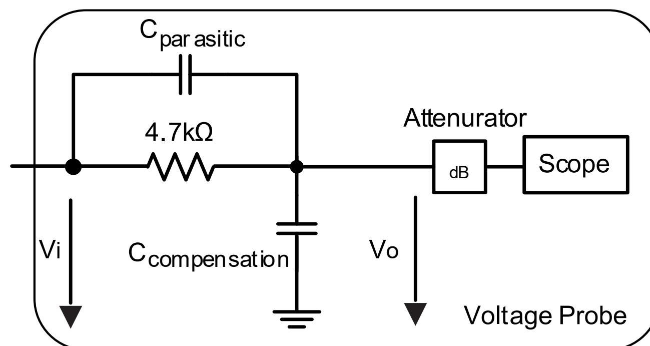

Figure 2.15: Configuration of the voltage probe with the compensation of parasitic capacitance.

The test boards TB1 and TB2 for the HMM measurements are implemented for the verification. A 2.2 Ω resistor as DUT is tested on TB1 and TB2. A very good resolution of transient measurements is obtained on TB1 as shown in Figure 2.16. The arrows and circles mark the waveforms and the respective y-axes: the left y-axis for the voltage waveforms and the right y-axis for the current waveform. In the figures of this work hereafter, similar marks for y-axes are used. By looking at the transient voltage and current in the broad peak range, 2.2 Ω resistance is measured by $V(t = 30ns)/I(t = 30ns)$ precisely. In the zoomed diagram, it is observed that first voltage peak is slightly earlier than first current peak. $V(first\ peak)/I(first\ peak)$ is also larger than 2.2 Ω. This is due to the parasitic inductance in the package of the used 2.2 Ω resistor and on the PCB.

On the other hand, the same 2.2 Ω is tested using TB2 setup. However, according to the results the voltage transients cannot be really measured with this setup because the difference of V_2 and V_1 is much smaller than V_1. The signal to noise ratio is then too small for the extraction of the voltage drop across the low-resistive DUT. Figure 2.17 shows the results where the voltage measurement with the TB2 setup fails. As a result TB1 setup is clearly preferred for the HMM test setup.

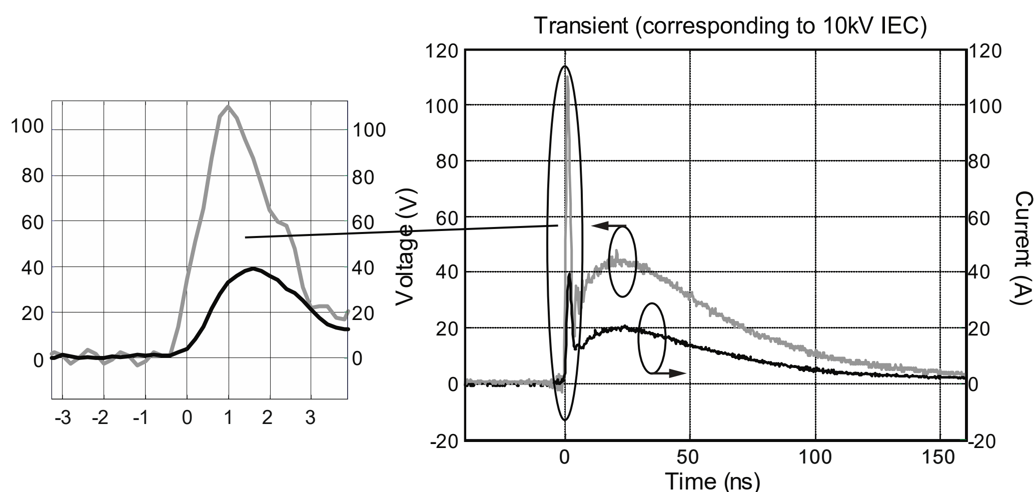

Figure 2.16: Transient measurement results of a 2.2 Ω resistor as DUT with TB1.

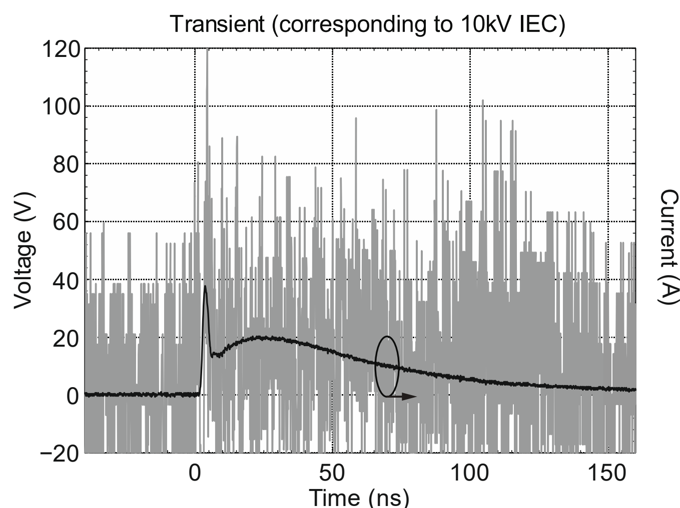

Figure 2.17: Transient measurement results of a 2.2 Ω resistor as DUT with TB2. Only the current is measured with sufficient quality whereas the voltage waveform(in grey) is completely noisy.

2.2.1.3 Measurement Setups for Wafer Tests

The HMM pulse system based on the TLP system can not only be used for PCB level testing but also be applied on wafer level measurements. The concept of the TB1 can be straightforwardly adapted for the wafer level HMM. The major work of the wafer-level setup is to implement the four point probing method [40] with a modified probe needle to produce approx. 97 Ω source impedance as shown in Figure 2.18. The pulse generator delivers HMM pulses out of a transmission cable while the pulse sense needle works as a normal voltage probe directly at the DUT. The setup is verified in the same way as for PCB setups using a 2.2 Ω resistor as the DUT. The results show that the wafer-level setup provides reliable measurement of the transient waveforms with minimal parasitic effects involved. The current waveforms can be measured directly using a current probe. In that case only one voltage probe on the modified pulse force needle is required.

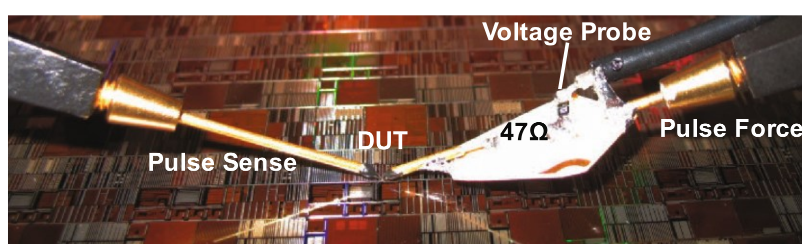

Figure 2.18: Photograph of a wafer-level HMM setup with the modified pulse force needle.

2.2.2 HMM vs. IEC: Transient Waveforms

For the verification of the newly developed HMM tester, it must deliver the same results as a well calibrated IEC generator when testing a DUT. This section gives the comparison of HMM and IEC with respect to the transient waveform at first. That is the transient responses of DUT to HMM and IEC pulses on the same discharge level must be comparable. Different types of DUTs are enclosed in the study. All the DUTs are intentionally selected to sustain the ESD stress levels without being damaged. The measurement setup with TB1 introduced earlier is used to record the transient

waveforms during the HMM tests. On the other hand, a current probe and a large ground plane are employed in the common test setup of the IEC tests.

2.2.2.1 DUT A

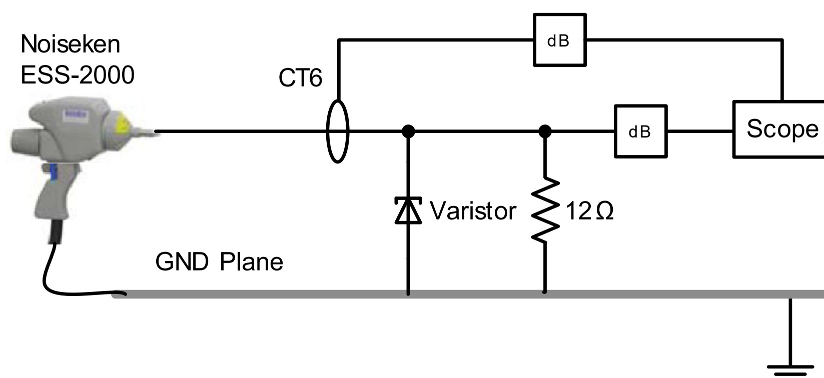

Figure 2.19: Measurement Setup using Noiseken (ESS-2000) IEC ESD generator for DUT A: CT0603K14G parallel connected to equivalent 10 Ω. Tektronix CT6 is used for current probing.

As depicted in Figure 2.19, a varistor CT0603K14G by EPCOS connected in parallel to a resistance of approximately 10 Ω is defined as the DUT in the IEC tests. Note that this resistance is implemented with a 12 Ω resistor and 50 Ω attenuators in parallel for the voltage measurements. The reason of defining such a DUT is that in this particular case the voltage measurements in the IEC tests can be accurately done without suffering from the limited measurement bandwidth. The 50 Ω attenuators are directly connected to the discharge path as a part of the DUT. In a practical consideration, varistors are often chosen as off-chip ESD protection devices. 10 Ω resistance is assumed as one of the typical impedances of an ESD protected IC pin during ESD. DUT A can thus represent a test item consisting of a fictive IC pin in conjunction with an off-chip ESD element.

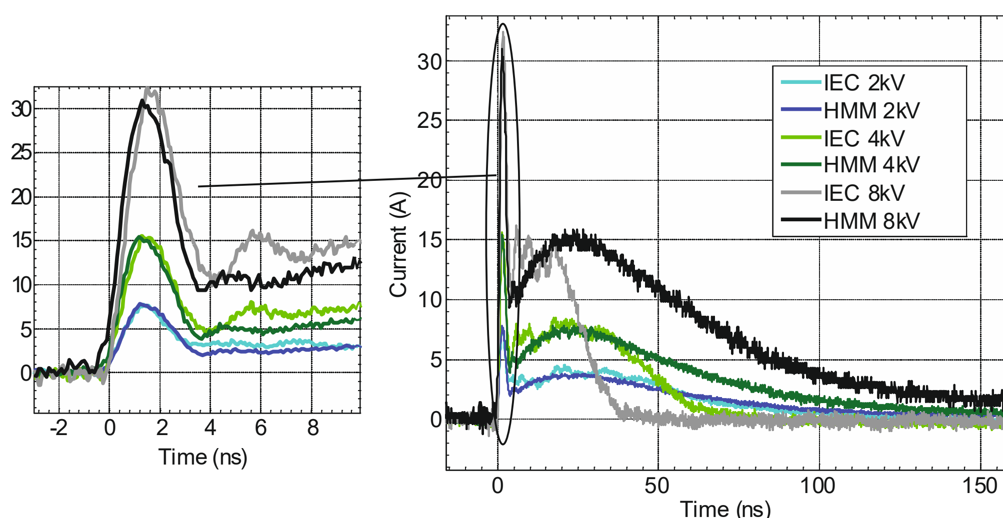

Figure 2.20: Comparison of current waveforms with enlarged first peak range at 2 kV, 4 kV and 8 kV IEC levels for DUT A.

On the other hand, the same DUT A - CT0603K14G in parallel to 10 Ω - is also tested with the HMM tester on the TB1 configuration described in Figure 2.14. In this case a 10 Ω resistor is simply used instead of 12 Ω in parallel to 50 Ω.

The current waveforms are shown in Figure 2.20 at three different discharge levels. The HMM levels are already converted to the corresponding levels of IEC. On 2 kV level, the current waveforms from both IEC and HMM tests agree perfectly while for higher levels, the measured IEC current is distorted due to the saturation effect of the Tektronix CT6 current probe. The CT6 current probe is used for higher resolution at the first peak range as it delivers higher measurement bandwidth. The HMM tests utilize the other current measurement technique without this problem. Further, the current transients actually match at all levels in the first peak range where the CT6 probe excellently displays the high-frequency part of the pulses.

Since the ESD testers act usually as current sources giving the defined current waveforms, the results of comparing the voltage transients become more attractive. Figure 2.21 shows three pairs of the voltage waveforms (HMM vs. IEC) on the DUT A corresponding to the current pulses in Figure 2.20. Thanks to the proper test setups, the voltage waveforms over the entire pulse including even the first peak range are perfectly matched in the HMM and IEC tests. Very good agreements on all levels provide evidence for the comparability of the IEC and HMM tests on the IC pins. Note that DUT A is particularly chosen for the precise voltage measurements in the IEC tests for a straightforward comparison of the HMM and IEC tests. Further examples show however, the drawback of the IEC tests when measuring the voltage signals.

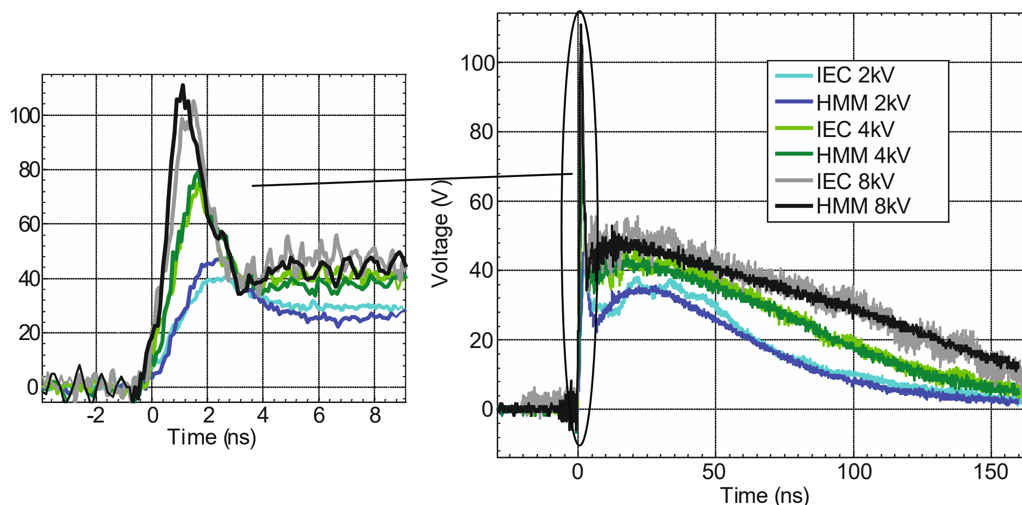

Figure 2.21: Comparison of voltage waveforms with enlarged first peak range at 2 kV, 4 kV and 8 kV IEC levels for DUT A.

2.2.2.2 DUT B

Another DUT is defined with the stand-alone varistor CT0603K14G without parallel resistors. It is interesting to investigate how good will be the clamping capability of a stand-alone off-chip device during system-level ESD stresses. In this case the HMM setup remains unchanged. However, in the IEC setup, 50 Ω attenuators and scope input are not allowed to be directly connected to the DUT. The impedance of the varistor comparing to 50 Ω is not negligible small so that a considerable amount of current would flow into the attenuators. Therefore, a voltage probe implemented with an high-resistive isolation resistor has to be applied as shown in Figure 2.22.

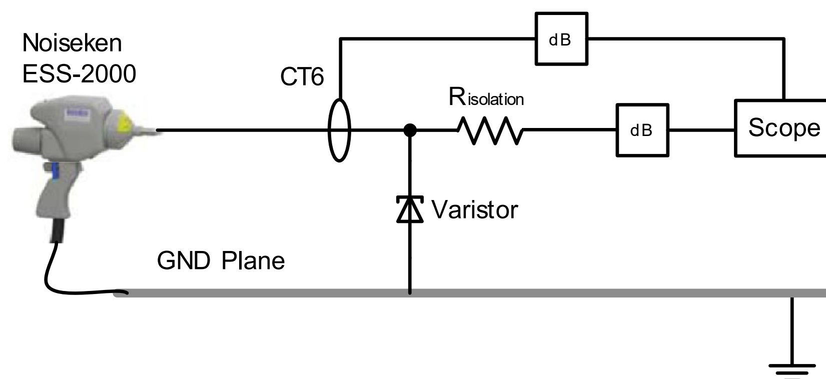

Figure 2.22: Measurement Setup using Noiseken (ESS-2000) IEC ESD generator for DUT B: stand-alone CT0603K14G.

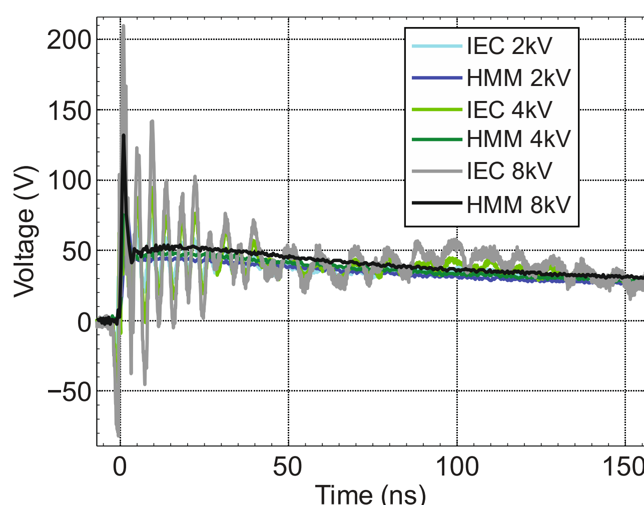

Figure 2.23: Comparison of voltage waveforms at 2 kV, 4 kV and 8 kV IEC levels for DUT B.

The measured current waveforms are roughly the same as depicted in Figure 2.20 because both ESD generators exhibit nearly as current sources without being too much affected by the DUTs. Figure 2.23 shows comparison of the voltage transients where the HMM results show very clean waveforms and the IEC results instead display oscillated waveforms due to the poor voltage measurement capability in the IEC setup. The parasitic capacitor and inductor introduced by the isolation resistor have a big impact resulting in test artifacts. The radiation and the coupling effect due to the IEC generator have also negative influences. Nevertheless, a rough agreement of the voltage waveforms from the HMM and IEC tests can still be found by the signal envelopes. In this case details of the clamping behavior of the varistor is only visible in the HMM tests.

2.2.2.3 DUT C

If allowed in the applications, capacitors are often used as very simple and effective off-chip ESD protections against system-level ESD. A 10 nF capacitor 0805 X7R by EPCOS is used as the third DUT example for the comparison of the transient current and voltage waveforms in the HMM and IEC tests. Measurement configurations are reused as depicted in Figure 2.14 and Figure 2.22 in HMM and IEC tests, respectively.

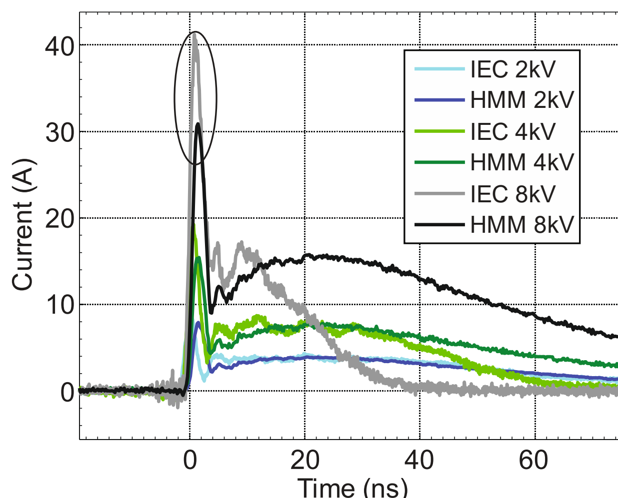

Figure 2.24: Comparison of current waveforms at 2 kV, 4 kV and 8 kV IEC levels for DUT C.

The current waveforms at the 10 nF SMD capacitor are shown in Figure 2.24. As shown in the plot, the first current peak in the IEC tests is larger than 3.75 A/kV, which is still valid for the HMM current peaks. This is because the current values in IEC 61000-4-2 are only standardized for the 2 Ω current target as the load. For DUTs with other impedance, different IEC generator can exhibit different behaviors [41]. On the other hand in the HMM test system, the current values do not change much as long as the DUT is low resistive compared to the approximately 100 Ω system source impedance. The voltage measurements show nearly the same phenomena as in the case of DUT B. The IEC tested waveforms are quite distorted with LC oscillations depicted in Figure 2.25. However, the later part of the pulses can be considered as the agreement between the IEC and HMM tests.

As a conclusion for the comparisons of the transient waveforms derived from the HMM and IEC tests, the stand-alone devices as well as the protection networks respond identically to the discharges on the same level. Therefore the correlation between HMM and IEC is considered to be sufficiently high.

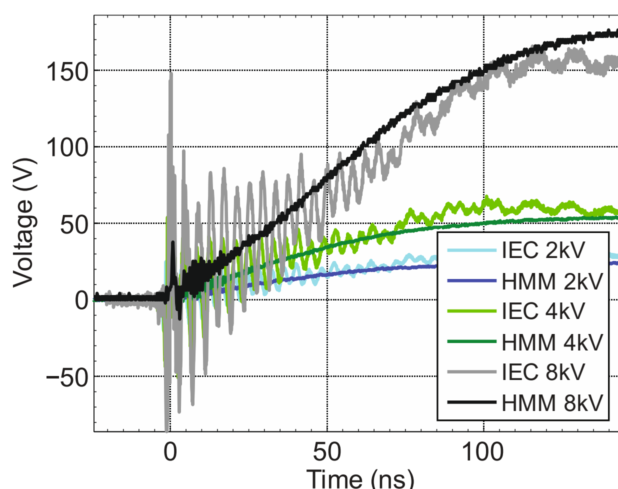

Figure 2.25: Comparison of voltage waveforms at 2 kV, 4 kV and 8 kV IEC levels for DUT C.

2.2.3 HMM vs. IEC: Failure levels

The second part of comparing the HMM pulses and IEC pulses on the same DUT is to verify the correlation of the failure levels of DUTs caused by both discharges. In general, two main ESD failure mechanisms are associated with the thermal damages and the electrically induced failures such as dielectric ruptures. In this section, two types of failure mechanisms are involved in two DUTs which intend to cover a broad range of the comparison on the failure levels.

2.2.3.1 Thermal Failure Levels

An ESD protected LIN transceiver chip is encapsulated in the plastic package P-DSO-8 and used as the first DUT. The pin combination BUS vs. GND is designed to sustain at least ±8 kV IEC system-level ESD stresses. It fails thermally in the end by reaching a certain IEC stress level. A curve tracer as the failure detection is used in the IEC testing. The DUT shows repeatable 10 kV system-level ESD hardness according to the curve tracer. The failure root cause is estimated to be the thermal defects in the protection device as the destructive heat generated by the ESD energy cannot be dissipated within the pulse duration. However, this cannot be examined and proved with lack of the voltage waveforms during the conventional IEC tests. On the contrary, the HMM tester can provide decent transient voltage measurements. The HMM tests at the LIN BUS pin are performed using the TB1 setup with a 25 V increment of charge voltages. Also, a HMM hardness corresponding to 10 kV IEC level is measured. The failure detection is done by the leakage current measurements. In the transient waveforms, the thermal failure is clearly demonstrated at latter part of the destructive pulse as depicted in Figure 2.26. The failure energy can be even easily calculated with the integral of the failure power over time. Note that also small oscillations can be observed in the waveforms, which are mainly caused by the package parasitic.

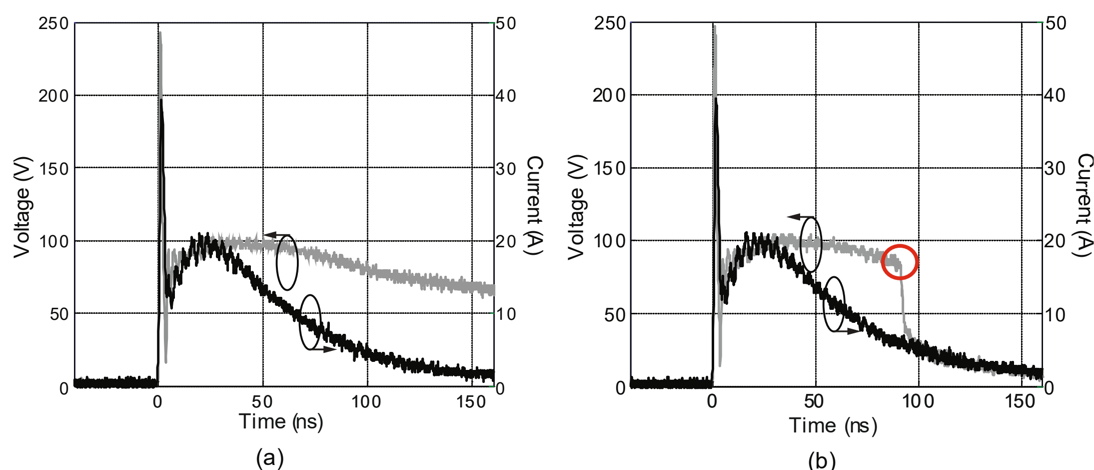

Figure 2.26: Current and voltage waveforms of positive HMM tests on a LIN bus pin: (a) last stress before failure (b) stress to denoted thermal failure. The red circle indicates voltage collapse indicating a short circuit i.e. the damage of DUT

2.2.3.2 Electrical Failure Levels

The HMM and IEC tests have delivered the same levels of thermal failure as described in the previous example. The correlation of the HMM and IEC tests on the electrical induced failures (hereafter electrical failures) of DUTs is also of interest. In the field of

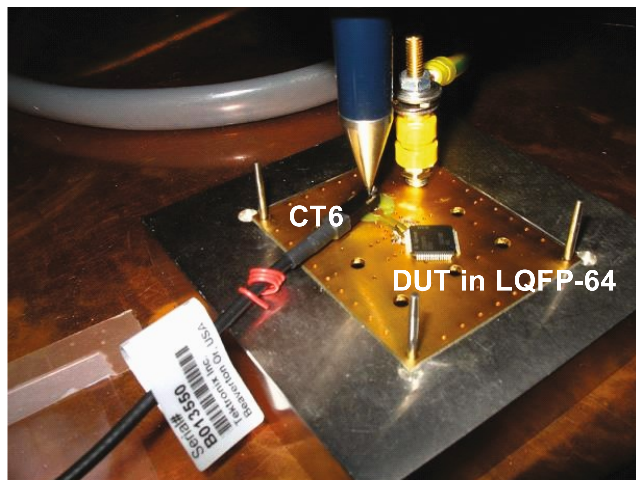

Figure 2.27: Picture of IEC test setup for electrical failed DUTs

on-chip ESD protections, actively controlled MOSFET – so-called active clamp - is widely used as a type of ESD protection elements, as its principle is generally easy to apply and relatively technology independent. The ESD capability of the active clamps is often limited by the electrical safe operating area of the used MOSFET transistor. The active clamp engages its robustness limit and is damaged when the electrical parameters such as voltage and current density at the transistor exceed the critical values during ESD even with very short pulse durations e.g. 5 ns. This means that in many cases the failures of the active clamps are induced by the first peak of the system-level ESD pulses. The high-voltage active clamps and their failure modes will be discussed in detail in later chapters.

In the study of the HMM tester, several active clamps with different sizes are used as DUTs which are all expected to have electrical failure levels. In the IEC tests, the test structures are assembled in the plastic package LQFP-64 and stressed with a Schaffner

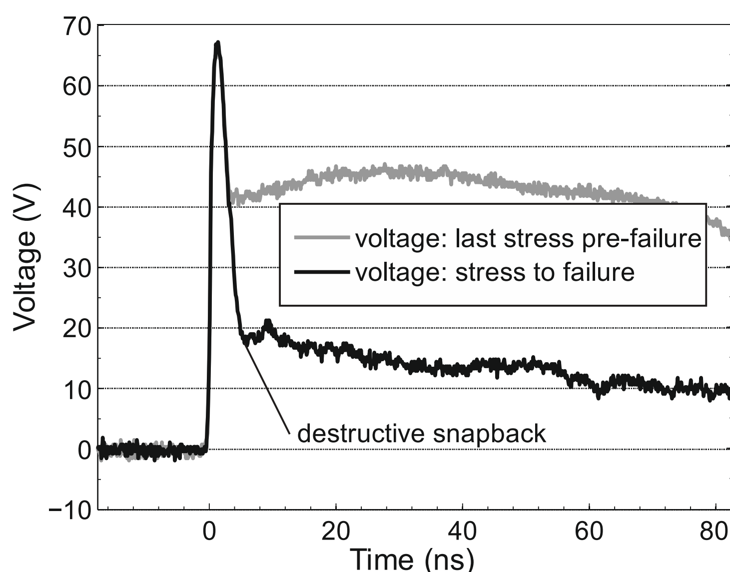

Figure 2.28: Voltage waveforms derived from the HMM test for a 25 V active clamp with electrically induced damage denoted in the first peak range. The DUT fails at 6.8 A broad peak current corresponding to 3.4 kV IEC level which is shown in Figure 2.29.

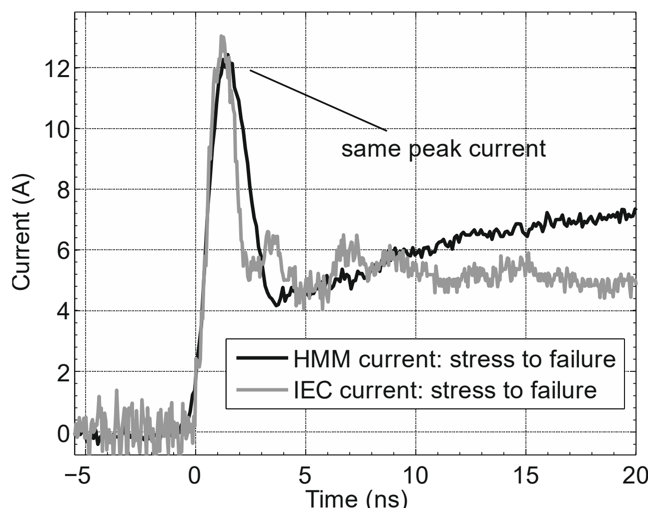

Figure 2.29: Comparison of current waveforms at stresses to failure for active clamp A.

ESD generator, model NSG-438 150 pF/330 Ω. Current waveforms are measured by CT6 current probe in the test setup shown in Figure 2.27. The HMM tests are performed on the same structures with the TB1 setup but using CT6 for the current probing. Figure 2.28 depicts the waveforms of stresses pre- and post-failure for a 25 V active clamp A. The electrically induced destructive snapback is clearly visible as the voltage collapses at the beginning of the pulse. The spot leakage is also plotted indicating the failure current level during the HMM test corresponding to about 3.4 kV IEC level. In the IEC tests, the active clamp A passes 2.9 kV and fails at 3.1 kV. In Figure 2.29, the zoomed stress-to-failure IEC current pulse measured by CT6 is compared to the stress-to-failure HMM current, showing a very good agreement of the failure levels. A correlation of the HMM and IEC tests on the electrically induced failures is therefore given.

Several other active clamps are tested and compared in the IEC and HMM tests. The results for the different DUTs are summarized in Table 2.4 and show good agreements between IEC and HMM. Note that all the failure levels from the HMM tests are very reproducible. The HMM “kV” levels are determined according to the current values in the IEC standard. The IEC tests show some minor fluctuations with acceptable reproducibility.

Table 2.4: Summary failure levels of various active clamps as DUTs for comparison.

Device Name	Sample	HMM	IEC	
		Fail (kV)	Pass (kV)	Fail (kV)
Active clamp A	#1	3.4	2.9	3.1
Active clamp B	#1	2.2	1.9	2.1
Active clamp C	#1	2.8	2.6	2.7
	#2	2.8	2.5	2.6
Active clamp D	#1	3.2	2.8	2.9
	#2	3.2	2.9	3.0

Above all, the correlation of the HMM and IEC tests on the failure levels is found. The TLP based HMM tester provides a reliable test method which delivers the same results as obtained in the traditional IEC system-level ESD tests for the devices and circuits under test. The HMM tester further enables accurate voltage measurements and is easily applicable for board or wafer-level tests.

2.2.4 Discussion and Summary

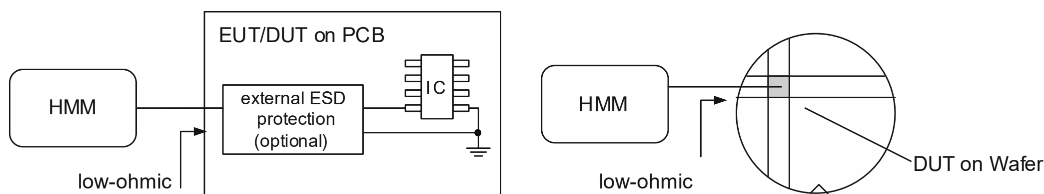

Figure 2.30: HMM tester for board- and wafer-level component tests. DUT must fulfil the condition to be low-ohmic during ESD events.

As already discussed earlier, to obtain reproducible and reliable HMM test result, several conditions have to be fulfilled. The most important one is that the DUT must be low resistive during the test. From the ESD protection point of view for IC components, DUTs are in the majority of cases low resistive based on the consideration: The ESD protection elements have the task to safely discharge ESD currents via a low-impedance shunting path the ground. The DUT with high-impedance interface which can safely limit the ESD current is straightforwardly ESD protected hence is not in focus of this work. As depicted in Figure 2.30, the HMM test can be done on wafer- and PCB-level. The applied HMM setup is based on TB1 configuration introduced in Figure 2.14. The HMM tester symbolized in Figure 2.30 contains the IEC-like pulse generator and a robust 47 Ω serial resistor.

The usage of the TLP based HMM has its limitation. If the HMM pulses are intended to be applied at arbitrary location on a system board such as at a random copper trace or a connector, the pulse reproducibility and quality is then limited by the pulse delivery technique. This is mainly due to the grounding in the measurement setup. To investigate how the pulse waveform will be affected in case of non-optimized ground connection, experiment was carried out with the setup shown in Figure 2.31. The HMM pulse is applied to a 2 Ω current target mounted on a large metal ground plane which is usually used for the calibration of IEC pulse generators. In this case, the HMM discharging pulse cannot be implemented with SMA connection but through a metal tip to enable the contact discharge. In the HMM test setup, 50 Ω system is turned to a nearly 100 Ω source impedance with the 47 Ω resistor in place. The ground connection can easily

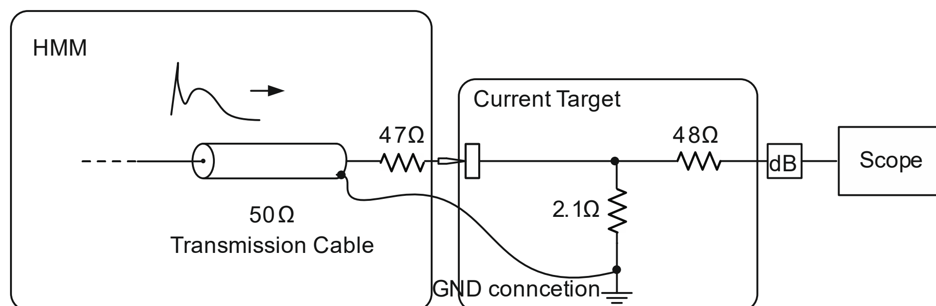

Figure 2.31: Experiment of applying HMM at a 2 Ω current target through a metal discharge tip.

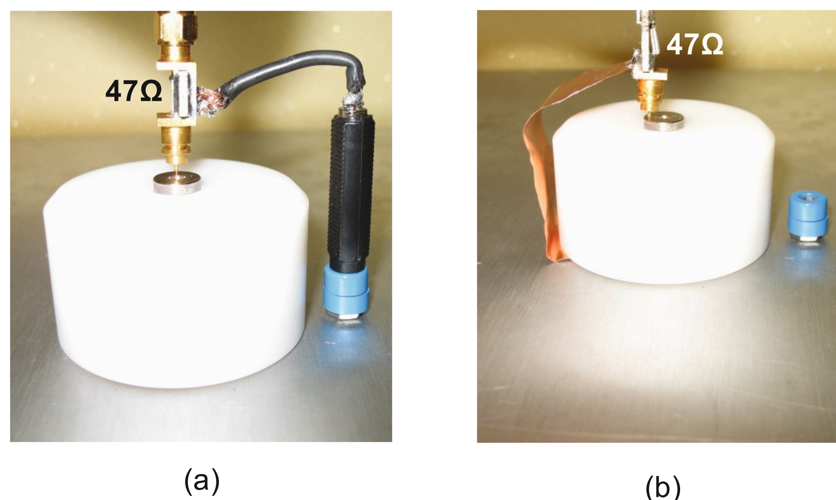

Figure 2.32: Picture of HMM test setup described in Figure 2.31with different ground connection: (a) cable and (b) copper slice.

introduce significant parasitic inductance that distort the HMM pulses. Figure 2.32 describes two implementation of the ground connection implemented with cable and copper slice, respectively. Both connections are kept as short as possible to minimize the parasitic inductance. The length is in the range of 10 cm. A strong dependence on grounding methods was found in the test results as depicted in Figure 2.33. A 20 nH ground inductance was added in the simulation for the comparison. Both grounding methods result in distortion of the HMM pulse with significant reflection peak observed in the waveforms. The position of the reflection peak is a function of the transmission cable length. Additionally, the first peak current is also deteriorated by the ground inductance. The 10 cm copper cable introduces larger impact on the HMM pulses while the copper slice shows a better result compared to the IEC standard. Based on the simulation the ground inductance should be kept below 20 nH in order to deliver acceptable pulse quality in the HMM test setup. In practice however, it is challenging to ensure a ground line between coaxial shielding and DUT ground with less than 20 nH during the HMM test.

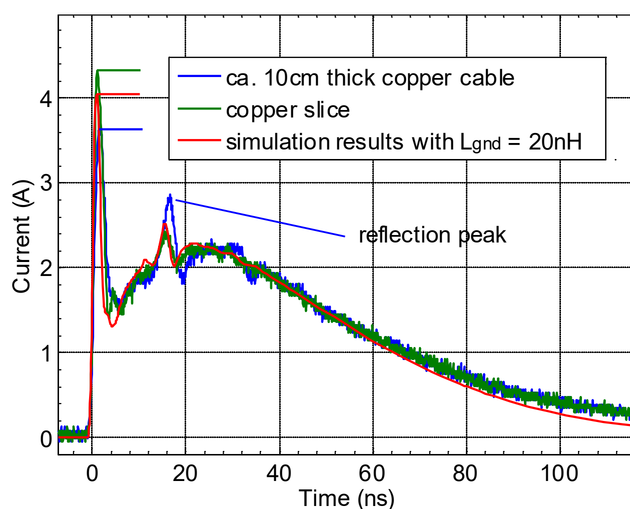

Figure 2.33: Comparison of current waveforms at same stress level using different grounding.

Furthermore, other limitation of the TLP based HMM tester is the maximal stress level. In this work, the TLP based HMM can provide a stress level corresponding to 10 kV IEC discharge. Compared to the commercial IEC generators which provide usually up to 30 kV discharge voltage, the HMM stress level is limited. For DUTs having higher ESD hardness, the HMM stress cannot reach the failure levels.

Despite the limitations of the HMM tester, there are several essential advantages to develop the TLP based HMM when performing system-level ESD tests on components. One of the major advantage of using HMM instead of the conventional IEC generators is the improved measurability of transient signals especially voltage transient waveforms. In the IEC setups, voltage measurements are very challenging. Even using the same measurement setup - the same high bandwidth voltage probe designed for the HMM system (Figure 2.15), the IEC test cannot deliver good voltage measurements. As shown in Figure 2.34, the first peak voltage in the HMM test is visible while in the IEC tests, the resolution of the first peak is not satisfying. The reasons are multi-fold. One of them is the IEC generator produces strong electro-magnetic radiation, which is difficult to be shielded [42].

As a summary, the advantages of the TLP based HMM compared to the IEC generators are found:

- TLP based HMM generates very repeatable IEC-like ESD pulses according to the standard IEC 61000-4-2. IEC generators show less reproducibility;
- Fast signals especially voltage waveforms are well measurable with proper test setups in HMM. Voltage measurement in IEC setup is very difficult;
- Wafer-level HMM measurement is easy-to-implemented based on the TLP setups. IEC discharge on wafer-level requires higher effort;
- Simulation of HMM is straightforward. The spread of radiated fields is not controlled and varies strongly between different IEC generator models [43].

Also several drawbacks of the HMM tests are described:

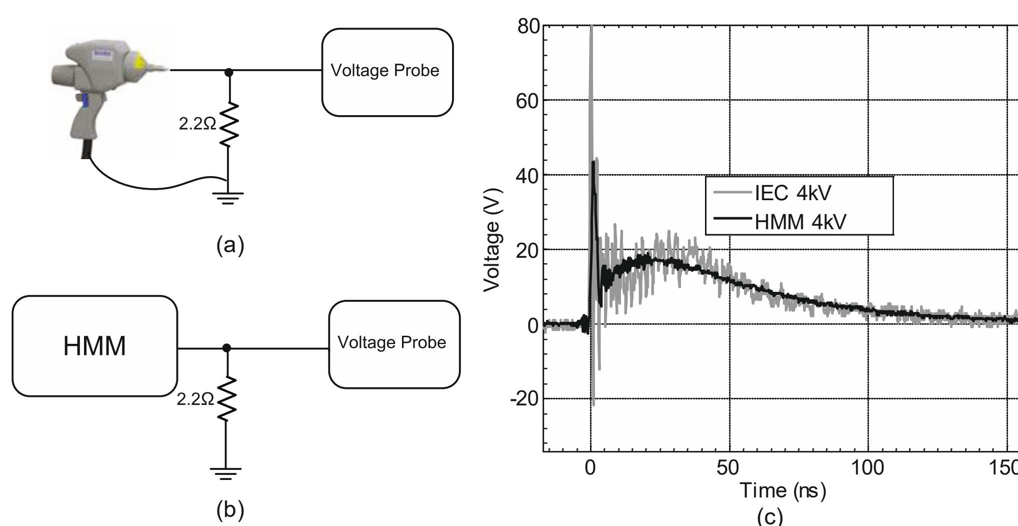

Figure 2.34: Comparison of transient voltage measurement performed with (a) the IEC setup and (b) the HMM on 2.2 Ω resistor as DUT. The voltage transients are measured via the same voltage probe. Different signal clarity is shown with (c) the waveforms at 4 kV IEC level.

- TLP based HMM testing has a focus mainly on IC components or simple PCB-level ESD protections. It may not be applicable for ESD tests on a high-level system;
- The introduced HMM tester prototype provides a maximal stress level of up to 10kV corresponding to IEC level;
- 100 Ω instead of 330 Ω source impedance is implemented within the TLP based HMM system. Parasitic inductance in the ground connection can affect the pulse waveform;
- HMM test is limited to contact discharge while the IEC generators enable also air discharge tests.
- Radiated fields can cause IC failures and cannot be tested with the HMM tester

As a summary, a TLP based HMM test equipment and the measurement setups are introduced and optimized. The correlation of HMM and IEC tests regarding transient waveforms and failure levels are verified and confirmed with different DUT examples. Further, the main differences of both tests are also discussed and summarized.

2.3 Conclusion

Rise-time of ESD pulses can affect the ESD performance of protected circuits in a significant manner. This chapter proposes a generic low-reflection low-pass filter design, which is theoretically and experimentally promising to be highly useful for TLP measurement system. In later chapters, rise-time of TLP is substantially important for the investigation on ESD protection elements as the behavior of ESD devices can vary to different rise-times.

The HMM system developed in this work can deliver IEC-like pulses according to IEC 610004-2 contact discharge into component pins or into ESD protection networks. During the HMM tests, DUTs behave similarly as they experience the system-level ESD tests employing IEC generators. Conventionally, ESD tests using IEC generator only delivers the failure levels of DUTs as ESD qualification tools. In case of insufficient ESD robustness, very limited information is obtained from the measurement readout, which makes the failure analysis and improvement of ESD protection difficult and time-consuming. With the precise voltage and current measurements in the HMM test setup, the transient waveforms can be used for example to identify failure mechanisms, to measure the pulse power and energy at different time instants and to evaluate the real clamping performance of the ESD protection devices considering the first peak current of IEC pulses. Not only the failure levels but also the failure modes of different DUTs derived from the HMM and the IEC tests show good agreement that validates the usefulness of the developed HMM setup.

The ESD testing techniques introduced in this chapter facilitates significantly the ESD study throughout the work with different topics, including ESD protection characterization, ESD protection design and ESD device modeling.

Chapter 3

Failure Levels, Criteria and Case Studies of On-Chip Protections

High-voltage ESD chip-level design requires reliable protection elements. In the scope of this chapter, three types of typical high-voltage on-chip ESD protection elements are studied. Their failure levels and failure criteria are of enormous importance to establish area efficient and protection effective design. Because nowadays, ESD protection for IC products especially in high-voltage wafer technologies generally does not work with "plug and play" of protection devices. Only if one understands deeply the differences of ESD protection devices in terms of their advantages, disadvantages and their interactions with protected devices and structures, effective protection can be designed. Compared to low-voltage ESD protection concept high-voltage ESD devices are inherently larger due to higher power dissipation (higher clamping voltage at specified ESD current) requiring more silicon area or volume. Hence, the area efficiency of overall ESD protection is often dominated by high-voltage ESD

In this work, three representative types of ESD devices including npn-bipolar transistor (BJT), pn-diode and active controlled power MOSFET (hereafter active clamps) are discussed in this chapter. Using TLP with different pulse durations and rise-times, the device characteristics with respect to HBM, CDM as well as system-level ESD are experimentally and comprehensively summarized. The root causes of devices' failures by reaching their inherent ESD capabilities are also studied in detail.

In addition to the ESD protection elements by themselves, the protected devices are also combined with the ESD protection in the study to verify the on-chip ESD protection effectiveness. Combining ESD protection and ESD protected devices is usually named ESD concept and is a part of the ESD development. In this chapter, diverse particular effects shown in the various ESD protection concepts are demonstrated with assistance of device simulation. Based on the devices' characteristics, the impact of the protection elements to the circuits being protected is carefully evaluated. In order to improve the efficiency and effectiveness of the ESD protections, advanced concept solutions and novel protection elements are developed and investigated accordingly.

3.1 Failure Levels Studies of On-Chip ESD Protections

In this section, the failure levels of on-chip ESD protections, in particular the ESD devices for automotive applications are investigated for comparison [44]. Among different types of ESD protection devices, non-snapback devices are studied more in detail. The reasons of the focus mainly on non-snapback ESD devices are multi-fold. The continuously increasing importance of system-level ESD test demands the testing of events that can occur in systems in either powered up or powered off states [45]. It is of crucial danger for snapback devices when the protected IC experiences ESD events in powered up states. If the holding voltage of snapback devices is below the supply voltage, the power supply can easily cause permanent damage with its “unlimited” energy from ESD perspective. In addition, snapback ESD devices can suffer from the existing external capacitance during system level ESD. The large capacitance can be charged up to the trigger voltage of ESD devices and store a large amount of energy. In case a deep snapback process occurs, the capacitance will discharge the energy directly to the snapback ESD device and cause damage. Another important reason which can degrade snapback devices for high-voltage ESD protection is the potential danger of the voltage overshoots due to the relative slow snapback process regarding the base-transit-time [46]. The transient responses of snapback devices are generally sensitive to the stress level and rise-time of the ESD pulses [47] [48] [67].

Although the snapback device can produce risks in some of the high voltage ESD applications, its ESD current capability per unit area is usually much higher than the non-snapback devices. Hence, the characterization of the snapback devices is also of interest. In this failure levels studies one snapback ESD protection – an npn type bipolar transistor is studied as an example. Nevertheless, the non-snapback devices remains focus due to the reasons discussed above.

Failure levels of semiconductor devices regarding thermal runaway are introduced in the Wunsch-Bell criterion [19] back in 1960s, providing a chance to estimate failure power or energy concerning different pulse durations. Based on the Wunsch-Bell theory, failure threshold for an electrical device depends on pulse duration. The power in the pulse continuously increases the temperature of the device and under circumstances induce thermal failure. This process is certainly affected by the pulse duration. The longer the pulse the lower is the failure power. In fact, ESD events with wide range of pulse durations exist in automotive systems [102]. Moreover, it is often desirable to investigate and systematically compare the failure levels of various ESD structures under stress pulses even beyond ESD time range. The deep understanding of the ESD capabilities and robustness under stress of such devices considering ESD window is one of the prerequisites to improve the concepts of ESD engineering.

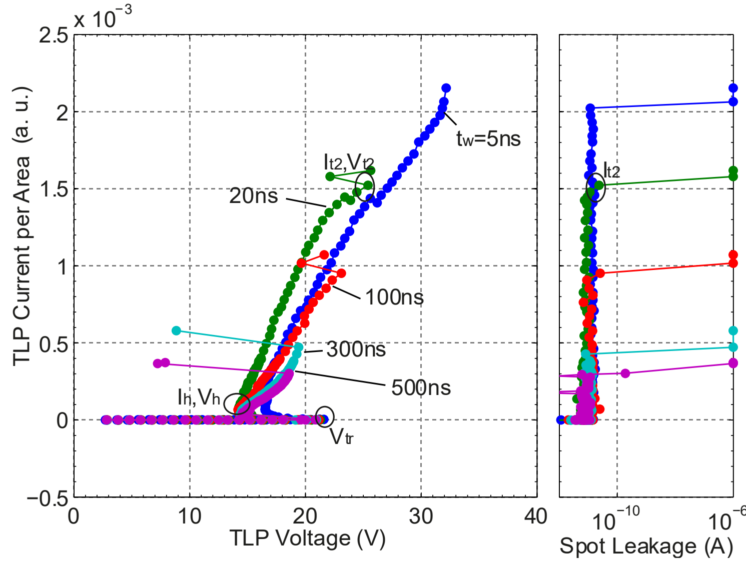

Figure 3.1: TLP I-V characteristics and spot leakage results of a 15 V npn-BJT named npn-e15a2 tested with various pulse widths from 5 ns to 500 ns. The pulse rise-time is 300 ps. In the used naming convention, e15 indicates the voltage class while a2 is related to the device size.

In this section, various pulse widths (t_w) and rise-times (t_r) are used as parameters for the devices characterization. In the used TLP system introduced in Chapter 2, t_w is adjustable from 2.5 ns to 1.5 µs, which covers the pulse width of most ESD pulses. For longer pulses in the range of electrical overstress (EOS), a square pulse generator is applied instead of TLP with t_w from 10 µs to 10 ms. The rise-times in the TLP setup, variable between 100 ps and 45 ns are used to characterize the turn-on behavior of the ESD devices. The devices are characterized on wafer-level with TLP, and on package-level with the square pulse generator as the used square pulse generator with the pulse widths ranging from 10 µs up to 10 ms can be only used for package-level tests.

3.1.1 npn-BJT

A bipolar junction transistor (BJT) is actually the underlying building block of many snapback devices such as silicon controlled rectifiers (SCR), grounded-gate NMOS (ggNMOS) and etc. Hence, the characterization of npn type of BJT (npn-BJT) is representative for snapback devices by means of failure levels study. For ESD protection purpose, an npn-BJT is supposed to divert currents when so called second breakdown occurs. An abrupt decrease in device voltage marked as snapback occurs with a simultaneous internal constriction of current [49]. The trigger voltage V_{tr} is determined by the avalanche breakdown at the collector-emitter under the open-base condition; while the voltage at the onset of snapback V_{t1} and the holding voltage V_h are directly related to avalanche multiplication factor, base width, current gain and resistance in the path [50].

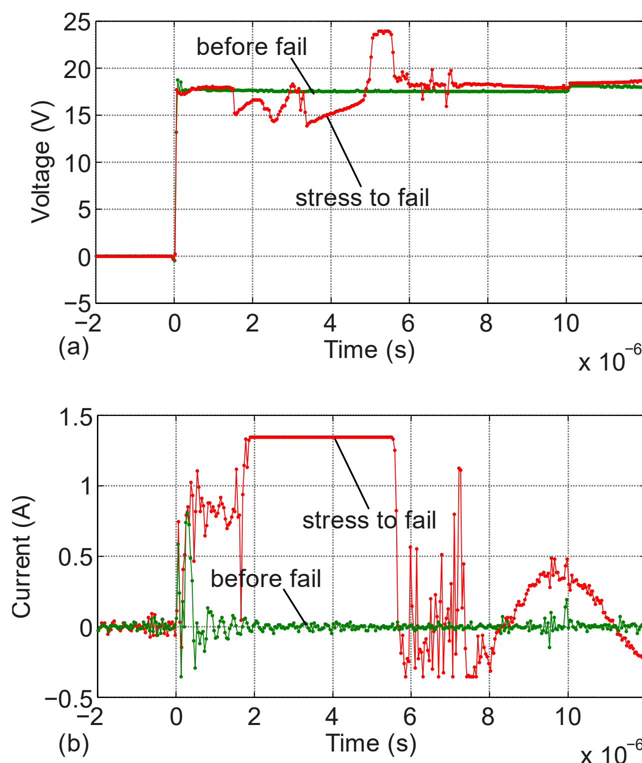

Figure 3.2: (a) Voltage transient waveforms derived from a 10 µs square pulse characterization for the npn-e15a2. (b) Current transient waveforms derived from a 10 µs square pulse characterization. 17.5 V stress voltage is applied, as the snapback device is not yet triggered. At 18 V the stress triggers the device causing device failure.

Figure 3.1 shows the TLP characterization results of a typical high voltage npn-BJT at 15 V voltage class (npn-e15a2). The TLP characterization was done using different pulse width. The averaging window for the quasi-static voltages and currents of the TLP I-V is normally applied between 70% and 90% of the TLP transient voltage and current waveforms, respectively. The spot leakage currents are measured after each TLP stress by applying a defined spot voltage across the DUT e.g. at the voltage class 15 V. A sudden increase of the spot leakage currents determines the stress level resulting in device failure. The failure voltage and current V_{t2} and I_{t2} as well as the trigger voltage V_{tr} and holding voltage and current V_h and I_h are denoted in the plot for 20 ns TLP for example. The measured TLP currents are specified to the device area on the silicon with the intention for later comparison of different devices. For confidentiality purposes, only arbitrary units (a.u.) are used for the device area related comparison. It applies to the respective figures hereafter.

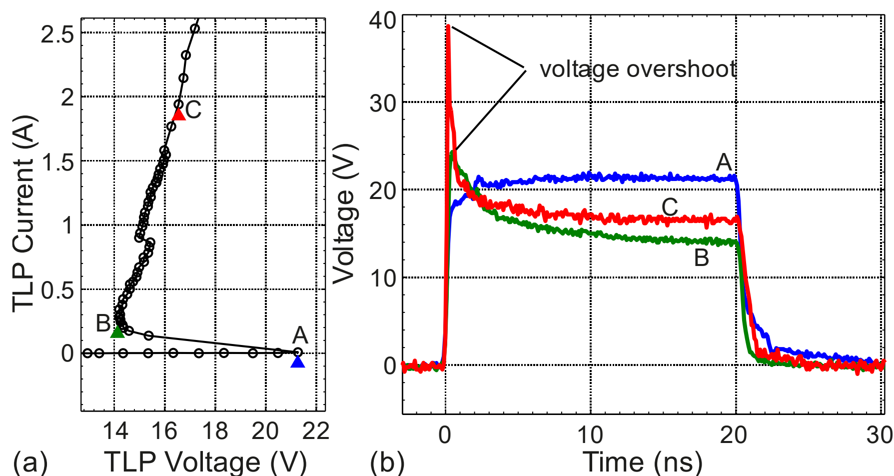

Figure 3.3: (a) TLP I-V characteristics of the npn-e15a2 with pulse width of 20 ns and rise-time of 300 ps. A, B and C indicate the I-V points with the corresponding voltage transient waveforms shown in (b)

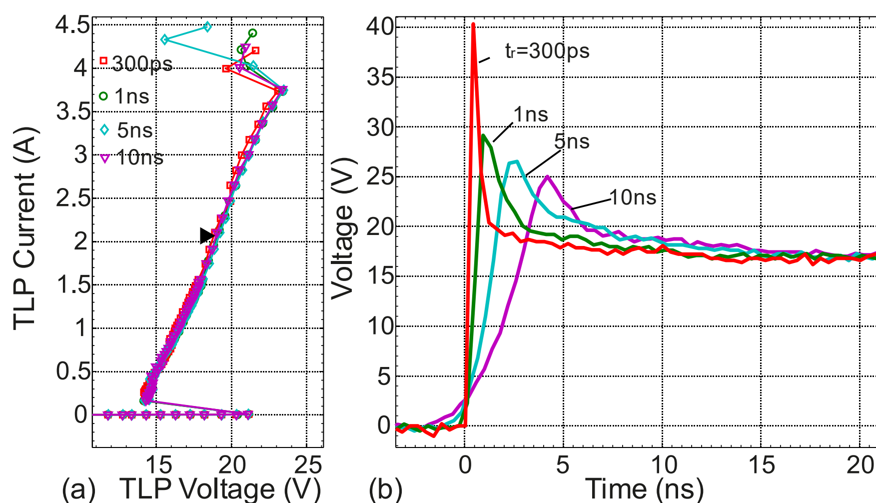

Figure 3.4: (a) TLP I-V characteristics of the npn-e15a2 with pulse width of 100 ns and rise-times of 300 ps, 1 ns, 5 ns and 10 ns. The voltage transient waveforms corresponding to 2 A TLP current are shown in (b)

As shown in the TLP I-V, the failure levels of the snapback device depend strongly on the pulse duration. With the profound ESD device designed by engineering the ballasting resistance that helps to distribute the ESD current homogenously through the ESD devices after the snapback [51], and the failure current I_{t2} does not drastically decrease for pulses width up to 500 ns. This guarantees the usage of npn-e15a2 as an effective ESD protection device for the ESD pulse range. However, the failure voltage V_{t2} drops drastically for longer stress pulses, which implies in the EOS case the snapback BJT can be damaged when it is false-triggered. A homogenous triggering of this npn-BJT may not be fulfilled. To verify this assumption, a 10 µs square pulse generator is applied for the long pulse characterization. The device npn-e15a2 is packaged in a plastic package LQFP-64 for the tests. Figure 3.2 shows the measurement results. With 17.5 V at the DUT (before fail in Figure 3.2 (a)), the npn-BJT is not triggered. The current ringing in Figure 3.2 (b) is caused by the tester parasitics. As the next stress at 18 V is applied, the device is triggered and it failed during the stress. The current drastically increases after approximately 2 µs and it is limited by the current

constraint. Similar results were observed during the square pulse tests with 100 µs and 10 ms pulse durations. As a result, the snapback device npn-e15a2 is not allowed to be triggered for the pulses longer than 1.5 µs.

In addition to the long pulse characterization, the voltage overshoots of the snapback device depending on the current levels and rise-times are investigated. Figure 3.3 shows the voltage responses of npn-e15a2 at three different 20 ns TLP stress levels as indicated with A, B and C. The rise-time of the TLP pulses is 300 ps. The voltage overshoots are clearly visible and become larger at higher current levels. Figure 3.4 gives the comparison of 100 ns TLP I-V characteristics of npn-e15a2 using different rise-times. Although the failure voltage and current of the npn-BJT are not affected by the rise-times (as indicated with the second snapback in Figure 3.4 (a)), the voltage transients at 2 A TLP current show however a strong impact of the rise-time on the voltage overshoots. Larger overshoots are observed at shorter rise-times. Hence, for overshoot sensitive circuits being protected the snapback devices can be less effective for ESD protection when the voltage overshoots are already critical.

3.1.2 pn-Diode

Pn-junction diodes (pn-diodes) operating as non-snapback ESD devices belong to a type of the most simple but effective ESD protections. For the high voltage protection, they are often designed as vertical devices, which provide very efficient use of silicon area because very robust vertical pn-junction is available in the smart power technologies. Reverse biased pn-diodes utilizing avalanche breakdown mechanism focus mainly on the engineering of doping profiles along the abrupt pn-junction relatively deep below the silicon surface [44]. Avalanche multiplication, or impact ionization, is the most important mechanism in the junction breakdown. Under ESD conditions, a pn-diode is designed to carry high current when avalanche generation occurs [50] [52]. With a given doping profile, the breakdown voltage, or in the same meaning, the trigger voltage V_{tr} of the pn-diode increases with increasing temperature and decreases with decreasing temperature [49]. The design of the breakdown voltage

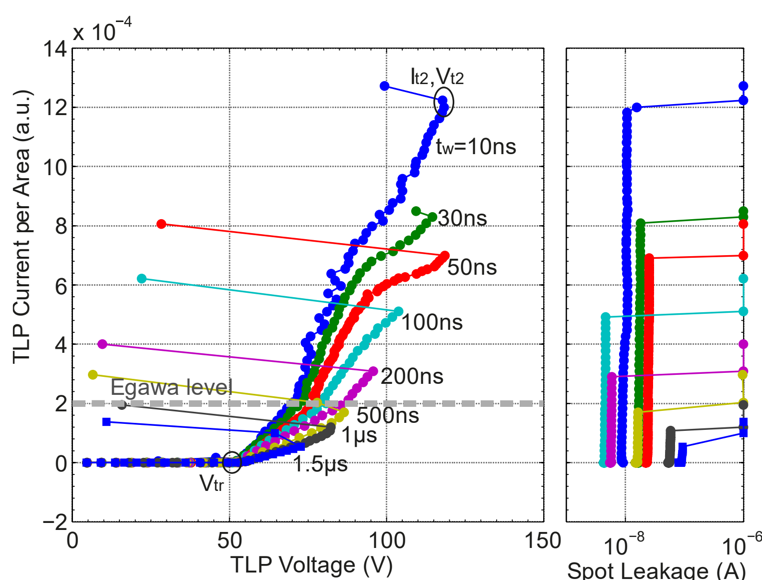

Figure 3.5: TLP I-V characteristics and spot leakage results of the 45 V pn-diode pn-e45a2 tested with various pulse widths from 10 ns to 1.5 µs. The pulse rise-time is 1 ns. Parameter e45 indicates the voltage class, while a2 is related to the device size.

has to concern the temperature coefficient and process variation, which is not the focus of the study. For given ESD diodes designed for certain voltage classes, the device behavior under ESD condition is of interest. Because the ESD requirements are standardized for room temperature, V_{tr} hereafter shown in the device characterization is meant to be the trigger voltage of the ESD protections under room temperature.

Figure 3.5 shows the TLP measurement results for a typical pn-diode for 45 V voltage class named pn-e45a2. Compared to npn-e15a2 shown in Figure 3.1, I_{t2} is smaller while V_{t2} is significant larger in conjunction with the higher trigger voltage. Note that the trigger voltage V_{tr} is around 55 V at room temperature for the temperature dependence and process margin for 45 V voltage class. The avalanche breakdown is not allowed to be drifted below 45 V at -40 degrees Celsius and at the process corner. The rise-time of all the TLP pulses in the characterization is 1ns. Same to the studied snapback BJT npn-e15a2, rise-time has no significant impact on the I-V curves of pn-diodes because the TLP (quasi-static) voltages and currents are derived by averaging the later part of the pulses (70% to 90%). Hence the transient behavior and after all the turn-on speed is not described in the quasi-static I-V curves. Besides, the pn-diodes stand-alone are expected to have the failure mechanism of thermal runaway. Therefore, as long as the rise-time has no substantial influence on the total pulse energy for the same pulse width, the failure levels of the pn-diodes do not depend on the rise-time, which is the case in our study.

In Figure 3.5 the spot leakage currents at 45 V determine the devices failure while the failure voltage and current are denoted by V_{t2} and I_{t2}, respectively. The different leakage currents in the spot leakage plot are caused by different sense needles used in the wafer-level TLP tests. The used sense needles have tens to hundreds of nano Amps leakage current, which are higher than the DUT leakage current itself. The sense needles have however practically no influence on the measured failure levels. The TLP currents are also normalized to the device area with the intention for comparison of different types of devices. The failure levels of the pn-diode depend strongly on pulse duration, which confirms the Wunsch-Bell theory. The longer the pulse the lower is the failing level. In addition, the ESD on-resistance R_{on} derived from TLP I-V curves is a function of t_w defined as follows,

$$R_{on} = \frac{V_{TLP}(t_w) - V_{tr}}{I_{TLP}(t_w)} = f(t_w). \tag{3.1}$$

The mean TLP voltages and currents (V_{TLP} and I_{TLP}) are calculated by averaging the TLP transient voltage and current waveforms in the averaging windows, respectively. At the same stress level with constant pulse power, the pulse energy dissipated in the device is proportional to the pulse duration, generating more heats and causing stronger temperature rise localized in the junction area. It is trivial that within the TLP pulse, the ESD on-resistance of the current path in the triggered ESD device is increasing with the time since the charge mobility has negative temperature coefficients. Consequently, it is valid in the TLP measurements with the given source impedance (50 Ω) when $t_{w1} < t_{w2}$:

$$V_{TLP,t_{w1}} < V_{TLP,t_{w2}},\ I_{TLP,t_{w1}} > I_{TLP,t_{w2}}, \tag{3.2}$$

As a result, the on-resistance derived with shorter pulses is smaller than that with longer pulses according to3.1.

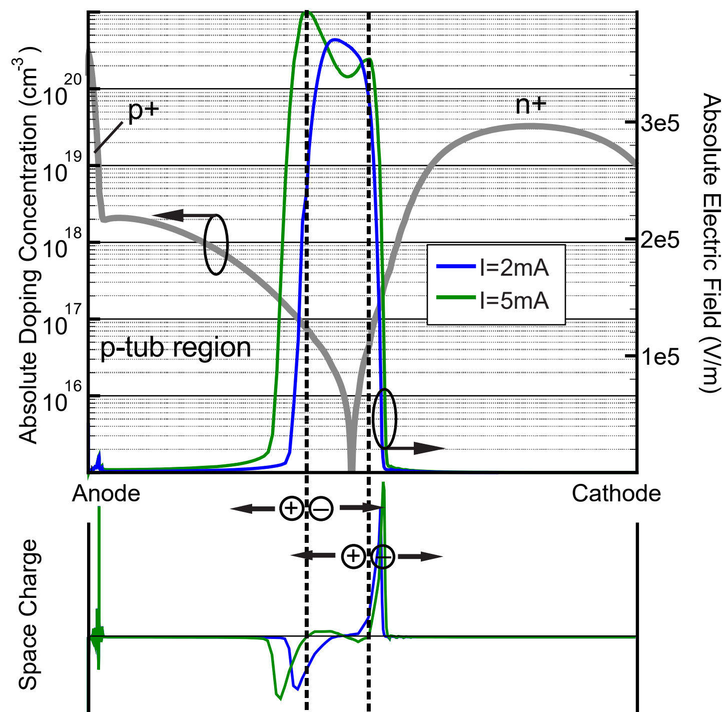

Figure 3.6: 1-D TCAD simulation for the pn-diode pn-e45a2 in the reverse-biased condition shows the differences in the electric field with or without the Egawa effect. Doping profile is shown as well. With 2 mA current biasing, only one local electric field maximum exists along the diode from anode to cathode, where double peaks are observed at 5 mA bias current.

For pulse widths smaller than 200 ns, current density in the pn junction reaches the level where the Egawa effect [53] takes place and changes the slope of I-V characteristic of the pn-diodes. The slope changing points according to the I-V characteristics with different pulse durations generate a nearly horizontal dashed line (Figure 3.5), which implies the current density level is the key parameter for the Egawa effect. In order to have a detailed observation for this phenomenon, 1-D Technology Computer-Aided Design (TCAD) simulation [54] is used to show qualitatively the behavior of the 45 V pn-diode under high current injection condition. Figure 3.6 shows the simulation results where the second local maximum of electric field appears at the higher current rather than at lower current density. When the current reaches a critical value under high injection condition, the holes and electrons densities lead to a modification of the space charge distribution, forming two one sided abrupt p-n (or n-p) junctions hence resulting in double peaks of electric fields. Compared to a single E-field maximum, double field peaks induce substantially more impact ionization within the same increase of potential. This imposes the change of $\Delta I/\Delta V$ and R_{on}.

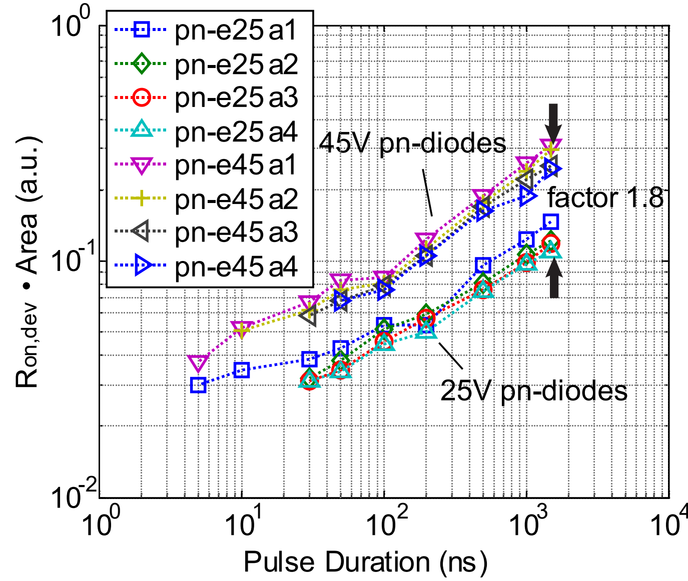

Figure 3.7: $R_{on,dev} \cdot area$ product versus pulse duration for two groups of pn-diodes in 25 V and 45 V voltage classes. a1 to a4 denotes chip area of the devices with the relation a4≈1.33×a3≈2×a2≈4×a1.

For ESD protection, pn-diodes can benefit from the Egawa effect, which lowers the total on-resistance of the devices, resulting in improvement of on-chip ESD area efficiency. In addition to pn-e45a2, many other pn-diodes implemented for two voltage classes are also characterized using the similar TLP test method as introduced above. If one simply linearizes the I-V curves by defining the device on-resistance $R_{on,\ dev}$

$$R_{on,dev} = \frac{V_{t2} - V_{tr}}{I_{t2}}, \qquad 3.3$$

with respect to the failure levels without concerning the change of R_{on} due to e.g. the Egawa effect, the dependence of $R_{on,dev} \cdot area$ product on the pulse duration can be derived from the measurement results as depicted in Figure 3.7. As expected, the diodes with the same breakdown voltage have nearly the same $R_{on,\ dev}$ referring to unit area, showing very good scalability. However, the pn-diodes for higher voltage classes have to be designed larger to obtain the same on-resistance. The weak doping concentration in p-tub region [55] for higher breakdown voltage increases the resistance in the current path significantly. This results in $R_{on,dev} \cdot area$ product of the 45 V devices with a factor of approximately 1.8 comparing to the 25 V diodes.

In fact, in the high voltage applications the ESD design windows often have upper limits of several tens of volts as constraints. Hence, very high V_{t2} might not be in advantage for an effective ESD design. Effective on-resistance $R_{on,\ eff}$ in terms of ESD window with defined maximal allowed voltage is a more practical measure, which can reduce the area efficiency of pn-diodes. This issue will be addressed in the comparison of various devices types in later sections.

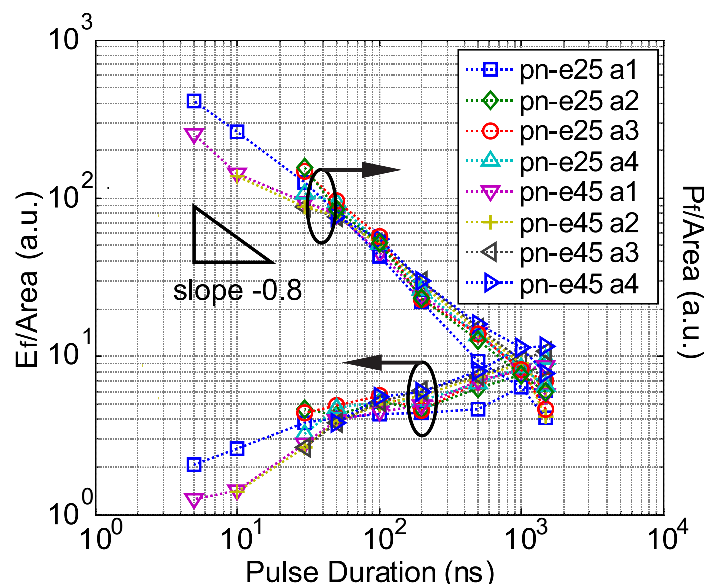

Figure 3.8: Energy and power to failure per area versus pulse duration for two groups of pn-diodes at 25 V and 45 V voltage classes.

In addition to the on-resistance, the failure power (power to failure) P_f and the failure energy (energy to failure) E_f as function of pulse duration are certainly also of interest in the investigation of junction robustness. Based on the TLP characterization, P_f is defined as product of V_{t2} and I_{t2}, while E_f is simply the product of P_f and the corresponding t_w. Figure 3.8 shows the characteristics of specific energy and power to failure of various ESD diodes. Almost overlapped power and energy lines imply the fact that failure levels per area of the pn-diodes are relatively independent on the voltage classes by proper design of the ESD pn-diodes with the given technology. Linear P_f and E_f per area in double logarithm plot basically confirm the Wunsch-Bell theory and the analytical thermal failure model published by Dywer [56] [57]. However, the experimental data do not show exactly the same slope as the power profile shape depicted in the Dywer's theory. The slope is approximately -0.8 in Figure 3.8 rather than -0.5 according to the Wunsch-Bell thermal model in the Wunsch-Bell region. Note that within the range of applied pulse durations, the slope change of P_f from the experimental results does not fit well to the Dywer model (Figure 3.9). The

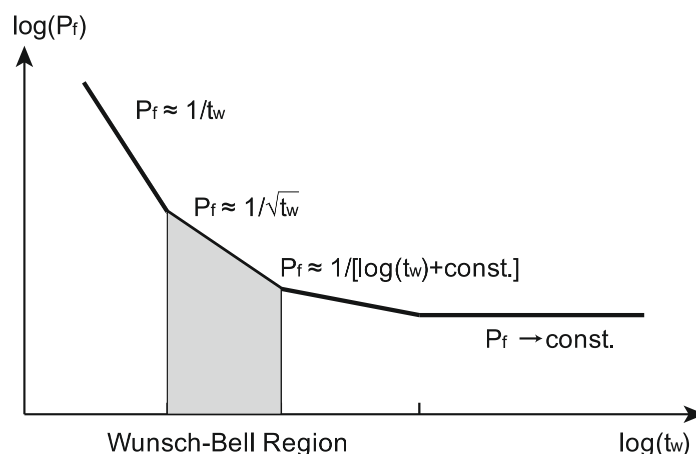

Figure 3.9: Asymptotic behavior of the power-to-failure vs. time-to-failure relationship according to [57].

analytical model was established by solving time-dependent heat diffusion equations for an infinite linear medium with a heat source. In the reality, the devices details become much more complex and depend on geometry, process, and boundary conditions.

Beyond the TLP pulse range, the same long pulse characterization for the snapback device npn-BJT was also applied to the pn-diodes implemented with various voltage classes and devices areas. By utilizing merely the avalanche current without encountering the current filament problem, the pn-diodes show their advantage to handle the long pulse stresses. The device is triggered and conducts current until P_f and E_f are reached at the thermal runaway. Table 3.1 gives the long-pulse characterization for a pn-e45a2 as an example. The failure voltage V_f and failure current I_f are obtained by averaging the voltage and current transient waveforms similarly to the TLP method.

Table 3.1: Long-pulse characterization of pn-e45a2.

Pulse Width (μs)	V_f (V)	I_f (A)	P_f (W)	E_f (mJ)
10	67.6	0.40	27.04	0.27
50	65.6	0.21	13.78	0.69
100	64.2	0.16	10.27	1.03
1000	63.8	0.125	7.98	7.98
10000	63.7	0.1	6.37	63.7

3.1.3 Simple Active Clamps

Another type of non-snapback on-chip ESD protection utilizes an active controlled power MOS field effect transistor [55]. On the contrary to traditional RC triggered MOSFET ESD circuits which have been applied as power clamps in the advanced CMOS or low voltage technologies for many years [51], this work aims to statically triggered high voltage diffusion MOS (DMOS)-based protection elements. To minimize the risks of false-triggering via RC coupling at transistor gate due to EOS disturbances or functional signal switching, a statically triggering concept using Zener diode string has become the preferred solution. This section focuses mainly on the failure level study on simple active clamps with a brief introduction on the Zener clamping circuitry.

3.1.3.1 Design and Evaluation of Simple Active Clamps

Among many possibilities which allow gate-biasing of the big DMOS transistor (bigMOS) during ESD stresses, two examples applying Zener diodes string as the trigger circuit for the static breakdown voltage definition circuit are demonstrated in Figure 3.10. This type of high voltage ESD active clamps are named as the type-A clamps hereafter. The active clamps are designed and fabricated in the smart power technology with the bigMOS implemented with an n-type lateral DMOS transistor (nLDMOS). Within the type-A clamps, type-A1 clamp has one Zener diode as gate protection while type-A2 clamp engages two Zener diodes. The gate-source voltage limitation is therefore different. The trigger voltage of the type-A clamps is denoted as V_{tr}. With the combination of forward- and reverse-biased Zener diodes in the Zener

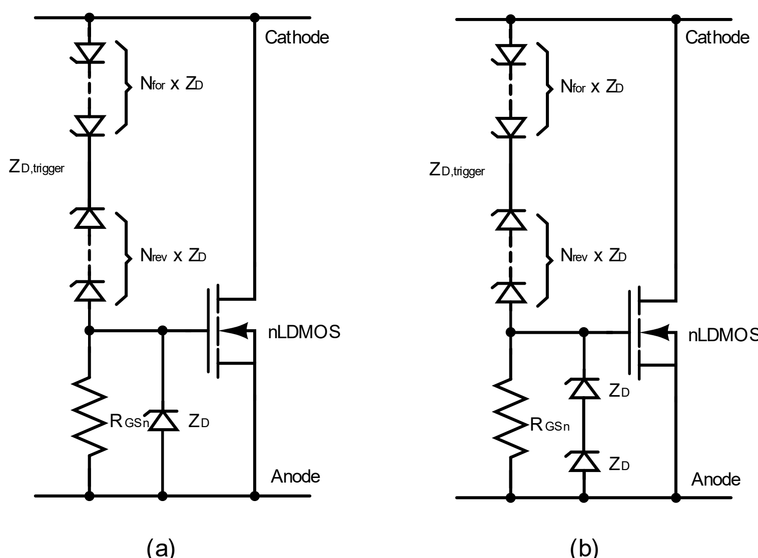

Figure 3.10: The type-A active clamps with (a) type-A1 single or (b) type-A2 two in series connected Zener diodes as gate protection. An active ESD structure can be considered as an ESD device with two terminals, cathode and anode, as in a pn-diode.

diode string, V_{tr} of the active clamps can be flexibly implemented. This is valid as long as the designed V_{tr} is considerably smaller than the avalanche breakdown voltage of nLDMOS with zero gate-source voltage (V_{GS}). In the type-A1 and type-A2 clamps, V_{tr} is designed for 25 V ESD protection circuits. The trigger circuit occupies much less layout area compared to the nLDMOS but should be robust to withstand the clamping voltage without being prematurely damaged. As designed, V_{GS} of nLDMOS can be temporarily biased up to one or two Zener voltages in type-A1 or type-A2 during ESD stresses, respectively.

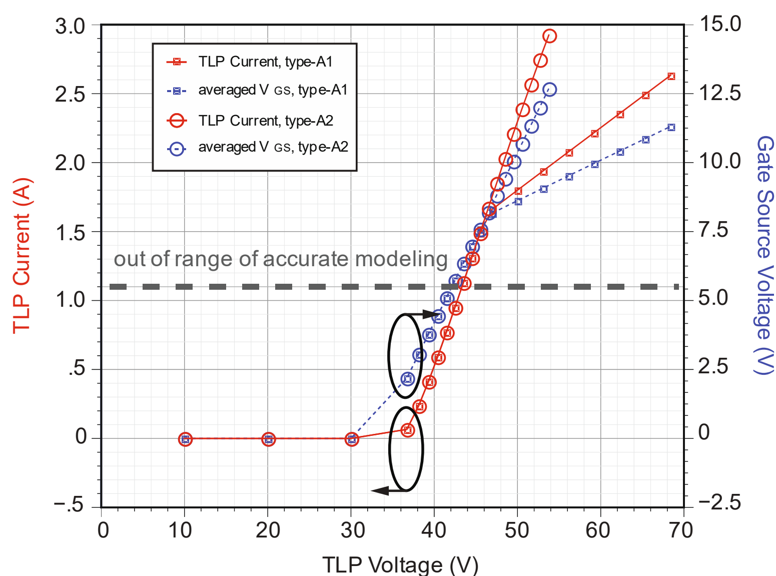

Figure 3.11: Simulated TLP characteristics of type-A1 and type-A2 circuitries in SPICE. TLP current and voltage as well as gate-source voltage of the nLDMOS are calculated using the averaging window between 70% and 90% of the pulses. Above marked current level (dashed line), simulation only delivers qualitatively the I-V characteristics of the structures.

Apart from the functional simulation in the product design, circuit-level ESD design often suffers from the lack of proper simulation models, which would precisely reproduce the physical behavior of circuit elements under high power and short time conditions. Hence, the usage of the results of SPICE simulation is limited. However, it shows qualitatively the voltage and current at every node of the circuits. The modeled output characteristic of the nLDMOS is extracted with DC measurements. The electrical safe operating area (SOA) of a power MOSFET stressed by short pulses in high drain-source voltage range is not included in the SPICE models by default. Figure 3.11 shows the simulation results for the active clamps. Trigger voltage of the active clamps and gate-source voltage of the nLDMOS are well simulated whereas the TLP current can only be qualitatively taken into consideration. Limited V_{GS} in type-A1 with one Zener diode protection directly affects the drain-source current of the nLDMOS. Although the SPICE simulation is not able to predict the on-resistance and the failure level of the active clamps, it is useful to obtain the gate-biasing and the trigger voltage of the circuit in order to do a first time right ESD design.

As mentioned earlier, with a big nLDMOS used as the main ESD circuit element, the physical limitation of ESD capability of the active clamp is given by the SOA of the nLDMOS. I-V points at the onset of snapback or triggering of the inherent bipolar transistor for different V_{GS} give the boundary in which the bigMOS is able to sustain ESD currents. In the given smart power technology, non-uniform snapback of DMOS often results in filament formation and immediate local burn-out [55]. This allows treating the snapback voltage and current as the failure voltage and failure current of the active clamps.

Derived from the experimental results with TLP, the pulsed I-V characteristics of the stand-alone nLDMOS at different V_{GS} (SOA) and the active clamps with designed V_{t1} of 35 V at room temperature are shown in Figure 3.12. Note that the SOA boundary formed by V_{t2} of nLDMOS at various V_{GS} (indicated with the dashed red lines) indeed restricts the snapback and failure points of the active clamps. Type-A2 clamp shows an

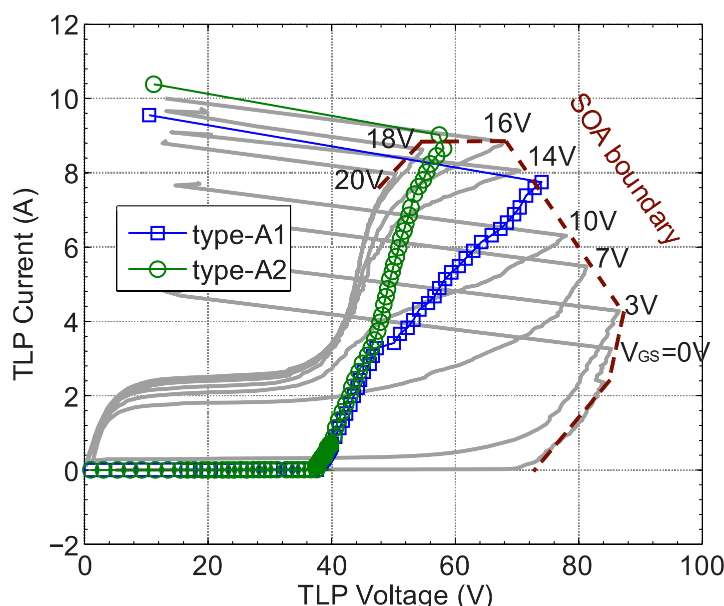

Figure 3.12: SOA characteristics of nLDMOS (grey lines) at different gate voltages overlapped with I-V curves of two 25 V active clamps using the same nLDMOS. Data is recorded in standard TLP measurements (10 ns rise-time, 100 ns pulse duration).

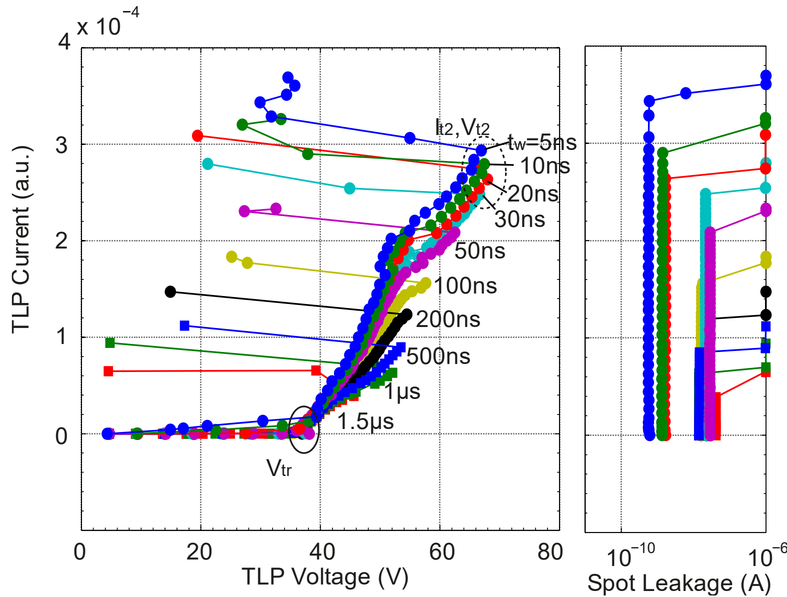

Figure 3.13: TLP I-V characteristic of a 25 V voltage class type-A active clamp named aca-e25a8 tested with various pulse widths from 5 ns to 1500 ns. The rise-time is 1 ns. Parameter e25 indicates the voltage class while a8 is related to the device size. The crowding of failure points tested with below 20 ns long pulses is indicated compared to the pn-diode in Figure 3.5.

advantage against type-A1 clamp, confirming the qualitative SPICE simulation results. With the given SOA, V_{GS} of type-A1 and type-A2 at failure points can be readily estimated using the plot without extra measurements with the test pad on gate [59]. V_{GS} of the type-A1 and type-A2 clamps are approx. 13 V and 17 V respectively. Further, it is shown that the key to the design of the active clamp is to reach the optimal operating point on the SOA boundary of the bigMOS. Since the type-A2 clamp using two Zener diodes at gate enables better control of the gate of the bigMOS, the type-A2 clamp with better gate protection is generally denoted as the type-A clamp hereafter.

3.1.3.2 Failure Levels Study on Active Clamps and nLDMOS

In order to study the failure levels of the active clamps, TLP tests with various pulse durations are applied. Figure 3.13 gives the TLP results of the 25 V type-A clamp employing an nLDMOS as described in Figure 3.12. Vf-TLP measurements with TDRs setup [34] are used for 5 ns pulse width tests. Compared to the pn-diode (Figure 3.5), I_{t2} and V_{t2} of the active clamp are smaller, which implies the intrinsic ESD robustness of pn-diodes is higher. Also unlike the pn-diodes, when the pulse widths are scaled down below 20 ns the onset of the destructive snapback of the active clamp start crowding together with less deviation of the failure voltage V_{t2} and failure current I_{t2}. In other words, with less energy content of the TLP pulses due to shorter pulses, failure power levels of the active clamps however do not increase significantly. Further, some other type-A clamps with different trigger voltages (V_{tr}) are also characterized with the same TLP method, showing a similar failure mechanism of failure points crowding.

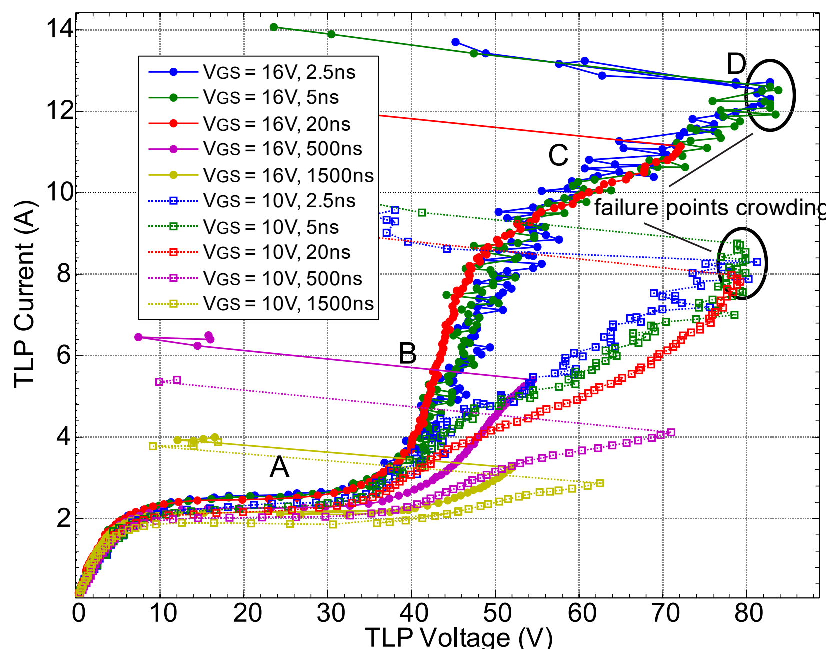

Figure 3.14: Transient electrical SOA of nLDMOS for V_{GS}=10 V and 16 V with different pulse durations (2.5 ns to 1500 ns). Pulses shorter than 20ns no longer enhance the SOA significantly. A to D indicates four different regions of I-V characteristics where the transistor gate is biased to higher voltage (e.g. V_{GS}=16 V) during ESD.

A s discussed, ESD capability of proper designed type-A active clamps relies on the bigMOS, which in this case is the nLDMOS transistor. To understand the effect of saturation of the failure power of the active clamps at short pulse durations, transient electrical SOA of the nLDMOS is investigated applying stresses with various pulse durations in addition to the standard 100 ns TLP. Two sets of measurements are performed for different V_{GS} as depicted in Figure 3.14. Note that for tests with 2.5 ns and 5 ns pulse durations, the failure points of the nLDMOS, defined as the onset of the snapback as well, remain nearly unchanged. This can explain the fact that the failure power of the active clamps is saturated as pulse duration is getting shorter. The SOA measurements are repeated also with different rise-times (100 ps and 1 ns), delivering the same phenomenon. No significant difference regarding rise-times is observed in the transient SOA characteristics in terms of the failure levels. This implies that the triggering of snapback of the used nLDMOS has no significant dependence on dV/dt or dI/dt.

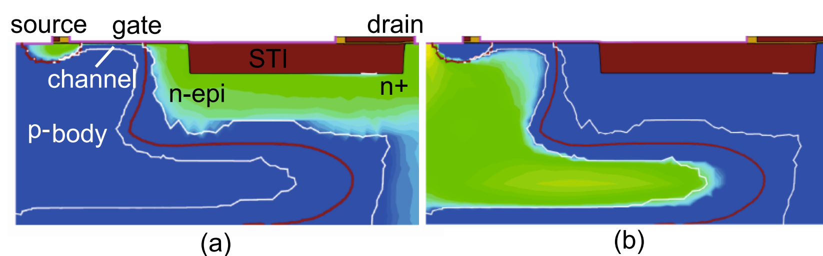

Figure 3.15: Simulation of (a) electron current density and (b) hole current density in the region A. Source and body contacts were shorted to ground while the gate was biased on 10 V. The same simulation setup was also applied to the region B, C and D.

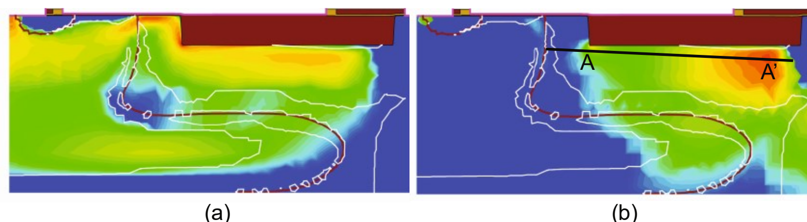

Figure 3.16: Simulation of (a) hole current density and (b) impact ionization amplitude in region B. Significant hole current starts flowing to the body contact in comparison with region A (Figure 3.15 (b)). The delocalization of the impact ionization maximums as well as electric field peaks along the cut line AA' represents the Kirk effect.

In the active clamps, the gate voltage of nLDMOS ought to be biased on a relatively higher level to facilitate a higher failure current. This encourages the further analysis of the used nLDMOS under high voltage gate-biasing [71] with 2-D TCAD simulation involved. As marked in Figure 3.14, A to D represents four regions which are important for the design of the active clamps:

- Region A: nLDMOS works in the saturation region as a MOSFET in usual operating condition, where the MOS channel is pinched off with total electron current flowing through the narrow channel to the drain contact. No additional holes through n-epi layer and p-body to the body contact can be observed. (Figure 3.15).
- Region B: In this region, avalanche multiplication occurs accompanied with strong local electric field [52] [60]. The electrons generated due to impact ionization flow to drain contact while the holes flow to the body, providing a significant addition on the total current (Figure 3.16). The

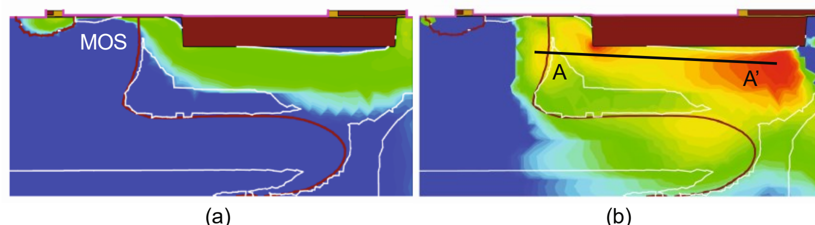

Figure 3.17: Simulation of (a) electron current density and (b) impact ionization amplitude in region C. Electron current is distributed similar as in region A. Along the cut line AA', three local maximums of impact ionization can be observed.

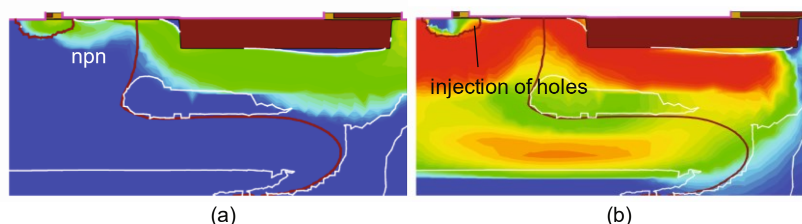

Figure 3.18: Simulation of (a) electron current density and (b) hole current density in region D. Comparing to the operation as MOSFET in Figure 3.15(a), the npn bipolar transistor is now dominating the nLDMOS behavior leading to snapback.

delocalization of the electric field peaks under high current density to the more highly doped drain region is called the Kirk effect [61] after its first investigator for bipolar transistors. It has a similar effect as so-called the Egawa effect in the pn-diodes described earlier.

- Region C: As the generation of the holes keeps increasing, additional local maximums of impact ionization can be observed at p-body to n-epi junction area (Figure 3.17), exhibiting the main difference of region C and B. Note that no significant electron current flows from source through p-body to drain indicating the parasitic npn bipolar transistor (drain-p-body-source) is not yet triggered.
- Region D: This region is defined at the moment when the bipolar triggering happens. As the hole current through p-body is sufficiently large to build up a voltage drop at the base-emitter junction, which is larger than the build-in voltage. The bipolar transistor is then triggered accompanied with significant electrons injected into p-body and holes into source. It forms the snapback as lower drain-source voltage - for the npn bipolar transistor the collector-emitter voltage – is required to sustain a higher collector-emitter current due to the bipolar amplification (Figure 3.18). When the nLDMOS enter into the region D, current becomes significantly large while the current flow becomes inhomogeneous. As a result the current filaments can easily occur, leading to the local overheating and device destruction.

In addition to the simulation results comparing the electrical parameters including impact ionization and charge carrier current in the four regions inside the transistor, transient device simulation using the commercial TCAD simulator SDEVICE is also

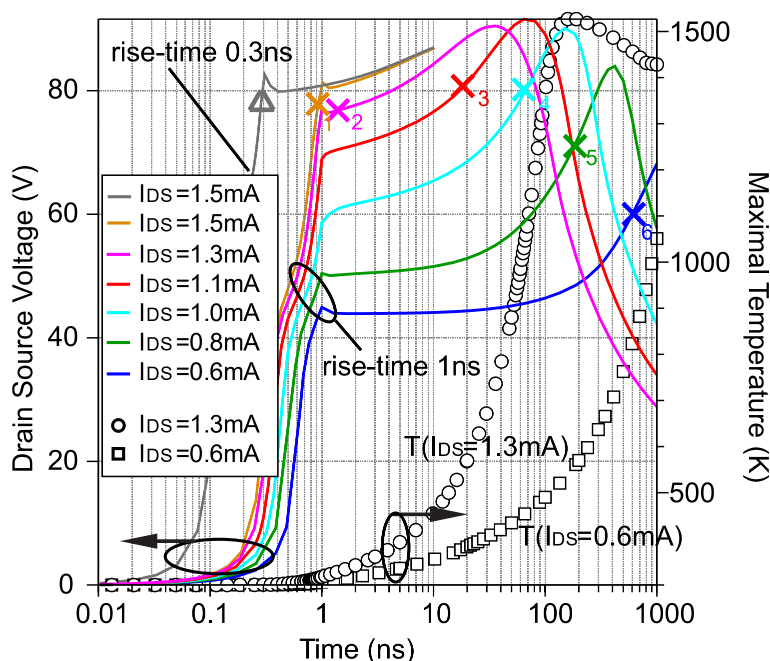

Figure 3.19: Transient simulation of drain-source voltage corresponding to various drain-source current pulses as function of time. The used rise-times are 0.3 ns and 1 ns. In case current reaches the critical level, the parasitic bipolar triggering takes place at very beginning of the pulse (indicated by X1 to X6). The simulated maximal temperatures as function of time are displayed for I_{DS}=0.6 mA and 1.3 mA.

performed for the used nLDMOS in electro-thermal mode. In this mode, thermal effect is coupled with electrical characteristic of the device.

Figure 3.19 depicts the simulated transient waveforms of the drain-source voltage V_{DS} and the maximal lattice temperature of the nLDMOS with V_{GS} of 10 V under various drain-source current (I_{DS}) injections. The drain-source current pulses with pulse amplitude from 0.6 mA to 1.5 mA and rise-time of 1 ns are forced as a current stimulation. For the 1.5 mA current pulse, 0.3 ns rise-time is also simulated. Note that all drain-source current pulses remain constant with the given amplitude during the simulated time period which is up to 1 µs. X1 to X6 denotes the time instants when the triggering of the parasitic npn bipolar transistor takes place. These specific time instants are extracted by examining the electron current density in the device cross section (Figure 3.17 (a)). A time instant is then marked, when large amounts of electrons are not only found in the MOS channel but also in the p-body region. This means the device was driven into the critical region D. In the measurements, triggering of the parasitic bipolar transistor is accompanied immediately with voltage snapback due to current filament (Figure 3.14). In the simulation however, the voltage snapback of an ideal homogenous device in the simulation occurs after a certain time period (tens of nanoseconds to hundreds of nanoseconds shown in Figure 3.19) beyond the bipolar triggering. The simulation accuracy in terms of the onset of voltage snapback is very limited. The simulated maximal voltage peaks observed in the transient waveforms are therefore not usable to identify the onset of the snapback or device failure in practice. Note that the simulation curve respect to the rise-time of 0.3 ns shows nearly the same failure voltage to X1 as indicated with Δ, where the self-heating of the nLDMOS is not significant according to the temperature curves. This simulation result confirms that the triggering of the bipolar transistor is not affected by the rise-time as observed in the measurements.

With X1 to X6 and Δ indicating the failure points of the studied nLDMOS, the power to failure level as a function of time is plotted in Figure 3.20. The power to failure is simply calculated as the product of V_{DS} and I_{DS} at the failure points. Note that the same effect comes out as described with the term failure points crowding (Figure 3.14). In summary of measurements and simulations, power to failure of nLDMOS as well as

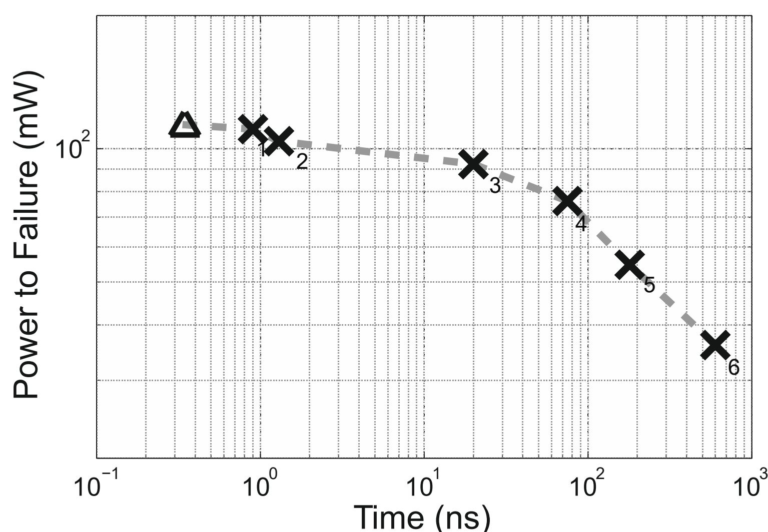

Figure 3.20: Simulated power to failure (the triggering of the bipolar transistor) of the nLDMOS at V_{GS}=10 V. Δ as well as X1 to X6 indicate the failure points as shown in Figure 3.19.

the active clamps using nLDMOS as the bigMOS cannot increase significantly by shortening the pulse width.

The long pulse characterization beyond 1.5 µs for the active clamps is also performed as it is done for npn-BJT and pn-diodes. The utilization of the nLDMOS as the bigMOS allows no bipolar snapback mechanism in the ESD devices design. Therefore the active clamps as non-snapback ESD devices show the capability to conduct current with longer pulse duration after the device triggering. The measurement results are presented in the next section.

3.1.4 Comparison of the ESD Devices

In addition to the major failure mechanisms of three types of ESD devices, which are detailed discussed above, a systematic comparison of the failure levels among the protection devices is given in order to obtain an overview.

Figure 3.21 compares the failure power levels P_f per unit area of various ESD devices calculated as the product of I_f and V_f per unit area. The overlapped curves of P_f per area within the device type pn-diodes as well as within the device type active clamps show an interesting result: the ESD failure power per silicon area depends on the device type and remain nearly the same within a device type regardless the voltage class.

In the ESD time range typically with a pulse width up to several hundreds of nanoseconds, although the failure current I_{t2} of the npn-BJT is higher than pn-diodes as shown in Figure 3.1 and Figure 3.5, P_f per area is however smaller due to the lower failure voltage V_{t2}. The active clamps show however the smallest P_f per area in this pulse range compared to the npn-BJT and the pn-diodes. For even shorter pulse durations below 20 ns, the curves of failure power of the active clamps become flat which is known as the failure level crowding effect measured and simulated for the nLDMOS (Figure 3.20).

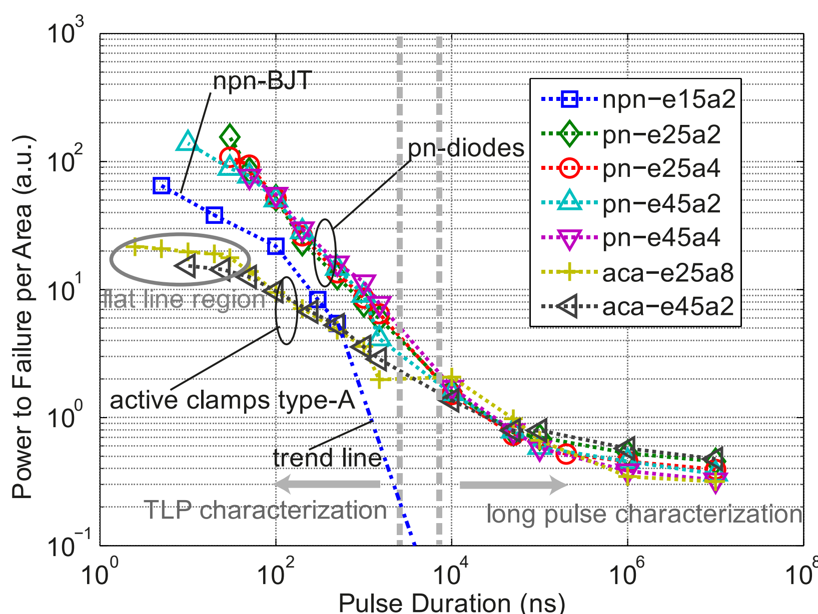

Figure 3.21: Failure power levels per unit area of various ESD devices with different device dimensions and voltage classes. pn-diodes show advantage in terms of the ESD power dissipation capability per unit area in short pulse range.

Robust junction of the pn-diodes exhibits the highest power to failure level in the ESD time range among the three device types due to the fact that the heat generated mainly in the deeper junction (several micrometers away from the silicon surface) can be dissipated in all directions in the vicinity of the silicon space. The npn-BJT is a device close to the silicon surface where the hotspot – the collector to base junction - is at about 2 µm depth. The hotspots in a DMOS based active clamp are located rather at the silicon surface with only the shallow trench isolation (STI) in between (Figure 3.15 to Figure 3.18). In addition, the onset of the bipolar snapback and the accompanied current filaments become the major constraints of the active clamps in the shorter pulse range. In contrast to this, ruggedness of the pn-diodes is only limited thermally rather than electrically in the entire studied pulse range.

With the longer pulse characterization ranging from 10 µs to 10 ms, all devices except for npn-e15a2 exhibit nearly the same failure levels. In this pulse range, the on-chip device interconnections (metallization), the chip packaging as well as the heat sink play an important role because the heat generated in the junction region during the longer pulse is dissipated towards outside of the chip. Time-dependent heat diffusion can reach the lead frame and the heat sink of the package boundaries [62]. Further, the metallization as well as the bond wires can limit the device robustness as the melting point of e.g. copper is lower than the silicon. All three types of devices are encapsulated in the same package LQFP-64 and tested using the square pulse generator. They share the same thermal boundary conditions hence showing similar thermal robustness. On the other hand as discussed earlier, the studied npn-BJT is not capable for the long pulse stresses due to inhomogeneous current flow for longer pulses. Figure 3.21 shows a trend line of the failure power to area indicating the device behavior.

Figure 3.22 compares the failure energy levels E_f per unit area of the investigated ESD devices calculated as the product of P_f and t_w per area. In the TLP characterization, the active clamps show lower E_f per area compared to the npn-BJT while the pn-diodes have the highest E_f per area as expected.

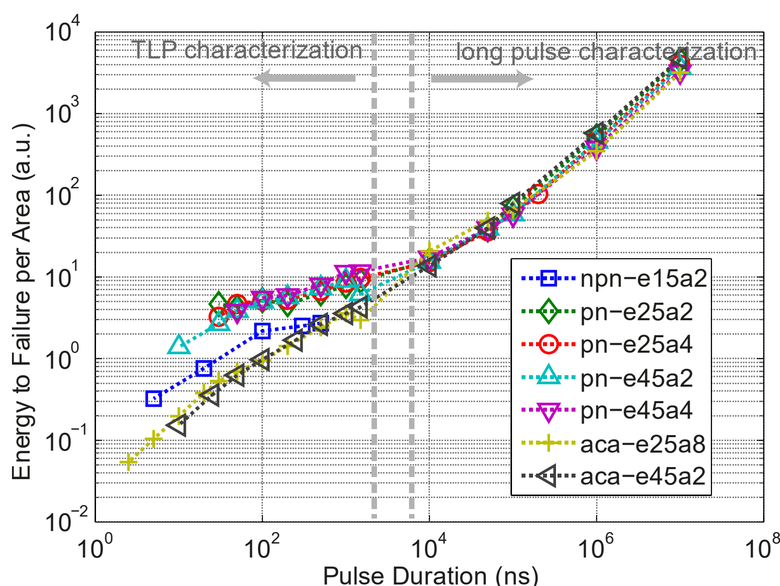

Figure 3.22: Failure energy levels per unit area of various ESD devices with different device dimensions and voltage classes. pn-diodes show advantage in terms of the withstand ESD pulse energy per unit area in short pulse range.

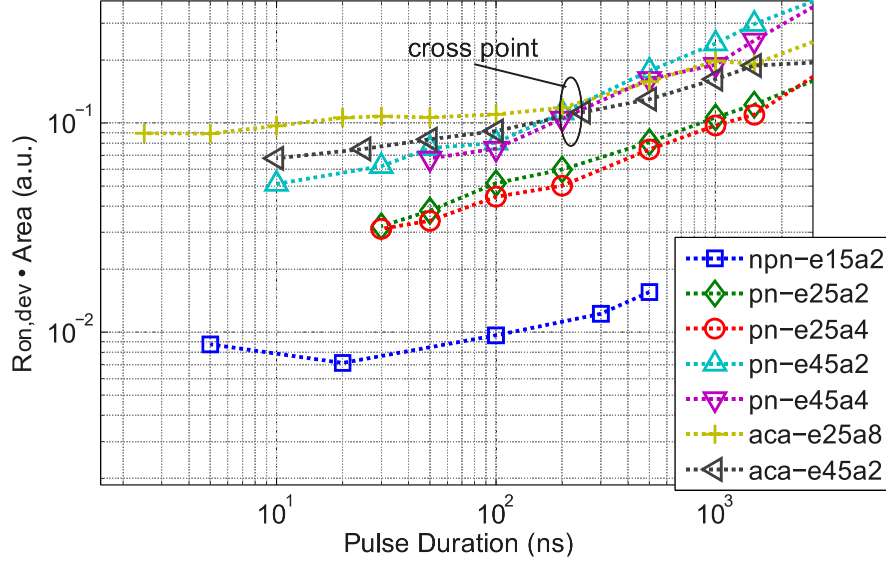

Figure 3.23: $R_{on,dev}$ area product of various ESD devices with different device dimensions and voltage classes in the range of TLP characterization. npn-e15a2 as a snapback ESD device shows the lowest $R_{on,dev}$ area product.

Figure 3.23 gives the comparison of the ESD devices in terms of area product with $R_{on,dev}$ defined in 3.3. As $R_{on,dev}$ is a parameter which is more relevant to the ESD design, only ESD pulse range is explicitly shown in the plot. For the npn-BJT, V_h instead of V_{tr} is used for the calculation of $R_{on,dev}$. The data points confirm that the on-resistance of the snapback devices is usually much lower than the non-snapback ESD devices. Interestingly for pulses longer than 200 ns, the active clamps show lower $R_{on,dev}$ compared to the 45 V pn-diodes as indicated as the cross point.

As discussed in section 3.1.2, the absolute maximum value of the current conducting capability or power to failure of stand-alone ESD device is not the only measure to evaluate the area efficiency of the ESD protection. The maximum allowed voltage V_{max} defined by the protected circuits in conjunction with the ESD design window must be considered. In many cases, V_{max} of the protected circuits is lower than the failure voltage of the ESD protection device, which makes the power to failure level of the stand-alone ESD device not relevant. Therefore, instead of $R_{on,dev}$ the effective on-resistance $R_{on,eff}$ considering V_{max} provides much better comparison of the area efficiency of different types of ESD protections. 3.4 and 3.5 define the effective R_{on} of the protection elements where V_{t2} and I_{t2} are the failure voltage and current, respectively,

$$R_{on,eff} = \frac{V_{max} - V_{tr}}{I_{@V_{max}}}, for\ V_{max} < V_{t2}, \quad 3.4$$

$$R_{on,eff} = \frac{V_{t2} - V_{tr}}{I_{t2}} = R_{on,dev}, for\ V_{max} \geq V_{t2}. \quad 3.5$$

In case V_{max} is larger than or equal to the failure voltage of the ESD device, $R_{on,eff}$ is equal to $R_{on,dev}$. Figure 3.24 shows $R_{on,eff}$ area product of the investigated ESD devices. V_{max} for 15 V, 25 V and 45 V devices are assumed as 35 V, 45 V and 65 V respectively as typical values from experience. Under these conditions, $R_{on,eff}$ of the npn-BJT and active clamps remains nearly unchanged compared to $R_{on,dev}$ of the same devices (Figure 3.23). $R_{on,eff}$ of the pn-diodes has comparable characteristics of their $R_{on,dev}$ but

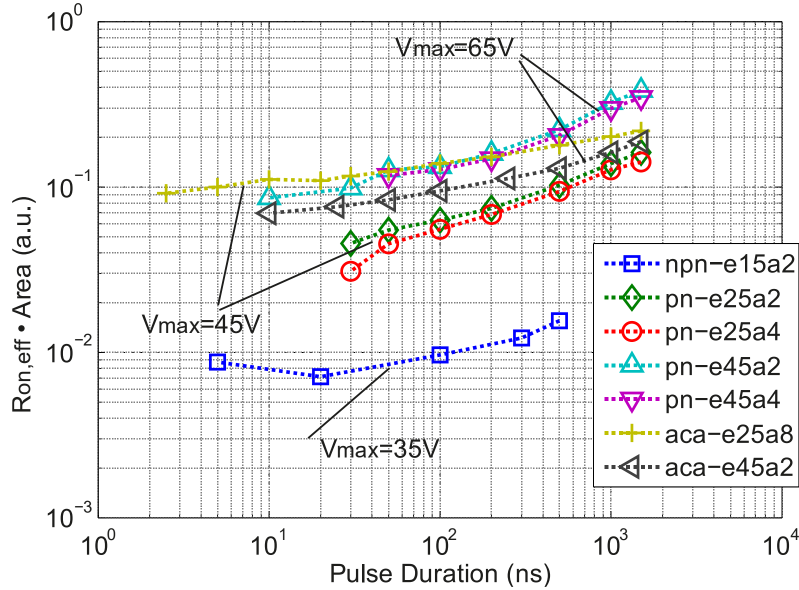

Figure 3.24: $R_{on,eff}$ area product of various ESD devices with different device dimensions and voltage classes in the range of TLP characterization. At 45 V voltage class, the active clamp becomes more area efficient within the whole range of TLP pulses compared to the pn-diodes.

are shifted to higher values due to the consideration of V_{max}. V_{max} practically limits the utilization of the Egawa effect respectively the slope change of R_{on} in the pn-diodes (Figure 3.5). As results, the 45 V type-A clamp provides lower effective R_{on} area product and becomes more area efficient compared to the 45 V pn-diodes in the total range of the applied TLP pulses. As indicated by the results, for ESD protections with higher voltage class, active clamps are more attractive due to lower $R_{on,eff}$. This allows the focus on the active clamps for high voltage ESD protection concepts. With more advanced designs shown in later sections, R_{on} of active clamps can be further improved.

Based on the failure level studies, several advanced features in favor of the active clamps compared to the pn-diodes are summarized as follows:

- Zener triggered active clamps give the possibility of defining V_{tr} in a more flexible way where pn-diode demands process design on device level which is much more time consuming for generating a new device with other trigger voltages. Several silicon learning cycles are usually required.
- In case of higher trigger voltages, needed in certain applications, pn-diodes are only realizable on extra cost of area efficiency. The trend is already shown with the $R_{on,effect}$ area product.
- Process fluctuation and temperature dependence of the high voltage pn-diode is usually much higher than the Zener diode in the active clamps.

It was noticed that the pn-diodes fail thermally whereas active clamps reach their maximal current capability thermally for longer pulses and electrically for shorter pulses. In order to address the impact of different failure mechanisms of the active clamps and the pn-diodes in a practical manner, the HMM tester based on the coaxial line technique introduced in Chapter 2 is used to simulate the system-level ESD pulses. The HMM tester provides an excellent resolution of transient voltage and current measurement.

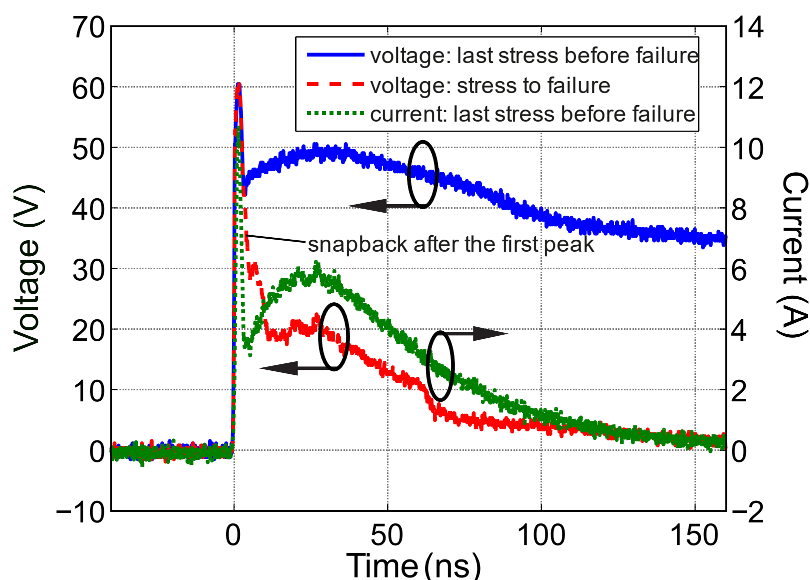

Figure 3.25: Active clamp aca-e25a8 tested with HMM. The snapback of the intrinsic bipolar transistor in the nLDMOS observed after the first peak of HMM causing damage of the aca-e25a8. This device sustains a 3 kV system-level ESD discharge (150 pF/330 Ω) according to the current.

Figure 3.25 and Figure 3.26 show the waveforms confirming two different failure mechanisms of the active clamps and the pn-diodes under HMM stresses. For the 25 V type-A clamp, the decisive damage due to snapback of the nLDMOS is induced by the first peak of ESD pulses. In the stress to failure, the voltage collapse after the first peak. For the pn-diode on the other hand, a thermal breakdown occurs when certain amount of energy is exceeded at the later part of the HMM pulse indicated in the voltage waveform of the stress to failure. Furthermore, the calculated first peak power per unit area is located on the flat line region of the power to failure level of the active clamps shown in Figure 3.21. The pn-diode is not damaged by the first peak because the peak power is below the power to failure level at the corresponding pulse duration.

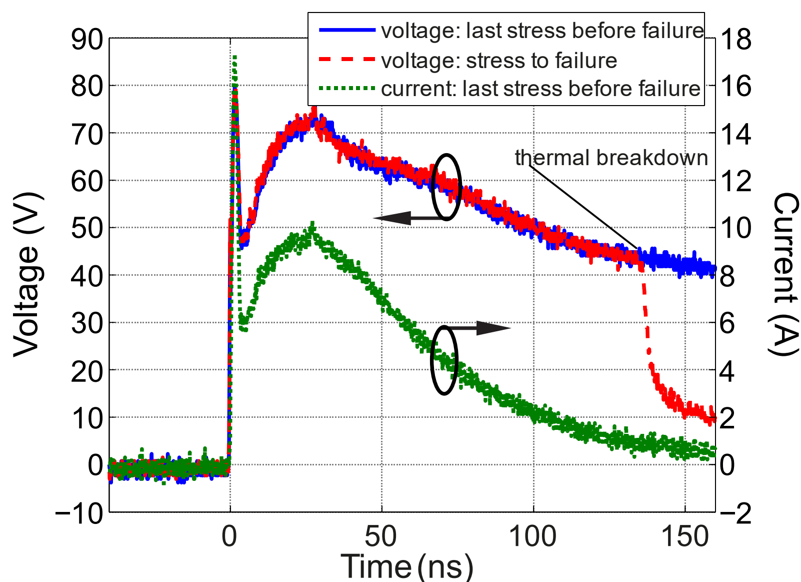

Figure 3.26: pn-diode pn-e25a2 tested with HMM. The thermal breakdown and the device failure observed at about 130 ns of the HMM pulse. This device sustains a nearly 5 kV system-level ESD discharge (150 pF/330 Ω) according to the current.

The HMM measurements performed on the stand-alone ESD devices are mainly used to show different failure mechanisms. As discussed earlier, applying ESD pulses on the single ESD devices delivers the ESD robustness of the ESD devices themselves but does not necessarily reflect the ESD protection capabilities in the applications. For example, a circuit protected by the 25 V pn-diode can probably not survive a 5 kV IEC discharge without taking additional measures since the voltage overshoot of the diode exceeds 80 V. Nevertheless from the effective R_{on} point of view, the first peak of the HMM pulse in the range of several nanoseconds and the broad peak in the range of tens of nanoseconds are still both in favor of the pn-diode for 25 V ESD protection according to Figure 3.24.

3.1.5 Summary

The npn-BJT as one of the high voltage snapback ESD protection devices is robust to shunt ESD current in many applications. It however shows weakness when long duration pulses are applied. In case of EOS related applications, the usage of the snapback ESD protection devices becomes much limited concerning disturbances ranging from micro- to milliseconds. The conventional avalanche pn-diodes with designed breakdown voltages for high voltage ESD protection utilize robust vertical junction deep inside the silicon and deliver inherently very good ESD ruggedness with high area efficiency. The Egawa effect provides an extra advantage of using pn-diodes under high current conditions. The ESD performance of the active clamps relies mainly on the used bigMOS, in this study, the nLDMOS. The unique saturation effect of the failure power levels at shorter pulse duration is shown and explained

Generally, the relatively lower area efficiency of the active clamps for short pulses implies that the pn-diodes furnish a better approach against system-level ESD pulses with a high power peak according to IEC 61000-4-2. The active clamps however are generally sensitive to the peak power due to the bipolar triggering in the nLDMOS. More detailed, on a certain voltage level across drain-source of nLDMOS, the current density in the body region will reach a sufficient value to trigger the parasitic bipolar transistor, driving the MOS transistor into a destructive snapback mode.

On the other hand, depending on the voltage class and the given ESD window, the active clamps can become eventually more area efficient compared to the pn-diodes. In fact, all three types of the studied ESD devices can be suitable as ESD protections. They all have their advantages and disadvantages. The best solution can be only chosen when the constraints and conditions of individual application are fully analyzed and understood. This makes an ESD efficient and effective design in high voltage products a challenging work.

3.2 Case Studies for Failure Modes of ESD Protections

The failure level studies of the ESD protection devices discussed in the previous section provide overview and give insight of protection efficiency in terms of respective device parameters such as power to failure and effective on-resistance concerning device area. However only considering protection device is a misconception. The ESD protection effectiveness can be evaluated with the ESD robustness of the ESD protected circuits consisting of the ESD protection and the protected circuits (also called monitoring circuits in the test structures). In fact the effectiveness depends strongly on the behaviors, in particular the failure modes of protected devices and structures. This section discusses mainly from the perspective of ESD protection effectiveness. To obtain high effectiveness, special concerns such as circuit configurations, impact of voltage overshoots have to be well addressed and taken into account. As previously introduced as an example, it is well known that the use of npn-BJT can be risky due to its limited turn-on speed and the induced harmful voltage overshoots. On the contrary, the following study uncovers an unique failure mode observed on LDMOS transistors even protected by pn-diodes [63].

Voltage overshoots due to finite turn-on speed of ESD protection devices often show negative impacts on ESD hardness and have become a matter of concern in design of advanced CMOS circuits for years [47] [64]. Harmful overshoots are frequently reported in low voltage technologies, mainly causing damages at thin gate-oxide. In the field of high voltage ESD protection, breakdown of thick gate-oxide is normally not a critical issue in ESD design. However, power transistors usually DMOS transistors are believed to be inherently weak against ESD depending on device sizes [65] [66]. As discussed in the previous section, as the voltage reaches the region in excess of the electrical SOA, current filaments can occur at the onset of snapback accompanied with the danger of locally thermal overload in DMOS devices. TLP within only several nanoseconds pulse duration actually result in destructive lateral DMOS snapback in case the critical voltage and current are reached.

To avoid the triggering of the parasitic bipolar transistor in the LDMOS transistor, voltage clamping devices such as avalanche pn-diodes are usually applied and connected in parallel to protect the weak LDMOS transistors with the upper limit of the ESD window given by the snapback trigger voltage V_{t2} which is destructive. Avalanche pn-diodes as protection devices belong to static-triggered voltage clamps. Thus, the robustness of a stand-alone pn-diode has no dependence on rise-time of the ESD pulse. However, TLP tests surprisingly showed this type of on-chip protection concepts do not provide the expected ESD hardness especially during the TLP tests with short rise-times. Using npn-BJT as a snapback device also does not effectively protect the LDMOS transistor.

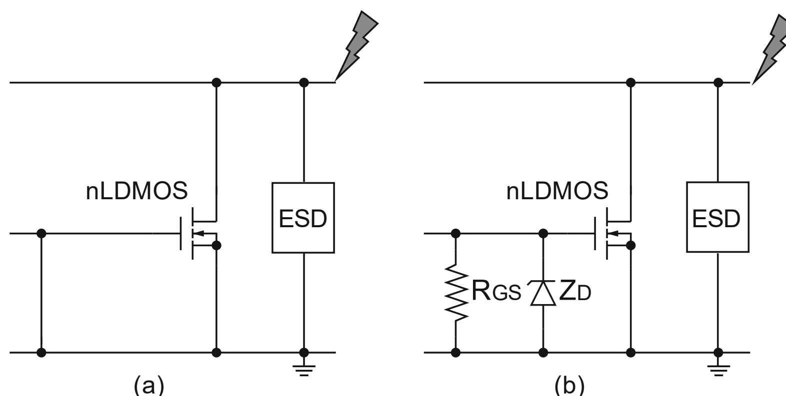

Figure 3.27: Schematic diagram of the tested structures: (a) gg-nLDMOS protected by the ESD device, (b) gc-nLDMOS with Zener protection on gate protected by the ESD device.

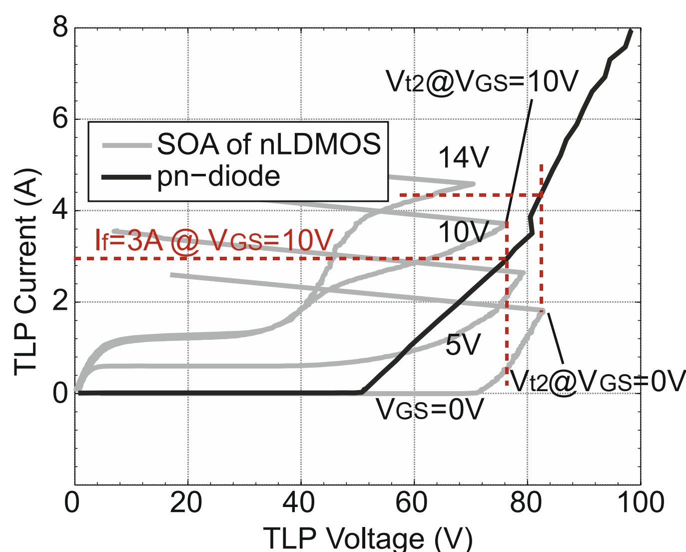

Figure 3.28: SOA of the large nLDMOS with gate-biasing from 0 V to 14 V and I-V characteristics of the pn-diode. Dashed lines show the current levels merely due to the pn-diode at different SOA limits (V_{t2}). Devices are tested using standard TLP with t_r=10 ns, t_w=100 ns.

To address the problems, this section presents the case studies of four different high voltage ESD test structures and explores two different failure modes in these concrete examples. Many measurement and simulation results are carried out accompanied with the detailed investigation of the nLDMOS as the device being protected. Device simulation is utilized to identify the unique failure mode of the LDMOS transistor as ongoing bipolar triggering. Suggestions of more effective ESD protection for voltage sensitive circuits against stresses with fast transients are provided.

3.2.1 Case Studies and TLP Results

Figure 3.27 shows the schematic diagrams of the studied test structures, which are very representative in the field of high voltage ESD applications. The nLDMOS transistor with two different gate biasing conditions is protected with an ESD device connected in parallel. In the grounded-gate (gg) configuration, gate and source are tied to ground. In the gate-coupled (gc) configuration, R_{GS} is designed to obtain a discharge time

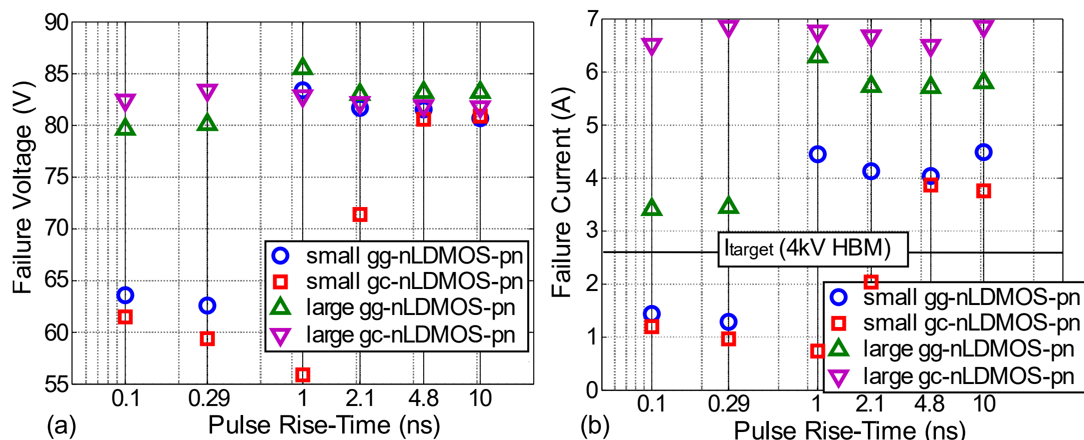

Figure 3.29: (a) Failure voltages of the four test structures (Figure 3.27) with a pn-diode as the ESD device depend on TLP pulse rise-time. (b) Failure currents of the four test structures depend on TLP pulse rise-time.

constant $R_{GS}{\cdot}C_{GS}$ of about 100 ns, which allows the transient gate-biasing of the transistor on a certain level during the stresses (e.g. pulse width t_w=100 ns). A Zener diode (clamping at 10 V) is used as overvoltage protection of the gate-oxide. In both cases, gate-oxide will not be initially damaged during ESD events. In addition, the bulk of the nLDMOS transistors are connected with source. Note that all the interconnections of the on-chip test structures are kept very short with negligible parasitic effects such as metal resistance.

For each circuit configuration two nLDMOS with different channel widths (device scaling parameter) in ratio 68:1 are implemented. The smaller nLDMOS can only divert current in the milliamp range with negligible contribution in the ESD performance, while the larger nLDMOS has a certain capability of self-protection. During the first study, the ESD protection device is implemented with a pn-diode in 45 V voltage class, characterized with standard TLP with the pulse width of 100 ns. The diode is used to

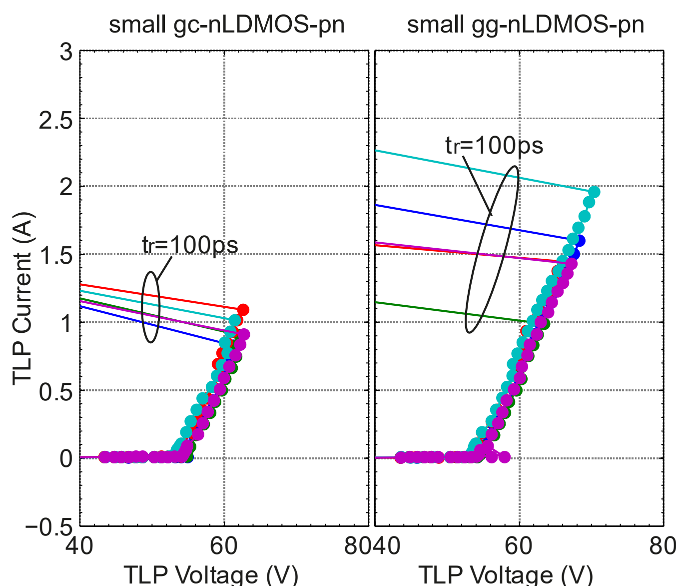

Figure 3.30: I-V characteristics of small (left) gc- and (right) gg-nLDMOS-pn test structures measured with TLP: t_r=100 ps, t_w=100 ns. The same TLP measurement is repeated five times for each test structure in different sub-dies on the same wafer, showing big fluctuations.

clamp the voltage across the nLDMOS and to keep it below the voltage limit determined by the electrical SOA of the transistor with the specified ESD ruggedness (current level corresponding to 4 kV HBM in this case study).

Figure 3.28 illustrates the pulsed SOA of the large nLDMOS used in the test structures overlapped with the I-V characteristic of the ESD diode (pn-diode). Note that even by neglecting the current diverted through the larger transistor, the pn-diode should provide sufficient ESD robustness. In the case of gc-nLDMOS for example, V_{t2} is smaller with V_{GS} of 10 V compared to the case of zero V_{GS} (gg-nLDMOS). As the current through the pn-diode is approximately 3 A at the voltage drop equal to V_{t2} with V_{GS}=10 V, the failure current of the test structure is estimated at least at 3 A as well. By assuming the correlation between 100 ns TLP and HBM, in the worst-case scenario, namely the small nLDMOS in the gc-configuration protected by the pn-diode (small gc-nLDMOS-pn), the current level is expected to be larger than 4 kV HBM (corresponding to 2.67 A). Since the pn-diode works as a static-triggered ESD protection element, no dependence on rise-times is expected in the test structures.

As a matter of fact, the target ESD performances are not well achieved during the measurements for four test structures: small gg-nLDMOS-pn, small gc-nLDMOS-pn, large gg-nLDMOS-pn and large gc-nLDMOS-pn. Figure 3.29 shows the strong dependence of failure voltage and current on rise-times t_r. TLP measurements are performed using different rise-times t_r but the same pulse width t_w=100 ns with the averaging window from 70 ns to 90 ns. For t_r of 10 ns, failure voltage and current meet the values which are predictable by using the TLP characterizations of the stand-alone pn-diode and the nLDMOS (Figure 3.28). Under faster rise-times however, failure levels of the structures with smaller nLDMOS are far below the expectation. For the large gg-nLDMOS-pn, the I_{t2} levels are also lower when rise-times are in sub-nanosecond range. By repeating the TLP measurements for the same test structure using the same TLP setup, big fluctuations are observed exemplarily shown in Figure 3.30. Note that the early failures of these test structures are measured in TLP tests without any pre-pulse voltage (PPV) on the discharge pins. The harmful avalanche breakdown delay of the pn-diode or DMOS described in [39] due to PPV is not the cause of the unexpected results.

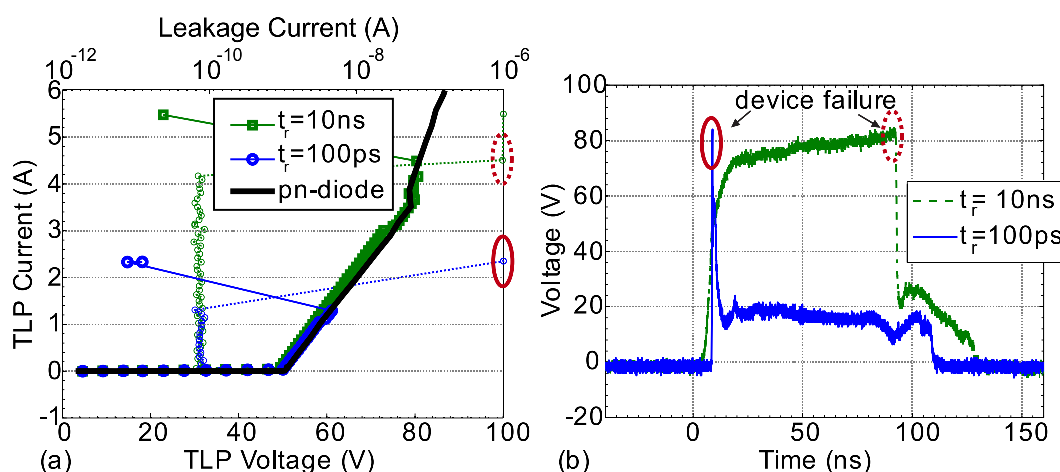

Figure 3.31: (a) TLP characteristics with the leakage current spots of the small gg-nLDMOS-pn tested with the rise-time of 10 ns and 100 ps. 100 ns TLP I-V curve of the pn-diode is also shown. Different failure levels are indicated in the spot measurements. (b) Voltage waveforms of the pulses causing failures of the small gg-nLDMOS-pn structure with the TLP rise-time of 10 ns and 100 ps. Device failures occur at completely different time instants.

In addition to the failure voltage and current derived from the TLP I-V characteristics, the transient waveforms of the TLP measurements are very interesting. As an example, the TLP I-V results and voltage transient waveforms of the small gg-nLDMOS-pn with the expected and the so-called early failures are illustrated in Figure 3.31, representing two different failure modes, depending on the rise-times. As the small nLDMOS barely conducts current, TLP characteristic of the small gg-nLDMOS-pn must follow the I-V curve of the pn-diode until the nLDMOS fails. For t_r=10 ns, the failure occurs at the end of the pulse because the electrical SOA is exceeded at about 80 V. The nLDMOS is driven into the destructive snapback condition. For t_r=100 ps on the other hand, the early failures are always found at the very beginning of TLP stresses. The failure levels of early failing devices become significantly lower. It turns out the voltage overshoot can be the root-cause of the early failures.

The used ESD protection device pn-diode is known as one of the most reliable and fast turn-on protection devices for high voltage applications. The voltage-overshoot-related issue is so far not reported for pn diodes. On the other hand, snapback devices are commonly known to be sensitive to pulse current and rise-time in terms of harmful voltage overshoots. As discussed in section 3.1, snapback devices produce voltage overshoots due to the snapback process which takes typically nanoseconds to tens of nanoseconds. The protected circuits can be thus threatened by the high voltage at the beginning of the pulses. To verify this in a practical manner, the test structures shown in Figure 3.27 are also implemented with a snapback device – 45 V npn-BJT - as the ESD protection instead of the pn-diode. Figure 3.32 shows the worst-case scenario with the small gc-nLDMOS protected by the npn-BJT as an example (small gc-nLDMOS-npn). The TLP rise-time is 100 ps and the pulse width is 100 ns. The stand-alone 45 V npn-BJT has a TLP failure current of about 3.5 A. The small gc-nLDMOS-npn however only reaches I_f of 1 A. Voltage waveforms show significant voltage overshoots. The stress to failure is similar to the failing pulse of the small gg-nLDMOS-pn with 100 ps rise-time (Figure 3.31 (b)). It indicates that in both cases, the small nLDMOS protected by the pn-diode or the npn-BJT, the transistor can fail due to the voltage overshoots. Therefore, the voltage overshoots induced by the pn-diodes must be investigated more in detail. Further, the failure mechanism of the nLDMOS introduced in subsection 3.1.3

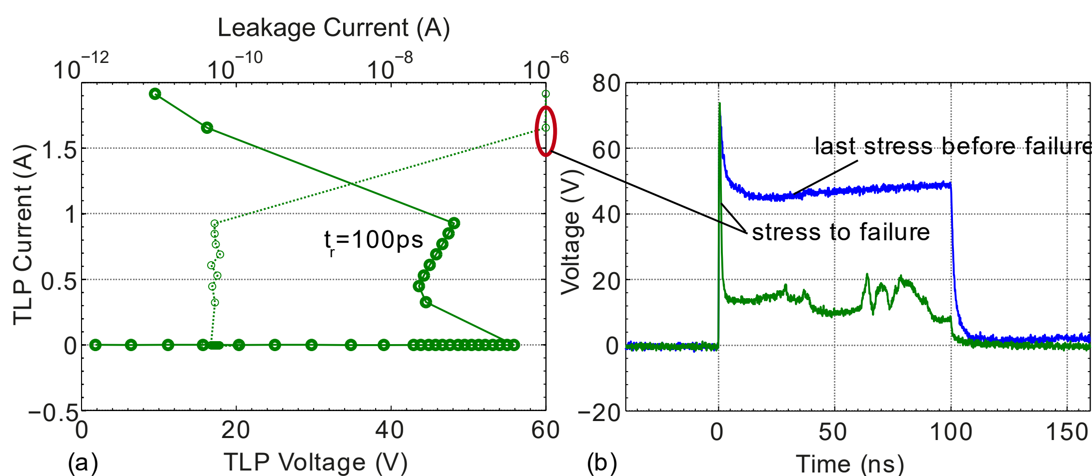

Figure 3.32: (a) TLP characteristics with the leakage current spots of the small gc-nLDMOS-npn tested with the rise-time of 100 ps. Device failure is indicated in the spot measurements. (b) Voltage waveforms of the last stress before failure and the stress to failure of the small gc-nLDMOS-npn structure with the TLP rise-time of 100 ps. Device fails at the very beginning of the pulse due to the voltage overshoot.

shows that the power to failure of the nLDMOS does not increase with decreasing pulse width. The behavior of the transistor as a protected device under voltage overshoots with respect to amplitude and duration is not yet fully understood, demanding further detailed studies on this issue.

3.2.2 Study on the Dynamic Issues

3.2.2.1 Test Artifacts in TLP

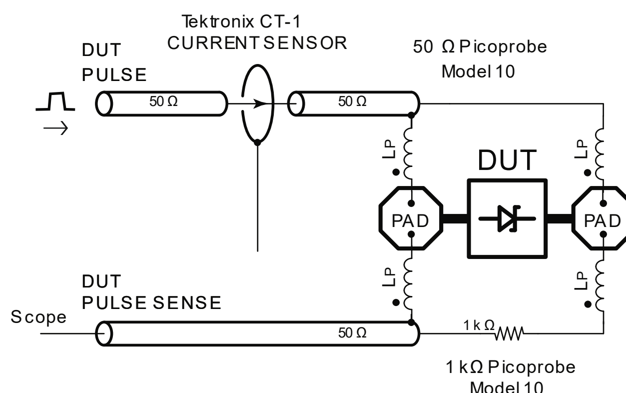

Figure 3.33: Wafer measurement configuration using four-point probes method.

Because the study on dynamic issues requires very accurate measurement techniques, the test artifacts in the wafer-level TLP measurements must be firstly evaluated. The four-point probes method [40] is applied in the TLP measurements as illustrated in Figure 3.33. The sense needle with integrated 1 kΩ resistor provides a measurement bandwidth of about 7 GHz which is limited mainly due to the parasitic capacitances of the 1 kohm at the needle.

The other parasitic effects caused by the inductances, primarily the mutual inductances L_P, are quantified with an on-chip short. The voltage spikes induced merely by the inductive couplings are very scalable and rather small as shown in Figure 3.34. For instance, the on-chip short with 4 A TLP current and 100 ps rise-time only produces a voltage overshoot of 1.2 V. Voltage overshoots with large amplitude are thus not due to test artifacts.

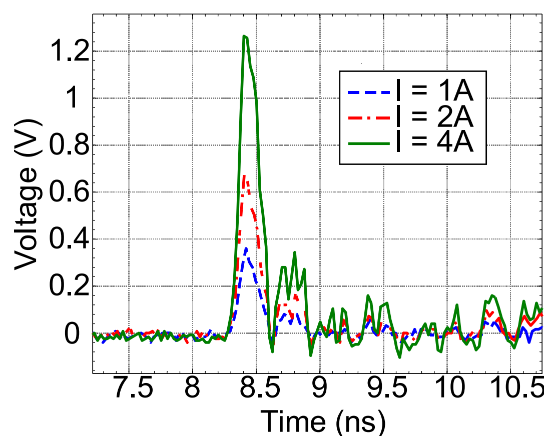

Figure 3.34: Inductive coupling tested for different current levels with an on-chip short.

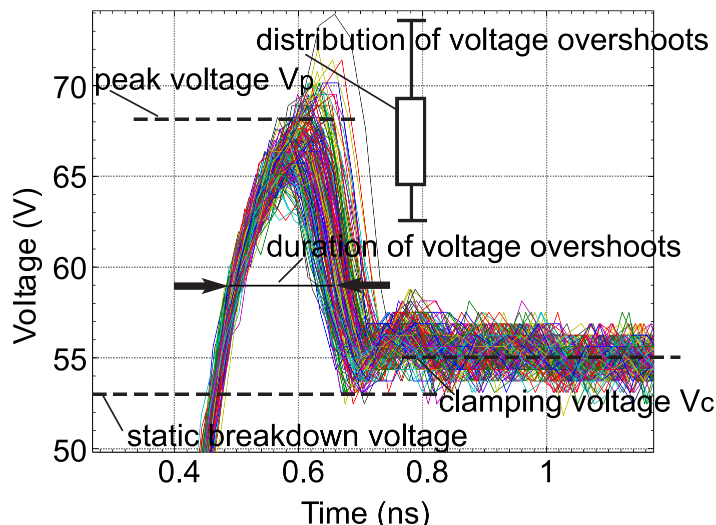

Figure 3.35: Voltage overshoots observed by testing the stand-alone ESD pn-diode with TLP (t_r = 100 ps). Same test is repeated 200 times in order to illuminate the distribution.

3.2.2.2 Voltage Overshoots of pn-Diodes

The voltage overshoots induced by the npn-BJT is obvious and significantly depend on the rise-time (Figure 3.4). The overshoot duration as well as the snapback process is in nanoseconds range depending on the device structure. This section concentrates on the overshoots issue of the avalanche breakdown based pn-diodes, which is for the first time in focus for ESD.

According to the TLP results, the nLDMOS as the device being protected suffers from early damage despite the ESD diode. Therefore, the detailed analysis of the protection pn-diode must focus on the avalanche breakdown process. The mean avalanche propagation speed when the current reaches its final value is rather fast and given by [68]. Depending on device geometry, the avalanche propagation time is very short (picoseconds to tens of picoseconds), representing the duration from high to low resistive state of the diodes after the avalanche breakdown. However, the time until a

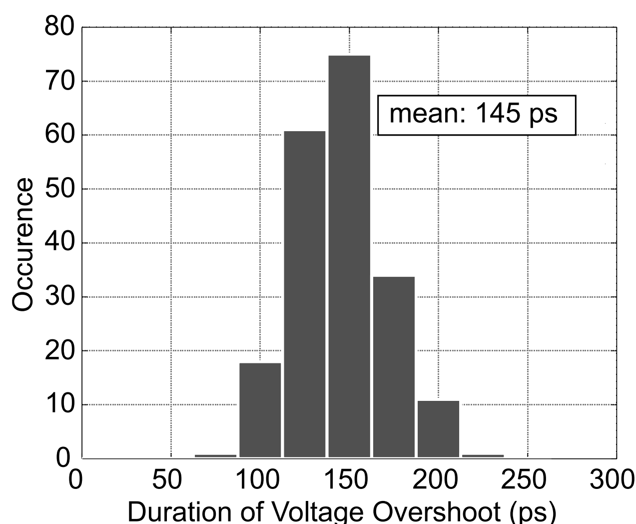

Figure 3.36: Statistical distribution of the overshoot duration according to Figure 3.35. Mean overshoot duration is about 145 ps.

free charge carrier becomes available to initialize the avalanche multiplication is statistically distributed. The result is voltage overshoot, which exceeds the static breakdown voltage when the diodes encounter dynamic events such as ESD.

Figure 3.35 shows the voltage spikes of the stand-alone pn-diode under TLP tests with t_r=100 ps and a TLP current of 1 A. The voltage waveforms are recorded using an oscilloscope with 40 GS/s sampling rate. The scattering in the rising edge of the pulses is much smaller than in the falling edge of the overshoots. Hence the different duration of voltage overshoots does not originate from fluctuation of the oscilloscope but is mainly due to the pn-diode itself. Figure 3.36 gives the statistical distribution of the overshoot durations. A faster triggering to avalanche breakdown produces a lower voltage peak. Note that the voltage peaks (over 10 V at 1 A TLP current) vary in a relatively wide range and cannot be test artifacts as discussed earlier (Figure 3.34).

It is also observed in the measurements that the average overshoot duration decreases with increasing TLP current because the peak voltage V_p is larger with a higher chance to find a free carrier to launch the avalanche multiplication (Figure 3.37 (a)). And vice versa, the time until a free charge carrier becomes available gets shorter, resulting in the smaller increase of V_p at higher current levels ($\Delta V_{p2} < \Delta V_{p1}$). Note that during the fast transients in the sub-nanoseconds time domain, the oscillations in the waveforms are recorded due to the parasitic inductance and capacitance in the probe needles. Also the peak voltages and overshoot durations might be not quantitatively excellent time-resolved due to the sampling rate of the oscilloscope. The qualitative behavior of the diode is however correct.

On the other hand, the average V_p is getting smaller with the longer rise-times at the same TLP current level. With rise-time above 5 ns, no significant overshoot can be detected (Figure 3.37 (b)). As a result, voltage overshoot on avalanche pn-diode is an inherent behavior, which should be carefully characterized and controlled in high voltage ESD designs, even without the existence of pre-pulse voltage.

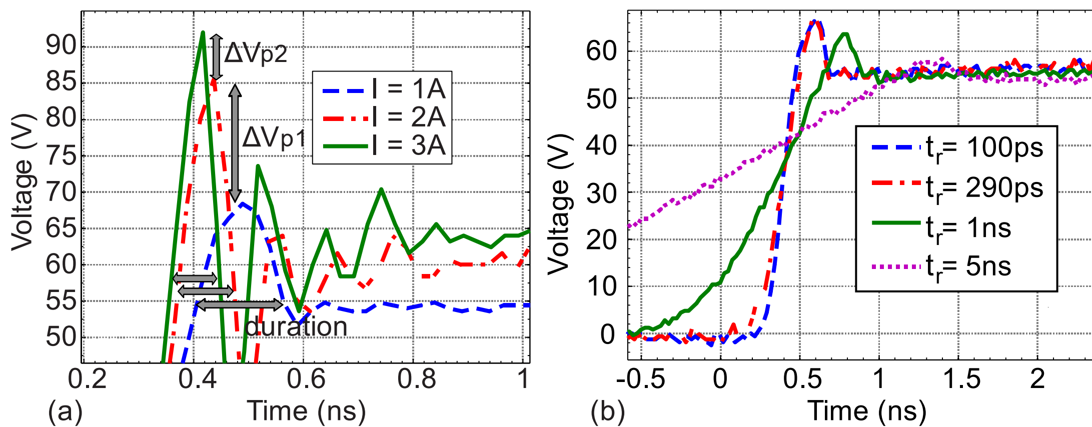

Figure 3.37: (a) Voltage overshoot and its duration as a function of TLP current levels with the same rise-time of 100 ps. (b) Voltage overshoot as a function of rise-times with 1 A TLP current. t_r=100 ps and 290 ps show almost the same slope because of the parasitic capacitance of the pn-diode.

3.2.2.3 Transient SOA of nLDMOS

Since it is believed that the voltage overshoot studied in the stand-alone pn-diode plays an important role for the early damages in the test structures, the safe operating area of

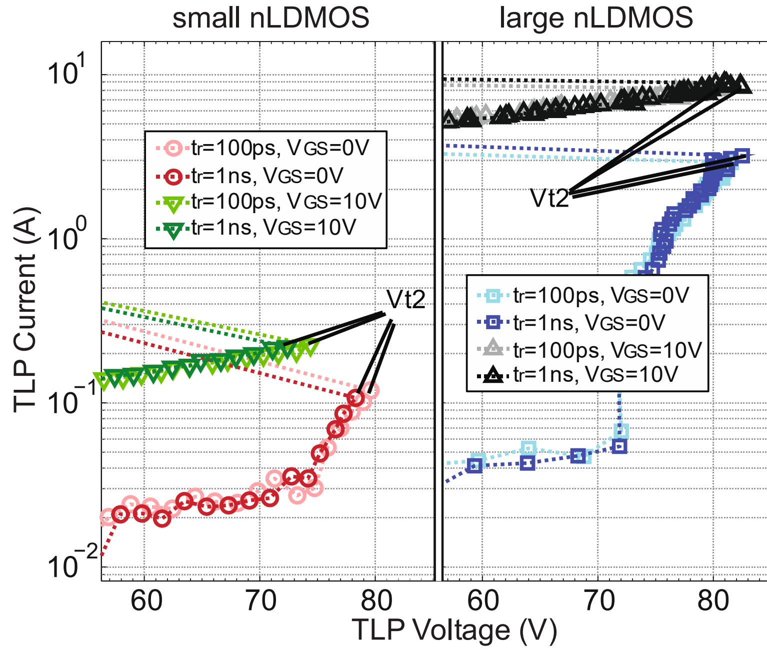

Figure 3.38: Transient SOA tested with 5 ns pulse width vf-TLP for a (left) small and a (right) large nLDMOS transistor. The average window is set between 50% and 70% of the pulses which is for 5 ns TLP the steady state for both used rise-times 100 ps and 1 ns.

the nLDMOS with different device sizes with respect to the protected devices is further investigated especially in short pulse range. In section 3.1.3, the onset of the parasitic bipolar snapback in the nLDMOS is studied with focus on different pulse durations. The electrical failure mechanism of the nLDMOS in the short pulse range is of particular interest. It encourages the study on the transistor behavior under voltage overshoots.

The term transient SOA introduced in [69] is used for the measurements in this work applying the vf-TLP setup with TDR method [70]. The measurement results are shown in Figure 3.38. 5 ns is used as the pulse width to simulate the voltage overshoots. V_{GS} is biased on 0 V and 10 V, corresponding to gg- and gc-configuration in the test structures, respectively. It is found that rise-times (100 ps and 1 ns) do not have considerable impact on V_{t2}, neither for the small nor for the large nLDMOS transistor. The triggering of the inherent bipolar transistor in the nLDMOS as a function of dV/dt or dI/dt is not observed.

In other words, the SOA of nLDMOS itself is not affected by rise-times but is limited through absolute values of drain-source voltage. Note that V_{t2} of the large nLDMOS

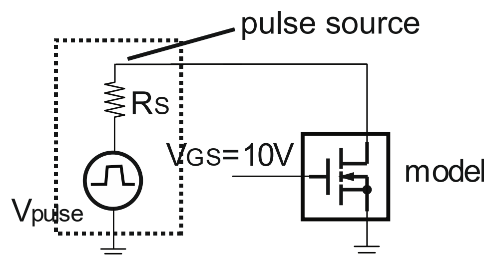

Figure 3.39: Schematic of simulation setup. In voltage conditioned simulation, V_{pulse} and R_s are set smaller representing the SOA measurement for the small nLDMOS. In current conditioned simulation, V_{pulse} and R_s are set larger representing the measurement for the large nLDMOS.

should be smaller than the measured values since the contact resistance between the pulse needle and device pad is not de-embedded in the TDR setup. The voltage across the contact resistance contributes to the measured V_{t2}. In the large nLDMOS with V_{GS} of 10 V, the voltage across the resistance is larger compared to the case of zero V_{GS} due to larger drain-source current. As a result different V_{t2} of the small and the large nLDMOS are test artefact and are not expected.

In addition to the SOA characterizations using vf-TLP, the time evolution of the bipolar triggering inside the transistor is investigated by device simulation. The commercial SDEVICE simulator by SYNOPSYS is used. The simulation setup is schematically shown in Figure 3.39 with V_{GS}=10 V. The nLDMOS model is implemented with a 2-D physical model which contains the geometry and the doping concentration of the device. The model width of the nLDMOS is the third dimension and is set to a fixed value (e.g. 1 µm).

For the test structures with smaller transistor, the charged TLP cable acts like a voltage source since the nLDMOS exhibits much larger impedance compared to 50 Ω. Therefore, the pulse amplitude V_{pulse} and the source resistance R_s are set small for the voltage conditioned simulation to reflect the measurement case with the small nLDMOS as the DUT. For the structures with larger transistor, TLP becomes more like a current source since the impedance of the test structures is smaller than the impedance of the 50 Ω TLP system. V_{pulse} and R_s are set large for the current conditioned simulation to reproduce the measurement case with the large nLDMOS. The transient simulation is used to detect the onset of the bipolar snapback.

The pulse source acts as a voltage or a current source as in the TLP measurements by setting the resistance R_s according to,

$$R_s = 50\,\Omega \cdot \frac{DUT\ width}{model\ width} = 50\,\Omega \cdot \frac{DUT\ width}{1\ \mu m}. \tag{3.6}$$

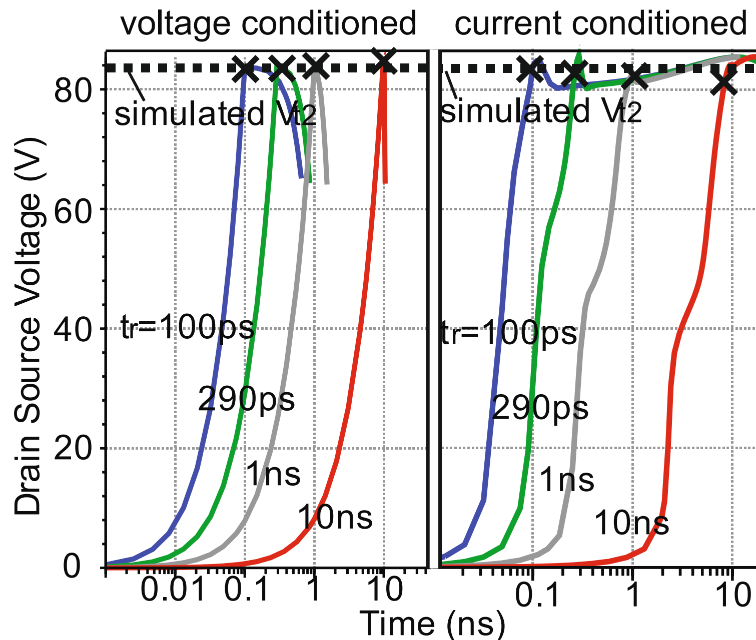

Figure 3.40: Simulated voltage waveforms of (left) voltage and (right) current conditioned setups with V_{GS}=10 V and various pulse rise-times. V_{t2} is marked by “X”, showing a fairly constant trigger voltage of the inherent bipolar transistor in the nLDMOS.

Figure 3.40 displays the simulated voltage waveforms. Note that in the voltage conditioned simulation, the pulse source as a voltage source is only valid before the bipolar triggering due to a substantial increase of current. On the other hand, the snapback of the drain-source voltage V_{DS} is not visible immediately after the bipolar triggering in current conditioned simulation due to current limitation (similar to Figure 3.19). Furthermore the nLDMOS is an ideal homogenous device in this 2-D device simulation not allowing current filaments. Hence, a destructive waveform with voltage collapse is not reproduced in the simulation. The triggering of the bipolar transistor can however be determined by inspecting the device cross section as introduced in subsection 3.1.3.2. The time instants when the triggering occurs are indicated with "X" in Figure 3.40. According to the simulation results, the bipolar triggering of the nLDMOS is purely electrical in sub-nanoseconds to nanoseconds range. Trigger voltage and current under voltage- and current-biasing conditions do not change with rise-time. Note that simulation is not calibrated with experimental data, hence without good agreement of V_{t2} values compared to Figure 3.38 with V_{GS} of 10 V. The difference is yet small. Based on experiments and simulations, the nLDMOS is not directly affected by shorter rise-time (dV/dt or dI/dt) effects. The reduction of the TLP failure levels of the tested structures using the pn-diode as the ESD protection must be caused by rise-time dependent voltage overshoots of the pn-diode.

The qualitative agreement between experiments and simulations additionally verifies the used simulation setup and results as reliable.

3.2.2.4 Ongoing Triggering of Parasitic Bipolar Transistor in nLDMOS

Figure 3.41 shows the transient response of the pn-diode and a small nLDMOS to a 5 ns long TLP pulse. The well-designed ESD diode exhibits overshoots only for several hundreds of picoseconds (Figure 3.36) and rapidly clamps the voltage to a lower value below V_{t2}. In this particular example, the nLDMOS snaps back and sustains the 5 ns

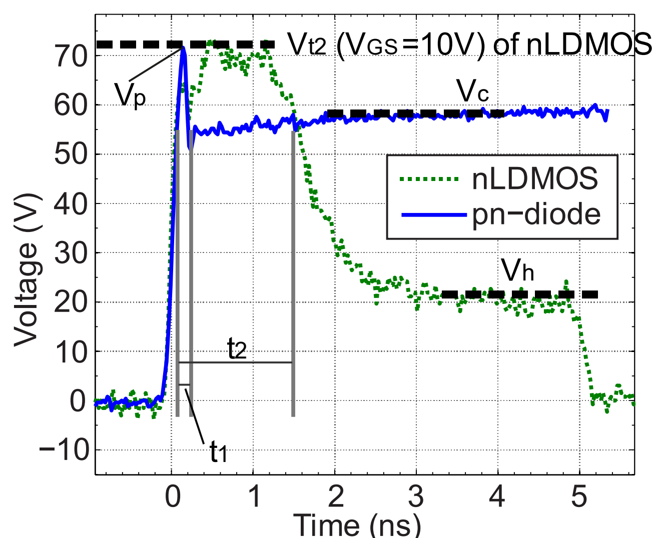

Figure 3.41: Transient voltage response of a stand-alone pn-diode stressed by 1 A TLP current with t_r=290 ps showing an overshoot reaching V_{t2} of the nLDMOS with V_{GS} of 10 V. Voltage waveform of a stand-alone small nLDMOS in snapback is also shown. The nLDMOS is stressed by 5 ns long TLP with t_r=290 ps at low current level without destruction. Gate-source voltage is biased on 10 V. Both devices are independently measured and the waveforms are time-aligned for comparison.

current without being damaged due to homogenous current flow and lower current level. It is clearly shown that the clamping process of the ESD diode is much faster than that of the LDMOS snapback ($t_1 < t_2$). It could be expected that the process of snapback in the nLDMOS transistor might be stopped before local burnout occurs if the voltage drop across the pn-diode falls from its peak value quickly below V_{t2}. This is obviously not always the case according to the early failures in our case studies discussed before.

To understand why the transistor suffers early failure due to voltage overshoots, the study on the interaction of the pn-diode and nLDMOS is necessary. Transient thermo-electrical TCAD device simulation is performed to give insight into the detailed physical behavior of the transistor in the first few nanoseconds. The simulation method described in Figure 3.39 is also applied here. The method is proven in Figure 3.40 as reliable for the transient SOA study of the nLDMOS. Figure 3.42 shows current responses of the nLDMOS biased at V_{GS}=10 V to voltage stresses with different peak voltage V_p and clamping voltage V_c, representing the voltage overshoots induced by the pn-diode. The voltage pulses are applied to the transistor with 1ns rise-time and

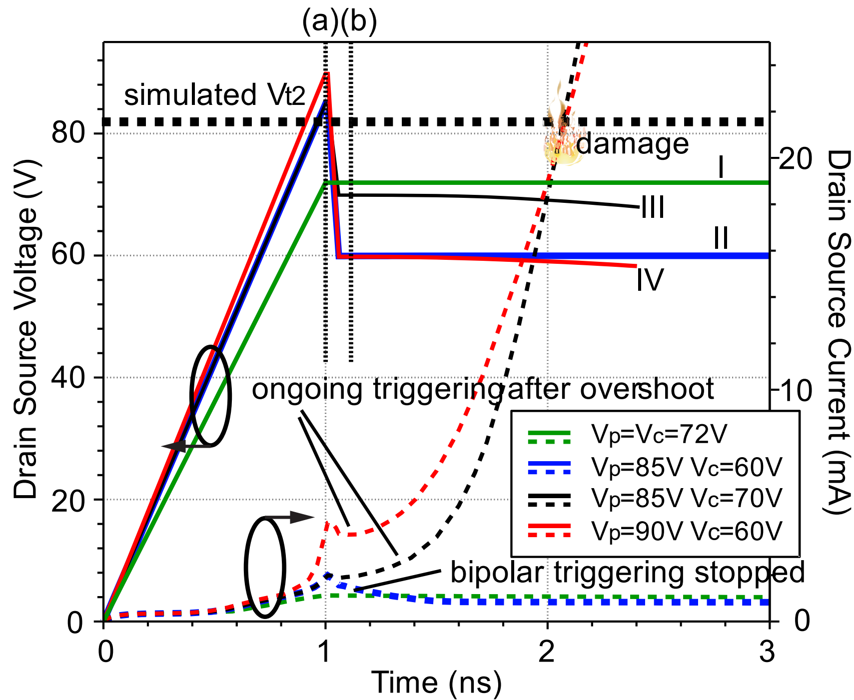

Figure 3.42: Voltage overshoots applied to the nLDMOS with V_{GS}=10 V in simulation, oriented to the test structures with gc-configuration. The unique failure mode where the bipolar triggering cannot be turned off depends on V_p, V_c and is identified by the current waveforms. Local burnout due to the temperature rise is indicated. This behavior leads to the term dynamic destruction of the nLDMOS beyond voltage overshoots.

Table 3.2: Case I to case IV defined for the transient device simulations with various V_p and V_c.

case I	V_p=V_c=72 V	V_p=V_c<V_{t2} without overshoot
case II	V_p=85 V, V_c=60 V	V_p>V_{t2}, V_c<V_{t2}
case III	V_p=85 V, V_c=70 V	same V_p, larger V_c compared to case II
case IV	V_p=90 V, V_c=60 V	same V_c, larger V_p compared to case II

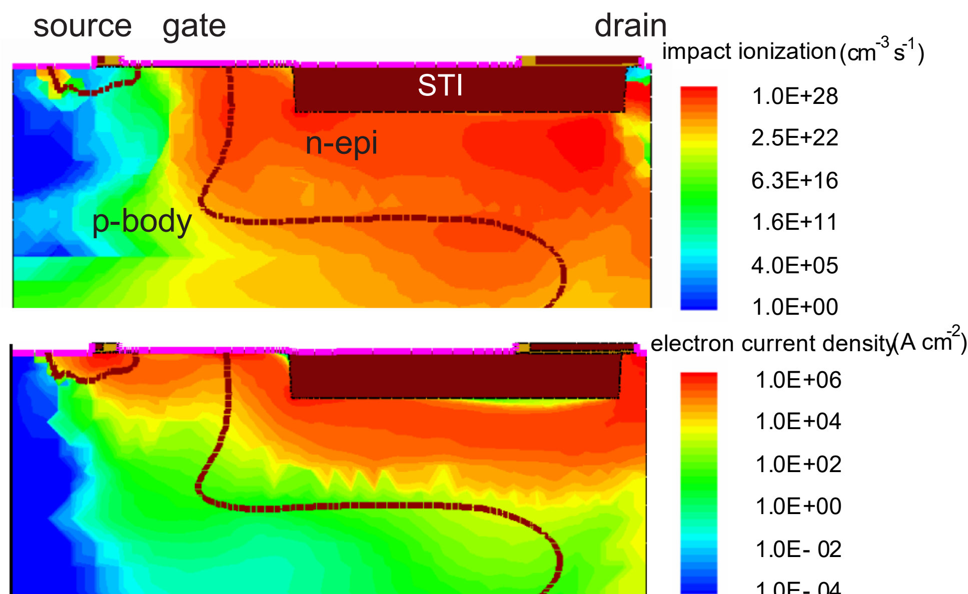

Figure 3.43: Simulation results of (top) impact ionization and (bottom) electron current density at time instant (a) in Figure 3.42 for V_p=85 V.

with only 10 ps peak duration. The fall-time from V_p to V_c is set to 50 ps corresponding to the previously found avalanche propagation time. This voltage conditioned simulation is oriented to the small gc-nLDMOS test structure with four cases described in Table 3.2.

If the maximal voltage remains at 72 V (case I) which is below V_{t2}, the bipolar triggering does not happen as expected. In case II (V_p=85 V and V_c=60 V), the parasitic bipolar transistor is initially activated and then turned off due to the lower clamping voltage. However in case III (V_p=85 V and V_c=70 V), the triggering starts in the same

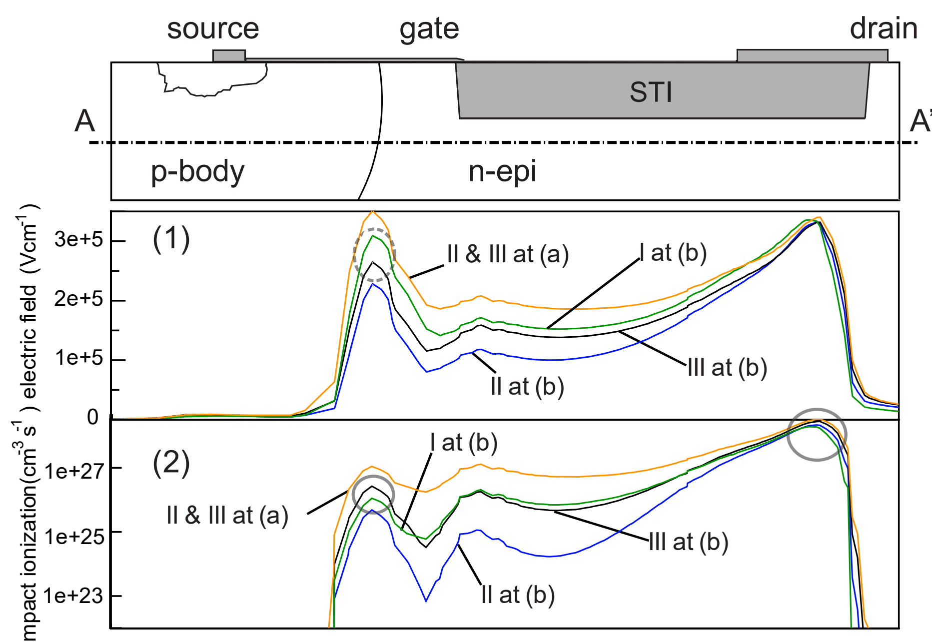

Figure 3.44: (Top) Cross section of the nLDMOS. (Bottom) Along the cutline A-A', (1) electric field and (2) impact ionization at V_{GS}=10 V for cases II & III at time instant (a), case I at time instant (b), case II at time instant (b), and case III at time instant (b), respectively.

way as in case II because of the same V_p but is not stopped due to the higher V_c. The result is device destruction even though V_c is much lower than V_{t2}. This transient simulation actually reflects the voltage overshoot due to the pn-diode and the destructive bipolar triggering. The overshoot duration is approximately 200 ps in the simulation case. Case IV (V_p=90 V and V_c=60 V) also gives a combination of V_p and V_c which result in the destruction of the nLDMOS.

Figure 3.43 shows impact ionization and electron current density in the device cross section for cases II and III at the same time instant (a) indicated in Figure 3.42. Strong impact ionization results in large generation of electron-hole pairs in the region around the STI. Large amount of electrons injected from source to body clearly indicates an active bipolar triggering in the nLDMOS transistor.

Figure 3.44 depicts a comparison of electric field and impact ionization for cases I, II and III at the different time instants (a) and (b) along the cutline beneath the STI. At time instant (b), the voltage is clamped to V_c and the electric field is higher in a larger area for case III compared to case II. The higher electric field in case III provides larger impact ionization and hence more holes in the p-body. The hole current further biases positively the base-emitter junction, resulting in more electron injection from the source. This keeps the bipolar triggering process ongoing due to a positive feedback. It leads to a drastic increase of current until thermal destruction. On the contrary, when the clamping voltage is below the critical level, impact ionization is not able to keep the bipolar triggering process ongoing. The current level then returns to the status where $V_{DS} = V_c$ as shown in case II.

Compared to case III, the electric field for case I at the location (indicated with dashed line oval) in Figure 3.44 is stronger due to higher electric potential. The impact ionization is however lower in the important drain n+ region and p-body to n-epi junction region (indicated with solid ovals) without reaching the critical level. This is because impact ionization rate is not only a function of electric field, but also depends on current density G [49]

$$G = \alpha_n \frac{|J_n|}{q} + \alpha_p \frac{|J_p|}{q}. \qquad 3.7$$

α_n and α_p denote ionization coefficients of electrons and holes which strongly depend on electric field. J_n and J_p are electron and hole current densities, respectively. q is elementary charge. In case III at (b), the ionization rate is above the critical level due to the existing current flow generated by the previous voltage overshoot. Hence, impact ionization is the key parameter which determines whether the process of ongoing triggering takes place.

In addition to the clamping voltage V_c, the unique process also depends on the precondition V_p. In case IV with the same V_c=60 V as in case II but a larger V_p of 90 V, the bipolar triggering does not terminate and dynamic destruction of the nLDMOS occurs due to the higher current density and impact ionization at time instance (b) caused by the previous larger voltage overshoot (Figure 3.42).

In an overview, the critical condition for ongoing triggering after a voltage overshoot as a function of V_c and V_p is shown in Figure 3.45 based on device simulation. At higher V_p, V_c must be lower to avoid ongoing triggering. As an example, if a pn-diode as ESD

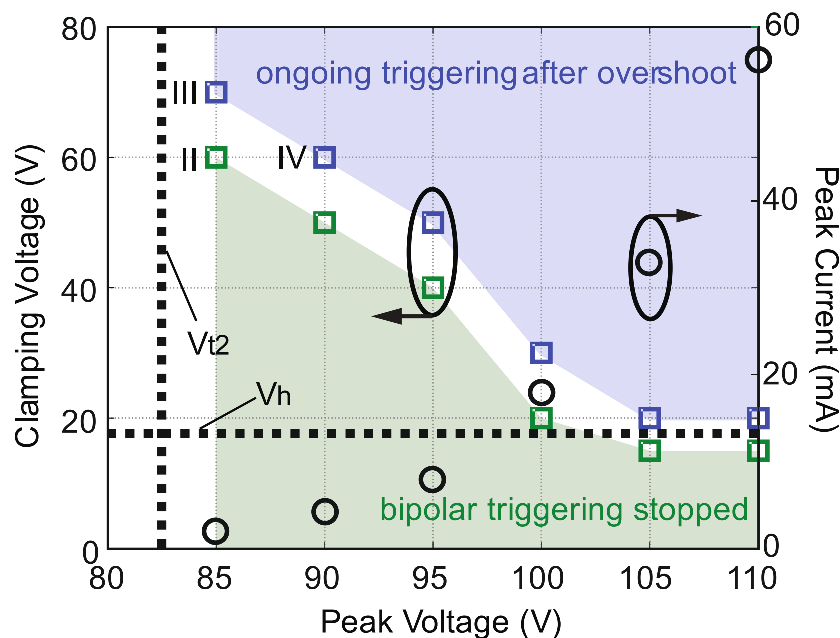

Figure 3.45: The critical condition for the nLDMOS for ongoing bipolar triggering based on the same transient simulation as described in Figure 3.42 with different combinations of V_p and V_c. II, III and IV indicate the cases defined in Table 3.2. The rise-time of the voltage pulses is 1 ns and the peak duration 10 ps. The transistor is biased with V_{GS}=10 V. Peak current as a function of V_p is also shown.

protection provides a fast clamping at 50 V, a voltage overshoot above 95 V is not allowed. If V_c is below the holding voltage V_h of the parasitic bipolar transistor, ongoing bipolar triggering does not occur in the investigated range of V_p.

The peak current I_p is defined as the drain-source current when the voltage reaches V_p. The higher the peak voltage, the larger the peak current is expected due to larger impact ionization at time instant (a) (Figure 3.42). Hence, from 3.7 the situation becomes more critical, requiring a lower V_c to start a recovery process from bipolar triggering. Again, the level of impact ionization determines whether bipolar triggering is ongoing or a recovery process takes place in the nLDMOS transistor.

Of course, for voltage stresses with other rise-times instead of 1 ns, ongoing triggering as a function of V_c and V_p is different in general due to different I_p.

The effect of ongoing bipolar triggering is also observed in the gg-configurations (V_{GS}=0 V) in simulation. The formation of ongoing triggering process depending on V_c and V_p is not as critical as in gc-case since the overall current density is lower without MOSFET channel current. Together with larger V_{t2} (Figure 3.38), it is clear that the small gg-nLDMOS becomes less sensitive to overshoots as shown in the TLP results (Figure 3.29).

Above all, the effect of ongoing bipolar triggering in the nLDMOS is found after a careful review of the overshoot of the pn-diode and the transient SOA of the nLDMOS. The dynamic destruction of the nLDMOS beyond voltage overshoots is believed to be

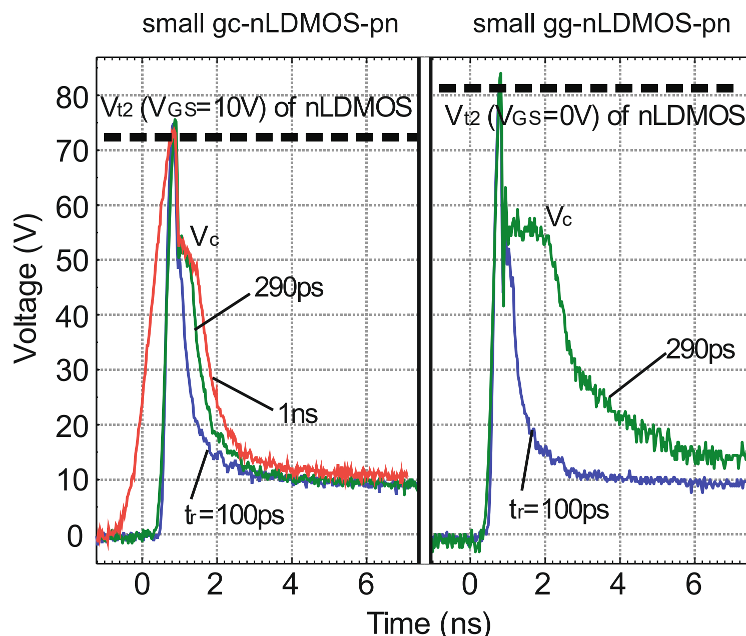

Figure 3.46: Waveforms of stresses to failure regarding voltage overshoots for small (left) gc- and (right) gg-nLDMOS-pn with various rise-times. Ongoing triggering is launched, causing dynamic destruction. The curves are time-aligned according to the voltage peak for better comparison.

the reason of the early failures of the test structures protected by the pn-diode in the TLP characterization. The voltage transient waveforms of the failing pulses with respect to the early failures (Figure 3.31 (b)) become more explicable.

Figure 3.46 displays further the measured transient waveforms of the stresses to failure in the first nanoseconds for small gg- and gc-nLDMOS-pn. The waveforms demonstrate the dynamics of ongoing triggering. After the overshoot, the voltage is initially clamped to Vc due to the ESD pn-diode for a short time. Then a further voltage reduction to approximately 10 V becomes visible. This implies the destruction of the nLDMOS because the voltage falls lower than the non-destructive holding voltage shown in Figure 3.41.

The duration of destruction can be related to the rise-time at least for the same test structure. The longer the rise-time, the longer takes the destruction process. A possible reason is the effect of rise-time on initial distribution of current filaments [72]. The shorter rise-time induced current filaments can be multiple and delocalized in the small nLDMOS, resulting in stronger heating and faster thermal damage under the stress of a voltage conditioned pulse source.

3.2.3 Failure Analysis and HBM Results

In the previous sections, two failure modes have been investigated. The first failure is caused by exceeding the quasi-static SOA derived from 100 ns TLP. The parasitic bipolar transistor is triggered and the nLDMOS fails by the end of the pulse during TLP characterization. Due to self-heating the voltage increases during one TLP pulse and reaches the critical voltage by the end of the TLP pulse (Figure 3.31(b)). The second

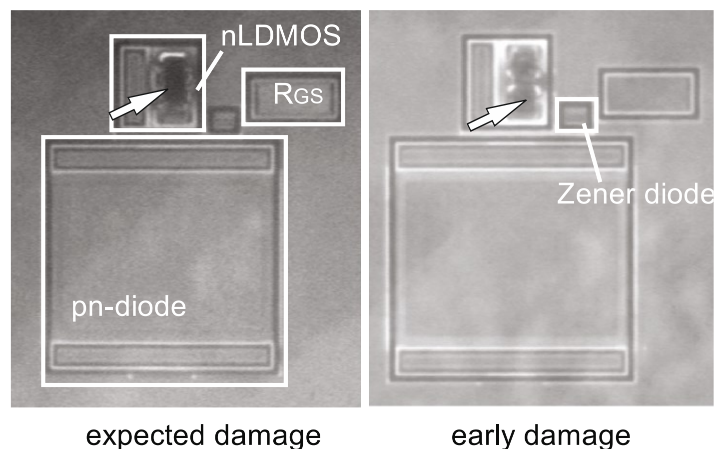

Figure 3.47: Failure analysis of (left) expected and (right) early damage in the test structure small gc-nLDMOS-pn caused by 100 ns TLP tests. Both pictures show the final result of thermal runaway in the nLDMOS.

failure of the nLDMOS is induced by the voltage overshoots of the ESD protection device. The peak voltage is larger than the trigger voltage for the parasitic bipolar transistor while the clamping voltage is not sufficiently low. As a result, the nLDMOS is damaged due to the effect of ongoing bipolar triggering at the beginning of the pulse.

Although the failures are based on quite different mechanisms, they both can be lead back to the snapback of the parasitic bipolar transistor. After the snapback, the remaining pulse delivers enough energy and finally results in a thermal destruction of the silicon due to current filaments and Joule heating. To confirm this theory, two samples stressed by TLP have been analyzed in the failure analysis, one sample with an expected and the other with an early damage in the configuration small gc-nLDMOS-pn. Figure 3.47 shows the results: the damages of both failure modes are located in the nLDMOS without any substantial difference.

In addition to the TLP characterization, standardized HBM tests have been performed to observe the HBM robustness of the pn-diode protected test structures. The studied structures are encapsulated in LQFP plastic package with 64 pins. The measurements are finished on a KeyTek ZapMaster HBM tester. In order to avoid PPV effects reported in [39] [73] [74] which can interfere with the test results, a 10 kΩ shunt resistor is connected to the HBM discharge pin and the reference ground pin.

Table 3.3 shows the test results for the four test structures. Several samples of each test structure have been HBM stressed. All structures passed at least 3.5 kV HBM level. The critical problem found in the TLP characterization with very short rise-times in sub-nanosecond range was not observed. The failure current of about 1 A shown in Figure 3.29 (b) did not agree on the lowest fail-level in the HBM tests. It is believed that parasitic capacitance in the HBM tester, test board, socket and package modulates the voltage rise-time to a relative longer range.

However, the lowest TLP failure current of the test structures without the early failures is characterized to nearly 4 A with 10 ns rise-time for the small gc-nLDMOS-pn (Figure 3.29 (b)). 4 A TLP current with pulse width of 100 ns corresponds to approximately 6 kV HBM stress-level (0.67 A per kV). The expected HBM pass-level is obviously not always obtained which can be a consequence of the early failures.

Furthermore, in the case of real world ESD discharges, e.g. from a charged person with lower capacitance in discharge path, reduction of the ESD performance due to overshoots can be more possible and significant. Further, the initial front rise (IFR) of the HBM pulse can be much shorter than 10 ns since it is given by the time needed for the voltage rising from zero volts to the breakdown voltage of protection element [75] [76]. Hence, voltage overshoots induced early damage belongs to a potential danger in this ESD protection concept according to the investigated test structures. For ESD requirements such as CDM and IEC 61000-4-2 with shorter rise-times, overshoot sensitivity of the ESD protection as shown in the case studies can lead to unpredictable performance thus must be prevented.

3.2.4 Improvement Proposals

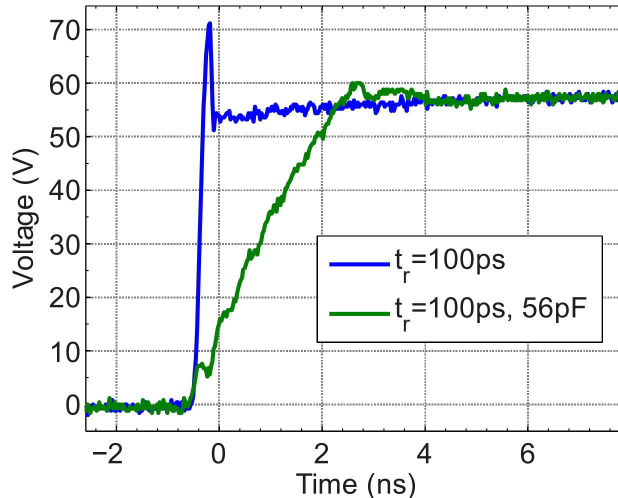

Figure 3.48: Voltage transient waveforms of the 45 V small gc-nLDMOS-pn with and without 56 pF capacitance parallel connected to the pn-diode. The TLP current is 1 A using 100 ps rise-time in the setup. The capacitor increases the rise-time for the DUT thus preventing the early damage.

The prevention of the voltage overshoot by increasing the capacitance between the discharge pins is the most straightforward solution. Wafer-level TLP measurements with additional capacitances (e.g. 56 pF for the small gc-nLDMOS-pn) connected in parallel to the test structures showed a successful suppression of the overshoots and

Table 3.3: HBM results of the 45 V ESD test structures in LQFP-64 package.

	highest pass-level	lowest fail-level
45 V small gc-nLDMOS-pn	>6 kV	5.5 kV
45 V small gg-nLDMOS-pn	>6 kV	4 kV
45 V large gc-nLDMOS-pn	>6 kV	6 kV
45 V large gg-nLDMOS-pn	>6 kV	4.5 kV

hence the prevention of the early damages. This solution equals a transformation of the ESD pulse with an RC-filter into a pulse with longer rise-time. Figure 3.48 shows the transient voltage waveforms corresponding to 1 A TLP current for the small gc-nLDMOS-pn. 100 ps rise-time is used in the TLP setup. The existence of a 56 pF capacitance has great impact on the voltage rising slopes, hence the overshoots. However, adding on-chip capacitances as an ESD protection method is area expensive and an off-chip capacitance is not always desired.

Another improvement possibility is the use of larger pn-diodes, which have higher ESD capabilities in the same voltage class. They keep the voltage drop during the ESD stress at lower levels. The larger area enables a higher possibility to find free charge carriers initializing the avalanche breakdown. A drawback of this strategy is again the reduced area efficiency. And this improvement is still not fully controllable due to statistic distribution of the avalanche breakdown.

Advanced ESD protection concepts using active clamps introduced in section 3.1.3 instead of pn-diodes are the solution which prevents the overshoot issue. Due to the

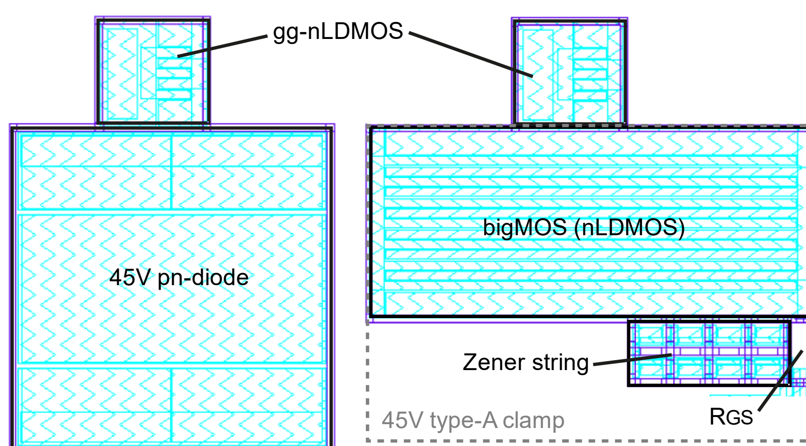

Figure 3.49: Comparison of the layout areas of the small gg-nLDMOS-pn and the small gg-nLDMOS-aca. The 45 V pn-diode and the 45 V type-A clamp occupy nearly the same area.

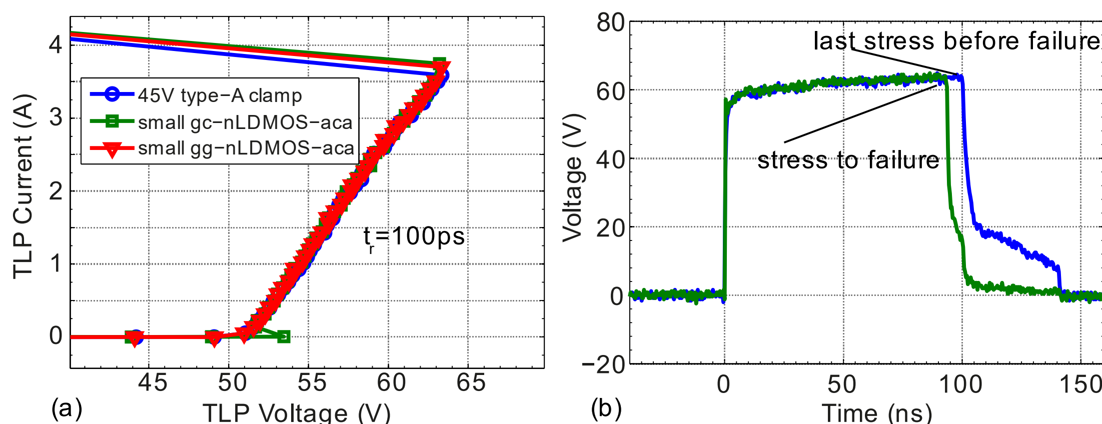

Figure 3.50: (a) TLP characteristics of the 45 V small gc-nLDMOS-aca and the 45 V small gg-nLDMOS-aca tested with the rise-time of 100 ps. The averaging window is 70 ns to 90 ns within the pulse width of 100 ns. 100 ns TLP I-V curve of the 45 V type-A active clamp as the ESD protection is also shown. (b) Voltage waveforms of the pulses causing failures of the 45 V small gg-nLDMOS-aca structure with the TLP rise-time of 100 ps showing no voltage overshoot issue.

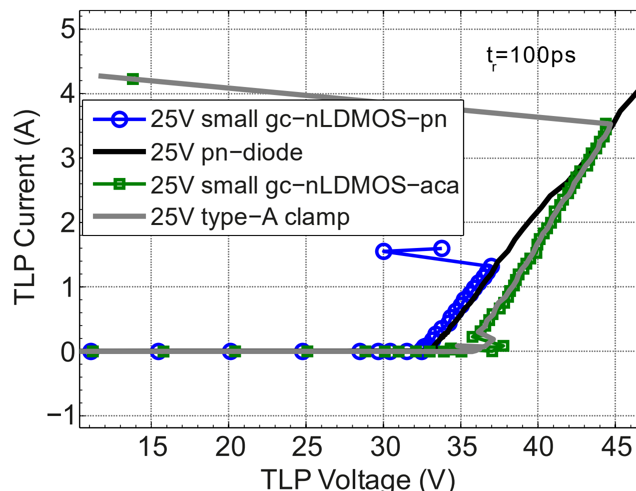

Figure 3.51: TLP characteristics of the 25 V small gc-nLDMOS-pn and the 25 V small gc-nLDMOS-aca compared to the TLP characteristics of the 25 V pn-diode and the 25 V type-A clamp, respectively. The pulse rise-time is 100 ps. The averaging window is 70 ns to 90 ns within the pulse width of 100 ns.

much faster turn-on of the channel current in large DMOS transistors, harmful voltage overshoots can hardly exist even with extremely short pulse rise-times (e.g. 100 ps). Active clamps are area efficient in higher voltage class (Figure 3.24). Figure 3.49 compares the layout footprints of the 45 V pn-diode protected small gg-nLDMOS and the type-A active clamp protected small gg-nLDMOS (small gg-nLDMOS-aca). The area consumptions of the both ESD protections are nearly the same. However, TLP measurements using 100 ps rise-time and 100 ns pulse width shows early failures of the small gg-nLDMOS-pn (Figure 3.31) while the small gg-nLDMOS-aca is not affected by the short rise-time and meets the desired TLP robustness (>3 A). Figure 3.50 depicts the TLP results where the I-V characteristic of the stand-alone 45 V type-A clamp is overlapped with the I-V characteristics of the small gg-nLDMOS-aca and the small gc-nLDMOS-aca. The failure levels of the protected test structures under TLP pulses with very short rise-time (100 ps) are determined by the active clamp. The early failures do not occur because the harmful overshoots are prevented by the active clamp.

Not only the 45 V ESD protection concepts are studied, but also the ESD protection in another voltage class is revealed. 25 V ESD protections using pn-diode and type-A clamp are verified in gc-configuration with small 25 V nLDMOS transistor as the protected device. TLP measurements show similar results compared to the 45 V test structures. At 100 ps rise-time, the 25 V pn-diode is not able to protect the small gc-nLDMOS sufficiently while the 25 V type-A clamp provides the desired TLP robustness. Figure 3.51 shows the TLP I-V curves of the stand-alone ESD protection elements and of their protected small gc-nLDMOS structures.

As a result, active clamps prevent the harmful voltage overshoots thus effectively protect the drain-source of nLDMOS transistor. They can be used as the robust ESD protections against the investigated unique failure mode as well as the ongoing bipolar triggering of nLDMOS.

3.2.5 Summary

Based on the evaluation of the failure levels and failure modes of the ESD devices given in the previous section, this section presents case studies verifying the ESD protection by using monitor structures protected by the ESD protection devices and structures. It is expected that the use of the high voltage npn-BJT with limited turn-on speed is critical to protect the monitor structures against ESD pulses with fast transient voltage rises. Surprisingly the pn-diodes are also not able to provide reliable ESD protection in case of extremely short rise-time of pulses and the voltage overshoots. The overshoot is caused by the finite reaction time of the avalanche breakdown diode which is already very short (<200 ps). The protected nLDMOS structures are still damaged because of the triggering of the inherent parasitic bipolar transistor. The triggering of the bipolar transistor into the snapback mode results in a significant degradation of the ESD protection's effectiveness.

Although the duration of the voltage overshoots at the pn-diodes are much shorter than the time for bipolar triggering in the nLDMOS transistor, the overshoots can still induce a unique effect so-called the ongoing bipolar triggering in the nLDMOS transistor. TCAD simulation is carried out for the detailed analysis of the effect. Rise-time (dV/dt or dI/dt) does not affect the bipolar triggering in the nLDMOS transistor directly but can certainly impact on voltage overshoots. Development of overshoot-free ESD protection devices insensitive to rise-time effects for example the active clamps is gaining more interest in order to eliminate early damages.

3.3 Novel On-Chip Statically Triggered Active Clamps

In the previous sections, active clamps show high area efficiency and high protection effectiveness, gaining a lot of attentions. In fact, as a type of the major ESD protection structures, active clamps especially the type-A clamps have been used for many years in the field of high voltage ESD protection. This section presents advanced and innovative trigger circuits in different types of active clamps which involve circuit-level ESD design and enable diverse new features. The active clamps are proven to be a very

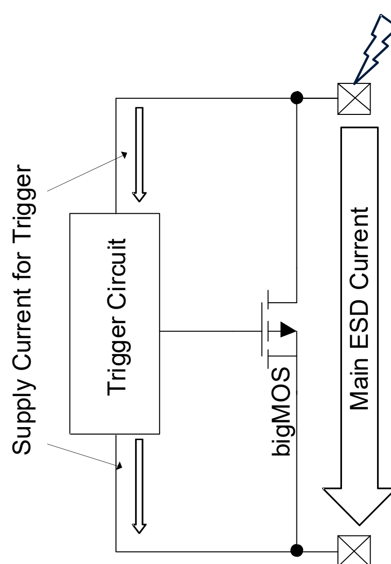

Figure 3.52: Schematic diagram of the high voltage active ESD clamp.

fast triggered ESD solution. Furthermore, considering flexibility, cost of development, voltage class and other factors, design of active clamps is more beneficial and even necessary as they belong to circuit-level instead of device-level ESD design.

RC-triggered ESD clamps for example as on-chip ESD protection are commonly used in CMOS technologies [50] [52]. Also in the field of high voltage (HV) ESD protection, transiently triggered active ESD clamps have been developed using various circuit topologies [77] [78]. The dynamic trigger circuit design however faces major challenges [58] [79] [80] [81]. It must prevent false triggering regarding slew rate detection. Also time-out control must be considered. In the high voltage applications especially for automotive products, numerous disturbances in the form of fast transient pulses can occur in the field. False triggering of ESD elements due to disturbances can even lead to critical safety issues with high severity. Avoiding such problems, this section focuses on statically triggered active ESD clamps which are turned on only if a designed trigger voltage V_{tr} is exceeded [82] [83]. Such active clamps can be designed more sophisticatedly with an improved trigger circuit. Many advantages like smaller ESD on-resistance R_{on} per area, larger failure current I_f and further advanced features for ESD applications with limited ESD windows can be realized by designing more complex trigger circuits. The development of such active high voltage ESD clamps with advanced trigger circuits is of essential importance. In this section, several types of high voltage active ESD clamps and their benefits are shown. The use of simple but effective triggering techniques allows a small area of the trigger circuit compared to the switch transistor (bigMOS as described in 3.1.3). The new types of active ESD clamps using the same size of the bigMOS demand less ESD design window and provide higher ESD robustness. Of course, the higher ESD robustness can be exchanged for lower area consumption in typical ESD applications.

3.3.1 Studied Active ESD Clamps

Figure 3.52 shows the basic idea of the ESD protection circuits using area efficient n-type bigMOS transistors. The active clamps differ mostly in their trigger circuits which define the trigger condition of the clamps. The bigMOS conducts the main ESD current.

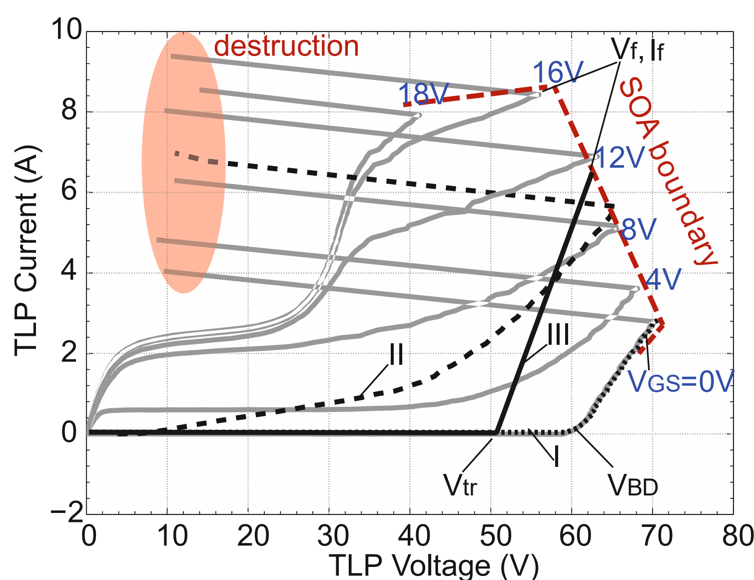

Figure 3.53: SOA characteristic of an nDMOS at different gate voltages. I indicates the grounded gate case (ggNMOS), II the floating gate case and III the actively controlled gate case.

Only a small amount of the current supplies the trigger circuit for the control of the bigMOS gate. The details of the trigger circuits and the bigMOS are outlined in the following subsections.

3.3.1.1 Safe Operating Area (SOA)

SOA and its meaning has been briefly introduced in 3.1.3.1. This section focuses more on the advanced active clamps which are essentially based on the utilization of SOA. Hence a more comprehensive understanding of SOA is required. Figure 3.53 shows the I-V characteristics of an n-type DMOS (nDMOS) at different gate-source voltages (SOA characteristic) from 100 ns TLP measurements. From the SOA characteristic, one can deduce the behavior of the power MOS transistor in three fundamental ESD protection configurations.

In the first configuration, gate and source of the nDMOS are shorted. Significant ESD current flows only after the avalanche breakdown has occurred at V_{BD} (curve I).

In the second configuration, the gate terminal is left floating. The gate-source voltage is defined by the inherent capacitive coupling [59]. Curve II shows the resulting pulsed I-V characteristic. This configuration reflects also the category of dynamically triggered active clamps. I-V curves of the dynamically triggered clamps can certainly differ from curve II in case of additional RC-based trigger circuits.

In the third configuration, the active clamp is statically triggered at V_{tr}. Curve III qualitatively displays a corresponding I-V characteristic. This configuration is the main focus of this section. The absolute current capability of the active clamp depends on the maximum allowed current given by the SOA. The trigger voltage V_{tr} of the active clamp and the voltage drop across the active clamp are not allowed to be larger than the trigger voltage of the inherent bipolar transistor. The voltage and current at the onset of the snapback are considered as the failure voltage V_f and failure current I_f, respectively. For the design of an active clamp, V_{GS} needs to be controlled and optimized for the

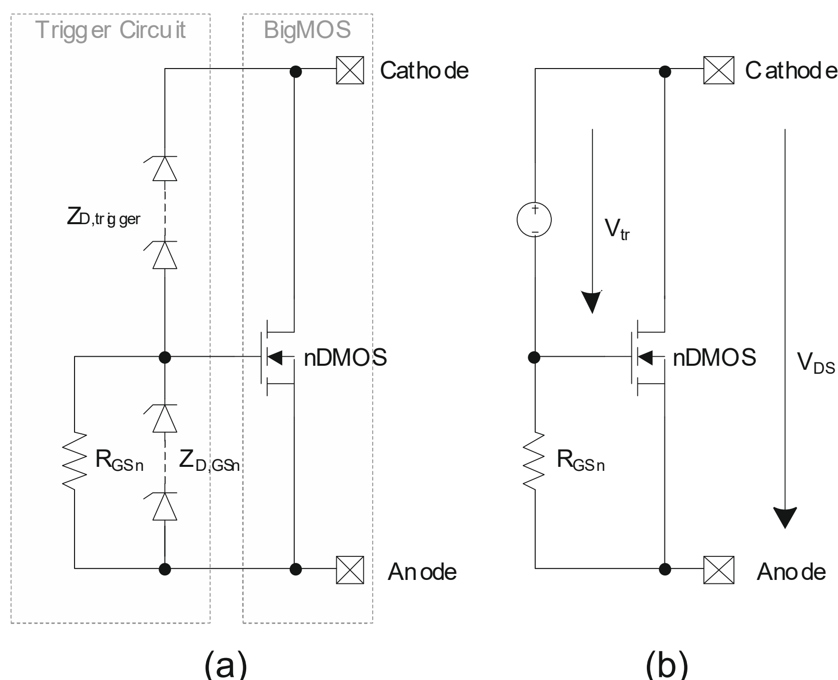

Figure 3.54: (a) Schematic view and (b) simplified equivalent circuit of the type-A active ESD clamp.

ideal utilization of the bigMOS, i.e. for reaching the maximal failing current $I_{f,max}$. In this particular example, V_{GS} between 16 V and 18 V grants the maximal failing current. Major efforts have been spent to the design of the trigger circuit based on these considerations.

3.3.1.2 Type-A Clamp

The state-of-the-art statically triggered active clamp has been introduced in section 3.1.3. This clamp including the trigger circuit is depicted in Figure 3.54 (a) again which is similar to the schematic shown in Figure 3.10. The type-A clamp comprises two circuit parts according to the basic idea in Figure 3.52. The bigMOS transistor, usually an nDMOS in power technologies, serves as the protective device in the circuit conducting the ESD current from cathode to anode. The cathode and anode indicate both terminals of the active clamp. They are also the two terminals of the inherent body diode (bulk-drain pn-diode) of the source-bulk shorted nDMOS transistor. The trigger circuit aims to control V_{GS} of the nDMOS. The Zener string $Z_{D,trigger}$ defines V_{tr} at which the active clamp is switched to conducting or non-conducting state. The Zener protection $Z_{D,GSn}$ prevents the overdriving of the nDMOS. The bias resistor R_{GSn} provides a defined gate-source discharge time constant for $V_{DS} < V_{tr}$, and on the other hand maintains the designed gate-source voltage if the active clamp is in conducting state. Note that in general the Zener string can consist of forward biased diodes and reverse biased Zener diodes in order to achieve the desired total breakdown voltage of the string (V_{tr}) in 0.7 V steps – the forward voltage at room temperature. Also the gate-source voltage can be limited in this type of Zener string.

The type-A active clamp works well in many cases as shown in the previous sections. However the achievable lowest R_{on} of the type-A circuit depends mainly on the size of the nDMOS. Figure 3.54 (b) depicts the ideal behavior of the type-A clamp by neglecting the resistance of the Zener diodes when conducting current. V_{tr} is therefore constant under this assumption. The nDMOS works in the ESD case with approximately a linear large-signal gain G_m in the transistor saturation region. It is

$$\Delta V_{DS} = \Delta(V_{DS} - V_{tr}) = \Delta V_{GS} = \Delta(V_{GS} - V_{th}), \quad 3.8$$

where V_{th} as a constant is the threshold voltage of the nDMOS. The R_{on} of the type-A clamp is then calculated by

$$R_{on} = \frac{\Delta V_{DS}}{\Delta I_{DS}} = \frac{\Delta V_{DS}}{\Delta(V_{GS} - V_{th}) \cdot G_m} = \frac{1}{G_m}. \quad 3.9$$

G_m depends only on the nDMOS size which determines the R_{on} of the type-A clamp. It implies that at the failing point given by the SOA (Figure 3.53), V_{GS} of the nDMOS cannot be larger than (V_f-V_{tr}). Depending on the DMOS SOA and the desired V_{tr}, the optimal V_{GS} may not be reachable with a type-A clamp.

3.3.1.3 Type-B Clamp

To improve the V_{GS} control, an amplification stage is implemented in the type-B active clamp which is schematically shown in Figure 3.55 (a). Compared to the type-A clamp, the trigger circuitry of the type-B clamp employs again a Zener string as the trigger voltage definition but a p-type DMOS transistor (pDMOS) as the current source driving the nDMOS during the ESD stress. Optional Zener protection diodes $Z_{D,GSn}$ and $Z_{D,GSp}$ protect the nDMOS and pDMOS transistors from overvoltage at the gate.

Compared to the type-A clamp, V_{GS} of the nDMOS can be biased higher due to the large-signal amplification of the pDMOS with the load R_{GSn}. R_{on} of the type-B clamp can be again calculated based on the ideal assumptions (Figure 3.55 (b)) similar as in the type-A clamp. With the conditions

$$\Delta V_{DSn} = \Delta(V_{DSn} - V_{tr}) = \Delta V_{GSp}, \quad 3.10$$

$$\begin{aligned}\Delta(V_{GSn} - V_{thn}) = \Delta V_{GSn} &= \Delta I_{DSp} \cdot R_{GSn} \\ &= \Delta V_{GSp} \cdot G_{mp} \cdot R_{GSn},\end{aligned} \quad 3.11$$

the R_{on} of the type-B clamp is given by

$$\begin{aligned}R_{on} = \frac{\Delta V_{DSn}}{\Delta I_{DSn}} &= \frac{\Delta V_{DSn}}{\Delta(V_{GSn} - V_{thn}) \cdot G_{mn}} \\ &= \frac{1}{G_{mp} G_{mn} R_{GSn}}.\end{aligned} \quad 3.12$$

For $G_{mp} \cdot R_{GSn} > 1$, smaller R_{on} can be obtained in the type-B clamp compared to the type-A clamp while using the same size of the nDMOS, which is dominating the total layout area of the active clamp. As long as V_f of the nDMOS at optimal V_{GS} is larger than V_{tr}, a type-B clamp can be designed to maximally utilize the current capability of the used nDMOS. Hence, a most area efficient ESD design can be achieved.

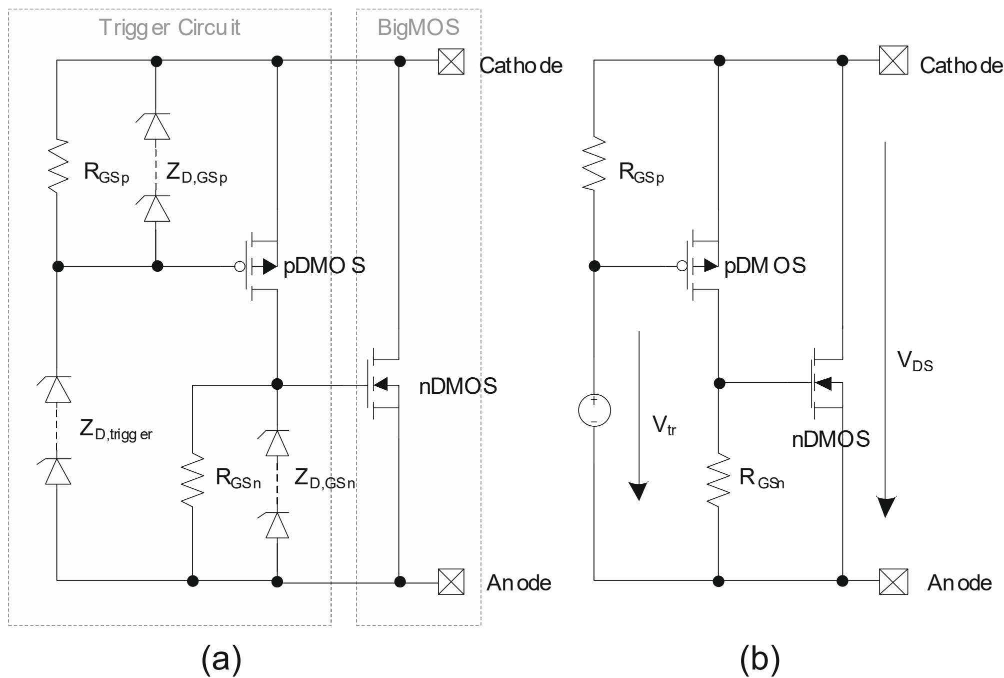

Figure 3.55: (a) Schematic view and (b) simplified equivalent circuit of the type-B active ESD clamp.

3.3.1.4 Type-C Clamp

Even using very large amplification with the type-B clamp, the optimal V_{GS} cannot be obtained if V_{tr} is larger than V_f for $I_{f,max}$. $I_{f,max}$ describes the maximal achievable failure current for the given nDMOS. For example in Figure 3.53, if $V_{tr} = 60\ V$, I_f at $V_{GS} = 16\ V$ can never be reached with a positive R_{on}. Fortunately, with proper circuit design of the active clamp, one can implement a solution for example with the type-C trigger circuit (Figure 3.56 (a)).

The type-C clamp works in the same way as the type-B clamp while the nDMOS2 keeps turned-off in so-called non-snapback mode. The type-C clamp triggers and conducts current at V_{tr} with the same R_{on} as described in 3.12 under ideal conditions. Once the threshold voltage of the shorting transistor nDMOS2 is reached, a part of $Z_{D,trigger}$ with break down voltage V_{short} is bypassed. The nDMOS2 operates in its linear region and acts as a resistor conducting several mA current. The bigMOS nDMOS is then forced to jump to another operating point and shows a snapback behavior in its quasi-static I-V. Once the snapback mode is established, the R_{on} of the clamp remains nearly unchanged because the resistance of the nDMOS2 is much smaller than R_{GSp} thus can be neglected (Figure 3.56 (b)). The remaining part of $Z_{D,trigger}$ with break down voltage V_{remain} and the drain-source voltage of nDMOS2 V_{DS2} define the holding voltage V_h of the clamp,

$$V_h = V_{tr} - V_{short} + V_{DS2} = V_{remain} + V_{DS2}. \qquad 3.13$$

Note that the voltage divider consisting of R_{GSn1} and R_{GSn2} controls the onset of the snapback depending on the threshold voltage of the nDMOS2. Hence, trigger current and voltage of the snapback are circuit design parameters. An appropriate setting of these design parameters prevents false-triggering in order to fulfill certain EOS or EMC requirements.

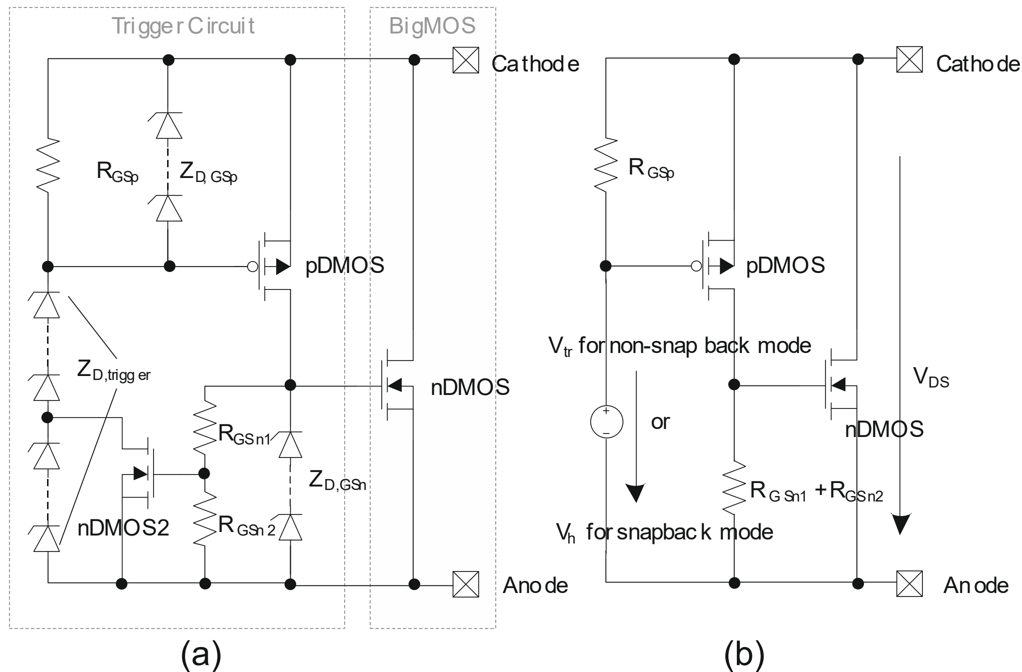

Figure 3.56: (a) Schematic view and (b) simplified equivalent circuit of the type-C active ESD clamp. In the non-snapback mode, the Zener string clamps at V_{tr}. In the snapback mode, V_h is the clamping voltage given by the voltage definition circuit consisting of Zener string and the nLDMOS2 transistor.

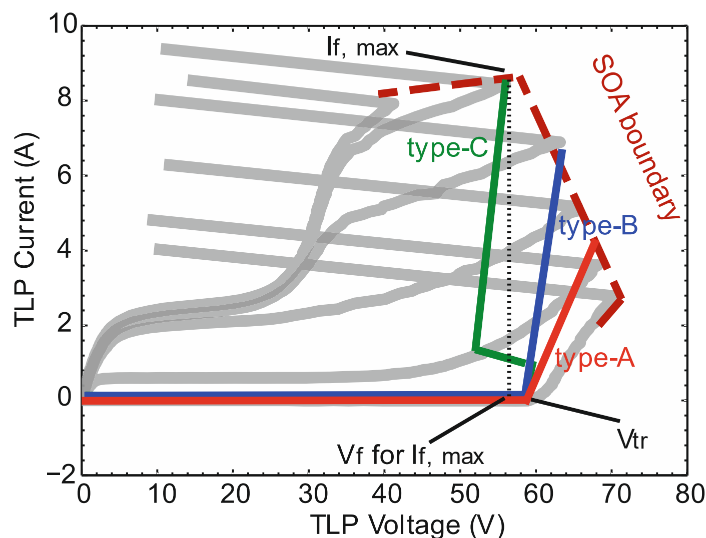

Figure 3.57: Qualitative comparison of the type-A, type-B and type-C active ESD clamps.

The prevention of the snapback during non-ESD pulses does not aim to protect the clamp from destruction but to avoid disturbance of the functional signals. Without involving any bipolar snapback mechanism, the clamp will not encounter the problems a bipolar snapback device usually deals with, such as current filaments, voltage overshoots etc. [64] [80].

The essential benefits of the type-C clamp are the low ESD window consumption (even V_f<V_{tr} is possible) as well as the maximal utilization of the nDMOS SOA. A qualitative comparison between type-A, type-B and type-C clamps are depicted in Figure 3.57.

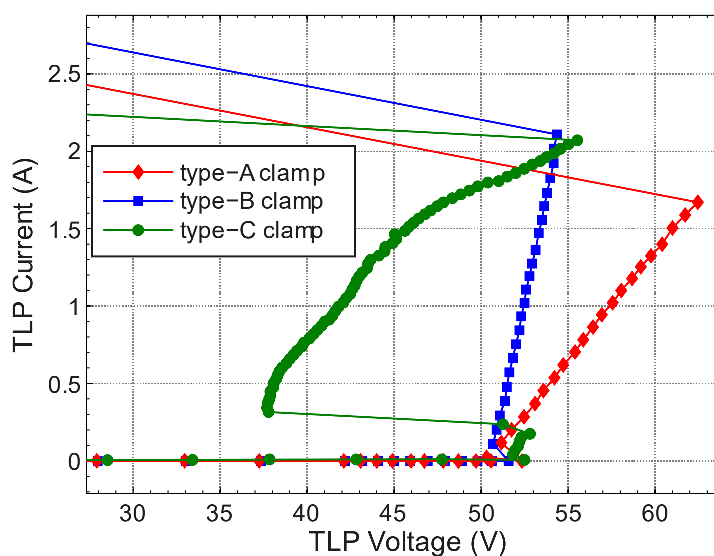

Figure 3.58: TLP characteristics of type-A, type-B and type-C clamps implemented with the same trigger voltage and with a comparable size of the nDMOS.

3.3.2 Measurement and Simulation

3.3.2.1 TLP Investigation

All three clamp types have been implemented on silicon and have been measured with standard 100 ns TLP using 10 ns rise-time (Figure 3.58). The experimental curves of the three clamps show the expected behavior regarding on-resistance and snap-back behavior (two Zener diodes shorted). A different nDMOS type has been used in the type-C clamp compared to the type-A and type-B clamps and hence a detailed comparison is not straightforward.

SPICE simulation is very useful to study and design the active clamps because it gives access to all circuit nodes. For example, the gate voltages are usually not measurable but are available in simulation. Also, depending on the model quality simulation enables more accurate design.

Figure 3.59 (a) displays the simulated quasi-static current I_{CA} (cathode to anode) through and voltage V_{CA} across the active clamps (all with the same nDMOS). The simulation results are qualitatively in good and quantitatively in acceptable agreement with the measurement results. In addition, Figure 3.59 (b) shows the quasi-static nDMOS gate-source voltages as a function of the voltage across the clamps.

All three clamps show a turn-on voltage of about 50 V due to the identical Zener diode string. The type-A clamp exhibits the highest on-resistance as expected. The gate-source voltage rises nearly linearly with the drain-source voltage of the nDMOS. The slope is ~0.8 accounting for the finite resistance of the Zener diodes. For a type-A clamp

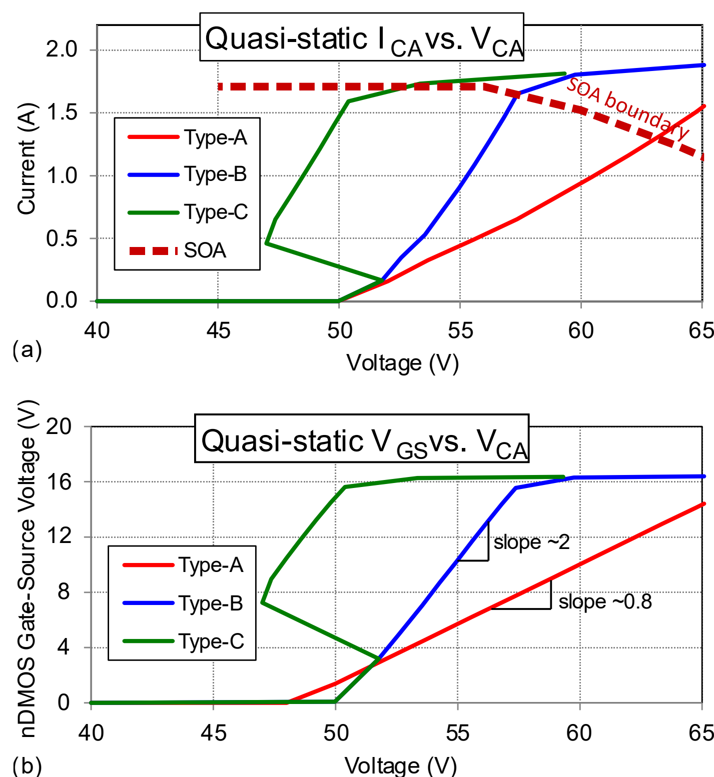

Figure 3.59: For the active clamps of type-A, type-B and type-C, simulated quasi-static (a) I-V curves and (b) nDMOS gate-source voltages as a function of the voltage across the clamps. The quasi-static values of voltages and currents are calculated by averaging the100 ns long TLP-like transient curves between 70 and 90 ns.

with an ideal Zener string (with zero resistance), the increase of the gate-source voltage equals the increase of the drain-source voltage (i.e. the slope is 1).

The type-B clamp has an improved on-resistance. Again, the gate-source voltage rises linearly with the drain-source voltage but the slope is ~2 showing the beneficial amplification due to the pDMOS.

The type-C clamp shows the expected snapback behavior (one Zener diode shorted in the simulation). The same resistance has been chosen for R_{GSn1} and R_{GSn2} in the simulation leading to a snapback trigger current of 200 mA. The type-C clamp shows roughly the same on-resistance than the type-B clamp in the current range above the snapback due to the identical pDMOS transistor and R_{GSn}. But the operation point is different due to the shorting of one Zener diode. Thus the voltage drop across the clamp is significantly reduced.

The type-B and type-C clamps show a distinct kink in their I-V at about 1.6 A. It is caused by the two Zener diodes between gate and source of the nDMOS. They turn on at this point and limit the gate-source voltage. While protecting the gate oxide of the transistor, the Zener diodes do not significantly reduce the protection capability of the clamps because the SOA boundary of the nDMOS transistor is also close to this point. In fact, the gate-source voltage limit is just another design parameter allowing to head for the optimal V_f and I_f values.

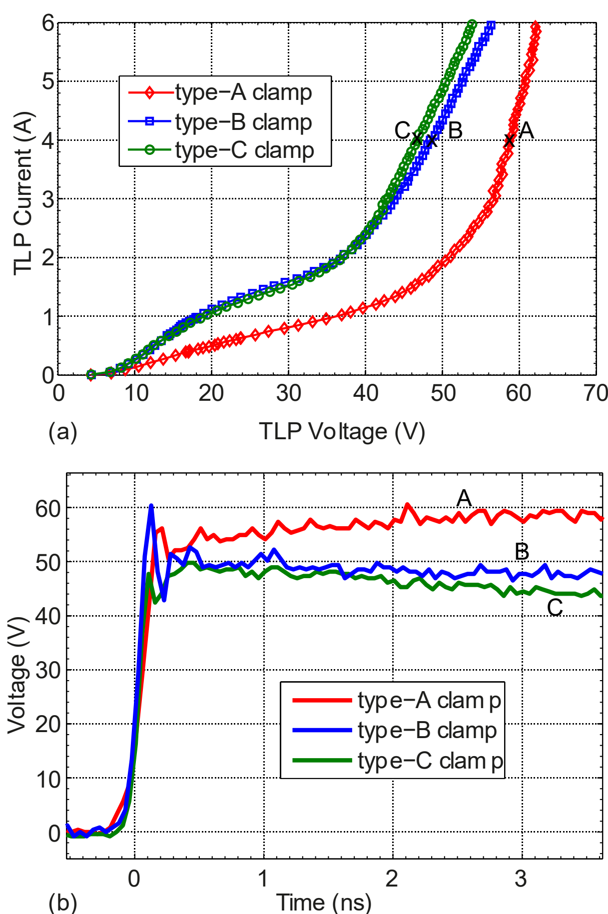

Figure 3.60: (a) TLP characteristics of type-A, type-B and type-C clamps using an average window between 1 ns and 3 ns, and a rise-time of 100 ps (b) Three transient voltage waveforms exhibit the turn-on behavior of type-A, type-B and type-C clamps at 4 A TLP current.

The measurement data and simulation show the strong improvement in the ESD window of the advanced active clamps: it drops from 13 V for the type-A clamp, over 7 V for type-B clamp to 3 V for type-C clamp in the simulation.

In addition, TLP is also applied to study the clamping behavior of the active clamps under CDM-like conditions. Thereto, the rise-time is set to 100 ps and the average window is chosen between 1 ns and 3 ns showing the peak voltage as function of TLP current. Figure 3.60 shows the TLP characteristics of type-A, type-B and type-C clamps with the bigMOS nDMOS transistor about 4 times larger than the nDMOS used in Figure 3.58. Figure 3.60 (b) shows the voltage transient waveforms as well as the turn-on of the three clamps at 4 A TLP current indicated by A, B and C.

In the CDM time domain (a few nanoseconds) the dynamic gate coupling due to parasitic capacitance plays a dominant role. Without pDMOS amplification stage, the type-A clamp has the lowest gate coupling and therefore the highest clamping voltage. The type-B and type-C clamps using the same pDMOS amplification exhibit the same I-V up to about 40 V. Above 40 V the type-C clamp shows even lower clamping voltage because the shorting transistor delivers more current into the Zener string and R_{GSp}, hence drives the pDMOS stronger. As a conclusion, this TLP investigation clearly indicates that active clamps also provide effective protection against CDM stresses.

3.3.2.2 HBM Investigation

Active clamps without any further protected circuitry have been stressed according to the HBM standard [85] to show their intrinsic ESD hardness. Figure 3.61 summarizes the HBM pass-levels compared to the TLP failure currents of various active clamps. In the HBM tests, the devices are zapped from 2 kV in 0.5 kV steps until failure occurs or until the tester limit of 12 kV is reached. All clamps which pass 12 kV HBM have not been damaged. In the TLP tests, 100 ps rise-time and 100 ns pulse width are used. The devices are assembled in the plastic package MQFP-44 for both types of measurements.

The clamps are realized with different nDMOS sizes hence different layout areas targeting on different HBM pass levels accordingly. The size of the nDMOS transistor

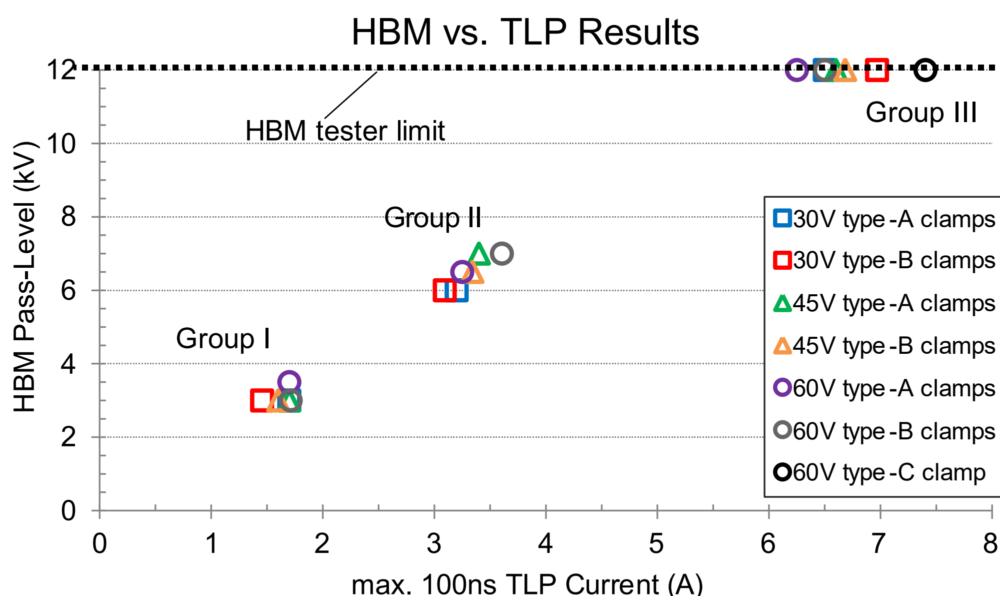

Figure 3.61: Type-A, type-B and type-C clamps stressed with TLP and Thermo Fischer MK2 HBM tester.

in the active clamps is doubled from group I to group II as well as from group II to group III. The HBM and TLP robustness clearly scales with the device size.

In each group, type-A and type-B clamps for 30 V, 45 V and 60 V voltage classes are tested. One 60 V type-C clamp is also included in group III. Within the same group and for the same voltage class, the type-B clamp is implemented with a smaller nDMOS compared to the type-A clamp. For example in group II, the layout footprint of the 45 V type-B clamp is about 20% smaller than the 45 V type-A clamp, yet shows comparable HBM and TLP hardness. The 60 V type-C clamp shares the same nDMOS size as the 60 V type-B clamp but the ESD robustness is higher according to the TLP results. These findings confirm the performance improvement of the type-C clamp compared to the type-B clamp, as of the type-B clamp compared to the type-A clamp. Among all the three types, the type-C clamp ensures the best utilization of the bigMOS SOA hence achieves the highest ESD robustness by itself.

In addition to the measurements, the response of the active clamps to a 2 kV HBM stress has been investigated using SPICE simulation as in the TLP investigation. Besides the insight into the differences between the three clamp types, HBM SPICE simulation is interesting because of the steep voltage rise at the beginning of the HBM pulse, and because of the exponential pulse decay over some 100 ns. Hence HBM reveals possible weaknesses of ESD clamps regarding turn-on (e.g. voltage overshoots) as well as turn-off issues (e.g. time-out in RC-triggered clamps).

Figure 3.63 shows the voltages across the clamps V_{CA}, the currents through the clamps I_{CA} and the nDMOS gate-source voltages as a function of time in logarithmic scale. The maximal clamping voltage of the type-C clamp is the lowest among the three clamps (Figure 3.63 (a)). No significant voltage overshoots are visible. The current waveforms are typical for 2 kV HBM stresses. The different voltage response of the three clamps together with the parasitic elements (e.g. cable inductance and test board capacitance modeled in the HBM source) result in slight differences in the current waveforms (Figure 3.63 (b)). In the type-C clamp, one Zener diode is shorted. Hence, the Zener diode string in the type-C clamp delivers more current than in the type-B clamp. The nDMOS gate is boosted to a higher voltage at about 10 ns (Figure 3.63 (c)) resulting in an enhanced clamping (Figure 3.63 (a)). The enhanced clamping of the type-C clamp

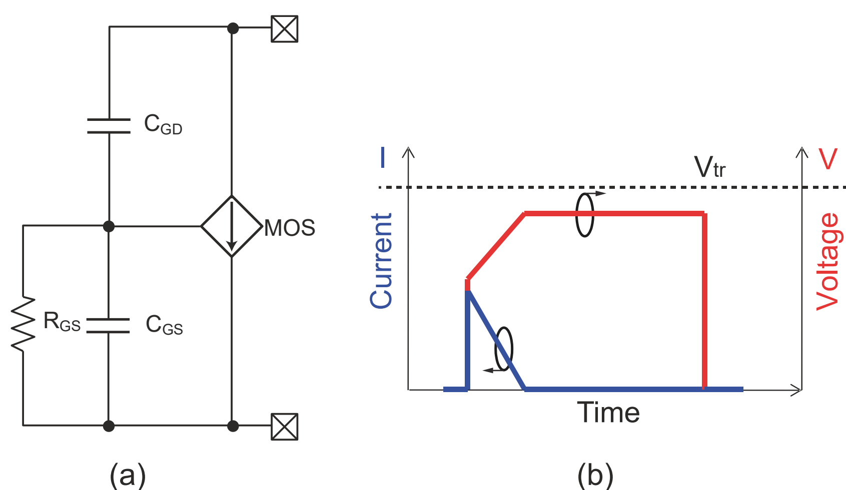

Figure 3.62: (a) Schematic of the simplified active clamp with gate discharge resistor R_{GS} and the parasitic gate capacitors C_{GD} and C_{GS}. (b) Transient turn-on of the DMOS due to capacitive gate coupling showing typical I/V waveforms when the stress voltage is below the designed V_{tr}.

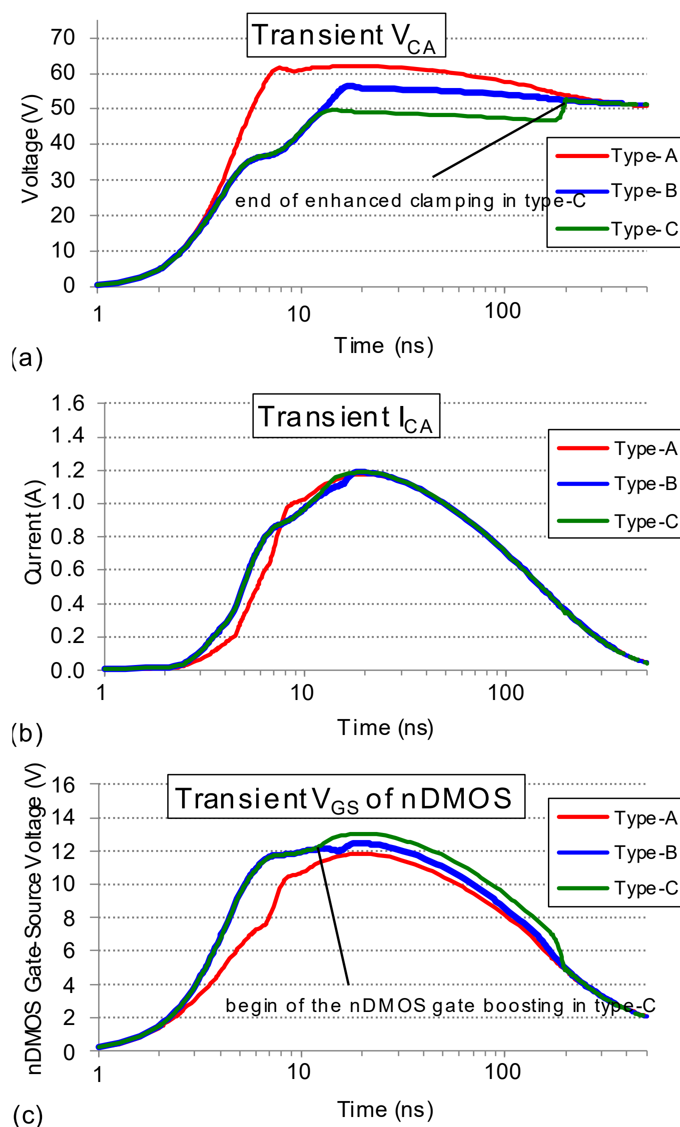

Figure 3.63: Simulated transient response of the active clamps of type-A, type-B and type-C to a 2 kV HBM stress. The individual pictures show (a) the voltage across the clamps, (b) the currents through the clamps and (c) the nDMOS gate-source voltages as a function of time in logarithmic scale.

ends around 180 ns when the gate-source voltage of the nDMOS2 drops to the threshold voltage. Nevertheless, the shorting transistor nDMOS2 has fulfilled its purpose and reduced the maximum voltage drop across the type-C clamp by approximately 4 V compared to the type-B clamp.

It is apparent from these simulation results that the active clamps do not show any turn-on delay. The simulation verifies in addition that the presented active clamps also do not suffer from any turn-off issues. During the exponential pulse decay, the Zener diode string ensures a turn-on of the active clamps if the voltage drop across the clamp is larger than the static trigger voltage. In the HBM simulation, the advantage of the type-C clamp with the lowest clamping voltage is clearly shown. The required ESD window is therefore smallest for the circuits protected by the type-C active clamp.

3.3.3 Discussion

3.3.3.1 Capacitive Coupling Effects

All active clamps and in general the switch based ESD protections encounter parasitic capacitive coupling effects. The bigMOS conducts current for a certain time period under normal operation due to fast switching. Also for the statically triggered active clamps, the transient turn-on of the nDMOS due to the capacitive gate coupling leads to significant current flow as exemplarily depicted in Figure 3.62 for a rectangular pulse. This behavior is preferred for ESD performance as shown in Figure 3.63. It might however limit the usage of active clamps for I/O or supply protection with functional steep voltage rise requirements or severe EMC specifications.

The impact of the capacitive coupling effect is reduced by shortening the gate discharge time. For the studied active clamps, the gate discharge time constant is a function of the parasitic MOS capacitance and the gate-source resistance R_{GS}. Adding additional capacitance in parallel with C_{GS} to change the capacitive divider would be an expensive solution. The straightforward solution is the reduction of R_{GS}.

This however affects directly the R_{on} during ESD as the resistance of the Zener string is not negligible. As a countermeasure, a larger pDMOS can be employed in the type-B clamp to compensate the effect of the small R_{GSn}. According to 3.12, the same R_{on} is achieved if

$$G_{mp}' \cdot R_{GSn}' = G_{mp} \cdot R_{GSn}. \qquad 3.14$$

R_{GSn}’ and G_{mp}’ describe the reduced R_{GSn} and enlarged pDMOS, respectively. However, the pDMOS also has the capacitive gate coupling effect delivering increased current to R_{GSn} at steep voltage rise. Therefore only increasing pDMOS size is not efficient enough to overcome the capacitive gate coupling without affecting R_{on}.

A more advanced solution applies the two-stage amplification as displayed in Figure 3.64. It shows a two-stage type-B clamp (named type-B2 clamp). The nDMOS3 of the second stage boosts V_{GSp} and hence the drain current of the pDMOS. With similar assumptions as used in 3.12,

$$R_{on} = \frac{1}{G_{mn3} G_{mp} G_{mn} R_{GSp} R_{GSn}}. \qquad 3.15$$

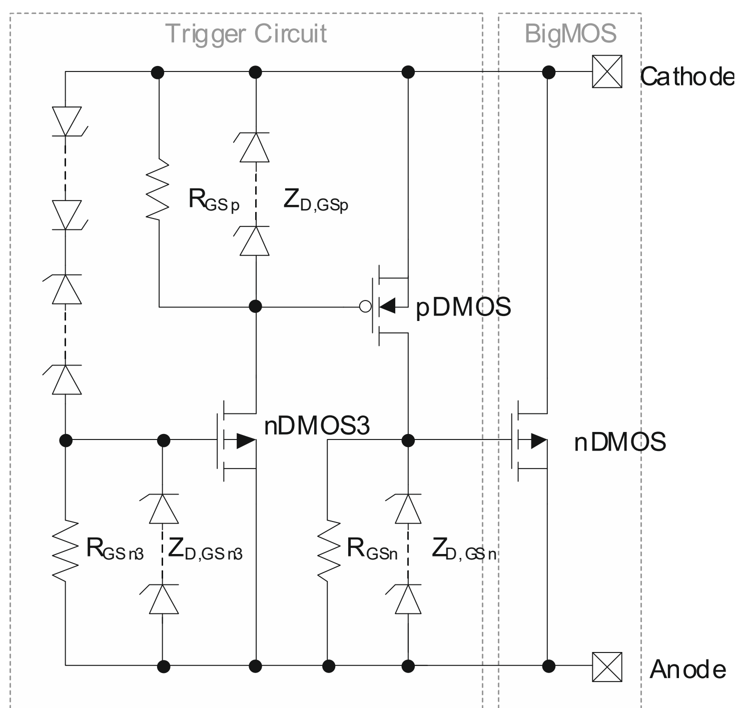

Figure 3.64: Schematic view of the type-B2 active ESD clamp with two-stage amplification and small R_{GSn}.

The terms G_{mn3} and R_{GSp} increase the amplification further and allow an even smaller R_{GSn}

Figure 3.65 gives an example, which shows the reduction of the gate-coupling effect in the active clamps by using the type-B2 clamp. The 45 V pn-diode with a layout area comparable to the active clamps is given as the reference device, which does not suffer from the gate coupling effect. All the active clamps are designed with the same nDMOS and with the same Zener string. The type-B clamp employs the same R_{GSn} as the type-

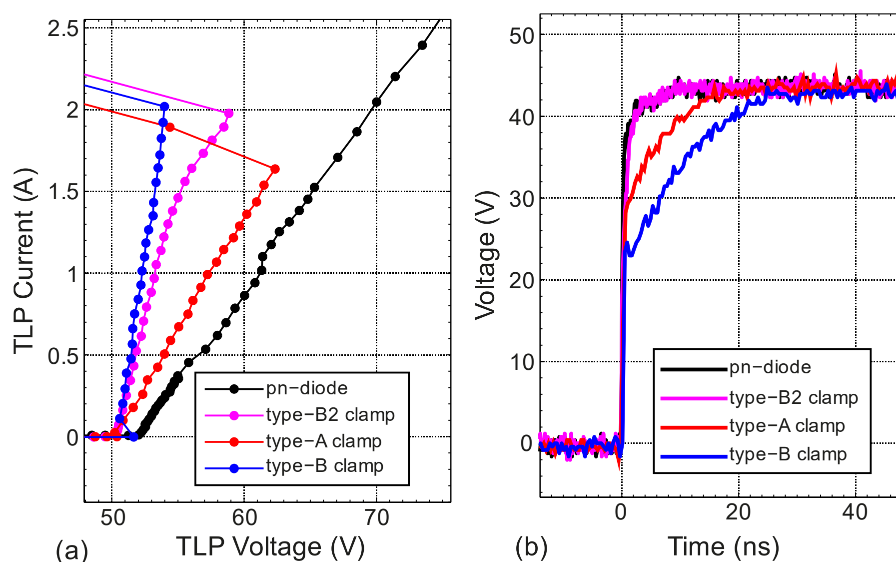

Figure 3.65: (a) 100 ns TLP I-V characteristics of 45 V active clamps and a pn-diode. (b) The transient voltage waveforms of the active clamps and a pn-diode at 43 V pulse voltage which is below the designed V_{tr}. The rise-time of the TLP is 100 ps.

A clamp. The gate coupling is more pronounced in the type-B clamp compared to the type-A clamp since the pDMOS boosts the gate-source voltage of the nDMOS (Figure 3.65 (b)). The type-B2 clamp uses a much smaller R_{GSn}. The gate-coupling becomes much less conspicuous. The ESD performance of the type-B2 clamp remains comparable to the type-B clamp since the optimal I_f is reached (Figure 3.65 (a)).

A similar two-stage type-C clamp is also feasible applying this technique.

3.3.3.2 ESD Window Considerations

From an ESD design window point of view [86], the proposed advanced active clamps allow improved design flexibility. The upper ESD limit is typically the minimum failing voltage of the protected devices. It is for example the maximal allowed drain-source voltage of a power transistor in many applications. By applying the same transistor type for the nDMOS and the protected power MOS, the protection is easily established with minor concern of process variations. Due to the SOA and improved control of V_{GS}, the failing voltage of the active clamp type-B or type-C can be designed smaller than that of the protected transistor so that the protected transistor is safe with the target ESD robustness granted by the active clamps.

The advanced trigger circuit can be combined with the functional circuit if the power transistor is already sufficiently large, e.g. a large driver. Moreover, regarding a rail clamp ESD concept, an advanced active clamp is preferred as the central clamp. The bus resistance depending on the interconnection length between the central clamp and the protected devices becomes an important constraint for the ESD design. The voltage drop across the forward ESD diode and the interconnection resistance must also be taken into account. These constraints can be relaxed with the reduced ESD window need of the type-B or type-C clamps. Figure 3.66 shows a test structure example. Both of the type-A and type-B clamps can effectively protect the small ggNMOS M2 with a

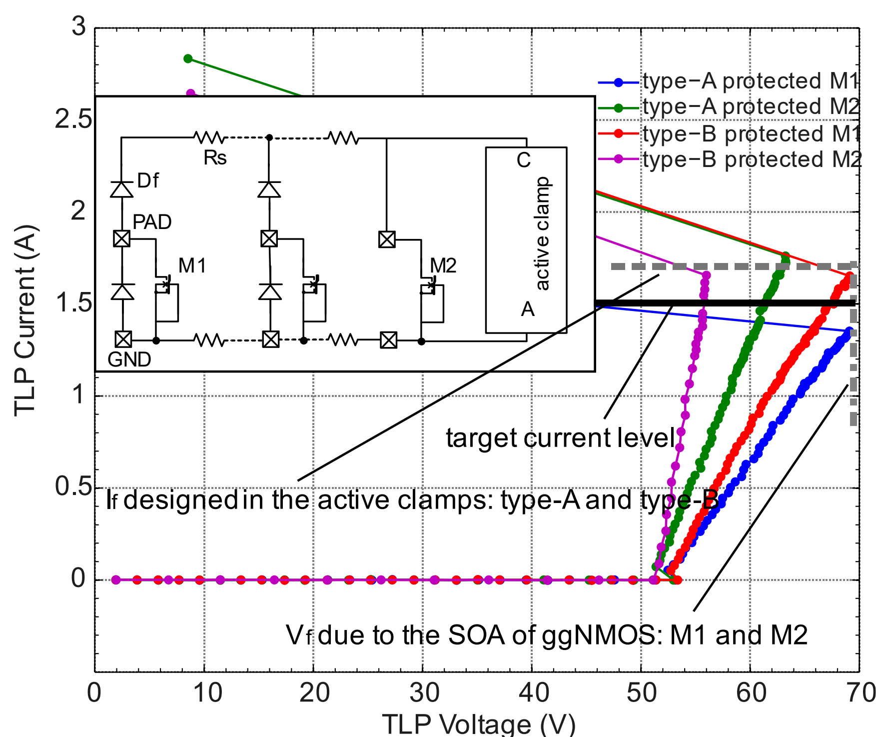

Figure 3.66: Example of a rail clamp ESD concept and the measurement results from 100 ns TLP.

low bus resistance as shown in the TLP characterization. In this case, the active clamps are destroyed above the target because the designed failing current levels of the active clamps are reached. In the case of a larger bus resistance R_s and involved forward diodes D_f, the type-A clamp cannot effectively protect M1. Despite the type-A clamp, the protected device fails since the SOA limit of M1 is violated. On the contrary, with the type-B clamp, the designed failure level is reached due to the lower consumption of the ESD window.

With the type-C clamp, even larger R_s and smaller D_f are allowed in the ESD protection concept due to the smaller clamping voltage. The use of the advanced clamps results in significant improvement of the ESD area consumption in applications.

3.3.3.3 Voltage Overshoot and Breakdown Delay

As discussed in the previous sections, voltage overshoots of the ESD protection devices have become one of the most critical concerns for the ESD protection. Hence, the rise-time dependence is often questioned. Shorter rise-times can induce larger voltage overshoots due to the finite response speed of the ESD elements such as SCRs, bipolar transistors or even pn-diodes. The active clamps proposed in this work are insensitive to the pulse rise-times since the transient SOA of the used nDMOS in the clamp is not influenced by dV/dt. Moreover, at the beginning of the ESD pulse, the gate of the nDMOS is biased by the capacitive coupling and the nDMOS immediately conducts channel current, thus preventing the voltage overshoots.

The breakdown delay in case of pre-pulse voltage (PPV) is another issue causing ESD failures in the field [87]. A pn-junction subjected to PPV can suffer from a significant delay of the avalanche breakdown. The ESD protection is diminished in this case [88].

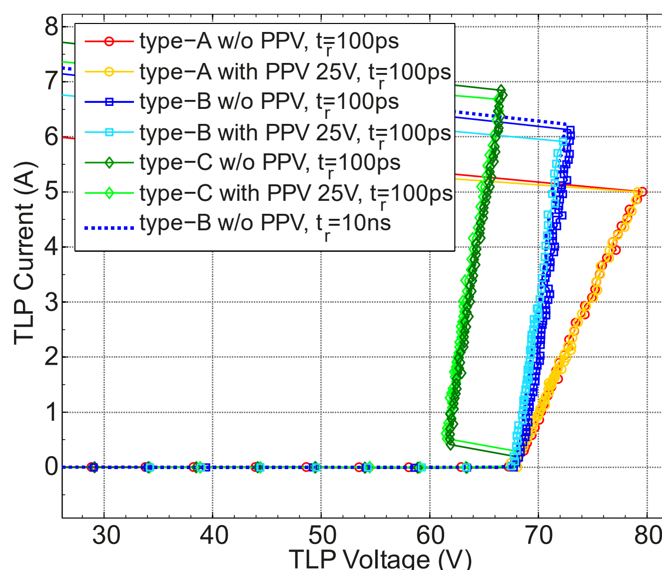

Figure 3.67: The type-A, type-B and type-C active clamps using the same nDMOS characterized by 100 ns TLP with and w/o 25 V PPV. The maximal utilization of the nDMOS SOA in the type-C clamp is experimentally confirmed.

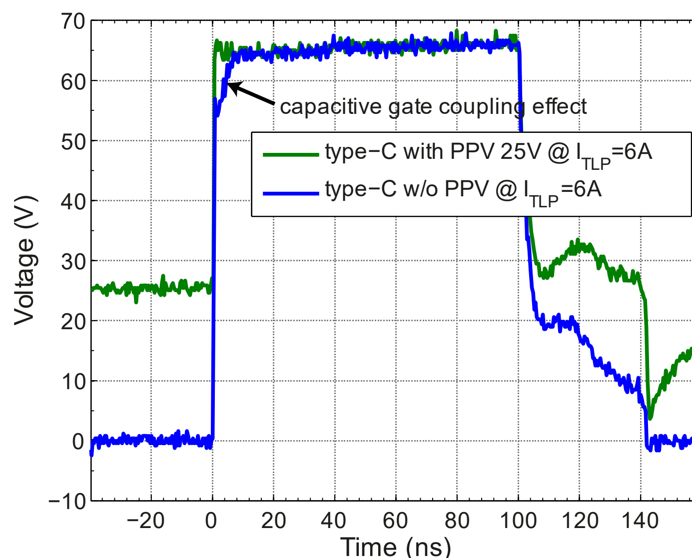

Figure 3.68: The voltage responses of the type-C active clamp to TLP with and w/o the 25 V PPV at 6 A TLP current.

The active clamps on the contrary do not work as a type of breakdown devices hence are usually not affected by the pre-pulse voltage. The Zener string itself is physically based on pn-junction breakdown. However for low breakdown voltages (<10 V) the breakdown delay under PPV condition is not observed. In fact, the triggering of low voltage diodes are much more insensitive to PPV compared to high voltage pn-diodes. Figure 3.67 shows the TLP characteristics of type-A, type-B and type-C clamps using equally sized nDMOS. All curves are derived from 100 ns TLP with 100 ps rise-time except for one I-V curve of the type-B clamp, which is measured with 10ns rise-time showing exemplary the rise-time independency of the active clamps. During the TLP, a pulse biasing of 25 V via a bias tee is applied to simulate the PPV. No breakdown delay and no significant reduction of the failure level due to PPV is observed in these cases.

However it must be pointed out that the active clamps as well as the ESD protection concepts using active clamps are not completely immune from PPV. In case that PPV is very large, the ESD robustness can decrease. It can be overcome or compensated by the proper design of the trigger circuit. Figure 3.68 displays the transient voltage waveforms of the type-C clamp at 6 A TLP current. Without PPV, the capacitive gate-coupling effect is clearly shown as indicated by the arrow in Figure 3.68. PPV reduces the increase of the drain-source voltage of the nDMOS during the initial voltage rise. This reduces also the V_{GS} bias due to capacitive coupling. A well designed trigger circuit provides the necessary V_{GS} bias to turn on the clamp. The design example in Figure 3.68 demonstrates clearly the feasibility. No voltage overshoot occurs and hence the trigger circuit with Zener diodes is sufficiently fast.

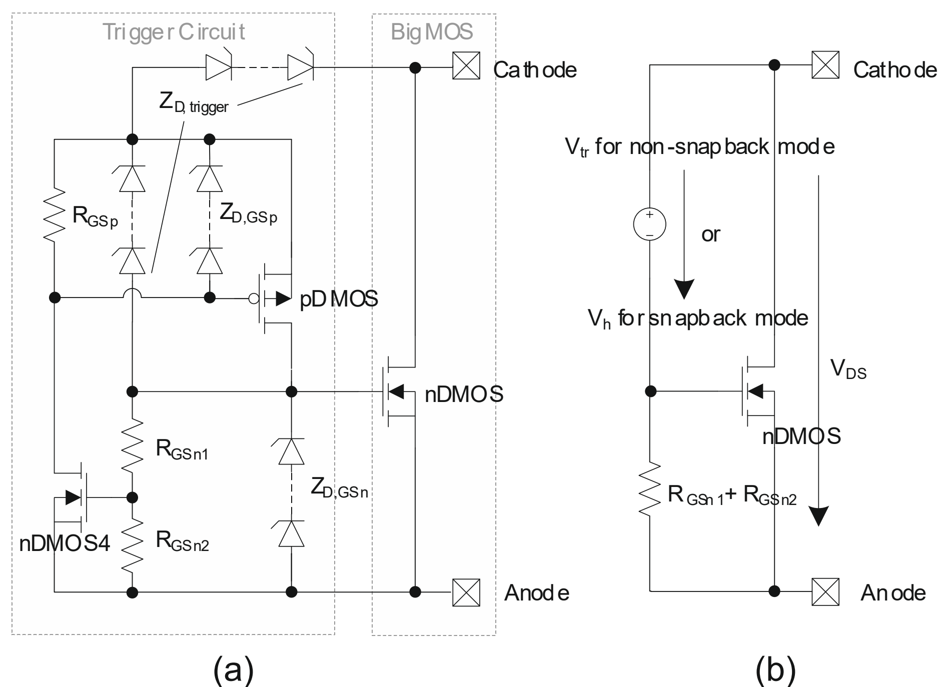

Figure 3.69: (a) Schematic view and (b) simplified equivalent circuit of the type-C2 active ESD clamp. In the non-snapback mode, the Zener string clamps at V_{tr}. In the snapback mode, V_h is the clamping voltage given by the voltage definition circuit consisting of Zener string and the pDMOS transistor.

3.3.3.4 Alternative Circuit Topology with Controlled Snapback

The main feature of the type-C clamp is the controlled snapback. It is based on the switching of the operating point of bigMOS in ESD case using circuit-level design measures. Various circuit implementations are possible. The type-C clamp illustrated in Figure 3.56 can be considered as an enhancement of the type-B clamp with an additional shorting transistor from a circuit topology perspective. Figure 3.69 (a) shows another circuit example, so-called type-C2 clamp that is related more to the type-A clamp and provides also a controlled snapback. The pDMOS is no longer used as an amplification stage but as the shorting transistor which bypasses part of the Zener string $Z_{D,trigger}$. The pDMOS is turned on once the small nDMOS4 is activated by a voltage divider similar to that in the type-C clamp. By removing the circuit part which enables the snapback mode including nDMOS4 and pDMOS as well as its gate-source resistor R_{GSp} and gate-source protection $Z_{D,GSp}$, the remaining circuit shares the same circuit topology as the type-A clamp (Figure 3.69 (b)).

Compared to the type-C clamp, the type-C2 clamp does not require a pDMOS with the same or higher voltage class. The pDMOS can be implemented at lower voltage class depending on the Zener diodes it bridges. Figure 3.70 (a) gives the TLP results of a type-C2 clamp and a type-C clamp using the same nDMOS. The failure currents of both clamps are nearly the same due to the SOA of the used nDMOS transistor. The R_{on} of the type-C2 clamp is higher than that of the type-C clamp because of the lack of amplification.

Depending on the application, another advantage of type-C2 clamp is the smaller gate coupling effect as discussed in Figure 3.65. The capacitive coupling of the type-C2 clamp is more like the one of the type-A clamp and thus has less pronounced gate coupling compared to type-C clamps as shown in Figure 3.70 (b).

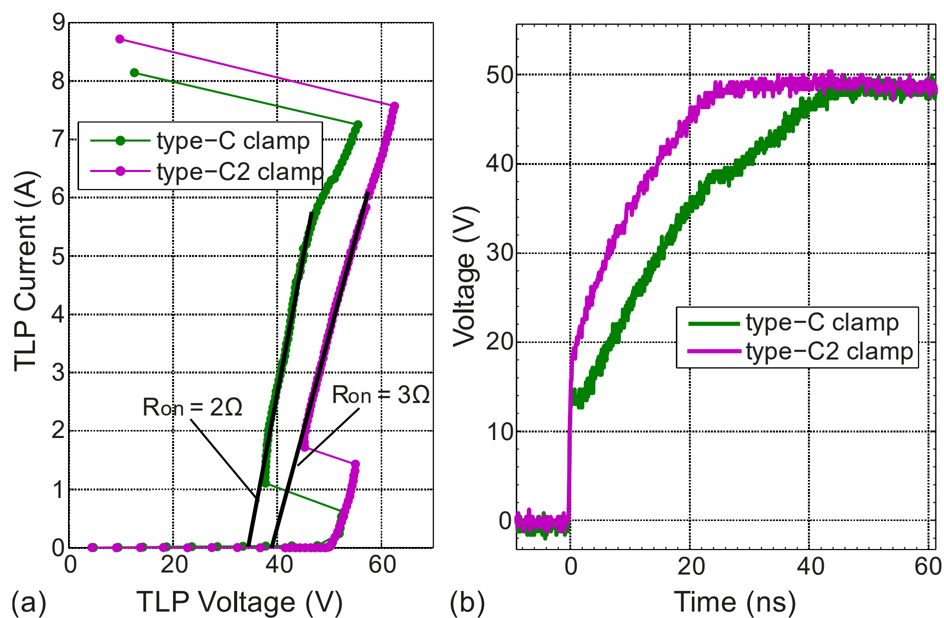

Figure 3.70: (a) 100 ns TLP I-V characteristics of 45 V type-C and type-C2 clamps. (b) The transient voltage waveforms of the active clamps at 50 V pulse voltage which is below the designed V_{tr}. The rise-time of the TLP is 100 ps.

3.3.3.5 Combinations of Active Clamps

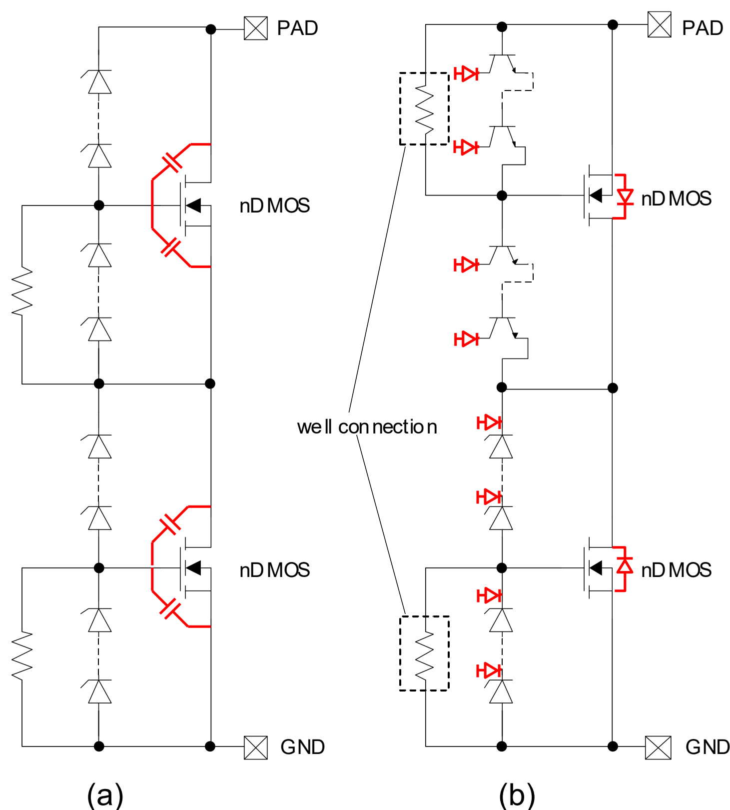

Figure 3.71: (a) stacked type-A clamps to achieve high V_{tr} with DMOS of lower voltage classes. (b) Anti-serial connected type-A clamps for the pads which require reverse voltage capability.

The active clamps provide high degree of freedom for the high voltage ESD design. In addition to the implementation of the trigger circuit such as type-A, type-B and type-C clamps, also various combinations of the single clamps are feasible. Figure 3.71 demonstrates two active clamp combinations. The type-A clamps are chosen for the simplicity.

It is common practice to achieve higher turn-on voltage by stacking existing ESD devices of lower voltage classes, e.g. ESD diodes. The total ESD R_{on} of in series connected ESD diodes is the sum of the R_{on} of all single diodes. The ESD area efficiency can be rather low because of the given ESD window. Active clamps are easily stacked (Figure 3.71 (a)) as long as parasitic breakdown voltages such as the substrate breakdown in the given power technologies do not become limiting factors. The increasing R_{on} of the stacked active clamps is of minor concern if type-B or type-C clamps are used.

Figure 3.72 shows TLP measurements of a single 60 V type-A clamp compared to a 120 V clamp implemented with two stacked 60 V type-A clamps. The I-V characteristics confirm the same failure levels for both clamps as expected (Figure 3.72 (a)). The 120 V clamp has nearly doubled R_{on} of the 60 V clamp.

Additionally, the capacitive coupling effect is reduced in case of stacked active clamps due to the cascaded parasitic capacitances as indicated in Figure 3.71 (a). The transient voltage waveforms at voltages below V_{tr} show the reduced gate-coupling effect of the stacked clamp (Figure 3.72 (b)).

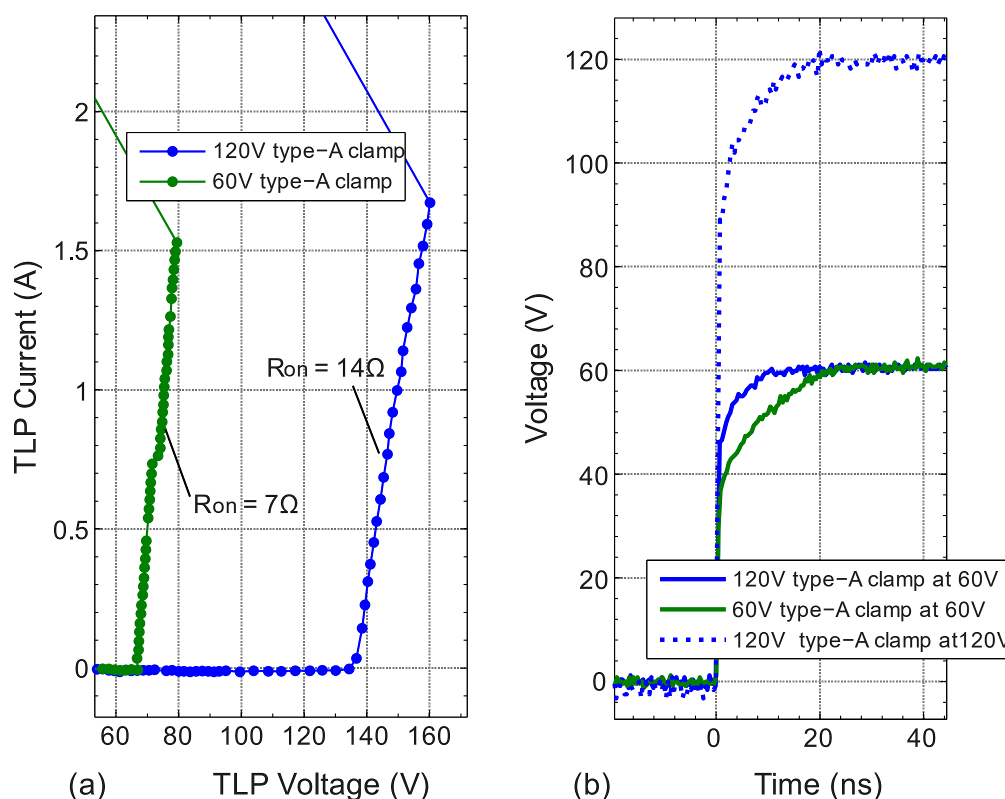

Figure 3.72: (a) 100 ns TLP I-V characteristics of 60 V and 120 V type-A clamps. (b) Comparison of the transient voltage waveforms of the 60 V and 120 V clamps at 60 V and 120 V pulse voltages. Rise-time of the TLP is 100 ps.

Other applications require reverse voltage capability for the high voltage supply or I/O pins. Figure 3.71 (b) gives a schematic view of an anti-serial combination (like anode-cathode-anode arrangement of two diodes) of active clamps for ESD protection. In many power technologies such as bulk technologies. The parasitic structures again have to be taken into consideration. Well connections as well as junction breakdowns as indicated by the substrate diodes must be considered to prevent unwanted leakage current paths. For the upper part of the anti-serial active clamp for example, the Zener diodes are implemented using emitter-base breakdown of an npn transistor. Its collector is appropriately connected for avoiding substrate leakage current while negative voltage is applied to the pad.

3.3.4 Summary

The advanced trigger circuits discussed in this section aim at optimizing the gate control of the nDMOS. Thereby they lower the differential on-resistance R_{on} and the clamping voltage of the active clamps thus also the requirement of the ESD window. This allows area savings due to relaxed bus resistance rules. Furthermore, the advanced trigger circuits enable the designer to reach the maximal failure current of the nDMOS (as given by the SOA) even if the corresponding failure voltage is smaller than the trigger voltage.

The capacitive coupling effect can be controlled. On the one hand, it is utilized to prevent voltage overshoots by turning on the clamp very quickly e.g. in CDM-like ESD cases. On the other hand, the capacitive coupling effect can be suppressed sufficiently to avoid unwanted current absorption of the clamp due to steep voltage transients e.g. during EMC events. The presented active clamps do not suffer from hazardous effects such as PPV induced breakdown delay, voltage overshoots (e.g. due to turn-on delay), and turn-off issues. The development of the active ESD clamps using advanced trigger circuits is a matter of circuit-level design. The wanted features, for example the controlled snapback, are implemented in different circuit topologies. The characteristics of the clamps are compared. Series stacking and anti-serial combination of active clamps are feasible. If applicable, the advanced trigger circuit can be even combined with the power transistor of a functional circuit. The power transistor is then used as the bigMOS of the active clamp in ESD case.

In the field of component-level ESD regarding HBM and CDM, active clamps show competitive protection capabilities and their special value in case of limited ESD windows. In addition, the active clamps are also decent protection devices for system-level ESD stresses (like IEC 61000-4-2) [89].

3.4 Conclusion

In this Chapter, failure levels, failure modes of high voltage on-chip ESD protections are discussed extensively including various case studies. Advanced active clamps show their advantages hence are investigated with further details.

Characterizations and failure level studies for high voltage snapback and non-snapback ESD devices are carried out. Experimental and simulation results show various failure mechanisms and I-V characteristics of the protection devices, which are of great importance in high voltage ESD design.

An aspect of evaluating ESD devices in a wide range of pulse duration is presented based on the Wunsch-Bell theory. One of the most important results is that in short

pulse ranges the DMOS transistors as well as the active clamps suffer from electrical failure mechanism rather than a thermal one. Based on the systematic comparison showing the drawbacks and advantages of the various ESD devices, it suggests proper decisions on ESD concepts according to the applications.

It was found in the case studies that voltage overshoots due to fast transients can lead to ongoing bipolar triggering in high voltage LDMOS transistors. This even happens due to the overvoltage caused by the finite reaction time of the avalanche breakdown diode, which is much shorter than the transition time for bipolar triggering in the nLDMOS transistor in the monitor structures. TCAD simulation is used to understand the unique effect called ongoing bipolar triggering. Improvement solutions are given clearly showing the benefit of the active clamps.

As the ESD protection concept using the high voltage active clamps draws more attention, the active clamps are designed with advanced trigger circuits enabling many sophisticated features and improving the on-chip ESD protection with high degree of freedom in ESD design. The active clamps significantly reduce the development effort of ESD protection devices because all relevant parameters are accessible by circuit design and do not necessarily require any process development.

Chapter 4

Concept for System-Level ESD Protection

System-level ESD protection has gained more and more attention especially in the field of automotive applications where the safety is of great importance in the criteria of the products. Instead of implementation of system-level ESD protection only on chip-level which is in many cases of high cost or even not applicable, the co-design of system-level ESD protection both on chip and on printed circuit board (PCB) is the one of the main challenges for system ESD designers. This Chapter provides several basic concepts and introduces behavior modeling methodologies which improve the system-level ESD design.

Different high-voltage on-chip ESD devices and protection approaches are characterized, compared and further developed in Chapter 3. In the scope of this Chapter, off-chip (external) ESD devices as a part of system-level ESD co-design are characterized also with TLP system, but with a different focus compared to on-chip ESD protections. In addition they are verified directly using the IEC 61000-4-2 ESD generator showing their clamping behaviors. Behavior modeling of on-chip and off-chip ESD elements aiming at system-level efficient design using ESD simulation is discussed. Particularly for the on-chip ESD protection, the so-called Wunsch-Bell characterization based modeling methodology gives the possibility to simplify the model complexity, yet improve the simulation accuracy by reproducing the self-heating effect in the on-chip devices susceptible to ESD.

4.1 Characterization and Systematic Evaluation of External ESD Protection Elements

ESD tests on system level according to IEC 61000-4-2 or ISO 10605 play today an important role in the electronic release process of components and systems. To fulfill ESD specifications, external protection elements are often used to protect the semiconductor devices on the PCBs against system-level ESD. Different types of external protection elements are possibly employed for ESD protection in system. However the required protection effectiveness cannot always be achieved. Although the external device descriptions in the datasheets are not wrong in general, the ESD test

conditions are often not sufficiently specified. That is even with the same external protection elements, different protected devices and systems often lead to different test results, making the system-level ESD robustness difficult to predict.

In this section, a general ESD characterization method is developed for the systematic comparison of the different types of off-chip protection elements e.g. varistors, TVS diodes, polymer devices and also discrete capacitors and resistors. The approach of characterization and evaluation of the ESD devices generally deliver informative and comparable device parameters in order to design more reliable and more straightforward ESD protection concepts for systems [90].

Same to the on-chip ESD device characterization as introduced in the previous chapters, TLP belongs to one of the most important characterization methods also for the evaluation of the off-chip ESD protection elements. In addition to TLP, IEC 61000-4-2 ESD generator were used to investigate the behaviors of the protection elements stressed by the standardized pulses. The characterization in the frequency domain by S11 measurements is a further prerequisite to determine the parasitic capacitances and inductances of the devices under test.

A systematic comparison of the ESD effectiveness of diverse off-chip protection elements such as varistors, TVS diodes, gas discharge tube and polymer enables on one hand, a proper choice of the protection elements for ESD protection in system. On the other hand, the ESD characterization method facilitates the data provision for the modeling of ESD protection elements. The parameterized model based on the characterization of the devices allows accurate ESD simulation improving also the on-chip and off-chip ESD co-design [91] [92].

4.1.1 High-Current TLP Characterizations

4.1.1.1 High-Current TLP Setup

As previously discussed in Chapter 2, TLP as well as vf-TLP are proved to be very commonly used measurement equipment for the characterization and evaluation of ESD protection devices. For on-chip ESD protection devices and for external protection elements, TLP parameters such as pulse width, rise-time as well as current or energy level allow profound characterization of the devices' properties in ESD time domain. The pulse width can be adjusted so that I-V curves of the devices under test are derived as function of pulse width, i.e. the Wunsch-Bell characterization as introduced in Chapter 3. The rise-time of the TLP is variable to determine the device reaction time depending on different ESD pulses.

External protection elements often used for the primary system-level ESD protection are more robust against ESD compared to on-chip ESD protection devices.

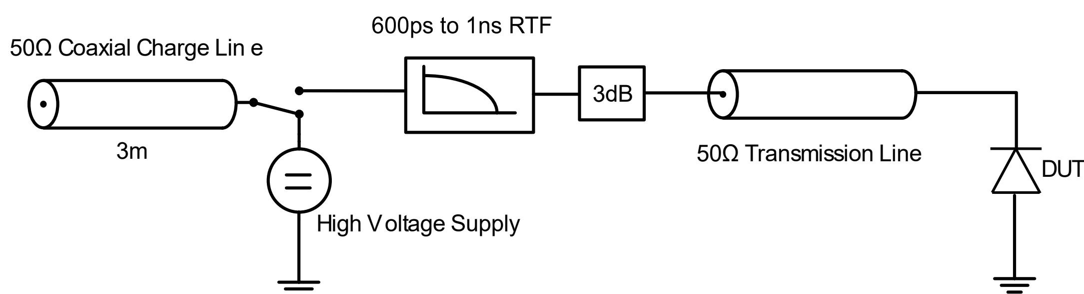

Figure 4.1: Simplified schematic of the high-current TLP system

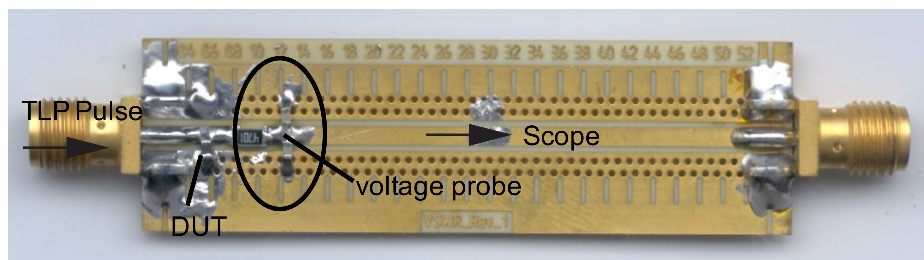

Figure 4.2: Test board with voltage probe for the TLP characterizations of external elements.

Conventional IEC 61000-4-2 compliant ESD generators deliver a discharge voltage up to 30 kV with an initial current peak of over 100 A. Hence, the standard TLP system must be modified to a high-current version to characterize the external elements at higher current levels. Figure 4.1 depicts a simplified schematic view of the high-current TLP system. The 3dB attenuator is the only attenuator for suppression of reflected TLP pulses due to load mismatch. The high voltage relay in the prototype of high current TLP works up to 4 kV. This implies that the maximal current flow into the DUT is $4\,kV/50\,\Omega\cdot\sqrt{2} = 56.6\,A$ when the DUT is 0 Ω. The pulse duration was set to be comparable to IEC 61000-4-2 pulses with a length of the charge cable of about 3 m corresponding to 30 ns. Further, 600 ps and 1 ns rise-time filters were used to match the rise-time of IEC ESD pulses in contact discharge mode.

The current probing using CT1 from Tektronix allows sufficient measurement bandwidth for recording the current transient waveforms also in the high current region. With a 30 ns pulse width, the saturation effect at the current sensor does not occur up to the tester limit (56 A). The voltage measurement applies the same configuration with compensation of parasitic capacitance as described in subsection 2.2.1.2. It has a measurement bandwidth of 4.4 GHz according to S21-parameter measurements. Figure 4.2 shows a photograph of the test board for the TLP characterization with integrated RC network for the voltage measurement.

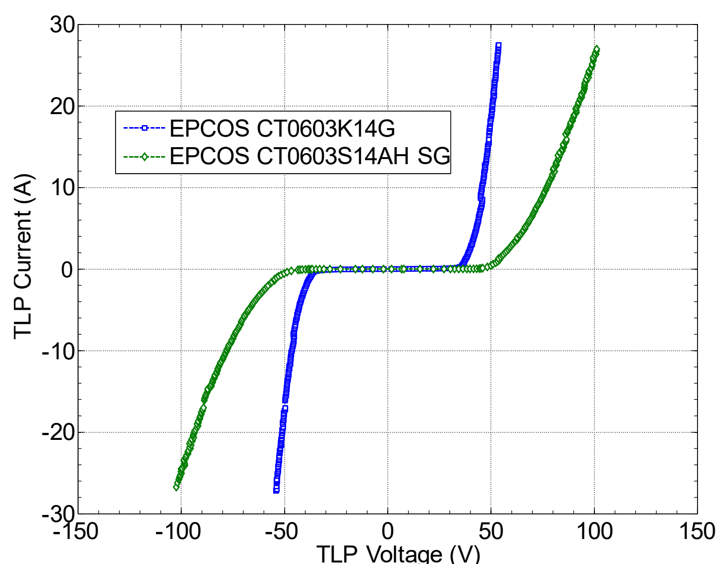

Figure 4.3: TLP I-V characteristics of varistors in high-current region.

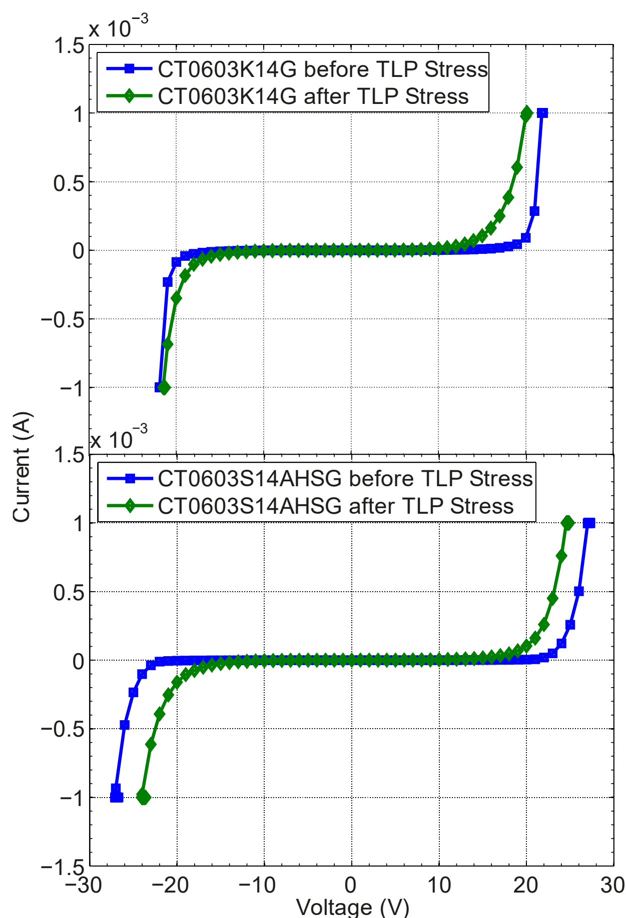

Figure 4.4: DC characteristics of varistors before and after high-current TLP stresses.

4.1.1.2 Characterizations of the protection elements using TLP

In this section varistors, TVS diodes as well as gas discharge tube and polymer are characterized using the high-current TLP system. In addition, external capacitors and resistors are also characterized using TLP to verify the behavior of these passive devices under high current or high voltage condition in the ESD time range.

A varistor is known as voltage dependent resistor whose name is a portmanteau of variable resistor. Varistors are often used as commercial devices to protect ICs against excessive transient voltages such as ESD by applying them into the circuit. When triggered, they should shunt the current away from sensitive components. In the scope of this work, two multilayer varistor from EPCOS EPCOS CT0603K14G and CT0603S14AHSG are investigated.

I-V curves of the varistors are depicted in Figure 4.3. A symmetric behavior of the varistors in positive and negative stress polarities is observed. Although the breakdown voltages are nearly the same, these two varistors show very different dynamic behaviors in terms of their dynamic on-resistances. This very important information for ESD is normally not provided in the device datasheet.

Also, it is observed that these two varistors show noticeable deviation of the leakage current or the breakdown voltage prior and post to high current stresses. Figure 4.4 compares the DC characteristics of the varistor CT0603K14G and CT0603S14AHSG before and after the TLP stresses where increase of leakage current and decrease of breakdown voltage are clearly observed. This is a known phenomenon especially for

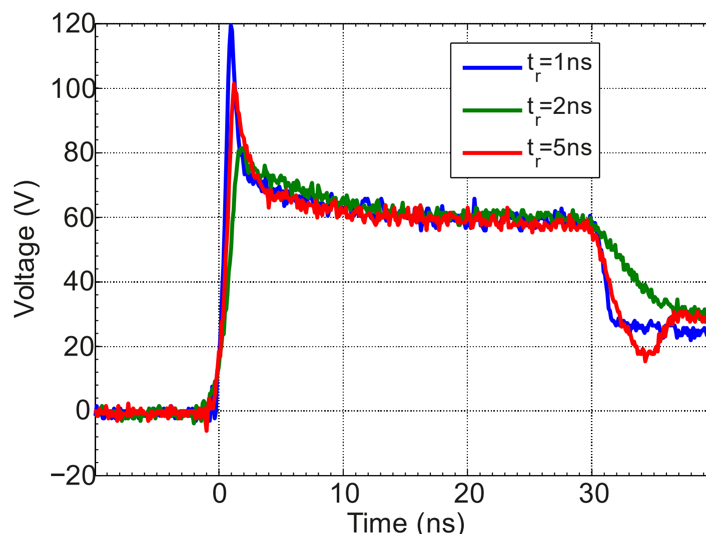

Figure 4.5: Voltage waveforms of CT0603K14G as a function of rise-time at 40 A TLP.

ZnO-Bi based varistors as described in [93]. As long as the decreased breakdown voltage is still far beyond the operating voltage under the use condition, varistors can be still considered as good off-chip ESD protection devices.

Not only delivering quasi-static I-V curves, the TLP characterization also captures the dynamic behaviors of the DUT. Various rise-times are used in the TLP setup to obtain the transient response of the varistors to fast energy pulses. Figure 4.5 shows the different voltage overshoots depending on different pulse rise-times. The voltage overshoots are at least partly due to the parasitic inductance of the varistor so that the voltage peak can reach 120 V at 40 A TLP current. For all three pulses with different rise-times, the voltage falls to a steady state of about 60 V after about 10 ns. In general, the voltage overshoots must be considered in case the protected devices are sensitive to voltage peaks as discussed in Chapter 3. For example to protect chips with snapping on-chip ESD protections, the off-chip protection elements might lose their protection effectiveness due to the overshoots [94].

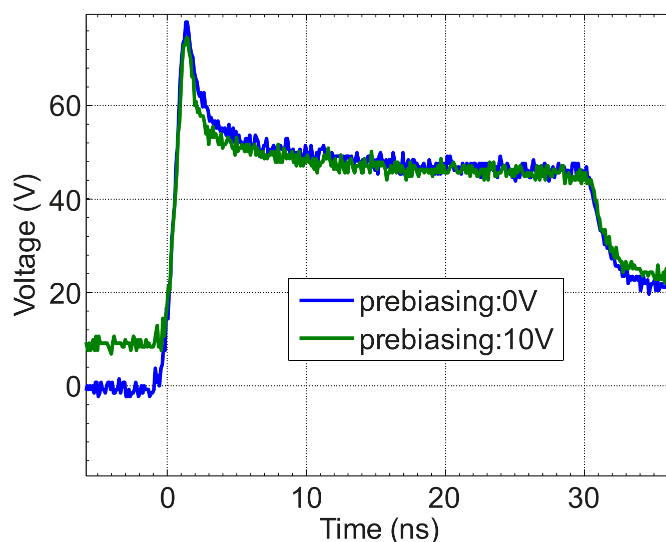

Figure 4.6: Voltage waveforms of CT0603K14G with and without 10 V pre-biasing at 10 A TLP.

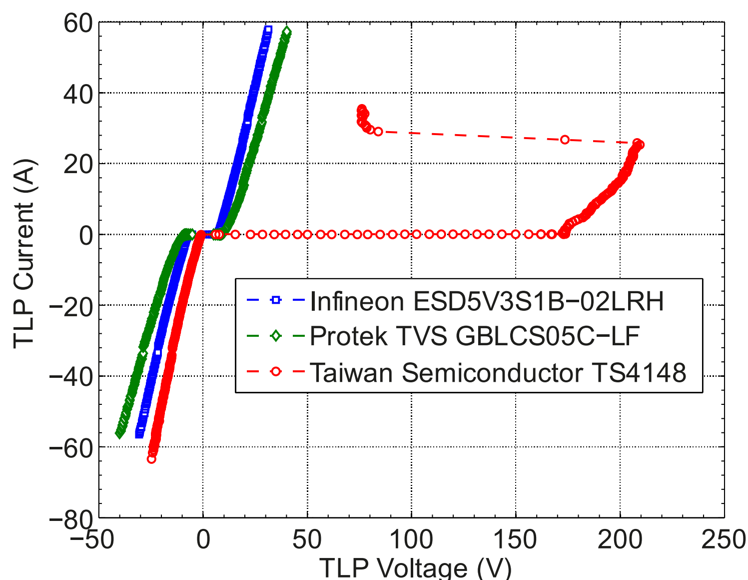

Figure 4.7: TLP I-V characteristics of TVS diodes in high-current region.

It was shown in [95] the effect of the pre-pulse voltage (PPV) which is a voltage built up across the DUT before the actual ESD takes place can be present in real world ESD. The question has been raised whether this effect which is observed for many on-chip protections (Chapter 3) could cause also significant turn-on delay of the external protection elements. In fact, this is not expected at least for varistors because the breakdown mechanism of the varistors is different to the avalanche breakdown which then suffers from the breakdown delay when PPV is applied. Figure 4.6 compares the voltage waveforms of CT0603K14G with and without 10 V pre-biasing voltage at 10 A TLP current. No breakdown delay is shown in the voltage waveform under pre-biasing condition.

In addition to varistors, transient voltage suppression (TVS) diodes shunt usually ESD currents with the robust pn junctions. Zener or avalanche breakdowns allow the diodes clamp excess voltages induced by ESD. I-V curves of the characterized TVS diodes are

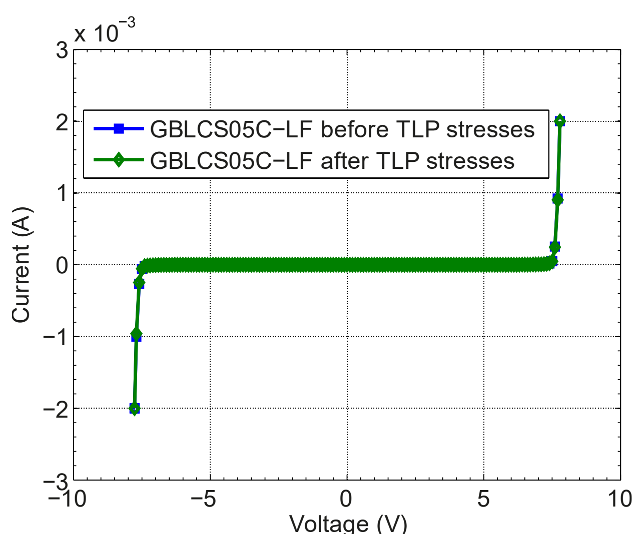

Figure 4.8: DC characteristics of TVS diode GBLCS05C-LF before and after high-current TLP stresses.

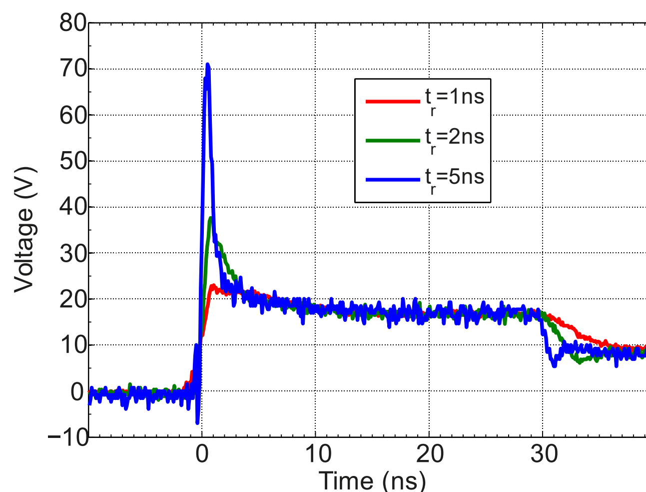

Figure 4.9: Voltage waveforms of GBLCS05C-LF as a function of rise-time at 10 A TLP.

depicted in Figure 4.7 showing one-directional and bidirectional protection diodes. Unlike varistors, the TVS diodes does not show degradation after high current stresses. Figure 4.8 compares the DC characteristics of the TVS diode GBLCS05C-LF before and after TLP stresses. No degradation is observed. The voltage overshoots of TVS diodes are also measured using different pulse rise-times. Figure 4.9 shows for example the voltage waveforms of the diode GBLCS05C-LF, displaying an even stronger dependence on rise-time compared to the investigated varistors. The impact of PPV on the TVS diodes is also investigated using pre-biasing TLP measurements. Under 6 V pre-biasing, the diode GBLCS05C-LF shows no breakdown delay. This is also expected because breakdown delay usually occurs with higher PPV at pn-junction with higher breakdown voltage.

Furthermore, a gas discharge tube Mitsubishi CSA-30 and a polymer SurgX 0805ESDA-SP1 are chosen as alternative of the external protection elements. Both devices exhibit a snapping behavior with very high breakdown voltages (Figure 4.10). Hence, the DC characterization showing devices' breakdown was not possible due to

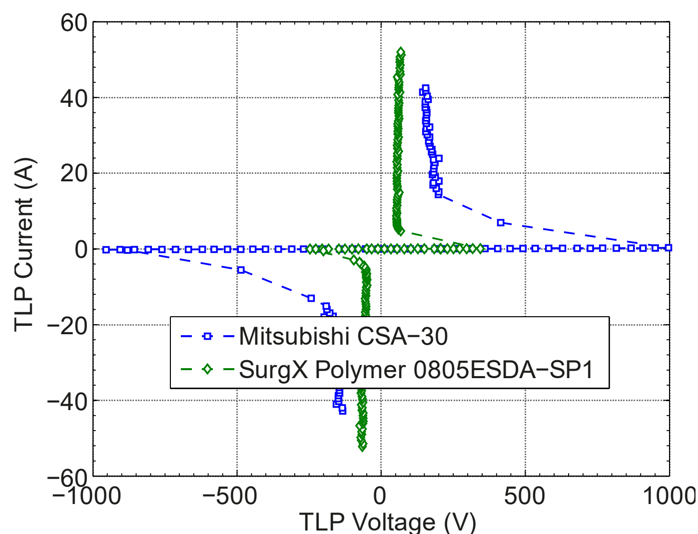

Figure 4.10: TLP I-V characteristics of a gas discharge tube and a polymer in high-current region.

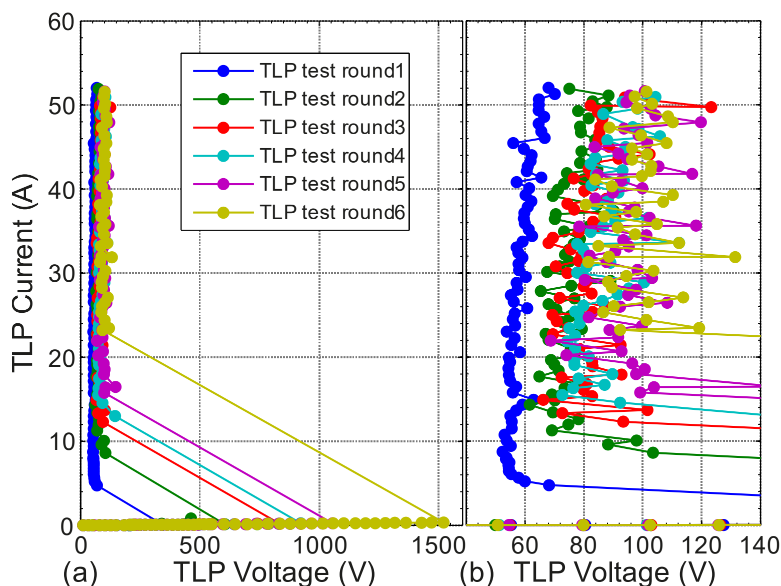

Figure 4.11: (a) breakdown voltage of the polymer as a function of the TLP test round. (b) Detailed TLP characteristics show holding voltage as a function of the TLP test round.

the hardware limit of the used source measurement units (SMU). TLP shows the benefit to characterize the extremely high breakdown voltages. An interesting device behavior was observed: the breakdown voltage of the polymer increases significantly after each TLP test round i.e. multiple TLP stresses at higher current level (Figure 4.11 (a)). The holding voltage also increases during the TLP characterization (Figure 4.11 (b)). This effect must be considered when the polymer is applied as a protection element.

Stressed by high power pulses such as ESD, the external resistors show the dynamic TLP on-resistances same to their specified resistance values. However, the reliability deterioration of the SMD resistors is a known issue where the change of the resistance value is observed after multiple ESD stresses [96] [97]. In this study, TLP measurements on external resistors gained no novel results hence is not explicitly

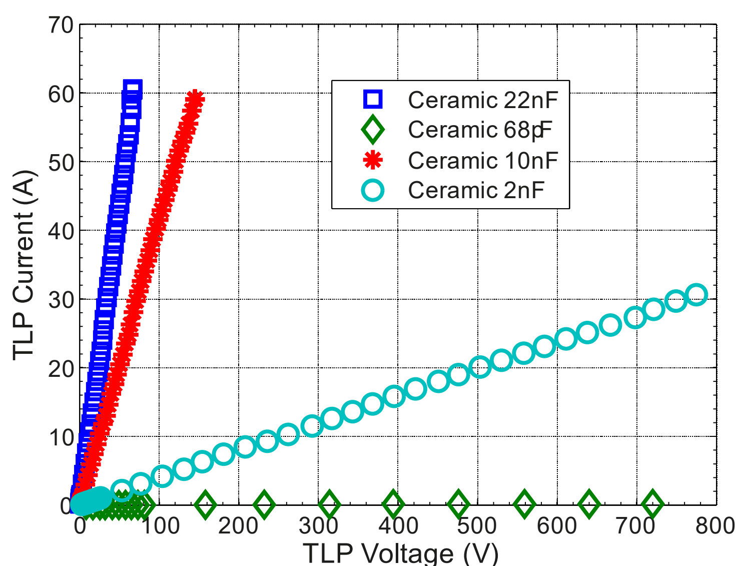

Figure 4.12: 100 ns TLP characteristics of ceramic SMD X7R_1206 capacitors 68 pF, 2 nF, 10 nF and 22 nF. Average window is between18 ns and 25 ns.

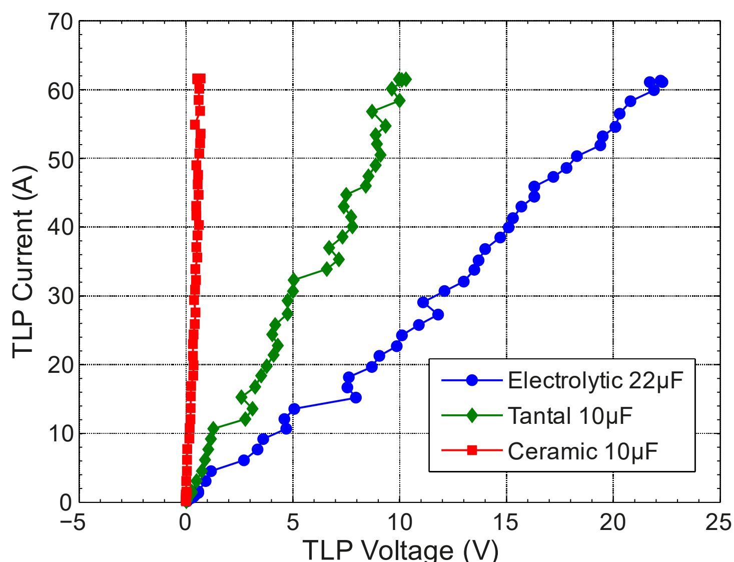

Figure 4.13: TLP characteristics of electrolytic, tantalum and ceramic capacitors

shown. The external capacitors are often used for stabilizing the supplies or I/O signals. At the same time they also work as protection elements which absorb the ESD current and clamp the voltage for the protected ICs. However, the capacitors even with large capacitance values only show limited protection efficiency or even fail to protect the ICs. DC voltage dependent capacitance of ceramic capacitors could be one of the reasons [98]. The parasitic inductance depending on the type of the capacitors can induce significant voltage overshoots when high current and fast pulses are applied. This effect can easily introduce failures if the ICs are sensitive to voltage overshoots (Chapter 3). Concerning the voltage overshoots, various types of external capacitors including SMD ceramic, SMD tantalum and through-hole electrolytic capacitors are characterized using TLP. Figure 4.12 shows the for example the ceramic capacitors with different capacitance values characterized by the high-current TLP system. The larger the capacitance the lower is the impedance hence a lower R_{on} is derived from the TLP quasi-static I-V characteristics. The TLP averaging window was chosen between

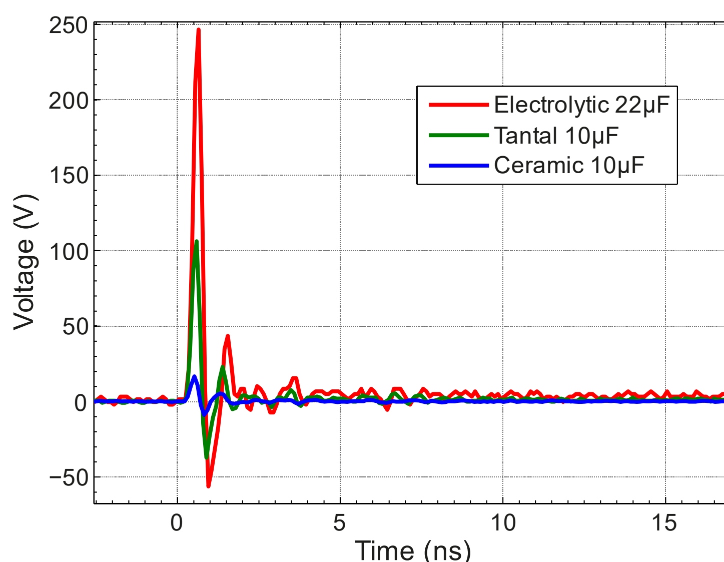

Figure 4.14: Voltage responses of electrolytic, tantalum and ceramic capacitors to 10 A TLP pulses.

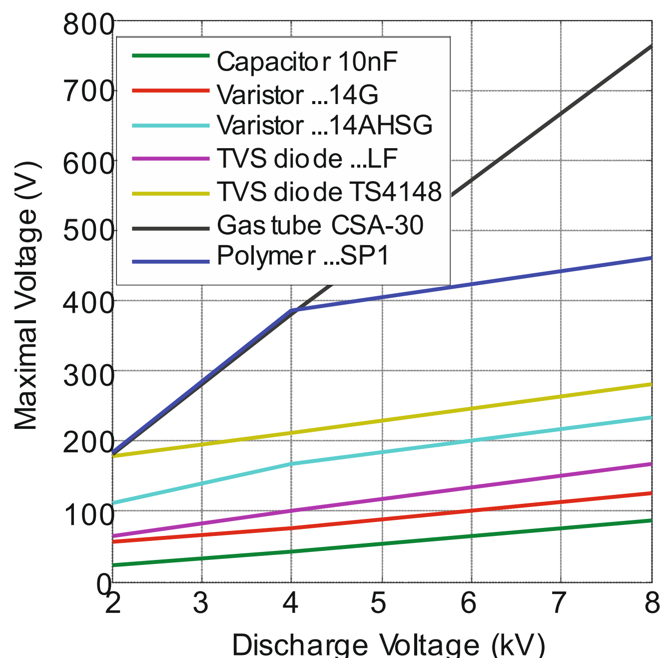

Figure 4.15: Maximal voltage at the protection elements parallel to a 25 Ω resistor as a function of the discharge voltage.

18 ns and 25 ns, which gives comparison of clamping voltages of different capacitors during typical ESD pulses. Further, due to the different types of the capacitor the R_{on} is not always the same with the same capacitance values. Figure 4.13 compares three µF range capacitors showing the lowest clamping voltage of the ceramic capacitor. In addition, the voltage overshoots induced by the TLP pulses confirms the voltage clamping of the SMD ceramic capacitors is preferable among the three tested capacitors (Figure 4.14).

4.1.2 IEC 61000-4-2 Generator Characterizations

In addition to the TLP characterizations, IEC 61000-4-2 ESD generator was used to characterize off-chip protection elements. To verify the effectiveness of the ESD protection concepts in a more realistic way, a defined load is connected parallel to the protection elements to mimic a protected device such as IC. Although the IC pins vary a lot in the input impedance, a 25 Ω resistor as the load was used during the IEC measurements for simplicity. Figure 4.15 depicts the maximal voltage (voltage overshoots) of various protection elements as a function of the discharge voltages. The protection element is connected parallel to a 25 Ω resistor during the IEC 61000-4-2 ESD test. Using the ESD generator characterizations, the protection effectiveness against ESD can be easily assessed which also matches the results from the TLP characterizations.

4.1.3 Characterizations using Network-Analyzer

The parasitic capacitance and inductance of the off-chip protection elements were measured. Typical values are summarized in the Table 2.4 derived from the S11 measurements using a network-analyzer.

Table 4.1: Parasitic capacitance and inductance of different protection elements.

Type	*Description*	*Parameter*	
		C	L
Resistor	EPCOS 1kΩ 0805	5 pF	4.0 nH
Capacitor	EPCOS 10nF 0805 X7R	n.a.	1.2 nH
Varistor	EPCOS CT0603K14G	155 pF	2.0 nH
	EPCOS CT0603S14AHSG	18 pF	2.0 nH
TVS Diode	Protek TVS GBLCS05C-LF	1.2 pF	1.8 nH
	Taiwan Semiconductor TS4148	750 fF	n.a.
Gas tube	Mitsubishi CSA-30	100 fF	1.8 nH
Polymer	SurgX 0805 ESDA-SPI	100 fF	n.a.
	Tyco PESD0603-140	200 fF	n.a.

4.1.4 Summary

From the high current TLP and IEC 61000-4-2 ESD test results it was found that varistors and TVS diodes can provide a very effective ESD protection, while gas discharge tube and polymer are only in particular cases of interest due to their higher breakdown voltages.

The quasi-static I-V curves as well as the dynamic behaviors especially the voltage overshoots demonstrate different behaviors of different types of off-chip protection elements under ESD stress conditions. It is important for the on-board ESD protection concept. Based on the gathered data the modeling of the protection elements for the system-level ESD simulation is enabled.

4.2 ESD Simulation with a Wunsch-Bell based Behavior Modeling Methodology

Conventional modeling methods for ESD protection especially for on-chip ESD protection can be specific to device types or cannot reproduce the self-heating effect. This section proposes a straightforward modeling methodology based on the Wunsch-Bell characterization method (Chapter 3) using TLP. It allows precise ESD simulation verified by measurements [99].

Traditional simplified models of ESD devices and structures reproduce their quasi-static I-V characteristics without concerning self-heating during ESD [100] [101]. In fact, as given by the Wunsch-Bell theory, the failure levels (failure power and failure energy) of semiconductor structures due to thermal run-away strongly depend on the pulse width (t_w) (Chapter 3). The power to failure as function of pulse width has different slopes between adiabatic region and Wunsch-Bell region according to Dwyer's works [56] [57]. In many ESD concepts, the ESD protection elements are designed to be firstly damaged above the ESD target level, and the modeling of ESD protection elements up to the high-current density regime or up to the failure level is of prime importance. Besides the failure levels, also the on-resistance (R_{on}) which directly affects the transient response of the ESD protections differs significantly because of self-heating when the ESD elements are carrying different pulse energies with different pulse durations. In fact, the ESD requirements of the semiconductor products have become manifold nowadays. Due to different ESD standards from CDM, HBM to system-level ESD with various pulse forms one has to expect different behavior of the ESD structures with respect to self-heating. Further, the robustness of ESD elements stressed by pulses which are even beyond ESD range such as EOS pulses has also gained increasing interest [102] [103]. Hence, the thermal effects and the modification of R_{on} in terms of stress duration need to be taken into account for the modeling issues. There are a few SEED [10] publications which addressed those modeling challenges. [15] is one of the important works in this area.

Apart from many compact physical models which are available for SPICE simulation [104] [105] [106] [107] [108] [109], this section introduces a novel Wunsch-Bell based

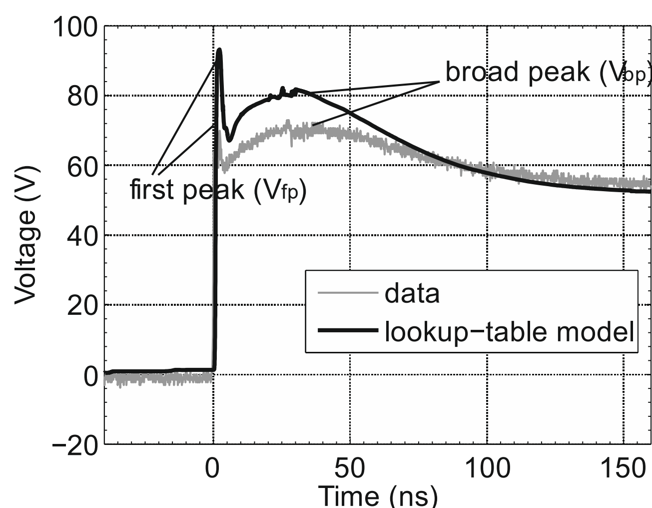

Figure 4.16: Simulated and measured voltage response of the pn-diode stressed with IEC-like pulse at 2 kV level. Corresponding current waveforms (not shown here) match very well due to the well modeled current source.

behavior modeling methodology which basically considers the ESD structure or protected I/O pin as a black-box without dealing with the details of the device physics. As the electro-thermal simulation or thermal equivalent circuits often required for physics-based models are not necessary any more in the proposed behavior modeling method, technology parameters and device geometries are out of concern simplifying the modeling significantly. I-V properties as well as the failure levels of the device of interest can be simply characterized with TLP in a wide pulse range. The behavior modeling itself is in principle language-independent. VHDL-AMS is chosen in this work for the modeling study. In prior publications, the behavior modeling methodologies using ETABLE operator [110] or lookup-table [111] focus mainly on the device characterizations with 100ns TLP. They can have very good usage for ESD simulation if self-heating in the protection elements is negligible. For most of the area efficient on-chip ESD protection devices, self-heating already becomes significant due to very high power density per unit silicon volume during ESD pulses. Hence it is often shown with 100 ns TLP characteristic only, that the model quality is not satisfying if an IEC 61000-4-2 system-level ESD pulse (hereafter called IEC pulse) is applied to the modeled pn-diode (Figure 4.16). The simulated first peak (also called initial peak) and the broad peak voltages deviate from the measured voltages. The only match of voltages is found at 100 ns because the lookup-table model reproduces the TLP characteristic. For the stress-level higher than 2 kV, the deviation of measurement data and model becomes even larger.

The modeling method in this work focuses on the one hand on the self-heating behavior and enables on the other hand the prediction of the robustness of the protection structures under various ESD stresses. A detailed modeling methodology is described. Since the individual physical details are not required, the proposed methodology can be generally applied to model different types of ESD devices or protection networks. Three modeling examples for various types of ESD protections are introduced in the following subsections. In addition, ESD simulation is performed in the co-design of on- and off-chip ESD protections to estimate their robustness.

4.2.1 Modeling Methodology

Aiming at successful ESD simulations, the model has to reproduce the transient responses of the ESD elements at first. Based on that, the power and energy dissipated in the modeled devices can be accurately calculated from correctly simulated voltage

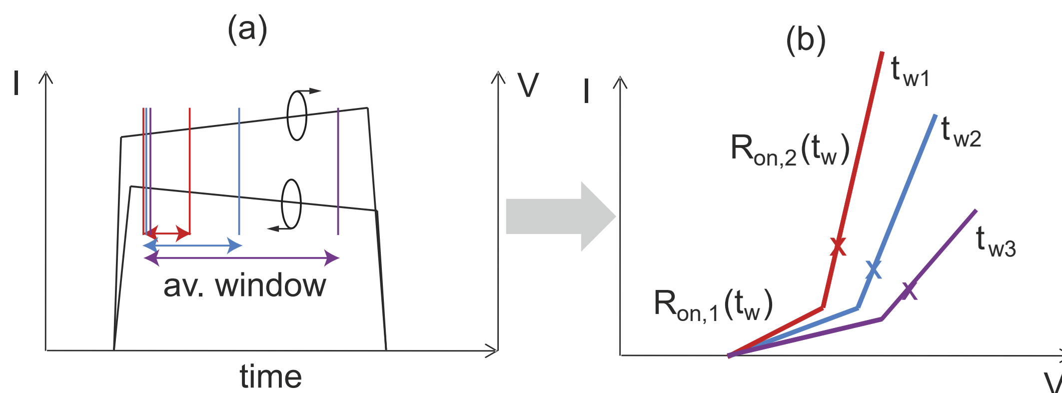

Figure 4.17: Based on (a) TLP characterization using the average windows of t_{w1}, t_{w2} and t_{w3}, (b) $R_{on,1}$ and $R_{on,2}$ are derived from averaged voltage and current transients as functions of t_w.

and current waveforms. The failure or the robustness of the ESD structure is then well predictable.

As described in Chapter 2, the ESD devices are characterized using TLP system with t_w from 5 ns to 1.5 µs. It was intended to cover a wide pulse range from component- to system-level ESD requirements. Figure 4.17 illustrates schematically the TLP characterization for a breakdown device using different pulse widths, in this example three different pulse widths. The characterization method as well as the measurement setup is similar as described in [107]. In Figure 4.17, the modeling principle is qualitatively shown based on a breakdown ESD device with two linear on-resistances $R_{on,1}$ and $R_{on,2}$. In practical cases, more than two R_{on} can be defined depending on the complexity of the device behavior such as pn diodes described in Chapter 3 and the target model accuracy. I-V curves derived from the different averaging windows correspond to different pulse durations t_{w1}, t_{w2} and t_{w3}. The calculated I-V point from the current and voltage transients in Figure 4.17 (a) is marked in Figure 4.17 (b) for each t_w. Note that with self-heating, the voltage across the device increases with increasing pulse width while the current decreases. Self-heating takes noticeable effect showing t_w dependent R_{on}. The device modeling reflects this device behavior by using a fitting function $R_{on} = f(t_w)$ within a linear segment of the I-V curves. In this example, two R_{on} ($R_{on,1}$ and $R_{on,2}$) as functions of t_w are used for the modeling. The quality of the R_{on} fitting functions relies on the numbers of t_w used in the TLP characterization.

During the simulation, Ron is modified for every time step taking the effective pulse width into account:

$$R_{on,t_1} = R_{on}(t_w = t_1 - t_0) \qquad 4.1$$

where t_1 is the present time instant and t_0 is the ESD device turn-on time which is detected by the model. A time instant is considered as t_0 when the current through the modeled ESD element exceeds a pre-defined limit or the voltage across the modeled ESD element reaches the turn-on voltage (V_{tr}). Hence, t_0 is in general not equal to the start time of the pulse generation. The present voltage and current values at t_1, $V(t_1)$ and $I(t_1)$ are self-consistently calculated by the simulator with the appropriate $R_{on,t1}$ given by 4.1.

Figure 4.18: illustrates the principle of building the failure criteria power to failure (P_f) or energy to failure (E_f) into the model with the fitting functions $P_f = f(t_w)$ or $E_f =$

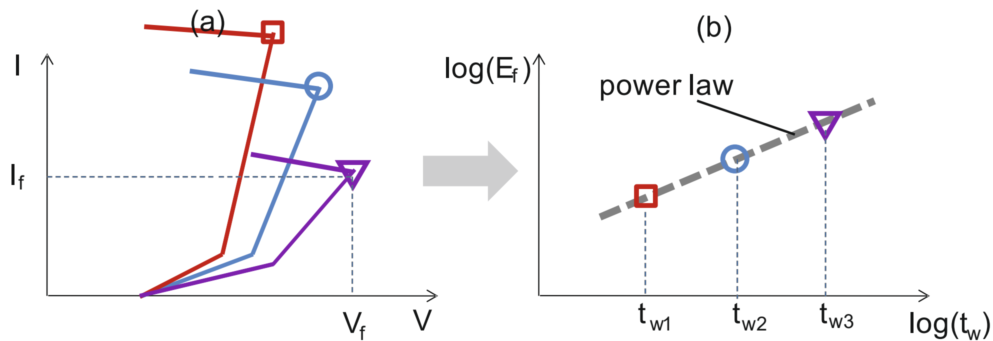

Figure 4.18: E_f as function of tw (b) derived from failure current and voltage in TLP characteristics (a).

```
begin
Ron1=F1(t); Ron2=F2(t);...
E=integ(V*I); Ef=F3(t);

if E<Ef use
        if I1>I>I0 use
        R=Ron1;
        V=F4(I,Ron1);
        elsif I2>I>I1 use
        R=Ron2;
        V=F5(I,Ron2);
        elsif ...
        ...
else
        Device is damaged!
end
```

Figure 4.19: Simplified VHDL-AMS modeling flow in Wunsch-Bell based behavior model. The switch conditions for fitting functions are the currents. Also voltage levels could be used as switch conditions.

$f(t_w)$. A power law is adequate for devices such as pn-diodes within the Wunsch-Bell region. In the simulation, the failure level limit at t_1, $E_{f,\,t1}$, is given by

$$E_{f,t_1} = E_f(t_w = t_1 - t_0) \qquad 4.2$$

The energy dissipated in the device E_{t1} is calculated as

$$E_{t_1} = \int_{t=t_0}^{t=t_1} I(t) \cdot V(t)dt \qquad 4.3$$

The modeled device is considered as thermally damaged at any t_1 if the condition $E_{t1} < E_{f,t1}$ is violated. Figure 4.19 gives the simplified modeling flow where all the fitting functions are defined by the Wunsch-Bell characterization. Note that by means of

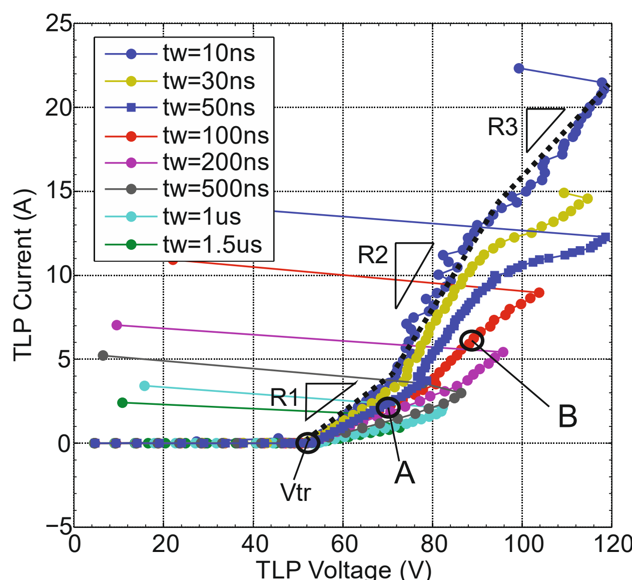

Figure 4.20: TLP characteristic of a 45 V pn-diode with t_w from 10 ns to 1.5 µs. As an example, the dashed lines represent different R_{on} (R1, R2 and R3) in three segments for the 10 ns I-V curve as approximation. For each t_w such R_{on} approximation is done showing t_w dependent R_{on}.

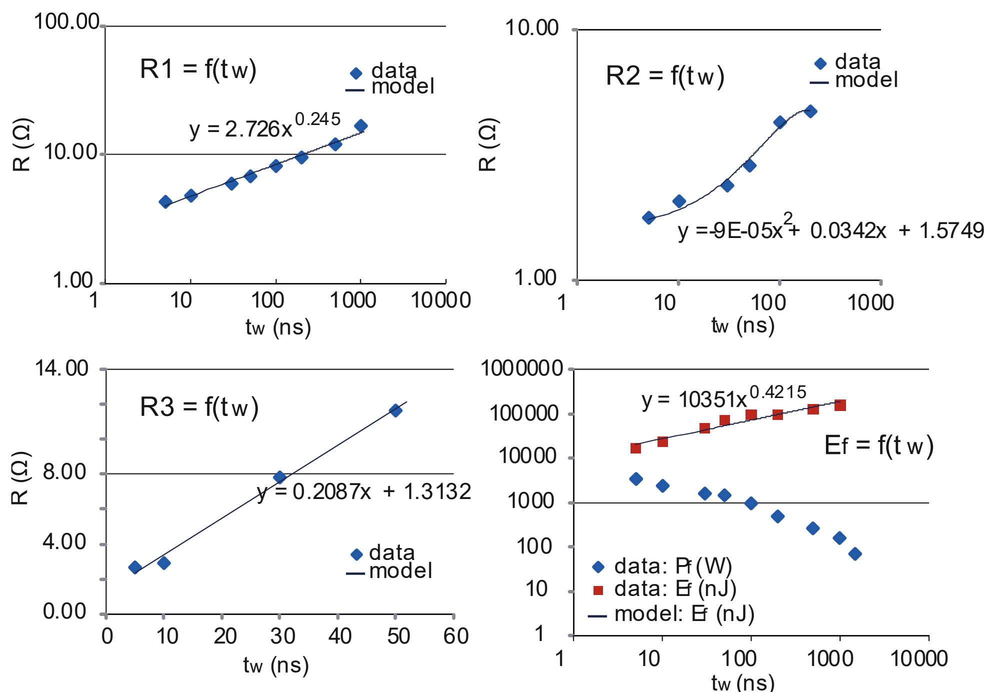

Figure 4.21: Fitting functions of the key parameters for the modeling of the pn-diode using TLP characterization.

Wunsch-Bell characterization, the choice of the pulse duration is not only limited to the Wunsch-Bell region. The fitting function of failure power does not have to follow the power law. In addition, for ESD structures eventually having electrical limits such as active clamps (Chapter 3), maximal allowed power (P_{max}) is used as an additional failure criterion.

4.2.2 Models of ESD Structures

4.2.2.1 Pn-Diode

Pn-diodes are known as very simple but also very effective and reliable non-snapping ESD protection devices. As described in Chapter 3 a typical 45 V pn-diode is characterized by TLP measurements with various pulse widths. In this chapter, the I-V characteristics are used for the behavior modeling where the key parameters included in the behavior model are the trigger voltage and the on-resistances e.g. R1, R2 and R3 for the three different linear segments within one I-V curve (Figure 4.20). The thresholds for R_{on} switching determine the transition between R1, R2 and R3. In this specific example, the switching from R1 to R2 happens at the same current level regardless of the pulse width, which implies that the current density is responsible for this transition (Egawa effect). The voltage around 93 V is used as the threshold between R2 and R3. The failure criterion is described with E_f because the investigated stand-alone pn-diode fails thermally. Figure 4.21 shows the fitting functions of the parameters depending on t_w. For the pn-diode eight different pulse durations are selected in the characterization which delivers eight data points for building the function $E_f(t_w)$ and $R1(t_w)$. For $R2(t_w)$ and $R3(t_w)$, there are less data points because the pn-diode does not reach the thresholds of corresponding R_{on} transitions in case of longer pulses.

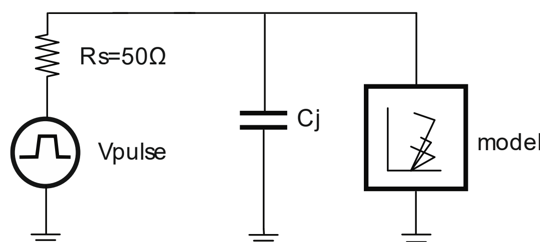

Figure 4.22: Simplified TLP simulation setup to perform the comparison of data and model. C_j is the junction capacitance of the DUT, which amounts 2 pF for the pn-diode.

TLP simulation is the first step to verify the proposed modeling methodology. A good agreement of model and data is expected because the modeling itself is based on the TLP characterization. The results of the simulated and measured transient waveforms show excellent agreement with a wide range of pulse durations. Figure 4.22 depicts the schematic of a very simplified TLP setup in the simulation. Figure 4.23 shows exemplary the simulated transients overlapped by the experimental results for 100 ns TLP. The corresponding I-V pairs ("A" and "B") are marked in Figure 4.20. The current probe was placed away from the DUT with tens of centimeters distance resulting in the test artefact due to reflected waves at the beginning of the current waveforms. Note the different levels of self-heating in the pn-diode in low and high current density regions. In addition to the waveform comparison, Figure 4.24 shows that the behavior model reproduces also the failure levels. A 1 μs TLP pulse is taken as an example. The waveforms of the last stress before failure and the failing stress clearly show the correct estimation of the simulated failure levels. As soon as the device is considered as damaged, for example $E_{t1} \geq E_{f,t1}$, the model will switch the ESD device to a low impedance (e.g. 1 Ω) to represent nearly a short indicating the device failure.

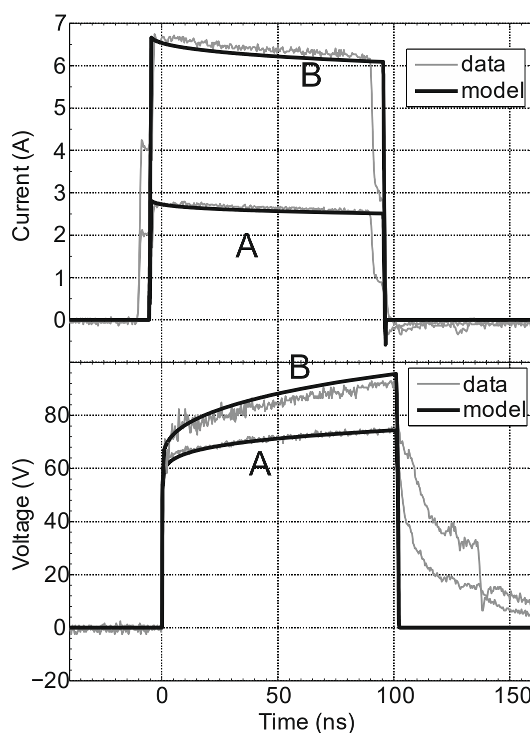

Figure 4.23: Comparison of Wunsch-Bell based model and TLP data with respect to transient responses of the pn-diode for t_w=100 ns. "A" and "B" denote the corresponding I-V waveforms.

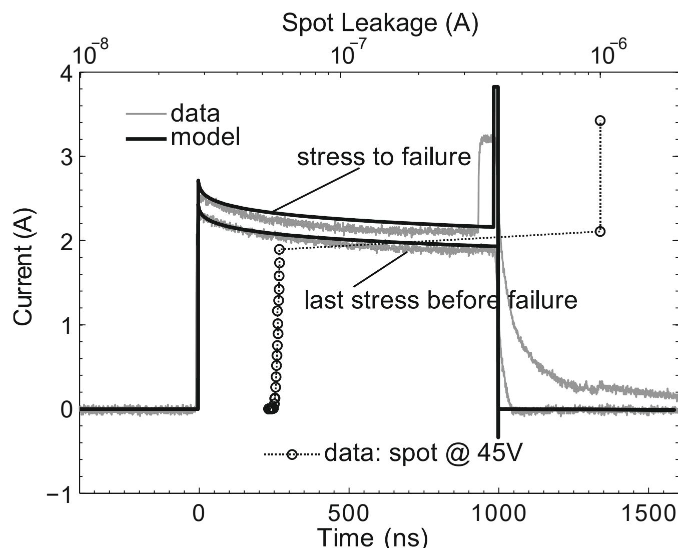

Figure 4.24: Comparison of Wunsch-Bell based model and TLP data for1 µs TLP regarding the failure levels of the pn-diode.

As a result, the current and voltage transients will change abruptly in the simulation and the device failure can be easily distinguished in the simulated waveforms. Error or warning message is certainly delivered as well. In the TLP measurements, the device failure is indicated by the transient waveforms and the current leakage spots while the device is stressed to fail.

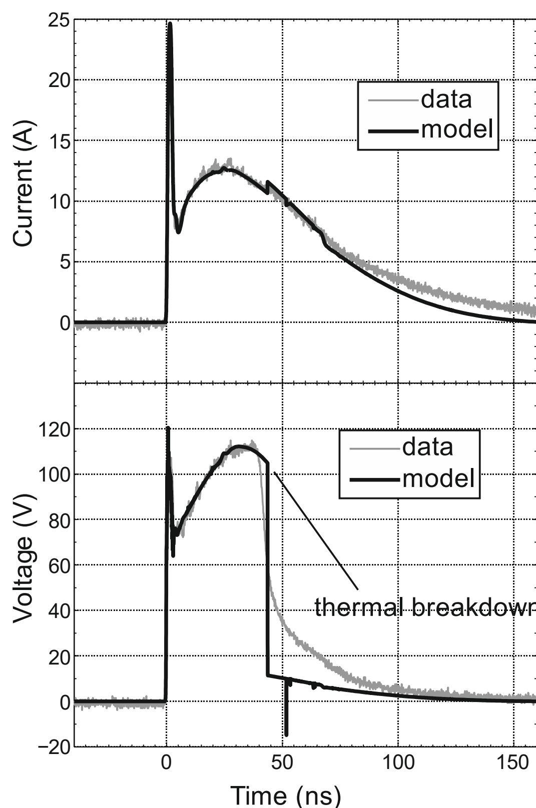

Figure 4.25: Simulated and measured waveforms for the pn-diode stressed by IEC-like pulses at 6 kV stress level (stress to failure). Thermal destruction is observed both in simulation and measurement.

In addition to the TLP simulation, ESD-like pulses with non-square waveform are more practical and convincing for the validation of the modeling method. Figure 4.25 compares the failure levels of the pn-diode stressed by IEC-like pulses applying wafer-level HMM tests (Chapter 2). The same failure current is found in simulation and measurement. Moreover, the voltage transients clearly show the improved reproduction capability of the proposed modeling methodology including self-heating compared to the 100 ns TLP based method in Figure 4.16.

4.2.2.2 Active Clamp

Standard active clamps as a type of non-snapping high-voltage ESD protection circuits have gained increasing attention and have been used as one of typical on-chip ESD solutions. Advanced design of active clamps have been introduced in the previous chapter. From the modeling point of view, the Wunsch-Bell based methodology can easily be adapted to various types of protection elements including also active clamps. Although the modeling method itself demands no details of the clamps, the understanding of the device behavior is however essential. The main difference of the active clamps compared to the pn-diodes from a modeling aspect is the transient turn-on behavior due to the capacitive gate coupling. The Zener-trigger defines the static trigger voltage of the active clamp. The DMOS transistor is designed to turn on and conduct ESD current for $V_{DS}>V_{tr}$. The transistor is supposed to be off if V_{DS} does not exceed V_{tr}. However for $V_{DS}<V_{tr}$ the capacitive coupled gate-source voltage can still turn on the transistor transiently. After the $R_{GS} \cdot C_{GS}$ discharging, the transistor is turned off when V_{GS} goes below the threshold voltage of the DMOS. Figure 4.26 shows the schematic of the active clamp circuitry as well as the transient turn-on behavior illustrated with the TLP waveforms for $V_{DS}<V_{tr}$.

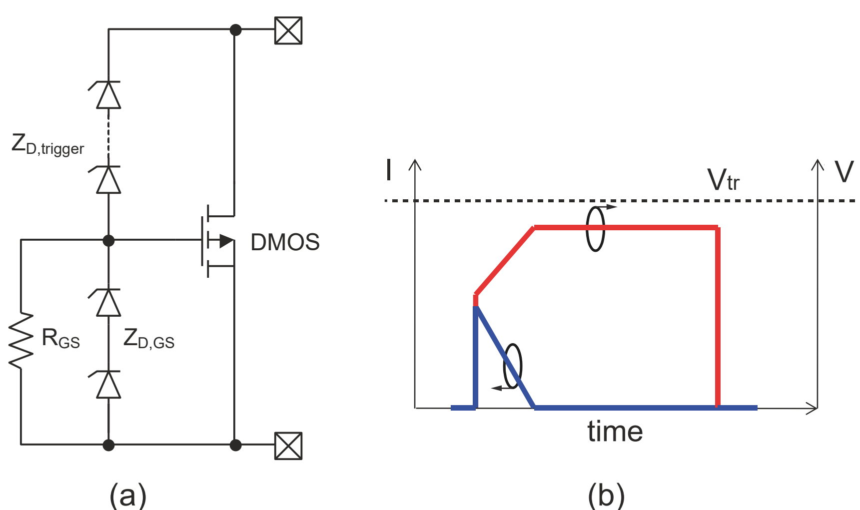

Figure 4.26: (a) The schematic of a Zener-triggered active clamp with gate discharge resistor R_{GS} and gate protection $Z_{D,GS}$. (b) The transient turn-on of the DMOS due to gate coupling showing typical I-V waveforms when the stress voltage is below the designed V_{tr}.

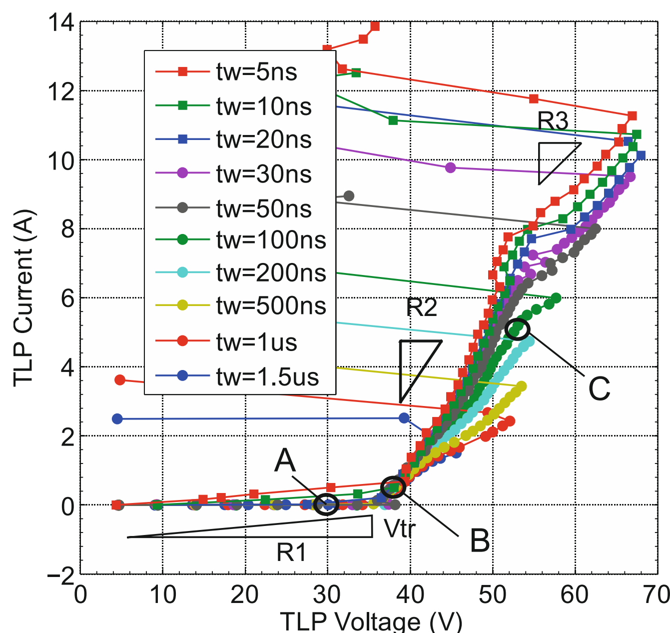

Figure 4.27: TLP characteristic of a 25 V active clamp with tw from 5 ns to 1.5 µs. R1 represents the transient turn-on behavior of active clamp where R2 and R3 represent different Ron after V_{tr} is reached.

Spectre modeling approach can be involved to accurately model the parasitic capacitances and the DMOS transistor in terms of the transient turn-on behavior [82] [83]. The consideration of self-heating under ESD conditions would be however very complicated using thermoelectric elements. On the contrary, the proposed behavior modeling in this work assumes that the active clamp exhibits a finite on-resistance also for $V<V_{tr}$ under short pulses. This effectively translates the transient turn-on of the active clamps into a t_w dependent R_{on}. Figure 4.27 shows the TLP characteristics of a 25 V active clamp: here R1 is defined for the segment between 0 V and V_{tr}. Figure 4.28 shows the agreement of data and model for 100 ns TLP with different voltage and current pairs indicated in Figure 4.27.

For the failure estimation of the active clamps, P_{max} is built in the model as electrical limit in addition to E_f. Simulation and measurement with IEC-like pulses confirms the prediction of the electrically induced failure and the failure level as shown in Figure 4.29. Note that there is a mismatch of the transient voltage waveforms after the device damage, which is not meant to be correctly modeled. The silicon melting in the device after damage exhibits a time dependent degradation leading to leakage increase. In the simulation however, the device model is simply switched to a 1 Ω resistance to indicate the failure.

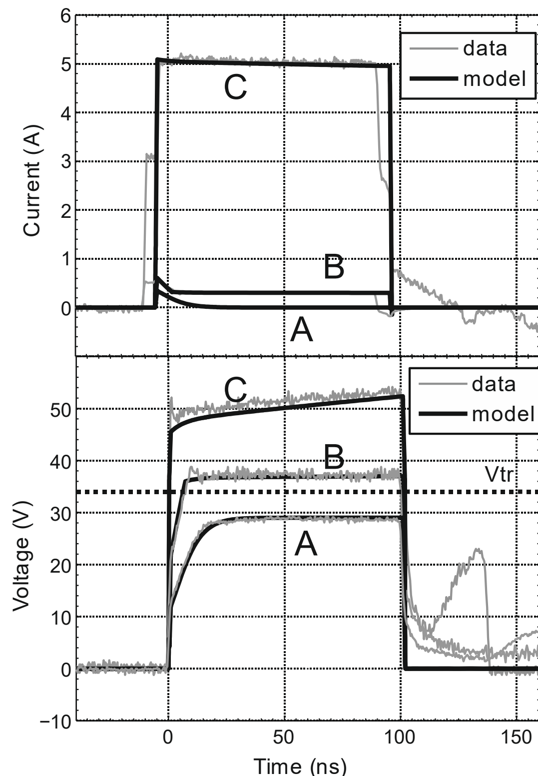

Figure 4.28: Comparison of Wunsch-Bell based model and TLP data with respect to transient responses of the active clamp. “A”, “B” and “C” denote the corresponded I-V waveforms.

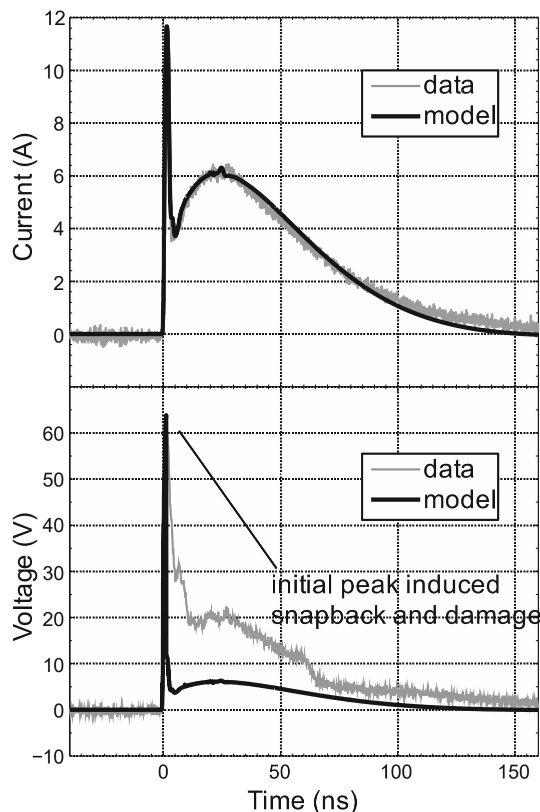

Figure 4.29: Simulated and measured waveforms for the active clamp stressed by IEC-like pulses at 3 kV IEC level (stress to failure). Electrical failure is observed both in simulation and measurement.

4.2.2.3 npn-BJT

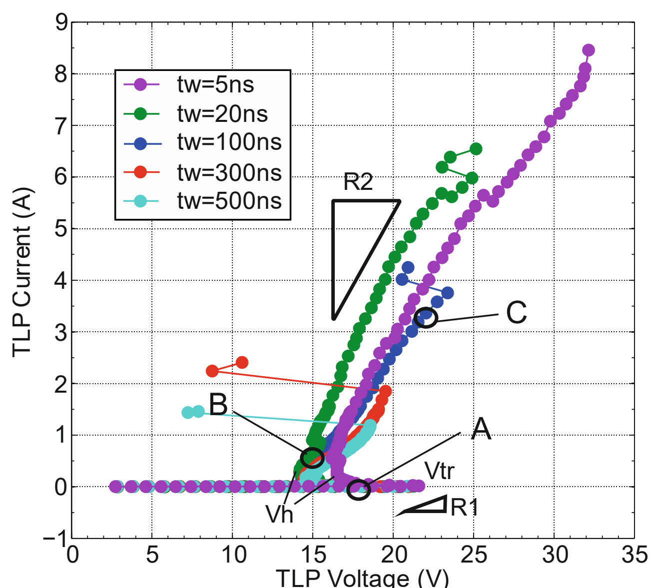

Figure 4.30: TLP characteristic of a 25 V active clamp with tw from 5 ns to 1.5 µs. R1 represents the transient turn-on behavior of active clamp where R2 and R3 represent different Ron after Vtr is reached.

Modeling of snapping ESD structures often encounters convergence problems in simulation. The behavior modeling methodology can be applied to snapping ESD elements without suffering from convergence issues. In addition, the self-heating behavior is also modelled using this methodology. An npn-BJT implemented in a power technology exhibiting snapback characteristic was chosen as another modeling example. The device characterization was introduced in Chapter 3. The TLP characteristics with various pulse durations are shown in Figure 4.30 with the focus on modeling. Note that for $t_w = 5\ ns$, the holding voltage V_h seems to be larger than for longer t_w. This is explained by the snapback process of the bipolar transistor, which takes several nanoseconds. The transient snapback from the trigger voltage to the steady-state voltage i.e. the holding voltage can last longer than 5 ns. The averaged pulse voltage in the first few nanoseconds is thus larger than the real V_h. Similar to the modeling of the transient turn-on behavior of active clamps, a virtual t_w-dependence of V_h can be utilized in the modeling to reproduce the snapback process of the device. With this approach, one can use the proposed methodology to model very complex behavior of snapping ESD devices such as specific turning-on and self-heating effects. Figure 4.31 confirms the agreement between model and measurement data with respect to transient waveforms in 100ns TLP. “A” to “C” indicate again the voltage and current waveforms corresponding to the I-V points in the TLP characteristics (Figure 4.30).

For the validation of the device model in reproducing the failure level, the same IEC-like pulse generator as in the study of non-snapping ESD protection elements is applied to the npn-BJT. The device fails thermally at 2.5 kV according to both, simulation and measurement (Figure 4.32).

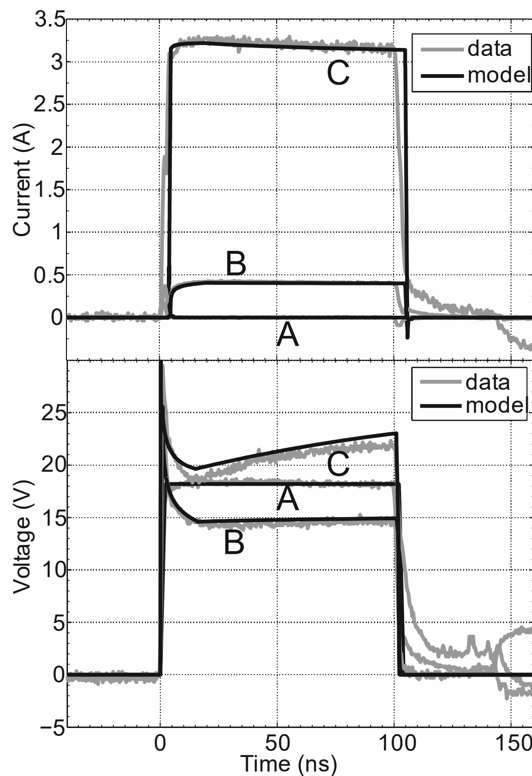

Figure 4.31: Comparison of Wunsch-Bell based model and TLP data regarding transient responses of the npn-BJT. “A”, “B” and “C” denote the corresponding I-V waveforms.

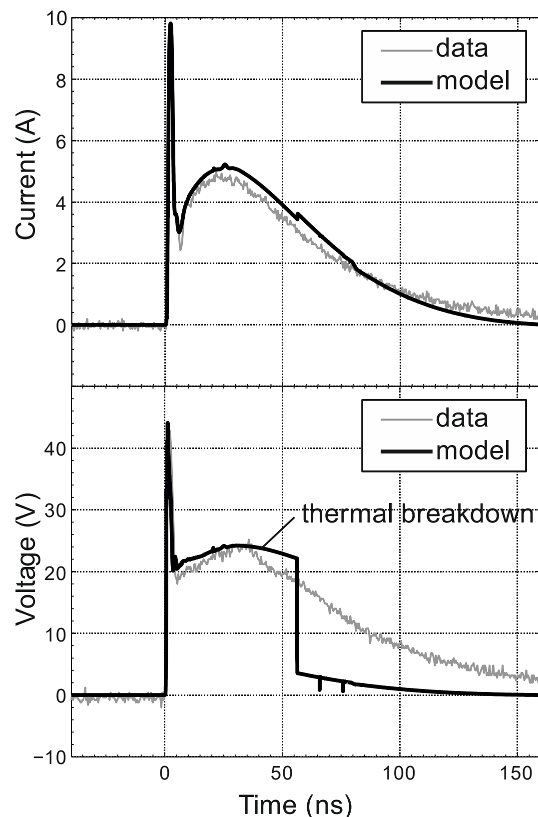

Figure 4.32: Simulated and measured waveforms for the npn-BJT stressed by IEC-like pulses at 2.5 kV IEC level (stress to failure). Thermal failure is observed both in simulation and test.

As a conclusion for the modeling examples demonstrated in this section, the Wunsch-Bell based behavior modeling is widely applicable for different types of ESD devices and circuits. The investigated stand-alone structures are modeled to reproduce self-heating and failure levels which are validated with experimental data.

4.2.3 Application of the Behavior Models

4.2.3.1 ESD Co-Design on PCB

As the on-chip ESD protection elements are characterized and described in VHDL-AMS, one of the most interesting applications of the models is the prediction of system-level ESD robustness. To achieve the ESD target level of the circuit on board, the co-design of on- and off-chip protection elements is often necessary. Capacitor, multi-layer varistor (MLV), TVS-diode et cetera are commonly employed as off-chip ESD protection elements. The ESD characterization of the off-chip elements are extensively discussed in the previous section. In general, accurate ESD simulations substantially help to select the proper off-chip devices in the system (PCB) design in an early stage of the product design e.g. ECU for automotive applications.

Combinations of diverse on-chip protection elements with off-chip devices are simulated and measured showing the straightforward application of the proposed modeling methodology. In the simulation setups, a discharge lumped element network including parasitic RLC is used as a common ESD generator (IEC) model which is similar to [112].

In the measurements, the on-chip ESD devices introduced earlier are assembled in the plastic package LQFP-64 and placed in a test socket on PCB. The ESD generator TESEQ NSG438 with the discharge network 150 pF/330 Ω is used to perform the system-level ESD tests. Figure 4.33 shows a photograph of the test PCB board with external devices and the IC socket. The pin to ground I-V characteristic by curve tracing before and after each stress is used for monitoring the leakage current as detection of the failure level in the IEC tests.

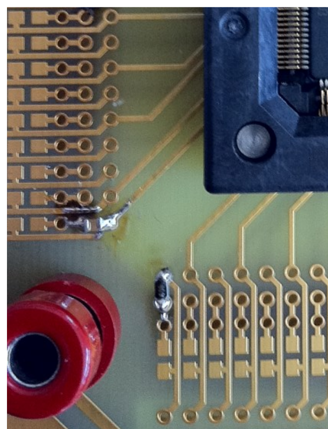

Figure 4.33: Photograph of the test PCB. Board traces, package and socket parasitics have negligible impact on the system-level ESD robustness in this design.

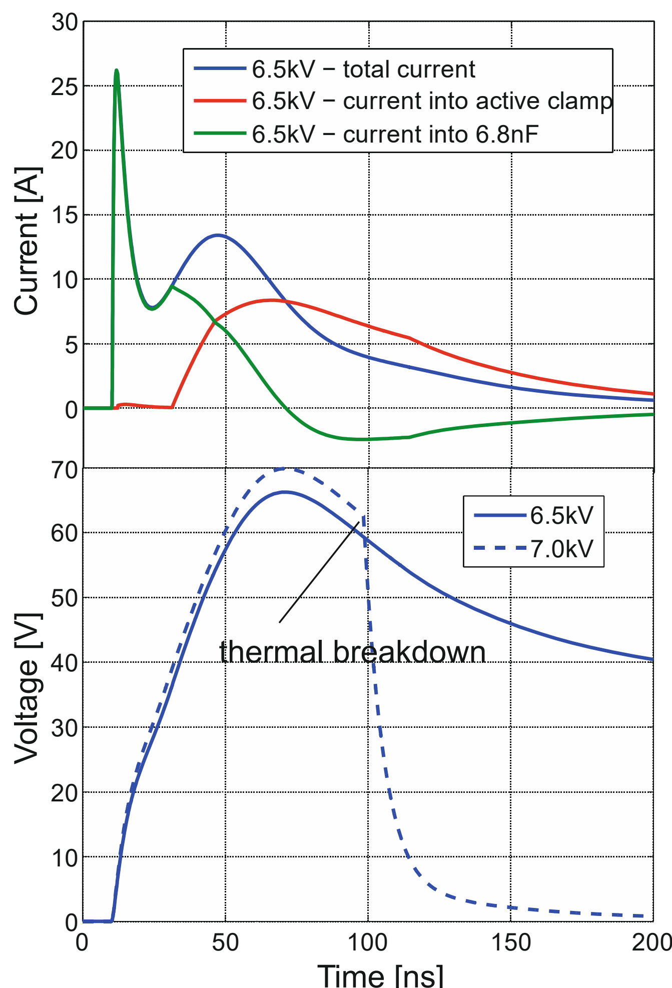

Figure 4.34: Simulated waveforms of a 6.8 nF ceramic capacitor in parallel to an on-chip 25 V active clamp under IEC stress. The current distribution is shown at 6.5 kV. The failing stress caused by thermal breakdown of the active clamp occurs at 7 kV.

The stand-alone active clamp fails at 3 kV stress level of IEC-like pulses according to the HMM measurement. The same failure level is confirmed by the IEC tests using the ESD generator. The simulation predicts an improved total ESD robustness of about 6.5 kV of the active clamp in conjunction with a parallel 6.8 nF ceramic capacitor. The on-chip active clamp fails in this case thermally rather than electrically in the stand-alone case according to the simulated waveforms (Figure 4.34). This result is validated by applying IEC tests where the failure occurs at 6.5 kV to 7kV stress levels.

Another example of ESD co-design is shown by using a 45 V pn-diode as the on-chip protection. A varistor with typical turn-on voltage of 60 V is used as the off-chip ESD device. The 100 ns TLP characteristic of the varistor is illustrated in Figure 4.35. The turn-on voltage is larger than V_{tr} of the on-chip diode (Figure 4.20). Note that the model of the varistor is simply generated using 100 ns TLP curves because the self-heating of off-chip devices is usually not as significant as for the on-chip devices due to their much higher energy dissipation capability. The stand-alone diode fails at approximately 6 kV IEC stress. According to the simulation, the failure level of the combined ESD protection – the ESD diode and the varistor - increases significantly to 19 kV. This is again confirmed by the test results.

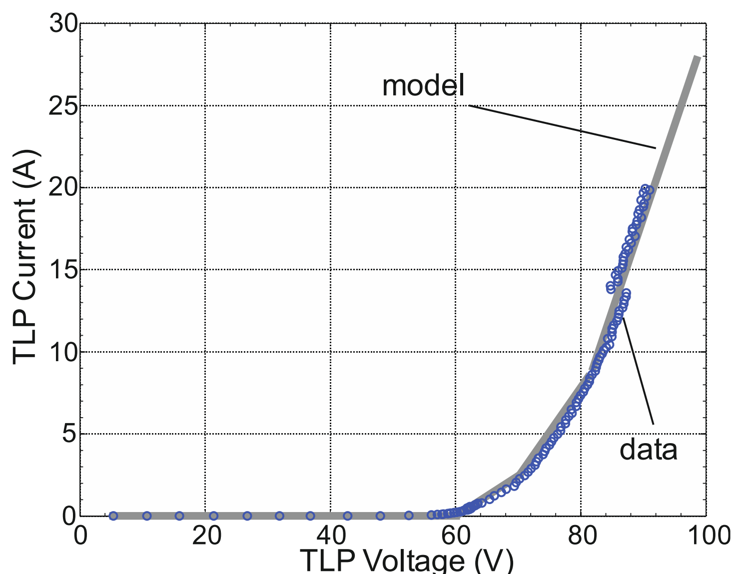

Figure 4.35: 100 ns TLP characteristic of the varistor. The model is generated using 100 ns TLP without self-heating effect.

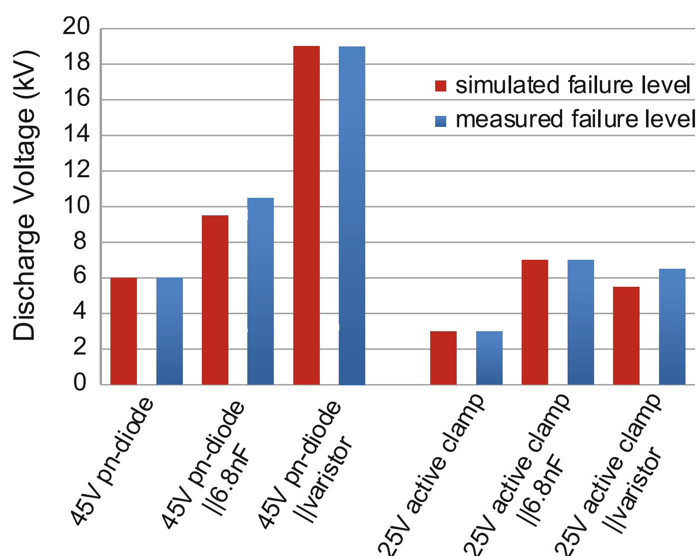

Figure 4.36: Comparison of simulated and measured failure levels (0.5 kV steps) for different combinations with on- and off-chip ESD protections.

Figure 4.36 further summarizes several system-level co-design case studies, clearly showing the accuracy of predicting the ESD robustness of the protection networks with the Wunsch-Bell based modeling methodology.

4.2.3.2 Various System-Level ESD Discharge Models

Due to the characterization of wide range of pulse width t_w, the proposed behavior models can also be used to estimate the ESD robustness of the DUTs when applying other system-level pulses such as defined in ISO 10605 [113]. In addition to the discharge network (150 pF/330 Ω) as defined in IEC 61000-4-2, the ISO 10605 standard includes more C/R values such as 330 pF/330 Ω, 150 pF/2 kΩ and

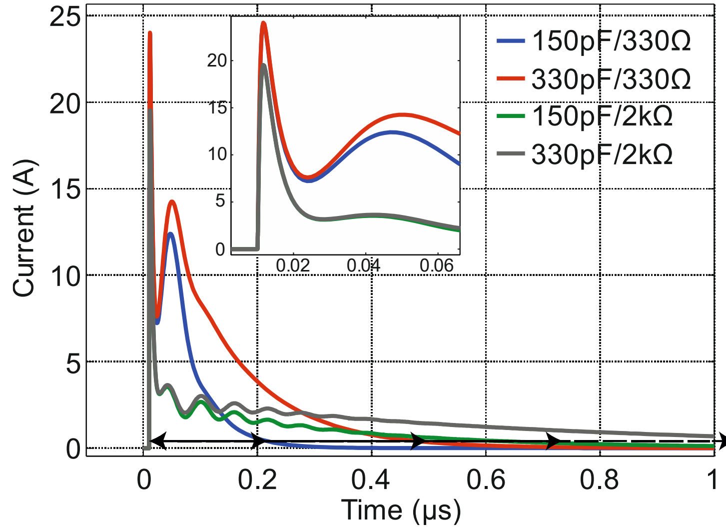

Figure 4.37: Simulated current waveforms of different discharge models showing different pulse duration at 6 kV on a 2 Ω load.

330 pF/2 kΩ, which represent various pulse lengths due to different time constants as depicted in Figure 4.37. The shown current waveforms are simulated 6 kV discharge into a 2 Ω load.

The 45 V pn-diode and 25 V active clamp are used as DUTs in this investigation. Table 4.2 and Table 4.3 show the devices robustness for the different discharge models obtained by simulation and measurement. The measurement results verify the simulation results. Note that for the 45 V pn-diode a certain mismatch is observed between data and model for the 330 pF/2 kΩ discharge network. The 330 pF/2 kΩ pulse shows the longest duration, i.e. time constant (Figure 4.37). Hence the mismatch gives an indication of the limit of the diode model which only reproduce the diode behavior for up to $t_w = 1.5\ \mu s$ pulses. This issue however does not affect the results for the active clamp since the device failure is induced by the first IEC peak (electrical failure).

Table 4.2: Comparison of data and model for the 45 V pn-diode stressed by different discharge networks according to ISO 10605.

45 V pn-diode	Sample	Model		Data	
C/R		Pass	Fail	Pass	Fail
150 pF/330 Ω	1	5.5 kV	5.6 kV	5.5 kV	6.0 kV
330 pF/330 Ω	1	4.1 kV	4.2 kV	4.0 kV	4.5 kV
	2			4.0 kV	4.5 kV
150 pF/2 kΩ	1	11.9 kV	12.0 kV	11.0 kV	11.5 kV
	2			10.5 kV	11.0 kV
330 pF/2 kΩ	1	8.8 kV	8.9 kV	7.0 kV	7.5 kV
	2			6.5 kV	7.0 kV

Table 4.3: Comparison of data and model for the 25 V active clamp stressed by different discharge networks according to ISO 10605.

25 V active clamp	Sample	Model		Data	
C/R		Pass	Fail	Pass	Fail
150 pF/330 Ω	1	2.7 kV	2.8 kV	2.5 kV	3.0 kV
330 pF/330 Ω	1	2.7 kV	2.8 kV	2.5 kV	3.0 kV
	2			2.5 kV	3.0 kV
150 pF/2 kΩ	1	3.4 kV	3.5 kV	2.5 kV	3.0 kV
	2			3.0 kV	3.5 kV
330 pF/2 kΩ	1	3.4 kV	3.5 kV	3.0 kV	3.5 kV
	2			3.0 kV	3.5 kV

4.2.4 Summary

The presented behavior modeling method is portable and easy-to-implement. Good correlations between silicon measurements and simulations have been achieved validating the methodology and the models. Details of the application examples including system-level ESD co-design and impact of different pulses on the robustness of the ESD devices are given. During the Wunsch-Bell characterization a wafer-level TLP setup is used which minimizes parasitic effects. In the system-level tests, the parasitic of the used test PCB, package and socket in the case studies has no significant impact on the simulation results. The robustness of the on-chip in conjunction with the off-chip devices is simulated and validated by the measurement results.

The main advantage of the proposed modeling methodology is the behavior description based on the profound TLP measurements. It avoids the emulation of physical parameters or circuit details, which can be complicated. The presented methodology easily allows generalizing the modeling method to different types of ESD protection elements. On the other hand however, the main drawback of the proposed behavior model is also due to the lack of the physical basis. The self-heating effect is obtained with the fitting function $R_{on} = f(t_w)$ which is derived from the TLP tests. In the real applications, the ESD pulse waveforms differ usually a lot from the rectangular TLP pulses. Fortunately, most of the real-world ESD pulses exhibit an exponential decay, where at the long tale of the pulse the current level is low enough so that the self-heating is not significant anymore. The inaccuracy of the R_{on} estimation for this pulse part is therefore negligible.

The application range of the proposed behavior modeling can be extended. In this study, the model is valid up to pulse length of 1.5 µs. An extended characterization up to the milliseconds range would enable the simulation of the robustness of protected devices and circuits stressed by electrical fast transient (EFT) or disturbances such as defined in ISO 7637 [114] [115] [116]. Moreover, for on-chip ESD design, with the ESD window given by the circuits being protected, different types of protection schemes can be simulated using the introduced modeling method to achieve the optimal design considering the area consumption and target robustness. The underestimation of the ESD device capability due to models without self-heating can lead to ESD overdesign and must be avoided with a cost efficient design.

4.3 Conclusion

The traditional characteristics of the off-chip protection devices provided in their data sheets are based on the data measured under DC or surge pulse conditions, which are only of limited usefulness for the evaluation of their ESD protection capabilities. In this Chapter, the off-chip protection devices including resistors, capacitors, varistors and other voltage limiting elements are characterized in the ESD time and power domain. With the presented characterization methods, on one hand the devices' behavior such as voltage overshoots and device degradation under ESD conditions is shown, which give a first instruction suggesting the proper ESD protection depending on the applications. On the other hand, the characterization of the protection devices enables the ESD modeling which is of essential importance for the ESD design on the module or PCB level.

The characterization of the off-chip protection is important. The same characterization methods can be also applied to the on-chip protection in an extended way. Because of cost reasons, the on-chip protection devices are usually only capable of limited ESD power and show more significant self-heating effects compared to the off-chip protection devices. It requires a more sophisticated modeling methodology to reproduce the devices' behaviors for ESD simulation. The presented modeling methodology is developed based on the so-called Wunsch-Bell characterization for DUT measured using various pulse widths. Using R_{on} modulation, failure power and failure energy criteria, the transient response as well as the failure level of the different types of on-chip ESD protection devices are reproduced in the ESD simulation. With the help of the off-chip device's models, representative ESD co-design investigations are carried out, showing agreement of the measurement and simulation results. The described ESD modeling methodology enables further data exchange between semiconductor vendor, Tier1 and OEM without concerning sensitive IP sharing. The ESD model is generated using a black-box approach.

Chapter 5
Conclusion and Outlook

This work has presented a variety of on-chip high-voltage ESD protection elements and their characterizations in a smart power technology that is used for automotive and industrial IC products with wide portfolios. The so-called Wunsch-Bell characterization – pulse length dependent failure levels - for typical on-chip ESD protection elements on different device concepts is systematically applied that not only enables detailed investigation and understanding of device failure mechanisms during ESD or longer disturbance pulses. The unique failure mode that was studied and understood in detail for the lateral DMOS transistors received large interest in the industry-wide ESD community.

The work also opens up a way of thinking in how efficient ESD protection and co-design of on-chip and on-board at system-level can be made. Only 100 ns TLP based IC characteristics cannot sufficiently provide required information that can predict the failure levels especially when the pulse shape and length is significantly different to ESD pulses like HBM. In the applications, e.g. in production of electronic components, it is the case that a large variety of disturbance pulses exist. Hence, the pulse length dependent models are essential for accurate ESD or EOS simulation. The modeling methodology not only can be used for system-level simulation and co-design, but also can be used for IC level ESD or ISO7637 protection concept design. In the follow-up studies, the modeling methodology is further improved to a more generic method that on one hand makes ESD or EOS troubleshooting much easier, and on the other hand even enables more requirements driven IC protection design in pre-silicon phase [118] [119] [120] [121].

In this work, different on-chip protection device concepts are compared concerning their failure levels and failure mechanisms. It shows advantage and disadvantage of each device concept. The knowledge is necessary for developing high performance protection devices and for choosing adequate device for protection depending on requirements. The novel high-voltage active clamps published as an invited paper on IEEE Transaction on Device and Materials Reliability [83] gains follow-up study and application even in the advanced CMOS world. Regarding the high-voltage active clamps that are more sophisticated clamps can be developed in the upcoming power

technologies with more advanced features, e.g. snapback clamps with self-switched-off capability.

ESD measurement technique and equipment is always a challenge as ESD pulses are high power and very fast pulses. In this work, several useful measurement methods e.g. rise-time filter and HMM tester are developed that enable advanced characterization and testing of protection devices. As new requirements and special device physical effects will be more and more discovered, ESD measurement technique is one of the important development areas in the modern ESD protection engineering.

Overall, an inside-out study of ESD and EOS protection has been presented in this work. From the exploration of detailed device-level physical phenomenon to the consideration of system-level protection optimization aspect, this work gives a brief overview of ESD protection in a smart power technology that supports further studies in this area of knowledge.

List of Abbreviations

AEC. *Automotive Electronics Council*

bigMOS. *big DMOS transistor*

BJT. *Bipolar Junction Transistor*

CAN. *Controller Area Network*

CDM. *Charged Device Model*

DMOS. *Double-diffused MOSFET*

DUT. *Device Under Test*

ECU. *Electronic Control Unit*

EFT. *Electrical Fast Transients*

EOS. *Electrical Overstress*

ESD. *Electrostatic Discharge*

ESDA. *EOS/ESD Association*

gc-nLDMOS. *gate-coupled nLDMOS*

gg-nLDMOS. *grounded-gate nLDMOS*

ggNMOS. *grounded-gate NMOS*

HBM. *Human Body Model*

HMM. *Human Metal Model*

I/O. *Input/Output*

IC. *Integrated Circuit*

IEC. *International Electrotechnical Commission*

IFR. *Initial Front Rise*

ISO. *International Organization for Standardization*

LED. *Light-Emitting Diode*

LIN. *Local Interconnect Network*

LQFP. *Low Profile Quad Flat Package*

MLV. *Multi-Layer Varistor*

MOSFET. *Metal-Oxide-Semiconductor Field-Effect Transistor*

nDMOS. *n-type DMOS*

nLDMOS. *n-type Lateral DMOS*

PCB. *Printed Circuit Board*

pDMOS. *p-type DMOS*

PPV. *Pre-Pulse Voltage*

SCR. *Silicon Controlled Rectifiers*

SEED. *System-Efficient ESD Design*

SMA. *SubMiniature version A*

SMD. *Surface-Mounted Device*

SMU. *Source Measurement Units*

SOA. *electrical Safe Operating Area*

STI. *Shallow Trench Isolation*

TCAD. *Technology Computer-Aided Design*

TDDB. *Time-Dependent Dielectric Breakdown*

TDR. *Time-Domain Reflectometry*

TLP. *Transmission Line Pulse*

TVS. *Transient Voltage Suppressor*

Bibliography

[1] H. Wallentowitz and K. Reif, Handbuch Kraftfahrzeugelektronik, 2. Auflage, Vieweg+Teubner Verlag, 2011.

[2] R. Rudolf, et al. “Automotive 130 nm Smart-Power-Technology including embedded Flash Functionality,” in Proc. ISPSD, 2011.

[3] ISO 26262-1: 2011(E) “Road vehicles — Functional safety — Part 1: Vocabulary.”

[4] IEC 61000-4-4: 2012(E) “Electromagnetic compatibility (EMC) – Part 4-4: Testing and measurement techniques – Electrical fast transient/burst immunity test.”

[5] ESDA/JEDEC “Joint Standard for Electrostatic Discharge Sensitivity Testing – Charged Device Model (CDM) – Device Level,” ANSI/ESDA/JEDEC JS-001-2014.

[6] AEC-Q100-002 Rev-E “Human Body Model (HBM) Electrostatic Discharge Test,” Automotive Electronics Council, 2013.

[7] AEC-Q100-011 Rev-C1 “Charged Device Model (CDM) Electrostatic Discharge Test,” Automotive Electronics Council, 2013.

[8] C. Reiman et al. “Practical Methodology for the Extraction of SEED Models,” in Proc. EOS/ESD Symposium, 2015.

[9] T. Li, et al. “An application of utilizing the system-efficient-ESD-design (SEED) concept to analyze an LED protection circuit of a cell phone,” in Proc. IEEE International Symposium on Electromagnetic Compatibility (EMC), 2012.

[10] White Paper 3: “System Level ESD Part II: Implementation of Effective ESD Robust Designs,” Industry Council on ESD Target Levels, 2012.

[11] White Paper 4: “Understanding Electrical Overstress,” Industry Council on ESD Target Levels, 2016.

[12] W. Stadler, et al. "From the ESD robustness of Products to the System ESD Robustness," in Proc. EOS/ESD Symposium, 2004.

[13] A. Ille, et al. "Reliability aspects of gate oxide under ESD pulse stress," in Microelectronics Reliability 49, pp. 1407–1416, 2009.

[14] G. Boselli, "On High Injection Mechanisms in Semiconductor Devices under ESD Conditions," Dissertation, 2001.

[15] S. Scheier, et al. "Simulation of ESD Thermal Failures and Protection Strategies on System Level," in IEEE Transactions on Electromagnetic Compatibility vol. 57, no. 6, pp. 1309-1319, 2015.

[16] M. Mergens, "On-Chip ESD Protection in Integrated Circuits: Device Physics, Modeling, Circuit Simulation," Dissertation, published by Hartung-Gorre Verlag, 2001.

[17] V. Vashchenko and M. Scholz, System Level ESD Protection, Springer International Publishing, 2014.

[18] T. Maloney and N. Khurana, "Transmission Line Pulsing Techniques for Circuit Modeling of ESD Phenomena," in Proc. EOS/ESD Symposium, pp. 49-54, 1985.

[19] D.C. Wunsch and R.R. Bell, "Determination of threshold failure levels of semiconductor diodes and transistors due to pulse voltages," in IEEE Trans. Nuc. Sci., NS-15 244-259, 1968.

[20] Y. Cao, et al. "Rise-Time Filter Design for Transmission-Line Pulse Measurement Systems," in German Microwave Conference (GeMiC), pp. 1-4, 2009.

[21] H. Johnson, "High-Speed Digital Design," Prentice-Hall PTR, 1993.

[22] A. R. Djordjevic, et al. "On a Class of Low-Reflection Transmission-Line Quasi-Gaussian Low Pass Filters and Their Lumped-Element Approximations," in IEEE Trans. on Microwave Theory and Techniques, vol. 51, pp. 871–877, 2003.

[23] J. Breitbarth, et al. "Absorptive Near-Gaussian Low Pass Filter Design with Applications in the Time and Frequency Domain," in IEEE Microwave Symposium Digest, MTT-S International, vol. 3, pp. 1303–1306, 2004.

[24] http://www.fastfieldsolvers.com

[25] http://www.agilent.com/

[26] http://www.mentor.com/

[27] http://www.coilcraft.com/

[28] http://www.atceramics.com/

[29] IEC/EN 61000-4-2: 2008 "Electromagnetic compatibility (EMC) - Part 4-2: Testing and measurement techniques - Electrostatic discharge immunity test", IEC International Standard.

[30] W. Stadler, et al. "From the ESD Robustness of Products to the System ESD Robustness," in Proc. EOS/ESD Symposium, pp. 67–74, 2004.

[31] S. Frei, et al. “Packaging- und Handling-Prüfungen nach ISO 10605: Wie vergleichbar sind Prüfungen mit unterschiedlichen ESD Generatoren?” in ESD Forum e.V., pp. 89–97, 2007.

[32] http://www.esda.org

[33] E. Grund, et al. “ESD Testing of Devices by Delivering the IEC 61000-4-2 Current Pulse through a Transmission Line”, in ESD Forum e.V., 2007.

[34] E. Grund, et al. “Delivering IEC 61000-4-2 Current Pulses through Transmission Lines at 100 and 330ohm System Impedances,” in Proc. EOS/ESD Symposium, pp. 132–141, 2008.

[35] K. Muhonen, et al. “Failure Detection with HMM Waveforms,” in Proc. EOS/ESD Symposium, 2009.

[36] M. Scholz, et al. “On-wafer Human Metal Model – system-level ESD stress on component level”, in Proc. RCJ EOS/ESD/EMC Symposium, pp. 91-97, 2008.

[37] M. Scholz, et al. “On-Wafer Human Metal Model Measurements for Sys-tem-Level ESD Analysis,” in Proc. EOS/ESD Symposium, 2009.

[38] Y. Cao, et al. “A TLP-based Human Metal Model ESD-Generator for Device Qualification according to IEC 61000-4-2,” in APEMC Symposium, 2010.

[39] D. Johnsson et al. “Avalanche Breakdown Delay in High-Voltage p-n Junctions Caused by Pre-Pulse Voltage from IEC 61000-4-2 ESD Generators,” in IEEE Transactions on Device and Materials Reliability, Volume 9, No. 3, pp. 412-418, 2009.

[40] E. Grund, “VF-TLP wafer level performance based on probe needle con-figuration”, in ESD Forum e.V., pp. 127-136, 2005.

[41] F. zur Nieden, et al. “Vergleich von ESD-System-Level Testmethoden für Packaging und Handling,” in ESD Forum e.V., 2009.

[42] M. Honda, “Measurement of ESD-gun Radiated Fields,” in Proc. EOS/ESD Symposium, pp. 323–327, 2007.

[43] K. Wang, et al. “Characterization of Human Metal ESD reference discharge event and correlation of generator parameters to failure levels – part II: Correlation of generator parameters to failure levels”, in IEEE Trans. EMC, Vol. 46, No. 4, pp. 505–511, 2004.

[44] Y. Cao et al., “A Failure Levels Study of Non-Snapback ESD Devices for Automotive Applications,” in Proc. IEEE IRPS, 2010.

[45] SP5.6-2008, “Electrostatic discharge sensitivity testing - human metal model (HMM),” in ESDA Tech. Rep., 2009.

[46] D. A. Neamen, an Introduction to Semiconductor Devices, 1st.ed. McGraw-Hill Companies, Inc., 2006.

[47] K. Esmark et al., “Transient Behavior of SCRs during ESD Pulses,” in Proc. IEEE IRPS, pp. 247-253, 2008.

[48] D. Linten et al., “Extreme Voltage and Current Overshoots in HV Snapback Devices during HBM ESD Stress,” in Proc. EOS/ESD Symposium, 2008.

[49] S. M. Sze and Kwok K. Ng, Physics of Semiconductor Device, 3rd.ed. New Jersey, USA: John Wiley & Sons, Inc., 2007.

[50] A. Z. H. Wang, On-Chip ESD Protection for Integrated Circuits – An IC Design Perspective, Massachusetts, USA: Kluwer Academic Publishers, 2002.

[51] K. Esmark, “Device Simulation of ESD Protection Elements,” Dissertation, pp. 60-69, 2001.

[52] A. Amerasekera and C. Duvvury, ESD in Silicon Integrated Circuits, 2rd ed. West Sussex, England: John Wiley & Sons, Ltd, 2002.

[53] H. Egawa, “Avalanche characteristics and failure mechanism of high voltage diodes,” in IEEE Transactions on Electron Devices, Volume 13, Issue 11, pp.754 – 758, 1966.

[54] http://www.synopsys.com/tools/tcad/

[55] M. Mergens et al, “ESD Protection Considerations in Advanced High- Voltage Technologies for Automotive,” in Proc. EOS/ESD Symposium, pp. 54-63, 2006.

[56] V. Dwyer. A. Franklin and D. Campbell, “Thermal Failure in Semiconductor Devices,” in Solid-State Electronics. Vol. 33. No. 5. pp. 553-560, 1990.

[57] V. Dwyer. A. Franklin and D. Campbell, “Electrostatic Discharge Thermal Failure in Semiconductor Devices,” in IEEE Transactions on Electron Devices, Volume 37 No. 11, pp. 2381-2387, 1990.

[58] M. Stockinger et al, “Boosted and Distributed Rail Clamp Networks for ESD Protection in Advanced CMOS Technologies,” in Proc. EOS/ESD Symposium, 2003.

[59] J. Willemen et al, “A TLP-Based Characterization Method for Transient Gate Biasing of MOS Devices in High-Voltage Technologies,” in Proc. EOS/ESD Symposium, 2010.

[60] M. Denison, “Single Stress Save Operating Area of DMOS Transistors integrated in Smart Power Technologies,” Dissertation, pp. 40-47, published by Shaker Verlag, 2004.

[61] C.T. Kirk, Jr., “A theory of transistor cut-off frequency (f_t) fall-off at high current densities”, in IRE Transactions on Electron Devices, Volume ED-9, pp. 164 – 174, Mar. 1962.

[62] U. Glaser, “Complex ESD Protection Elements and Issues in Deca-nanometre CMOS Technologies,” Dissertation, pp. 18-21, published by Hartung-Gorre Verlag, 2007.

[63] Y. Cao et al., “On the Dynamic Destruction of LDMOS Transistors beyond Voltage Overshoots in High Voltage ESD,” in Proc. EOS/ESD Symposium, 2010.

[64] T. Smedes et al., “Harmful Voltage Overshoots Due to Turn-On Behavior of ESD Protections during Fast Transients”, in Proc. EOS/ESD Symposium, pp. 357-365., 2007.

[65] Y. Chung et al., “Snapback Breakdown Dynamics and ESD Susceptibility of LDMOS”, in Proc. IEEE IRPS, pp. 352-355, 2006.

[66] M. Mergens et al., “Analysis of lateral DMOS power devices under ESD stress conditions”, IEEE Transactions on Electron Devices, Volume 47, Issue 11, Nov. 2000, pp. 2128-2137.

[67] V. Vashchenko et al., “Voltage Overshoot Study in 20V DeMOS-SCR Devices”, in Proc. EOS/ESD Symposium, 2007.

[68] A. Lacaita et al., “Observation of avalanche propagation by multiplication assisted diffusion in p-n junctions”, in Appl. Phys. Lett. 57(5), 1990, pp. 489-491.

[69] J. Liou et al., “Transient Safe Operating Area (TSOA) Definition for ESD Applications”, in Proc. EOS/ESD Symposium 2009.

[70] H.A. Gieser et al., “Survey on very fast TLP and ultra-fast repetitive Pulsing for Characterization in the CDM-Domain”, in Proc. IEEE IRPS 2007, pp. 324-333.

[71] S. Reggiani et al., “Explanation of the Rugged LDMOS Behavior by Means of Numerical Analysis”, in IEEE Transactions on Electron Devices, Vol. 56, No. 11, pp. 2811-2818, November 2009.

[72] D. Pogany et al., “Nonlinear dynamics approach in modeling of the on-state-spreading-related voltage and current transients in 90nm CMOS silicon controlled rectifiers”, in Proc. IEDM 2009.

[73] J. Barth et al., “Voltages Before and After Current in HBM Testers and Real HBM”, in Proc. EOS/ESD Symposium 2005.

[74] R. Ashton et al., “Pre Pulse Voltage in the Human Body Model”, in Proc. EOS/ESD Symposium 2006, pp. 326-334.

[75] J. Barth et al., “Correlation Considerations: Real HBM to TLP and HBM Testers”, in Proc. EOS/ESD Symposium 2001, pp. 453-460.

[76] J. Barth et al., “Correlation Considerations II: Real HBM to HBM Testers”, in Proc. EOS/ESD Symposium 2002, pp.155-162.

[77] O. Quittard et al., “ESD Protection for High-Voltage CMOS Technologies,” in Proc. EOS/ESD Symposium 2006.

[78] G. Notermans et al., “Designing HV Active Clamps for HBM Robustness,” in Proc. EOS/ESD Symposium 2007.

[79] J. Smith et al., “A MOSFET Power Supply Clamp with Feedback Enhanced Triggering for ESD protection in Advanced CMOS Technologies,” in Proc. EOS/ESD Symposium 2003.

[80] A. Gerdemann et al., “When Good Trigger Circuits Go Bad: A Case History,” in Proc. EOS/ESD Symposium 2011.

[81] J. Li et al., “A compact, timed-shutoff, MOSFET-based power clamp for on-chip ESD protection,” in Proc. EOS/ESD Symposium 2004.

[82] Y. Cao et al., “Statically Triggered Active ESD Clamps for High-Voltage Applications,” in Proc. EOS/ESD Symposium 2012.

[83] Y. Cao et al., “Novel Active ESD Clamps for High-Voltage Applications,” in IEEE Transactions on Device and Materials Reliability, Volume 13, Issue 2, June 2013, pp. 388-397.

[84] A. Gendron et al., “New High Voltage ESD Protection Devices Based on Bipolar Transistors for Automotive Applications,” in Proc. EOS/ESD Symposium 2011.

[85] ESDA/JEDEC “Joint Standard for Electrostatic Discharge Sensitivity Testing – Human Body Model (HBM) – Component Level”, ANSI/ESDA/JEDEC JS-001-2017.

[86] F. Roger et al., “Process variation aware ESD Design Window considerations on a 0.18µm Analog, Mixed Signal High Voltage Technology,” in Proc. EOS/ESD Symposium 2011.

[87] D. Johnsson et al., “Avalanche Breakdown Delay in ESD Protection Diodes”, IEEE Transactions on Electron Devices, Volume 57, No. 10, Sep. 2010, pp. 2470-2476.

[88] Y. Cao et al. "ESD troubleshooting using multi-level TLP," in Proc. EOS/ESD Symposium 2014.

[89] A. Rupp et al., “Active Clamp Design for On-Chip GUN Protection”, in Proc. EOS/ESD Symposium 2015.

[90] Y. Cao et al.,“ Charakterisierung und systematische Bewertung von externen ESD Schutzelementen”, EMV-Düsseldorf, Germany, 2010.

[91] B. Arndt et al., “ Modellierung und Simulation von ESD-Schutzelementen mit VHDL-AMS”, EMV-Düsseldorf, Germany, 2010

[92] B. Arndt et al., “ Simulationsbasierte Analyse von ESD Schutzelementen auf Systemebene”, ESD-Forum 2009, Berlin, Germany, 2009.

[93] http://www.joinset.com/catalog/s28-35_whatsvaristor.pdf, Technical Note, Joinset.

[94] M. Scholz et al., “Mixed-Mode Simulations for Power-on ESD Analysis”, in Proc. EOS/ESD Symposium 2012.

[95] D. Johnsson et al., “Pre-Pulse Voltage from IEC 61000-4-2 Generators, the Hidden Threat”, in ESD Forum e.V., 2009.

[96] “Resistor Sensitivity to Electrostatic Discharge (ESD)”, Technical Note, Vishay foil resistors.

[97] “Surface Mount Resistors,” Technical Note, Panasonic Corporation.

[98] “J. Cain, “Comparison of Multilayer Ceramic and Tantalum Capacitors”, Technical Information, AVX Corporation.

[99] Y. Cao et al., “ESD Simulation with Wunsch-Bell based Behavior Modeling Methodology,” in Proc. EOS/ESD Symposium, 2011.

[100] W. Li et al., “A Scalable Verilog-A Modeling Method for ESD Protection Devices,” in Proc. EOS/ESD Symposium, 2010, pp. 1A. 1-10.

[101] M. Mayerhofer et al., “ESD Review Methodology using Transient Simulations on Circuit Level and its Application for JEDEC/ESDA HBM and IEC 61000-4-2 Pulses in Automotive Circuits,” in Proc. ESD Forum e.V., 2009, pp. 129-139.

[102] B. Deutschmann, et al., “Robustness of ESD Protection Structures against Automotive Transient Disturbances,” in Proc. APEMC, 2010.

[103] F. Magrini et al., “Correlation between System Level Robustness and TLP Results of ESD Devices,” in IEW, 2011.

[104] H. Wolf et al., “Pulsed Characterization of a reverse biased pn-Junction for ESD HBM Simulation.” Microelectronics and Reliability, Vol. 36, Issues 11-12, pp. 1711-1714, 1996.

[105] C. Torres et al., “Modular, Portable, and Easily Simulated ESD Protection Networks for Advanced CMOS Technologies,” in Proc. EOS/ESD Symposium, 2001.

[106] M. Khazhinsky et al., “ESD Protection for Advanced CMOS SOI Technologies,” in Proc. EOS/ESD Symposium, 2005.

[107] M. Stockinger et al., “Characterization and Modeling of Three CMOS Diode Structures in the CDM to HBM Timeframe,” in Proc. EOS/ESD Symposium, 2006.

[108] L. Lou et al., “An Improved Compact Model of Silicon-Controlled Rectifier (SCR) for Electrostatic Discharge (ESD) Applications,” IEEE Transactions on Electron Devices, Vol. 55, pp. 3517-3524, 2008.

[109] J. Willemen et al., “Characterization and Modeling of Transient Device Behavior under CDM ESD Stress,” in Proc. EOS/ESD Symposium, 2003.

[110] F. Lafon et al., “ESD Analysis Methodology - From IC Behavior to PCB Prediction,” in Proc. EMC Compo, 2007, pp. 941-947.

[111] B. Arndt et al., “Simulation based Analysis of ESD Protection Elements on System Level,” in IEW, 2010.

[112] H. Baumgärtner and R. Gärtner „ESD-Elektrostatische Entladungen, Ein Zuverlässigkeitsproblem in der Elektronikindustrie“, R. Oldenbourg Verlag München Wien 1997, ISBN: 3-486-23803-5

[113] ISO 10605: 2008 “Road vehicles -- Test methods for electrical disturbances from electrostatic discharge”.

[114] ISO 7637-1:2002(E) “Road vehicles –Electrical disturbances from conduction and coupling – Part 1: Definitions and general considerations,” Second edition 2002-03-15, www.iso.ch

[115] ISO 7637-2:2004(E) “Road vehicles –Electrical disturbances from conduction and coupling – Part 2: Electrical transient conduction along supply lines only,” Second edition 2004-06-15, www.iso.ch

[116] ISO 7637-3:1995(E) “Road vehicles — Electrical disturbance by conduction and coupling — Part 3: Vehicles with nominal 12 V, 24 V or 42 V supply voltage - Electrical transient transmission by capacitive and inductive coupling via lines other than supply lines,”

[117] White Paper 3: “System Level ESD Part I: Common Misconceptions and Recommended Basic Approaches,” Industry Council on ESD Target Levels, 2010

[118] M. Ammer et al., “How to Build a Generic Model of Complete ICs for System ESD and Electrical Stress Simulation,” in Proc. EOS/ESD Symposium, 2017.

[119] M. Ammer et al., “Simulation of System Level ESD Robustness using Advanced Behavioral IC Models under Consideration of PCB Parasitics,” in ESD Forum e.V., 2017.

[120] M. Ammer et al., “Modeling the Transient Behavior of MOS-Transistors during ESD and Disturbance Pulses in a System with a Generic Black Box Approach,” in Proc. EOS/ESD Symposium, 2018.

[121] M. Ammer et al., “Bringing the SEED Approach to the Next Level: Generating IC Models for System ESD and Electrical Stress Simulation out of Design Data,” IEEE Transaction on Electromagnetic Compatibility, January 2019.

List of Own Publications

1. V. Issakov, D. Johnsson, Y. Cao, M. Mayerhofer, M. Tiebout, W. Simbürger, and L. Maurer, “ESD Concept for High-Frequency Circuits,” in Electrical Overstress/ Electrostatic Discharge (EOSESD) Symposium, Tucson, USA, pp. 3A.4-1 - 3A.4-7, September 2008.

2. Y. Cao, W. Simbürger and D. Johnsson, “Rise-Time Filter Design for Transmission-Line Pulse Measurement Systems,” in German Microwave Conference (GeMiC), pp. 1-4, Munich, Germany, March 2009.

3. B. Arndt, F. zur Nieden, Y. Cao, S. Frei, F. Müller and J. Edenhofer, “Simulationsbasierte Analyse von ESD-Schutzelementen auf Systemebene,” in ESD Forum e.V., pp. 1-8, Berlin, Germany, December 2009.

4. Y. Cao, B. Arndt, F. zur Nieden, M. Stecher and S. Frei, “Charakterisierung und systematische Bewertung von externen ESD Schutzelementen,“ in Internationale Fachmesse und Kongress für Elektromagnetische Verträglichkeit (EMV), pp. 561-568, Düsseldorf, Germany, March 2010.

5. B. Arndt, F. zur Nieden, Y. Cao, J. Edenhofer and S. Frei, “Modellierung und Simulation von ESD-Schutzelementen mit VHDL-AMS,“ in Internationale Fachmesse und Kongress für Elektromagnetische Verträglichkeit (EMV), pp. 313-320, Düsseldorf, Germany, March 2010.

6. F. zur Nieden, B. Arndt, F. Kremer, Y. Cao, J. Edenhofer and S. Frei, “Vergleichbarkeit von ESD-Prüfungen auf IC- und Systemebene oder welchen Einfluss hat eine Reduzierung der IC-ESD-Festigkeit auf die Systemfestigkeit?“ in Internationale Fachmesse und Kongress für Elektromagnetische Verträglichkeit (EMV), pp. 247-255, Düsseldorf, Germany, March 2010.

7. Y. Cao, D. Johnsson, B. Arndt and M. Stecher, “A TLP-based Human Metal Model ESD-Generator for Device Qualification according to IEC 61000-4-2,” in Asia-Pacific Symposium on Electromagnetic Compatibility & Technical Exhibition on EMC RF/Microwave Measurement & Instrumentation (APEMC), pp. 1-4, Beijing, China, April 2010.

8. B. Deutschmann, F. Magrini and Y. Cao, “Robustness of ESD Protection Structures against Automotive Transient Disturbances,” in Asia-Pacific Symposium on Electromagnetic Compatibility & Technical Exhibition on EMC RF/Microwave Measurement & Instrumentation (APEMC), pp. 1-4, Beijing, China, April 2010.
9. Y. Cao, U. Glaser, S. Frei and M. Stecher, “A Failure Levels Study of Non-Snapback ESD Devices for Automotive Applications,” in IEEE International Reliability Physics Symposium (IRPS), pp. 458-465, Anaheim, USA, May 2010.
10. Y. Cao, U. Glaser, A. Podgaynaya, J. Willemen, S. Frei and M. Stecher, “Impact of Voltage Overshoots on ESD Protection Effectiveness for High Voltage Applications,” in 4th Annual International Electrostatic Discharge Workshop (IEW), Tutzing, Germany, May 2010.
11. W. Stadler, T. Brodbeck, J. Niemesheim, R. Gärtner, H. Gossner, W. Simbürger, D. Johnsson, M. Stecher and Y. Cao, “IC Characterization for ESD System: Is the Human Metal Model the Right Approach?” in 4th Annual International Electrostatic Discharge Workshop (IEW), Tutzing, Germany, May 2010.
12. Y. Cao, U. Glaser, H. Gietler, Patent DE 10201003006A1, US 20110304940 “Protection circuit”
13. B. Arndt, F. Mueller, J. Edenhofer, F. zur Nieden, Y. Cao and S. Frei, “Simulation Based Analysis of ESD Protection Elements on System-level,” in 4th Annual International Electrostatic Discharge Workshop (IEW), Tutzing, Germany, May 2010.
14. J. Willemen, D. Johnsson, Y. Cao and M. Stecher, “A TLP-Based Characterization Method for Transient Gate Biasing of MOS Devices in High-Voltage Technologies,” in Electrical Overstress/ Electrostatic Discharge (EOSESD) Symposium, pp. 239-248, Reno, USA, October 2010.
15. Y. Cao, U. Glaser, J. Willemen, S. Frei and M. Stecher, “On the Dynamic Destruction of LDMOS Transistors beyond Voltage Overshoots in High Voltage ESD,” in Electrical Overstress/ Electrostatic Discharge (EOSESD) Symposium, pp. 283-292, Reno, USA, October 2010, Best Paper Award.
16. Y. Cao, U. Glaser, J. Willemen, F. Magrini, M. Mayerhofer, S. Frei and M. Stecher, “A Wunsch-Bell based Behavior Model for On-Chip ESD Devices,” in 5th Annual International Electrostatic Discharge Workshop (IEW), Lake Tahoe, USA, May 2011.
17. F. Magrini, Y. Cao, B. Deutschmann and M. Mayerhofer, “Correlation between System Level Robustness and TLP Results of ESD Devices,” in 5th Annual International Electrostatic Discharge Workshop (IEW), Lake Tahoe, USA, May 2011.
18. Y. Cao, U. Glaser, J. Willemen, F. Magrini, M. Mayerhofer, S. Frei and M. Stecher, “ESD Simulation with Wunsch-Bell based Behavior Modeling Methodology,” in Electrical Overstress/ Electrostatic Discharge (EOSESD) Symposium, Anaheim, USA, September 2011, Best Paper and Best Student Paper Award.

19. Y. Cao and U. Glaser, “Statically Triggered Active ESD Clamps for High-Voltage Applications,” in Electrical Overstress/ Electrostatic Discharge (EOSESD) Symposium, Tucson, USA, September 2012.

20. Y. Cao and U. Glaser, “Novel Active ESD Clamps for High-Voltage Applications,” IEEE Transactions on Device and Materials Reliability, VOL. 13, NO. 2, June 2013.

21. J. Willemen, Y. Cao, J. Lebon, M. Mayerhofer and U. Glaser, “Photon Accelerated Turn-on of High-Voltage ESD Diode Breakdown,” in Electrical Overstress/ Electrostatic Discharge (EOSESD) Symposium, Las Vegas, USA, September 2013.

22. M. Mayerhofer, F. Magrini and Y. Cao, “Pulsed System Level Stress Considerations for On-Chip Protection Design beyond ESD by Automotive Examples,” in ESD Forum e.V., Berlin, Germany, November 2013.

23. M. Mayerhofer, F. Magrini and Y. Cao, “Pitfalls by applying pulsed EMC & ESD System Level Stress Requirements to On-Chip Protection Design by Automotive Examples,” in International Conference and Exhibition Smart Systems Integration, Vienna, Austria, May 2014.

24. M. Mayerhofer, F. Magrini and Y. Cao, “Wunsch-Bell Based Area Estimation beyond ESD Stress,” in 8th Annual International Electrostatic Discharge Workshop (IEW), Villard de Lans, France, May 2014

25. U. Glaser, J. Lebon, Y. Cao and J. Willemen, “TLP Failure Level Extraction despite Reflected Waves,” in Electrical Overstress/ Electrostatic Discharge (EOSESD) Symposium, Tucson, USA, September 2014.

26. Y. Cao, “ESD Troubleshooting Using Multi-level TLP,” in Electrical Overstress/ Electrostatic Discharge (EOSESD) Symposium, Tucson, USA, September 2014.

27. A. Rupp, U. Glaser and Y. Cao, „Active Clamp Design for On-Chip GUN Protection”, in Electrical Overstress/ Electrostatic Discharge (EOSESD) Symposium, Reno, USA, September 2015.

28. J. Willemen, M. Mayerhofer, U. Glaser, Y. Cao, A. Meiser, M. Hell, M. Stecher and J. Lebon, Patent US 9263619 B2, “Semiconductor component and method of triggering avalanche breakdown”

29. Y. Cao, A. Rupp and U. Glaser, Patent US 9225163 B2, “Combined ESD active clamp for cascaded voltage pins”

30. J. Willemen, M. Mayerhofer, U. Glaser, Y. Cao, A. Meiser, M. Hell, M. Stecher and J. Lebon, Patent application 20150249078, “Integrated circuit having an ESD protection structure and photon source”

31. A. Rupp, Y. Cao and U. Glaser, Patent application 20150207313, “Noise-tolerant active clamp with ESD protection capability in power up mode”

32. M. Ammer, K. Esmark, A. Rupp, F. zur Nieden, Y. Cao, M. Sauter and L. Maurer, “Advanced Behavior Modeling of ICs for System-ESD Simulation

with Destruction Limits in SPICE," in 11th Annual International Electrostatic Discharge Workshop (IEW), Tahoe City, USA, May 2017.

33. M. Ammer, K. Esmark, F. zur Nieden, A. Rupp, Y. Cao, M. Sauter and L. Maurer, "How to Build a Generic Model of Complete ICs for System ESD and Electrical Stress Simulation," in Electrical Overstress/ Electrostatic Discharge (EOSESD) Symposium, Tucson, USA, September 2017.
34. M. Ammer, K. Esmark, F. zur Nieden, A. Rupp, Y. Cao, M. Sauter and L. Maurer, "Simulation of System Level ESD Robustness using Advanced Behavioral IC Models under Consideration of PCB Parasitics," in ESD Forum e.V., Munich, Germany, October 2017.
35. M. Ammer, A. Rupp, Y. Cao, C. Russ, M. Sauter and L. Maurer, "Modeling the Transient Behavior of MOS-Transistors during ESD and Disturbance Pulses in a System with a Generic Black Box Approach," in Electrical Overstress/ Electrostatic Discharge (EOSESD) Symposium, Reno, USA, September 2018.
36. M. Ammer, Y. Cao, A. Rupp, M. Sauter and L. Maurer, "Bringing the SEED Approach to the Next Level: Generating IC Models for System ESD and Electrical Stress Simulation out of Design Data," IEEE Transaction on Electromagnetic Compatibility, January 2019.